DEVELOPMENT OF MULTI-PARAMETER FIBRE OPTIC CHEMICAL SENSOR SYSTEM BASED ON LONG PERIOD GRATINGS MODIFIED WITH FUNCTIONAL THIN FILMS

Jiri Hromadka

Thesis submitted to the University of Nottingham
for the degree of Doctor of Philosophy

JULY 2017

Abstract

This work focuses on the development of fibre optic long period grating (LPG) based chemical sensors and the fabrication and evaluation of the appropriate sensitive coatings.

Fibre-optic sensing platforms have been considered as a promising platform for the development of new sensors. The current progress in the field of LPG based chemical sensors is provided. The proof of concept of LPG based metal organic framework (MOF) sensors for the detection of organic vapours and carbon dioxide is presented. The inappropriate indoor air quality negatively affects human health. Nutrients growth in aquatic environments causes eutrophication and thus changes in the chemistry of the whole ecosystem. The practical use of LPG based ammonia and VOCs sensors is demonstrated in the fields of seawater and indoor air quality monitoring. Real-time monitoring and development of new sensors are highly needed in these areas. An array of three LPGs was created in a single optical fibre, multiplexed in the wavelength domain. Sensors were calibrated in the laboratory and the simultaneous measurement of the key indoor air quality elements was undertaken.

In conclusion the project has successfully demonstrated the use of novel fibre optic sensors in laboratory and real conditions that are in a good agreement with commercially used techniques.

Author’s published research papers

1. J. Hromadka, S. Korposh, M. Partridge, S. James, F. Davis, A. Charlton, D. Crump and R. Tatam (2017):”Multi-parameter measurements using optical fibre long period gratings for indoor air quality monitoring”, *Sensors and Actuators B: Chemical*, 244, pp 217-225.
2. J. Hromadka, S. Korposh, M. Partridge, S. James, F. Davis, D. Crump and R. Tatam (2017):”Volatile Organic Compounds Sensing Using Optical Fibre Long Period Grating with Mesoporous Nano-Scale Coating,” *Journal of Sensors*, manuscript accepted, in print.
3. J. Hromadka, B. Tokay, S. Korposh, S. James and R. Tatam (2015): “Optical fibre long period grating gas sensor modified with metal organic framework thin films,” *Sensors and Actuators B: Chemical*, 221, pp. 891-899.
4. J. Hromadka, B. Tokay, S. James and S. Korposh (2016):”Applications of Metal-Organic Frameworks in sensing,” in P. Reeves (Ed.), “Metal-Organic Frameworks (MOFs): Chemistry, Technologies and Applications,” Nova Science Publishers, pp. 55-88.
5. J. Hromadka, R. Correia and S. Korposh (2016): ”Fabrication of fiber optic long period gratings operating at the phase matching turning point using an amplitude mask,” Proceedings of the Sixth European Workshop on Optical Fibre Sensors, Limerick, Ireland, paper ID 9916, 99160Y.
6. J. Hromadka, M. Partridge, S. James, F. Davis, R. Tatam, D. Crump, S. Korposh (2015): ”Volatile organic compounds sensing with use of fibre optic sensor with long period grating and mesoporous nano-scale coating,**”** *Proceedings of OFS24th: International Conference on Optical Fibre Sensors, Curitiba, Brazil, paper ID* 9634, 96344K.
7. J. Hromadka, B. Tokay, S. Korposh, S. James and R. Tatam (2015): “Detection of volatile organic compounds using optical fibre long period grating modified with metal organic framework thin films,“ Proceedings of *OFS24th: International Conference on Optical Fibre Sensors, Curitiba, Brazil, paper ID* 9634, 96344N.

8. J. Hromadka, S. Korposh, M. Partridge, S. James, F. Davis, A. Charlton, D. Crump, S.-W. Lee and R. Tatam (2017):”Multi-parameter measurements using optical fibre long period gratings for indoor air quality monitoring,” *Proceedings of OFS25th: International Conference on Optical Fibre Sensors, Jeju, Korea,* accepted manuscript.

9. J. Hromadka, B. Tokay, S. James and S. Korposh (2017):”Metal-organic framework thin films on a surface of optical fibre long period grating for chemical sensing,” *Proceedings of OFS25th: International Conference on Optical Fibre Sensors, Jeju, Korea,* accepted manuscript.

Acknowledgements

I would like to express my gratitude to everyone who encouraged me in doing this work.

First of all, thanks to Dr Sergiy Korposh for his guidance throughout the project, his suggestions, comments, leadership and the opportunity to do my PhD research in Nottingham. Thanks for everything I have learned for the last years.

Thank you to prof. Matt Clark for the meetings we had and for his constructive recommendations which helped me think about the project from the different perspectives.

I would like to express my very great appreciation to Dr Ricardo Correia who never hesitated to offer his assistance and for providing his knowledge and expertise with experiments.

Thank you to prof. Steve Morgan and prof. Barry-Hays Gill for their comments and suggestions to my work during our regular group meetings and thank you to prof. Stephen James from Cranfield University for his help with papers reviewing and recommendations.

Thank you to Dr Begum Tokay to give me the introduction to work with MOFs and for her advice and suggestions from the field of chemical engineering. Thank you to Dr Leo Marques for his advice on dealing with chemicals and thank you to Dr Malcolm Woodward from Plymouth Marine Laboratory for his help with ammonia project.

Thank you to Martin Roe and Dr Nigel Neat for showing me the principles of using SEM and XRD analysing techniques. Thank you to Dr Richard Smith for giving me the introduction into the work with lasers.

Thank you to my colleagues and mates from the group working on fibre-optic sensors, to Ulises Hernandez, David Gomez, Dr Qimei Zhang, Liang Liang, Chong Liu and Wan Zaki Wan, for their support and help.

Thank you to my colleagues from the office, Dr Wenqi Li, Paul Marrow, Dr Rikesh Patel and Bo Tan for making the working environment as friendly as possible.

At last I would like to send the special thanks to prof. Martin Branis, who showed me the first real principles of research and became my adviser and mentor.

Table of Contents

List of Figures

List of Tables

List of acronyms

1,3,5-benzene tricarboxylic acid (BTC)

Ammonia (NH_3)

Carbon dioxide (CO_2)

Coupled charge device (CCD)

Dimethylformamide (DMF)

Dip coating (DC)

Emission test cells (ETC)

Ethanol (EtOH)

Fibre Bragg grating (FBG)

Fibre optic sensor (FOS)

Field and laboratory emission cells (FLEC)

Gas chromatography-mass spectroscopy (GC-MS)

Indoor air quality (IAQ)

Infrared (IR)

Langmuir-Blodgett (LB)

Layer by layer (LbL)

Limit of detection (LOD)

Long period grating (LPG)

Lossy mode resonance (LMR)

Metal organic framework (MOF)

Non-dispersive infra-red (NDIR)

Phase matching turning point (PMTP)

Photo-ionization detectors (PIDs)

Polyacrylic acid (PAA)

Poly(allylamine hydrochloride) (PAH)

Poly(diallyldimethylammonium chloride) (PDDA)

Post-synthetic modification (PSM)

Potassium hydroxide (KOH)

Refractive index (RI)

Relative humidity (RH)

Scanning electron microscope (SEM)

Sick building syndrome (SBS)

Silica nanoparticles (SiO_2 NPs)

Sodalite (SOD)

Surface plasmon resonance (SPR)

Tetrakis porphyrin dye (TSPP)

Transmission spectrum (TS)

Ultraviolet (UV)

Volatile organic compounds (VOCs)

X-ray diffraction (XRD)

Zeolitic imidazole framework (ZIF)

Chapter 1: Introduction

Monitoring of a wide range of physical, chemical and biological parameters have become an integral part of the modern society. The number of different sensing devices have increased rapidly during the last decades, but there is still a need for new sensors, especially those that can provide high chemical selectivity and sensitivity operating in real time.

For practical applications, the sensor performance should consider not only application specific sufficient accuracy but also the cost and energy efficiency, size and fabrication process. High priority should be given to the monitoring of parameters affecting human health or the environment such as air and water quality or waste and drink water treatment (1).

People spend about 90% of time in indoor environments (2). There is significant scientific evidence that inappropriate indoor air quality (IAQ) can negatively affect human health. The real-time monitoring of key IAQ parameters (such as temperature, relative humidity, volatile organic compounds (VOCs) or carbon dioxide (CO_2)) is at high interest to get more data and thus improve the situation (3).

Water represents the key resource for humans and water ecosystems cover more than 2/3 of the Earth’s surface. High concertation levels of nutrients (nitrate, nitrite and ammonia) lead to eutrophication - a massive change in chemical balance that can cause algae boom (4)(5). Management of this phenomenon efficiently requires remote and real-time nutrient monitoring (6).

The techniques currently used for air and water quality measurement consist of the expensive equipment that requires well-trained operators, sampling collection and is limited to *in situ* applications.

Optical fibres have become a common part of day to day life due to their use in telecommunications. They can transfer light over the long distances with low losses of the information. During the last several decades there is a strong scientific interest to use optical fibres for the development of the optical fibre chemical sensors. With appropriate modification, the fibres can monitor physical or chemical changes in the environment. The response of the modified fibre optic sensor is not only qualitative, indicating the presence or absence of the analyte, but it can also provide quantitative information, i.e. measure the concentration of the selected analyte (7).

Optical fibre devices are considered to be attractive sensing platforms for the future as they are small, lightweight, immune to electromagnetic interference and as such can be used in extreme conditions, enabling remote real time monitoring with no electrical power needed at the sensing point (8).

Recently there has been considerable interest in the development of fibre optic sensors and especially chemical sensors based on fibre optic platform which represents the rapidly developing hot topic in science (9)(10).

Fibre optic sensors include a various range of platforms including fibre Bragg gratings (FBGs) (11), long period gratings (LPGs) (12), sensors based on the interaction with an evanescent wave (13) or electromagnetic resonances (14).

The deposition of the sensitive layer onto the LPG surface can endow the sensor with the specific chemical sensitivity. Fibre-optic sensing platforms based on long period gratings (LPGs) with functional coatings have been used to measure various measurands, including ammonia (15), antigens (16), carbon dioxide (17), hydrogen (18), relative humidity (19) and VOCs (20).

The principle of operation of the fibre optic chemical sensor based on the functional coating is shown in Figure 1-1.

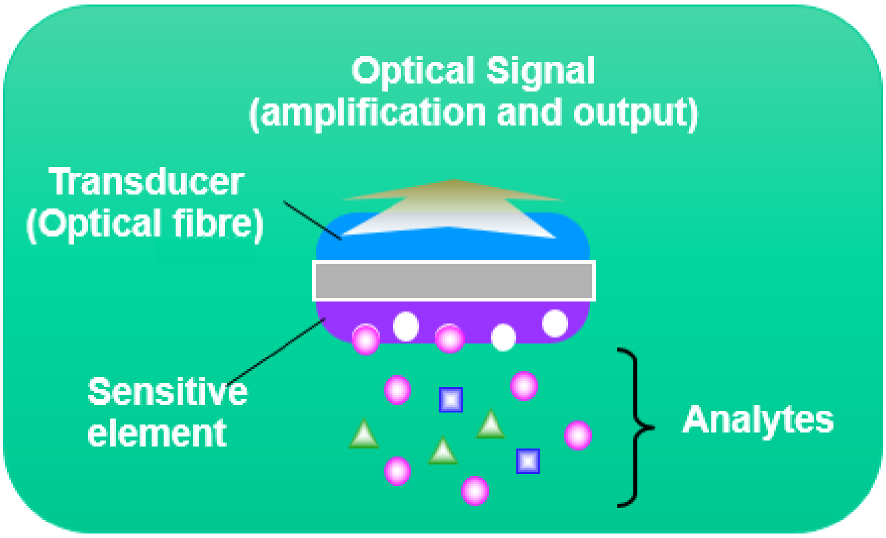

Figure 1-1: The schematic illustration of fibre optic sensor.

Development and fabrication of new fibre optic sensors (FOSs) covers the following research areas:

(i) discovery of the new materials suitable for application as the selective coatings,
(ii) employment of the existing materials that can be deposited onto various fibre optic sensing platforms,
(iii) optimisation of material properties (thickness, refractive index) and
(iv) deployment of the existing FOSs in the practical applications in real environments.

Metal organic frameworks (MOFs), because of their unique properties, offer an ideal platform for the development of the sensitive layer. They can be considered as crystalline materials with tuneable porosity, large internal surface area and organic functionality. The strong metal-oxygen-carbon bonds imbue the materials with high chemical and thermal stabilities (21).

There have been limited reports of MOF based sensors, but they indicate their potential to become powerful analytical devices (22). The main advantage is the high chemical selectivity enabled by the selection of the MOF with appropriate properties (23). However, there is a need to establish a suitable means of signal transduction to enable the use of MOFs for chemical sensing (24). This can be achieved by the fabrication of the MOF film on an optical sensing platform such as optical fibre.

An alternative approach could be based on the deposition of nanoparticles allowing to endow the fibre-optic platform with chemical sensitivity (25). As an example, silica nanoparticles have been used to measure relative humidity (26) and ammonia (15) or VOCs (27) (after infusion of the functional compound into the mesoporous structure of the film).

This thesis describes the project devoted to the development and fabrication of fibre optic chemical sensors using an LPG as a sensing platform. The complete pathways from the sensor design and lab tests to the real-world applications and multi-parameter sensing is demonstrated.

To the best of the author’s knowledge MOFs are used for the first time and comprehensive characterisation of these novel materials is provided. On the other hand, the work related to the nanoparticles enables to further investigate the performance of the FOSs coated with silica nanoparticles towards more specific applications in the real environment.

Chapter 1: Introduction

In this introductory chapter, a brief description of the project is given, the aims and objectives are stated and the structure of the thesis is provided.

1.1 Aims and objectives

1.1.1 Aims

The main aim of the project is to discuss and evaluate the possibilities to use fibre optic chemical sensors with functional coatings for multi-parameter measurements and implement the idea in the practise by fabrication of the sensors and the sensing arrays.

The possibility to use different types of materials from the MOF family deposited onto the optical fibre LPG as the selective material to enable chemical – particularly VOCs and CO_2 sensing is considered and the sensor are developed.

Attention is also given to practical applications of LPG based sensors coated with silica nanoparticles in the field of air and seawater quality.

The potential implementation of LPG coated by the sensitive layer to the multi-parameter sensing array and the use of this array in the real environment is investigated.

1.1.2 Objectives

The following set of objectives have been selected to fulfil the aim of the project:

- The literature review to provide the appropriate summary of the background knowledge in the field with main focus on:
  - Background information about i) IAQ, its parameters and currently used techniques for their measurement and ii) the role of ammonia in aquatic ecosystems and its detection principles;
  - Understanding the types, principles and fundamentals of fibre optic sensors, especially LPG, the theory and applications;
  - Selection of functional coatings applicable to the optical fibres, their types, properties and deposition techniques;
  - Summarize the properties of MOFs with regard to their application in sensing;
  - Selection of the appropriate MOFs that are applicable to the sensing purposes with the target of chemical vapour sensing; the properties of the MOF, the feasibility of its fabrication and possibilities of its deposition on optical fibre will be considered.

- Perform the deposition of MOF thin film on an optical fibre LPG and test the chemical sensitivity of the sensor:
  - Optimize the selected fabrication procedure of the desired MOF;

- Undertake a deposition of MOF film on the different types of substrates – glass, quartz and silica with the aim of subsequent structural characterisation;
- Learn the fundamentals of scanning electron microscope (SEM) imaging and use these knowledge in practice of taking SEM images of the substrates with MOF films;
- Evaluate the properties of the film using SEM and test the crystalline structure by x-ray diffraction (XRD) pattern analysis
- Evaluate the film thickness using ellipsometry;
- Conduct the laboratory trials to show the sensor's chemical sensitivity and optimize the thickness of the film;
- Familiarize with Spectrum Interrogation Routine (SIR) and getting advanced skills of Origin (both of them are software for transmission spectra evaluation);

o LPGs fabrication:

- Gain the theoretical knowledge about using lasers with accent on fabrication of LPGs with the use of UV laser beam technique;
- Design set up for inscription of LPGs in the core of the optical fibres; via amplitude masks and using point by point approach employing UV laser;
- Fabricate LPGs relevant to the project.

- Evaluation of the possible deployment of LPG based sensors and sensing array for the real environment applications:
  - Identify the appropriate environments for testing the performance of the sensor;
  - Plan and conduct experiments;
  - Benchmark sensor performance with the commonly used techniques.

- Preparation of the obtained results for the publication in scientific journals and conferences

1.3 Structure of the thesis

This thesis consists of 8 chapters, starting with introduction, Chapter 2 covers the theory and literature review and Chapter 3 describes the methodology of LPG fabrications via UV laser beam. Chapter 4 and Chapter 5 show the new development of MOF based LPG sensors and Chapter 6 focuses on the practical applications of the LPG sensors in the fields of air and seawater quality. Chapter 7 presents the idea of LPGs multiplexing and the use of the optical fibre sensor array for indoor air quality monitoring. The last chapter concludes the work and provides some suggestion for the future directions. Each Chapter is briefly summarized below.

Chapter 1: Introduction shows the introduction into the topic, presents aims and objectives of the project and thesis structure

Chapter 2: Background information and Literature review covers the areas of the indoor air quality and ammonia in seawater, with concern on the currently used measurement techniques. Fibre optic sensors, their theory and applications focusing on sensors based on long period gratings are described in the second subsection along with the brief summary of LPG fabrication techniques and newly developed LPG based chemical sensors. The last subsection gives the introduction into MOFs emphasizing the thin film synthesis and potential use of MOFs for sensing applications.

Chapter 3: LPG fabrication describes the experimental set up and fabrication process of LPGs that were used in the project using UV laser beam via the point by point technique and via the amplitude masks.

Chapter 4: Organic vapour sensor based on LPG modified with ZIF-8 reports the progress over the development and fabrication of ZIF-8 LPG based organic vapour sensor. This chapter provides the background information about ZIF-8, describes the methodology of the film fabrication, deposition onto the surface of LPG and characterization by SEM and XRD. The chemical sensitivity towards organic vapours is examined and presented.

Chapter 5: Carbon dioxide sensor based on LPG modified with HKUST-1 shows the potential of carbon dioxide monitoring using an LPG based sensor. This chapter has similar structure to Chapter 4 and gives the background information about HKUST-1, including the methodology of the film fabrication and deposition onto LPG sensors and characterization by SEM and XRD. The chemical sensitivity towards CO_2 is examined and presented.

Chapter 6: Chemical sensors based on LPG coated with silica nanoparticles shows two practical applications of LPG based chemical sensors in the field of air and seawater quality monitoring. The performance of the LPG based ammonia and VOCs sensors coated with silica nanoparticles infused with a sensitive element is described. Fabrication, lab calibration and the field experiments procedures are provided.

Chapter 7: Multi-parameter sensing using an LPG array presents the fabrication of LPG array consisting of three LPGs for simultaneous detection of temperature, relative humidity and volatile organic compounds. The performance of the sensor, its fabrication, lab experiments and field measurement of indoor air quality is reported.

Chapter 8: Conclusions represents a final chapter and provides the summary of the thesis with suggestions for the future work in the field of LPG based chemical sensors.

Chapter 2: Background information and Literature review

This chapter covers the literature review and provides the background information related to the project. It contains three main parts. At the beginning, the brief introduction into real world measurement challenges that will be described in this thesis such as indoor air and water quality is given. The summary of currently used techniques for the detection of volatile organic compounds, carbon dioxide and ammonia (in liquid phase) is provided and their main limitations are discussed. These parameters were chosen in respect to the newly developed sensors presented in Chapters 4-7.

The second part explains the principle of operation of fibre optic sensors in general with the main focus on LPGs followed by the description of the different LPG fabrication techniques. The principle of the sensitivity of LPGs to physical parameters such as temperature and external index of refraction is described. The deposition techniques used to endow the LPG with desired sensitivity to the analyte of interest are briefly discussed. The first part of this section is devoted to the actual progress in the field of the chemical and bio-chemical sensors based on optical fibre LPG.

The third part of this review chapter will provide the reader with the brief overview of properties of MOFs. The methodology and progress in the field of fabrication of thin films is discussed in depth and the last subsection is given to the use of MOFs in a sensor development.

Chapter 2: Background information and Literature review

2.1 Background information related to the project

2.1.1. Indoor air quality

During the last decade, interest in air quality control has shifted from outdoor to indoor environments, reflecting the changes in lifestyle associated with increasing levels of urbanization (28).

IAQ is influenced by a mixture of physical, chemical and biological factors, each with different sources and associated adverse health effects (3). Temperature, relative humidity (RH), carbon dioxide and VOCs represent the key factors of interest (29).

Temperature extremes represent a serious risk for human health, where low temperature during winter months can cause cardiovascular diseases and death within susceptible groups such as elderly people (30). Extreme heat can cause a range of adverse health effects with different severity, from heat rashes to heat stroke. Heat also negatively affects the respiratory and cardiovascular systems (31). Low RH can cause irritation of the eyes and mucous membranes of the respiratory system, increase sensitivity to aerosol particles and facilitate the spread of airborne diseases (32). On the other hand, high RH leads to higher occurrence of allergies that affect negatively respiratory systems, such as asthma, respiratory infections, coughs, wheeze and dyspnoea (33). The recommended values of RH for human well-being and that minimize possible adverse health effects are in the range of 40 to 60% (32).

Both temperature and RH are also essential parameters in the assessment of the performance of a building, because of their influence on energy demand. The reduction of the energy needed to obtain the appropriate IAQ is important for both people's health and for utility costs. There is a need to develop technologies for future homes, which optimise performance against these criteria (34).

The theoretical background concerning VOCs and carbon dioxide will be discussed in the following subsections.

2.1.2 Volatile organic compounds

VOCs in the indoor environment comprise a broad mixture of chemicals that are present in household products and that leaks from materials commonly present indoors (e.g. paints and furniture). VOCs are also product of combustion processes such as heating or smoking and their concentrations can increase by up to a 1000 times over short time periods. VOCs cause various short and long-term (delayed) adverse health effects (35). Some are proven as animal or human carcinogens, however not all VOCs represent a significant health risk. They are also determined as one of the possible causes of sick building syndrome (SBS) (36)(37). The material leakage represents the important indoor source of VOCs (one half, the other one is associated with human activities) the overall acceptable emission rate of the materials should be kept below 30 $\mu g.m^{-2}. h^{-2}$ (the approximation has been done for the size of the room, possible leakage surface area and ventilation rate) (37).

The legal framework concerning the testing of VOCs leakage from paints is covered by EU 2004/42/CE which sets the limits for VOCs emissions which occur due to use of organic solvents in certain paints, varnishes and vehicle refinishing products. The guidelines for material testing are also covered by ISO standards, where following are the most appropriate EN ISO 16000-9 - *Indoor air - Part 9 - Determination of the emission of volatile organic compounds from building products and furnishing - Emission test chamber method* and EN ISO 16000-10 *Determination of the emission of volatile organic compounds from building products and furnishing – Emission test cell method)*.

Passive flux sampling, emission test cells (ETC) and field and laboratory emission cells (FLEC) have been considered to be useful for material leakage measurements to determine the level of VOCs. Gas chromatography-mass spectroscopy (GC-MS) is used for VOC analysis in this case (38).

Passive sampling does not require an air pump and an air-flow meter, but very volatile agents can be lost because of the back diffusion. Passive samplers provide average concentration data for an exposure period that is often days or weeks to achieve appropriate sensitivity. When the concentration dynamic (changes of exposure in time) is required to be determined then the active (pumped) approach is applied (39). However, longer time averages may be more relevant when possible health effects of the pollutant are considered, but in the case of the chronic effects the concentration dynamic are in the centre of interest (39).

Passive badges use the charcoal or other medium as an adsorbent. The badge is left in the environment during the sampling period (commonly from 8h to 1 week) and then is sent to the lab for the further analysis (35).

The most precise and also the most expensive approach is active sorption/chemical analysis. The sampled air is flowed by the pumps into the tubes which include the sorbent of organic polymer resins (e.g. Tenax) or activated charcoal. The sorbent traps the present VOCs and the GC-MS is used for VOCs analysis. The VOCs are measured individually and then total amount of VOCs (TVOCs) is subsequently calculated (35).

Field and laboratory emission cell (FLEC®, Chematec) can be small and portable with typical volume of 0.035 dm^3 and can measure emission levels from an area of 0.0177 m^2. The chambers are usually fabricated from glass or steel, because there should be no reaction between the surface of the chamber and the analyte of interest. The condition inside the cells can be controlled and FLECs have the advantage that they can be used anywhere even outside the lab. The air flows through the cell to the tubes and trapped VOCs are then analysed by GC-MS (38).

Photo-ionization detectors (PIDs) represent the real time measuring approach, but the accuracy depends on the type of VOCs present in the actual mixture (35).

2.1.3 Carbon dioxide

Carbon dioxide is the product of the metabolism of organisms and it is naturally present in the atmosphere in levels between 350-400 ppm, with higher concentrations in urban areas and the levels are of scientific and public concern because of the global warming impact and climatic change.

The detection of carbon dioxide is necessary and important in a wide range of applications including indoor air quality (3) and food industry (40).

The monitoring of dissolved carbon dioxide (and related inorganic carbon) e.g. in seawater is at high interest and represents the other area where the new sensors for real-time and remote measurement are desired (41) as well as for monitoring of soil respiration (42).

Non-dispersive infra-red (NDIR) sensors (based on the effect of CO_2 absorption of light in infra-red region) represent the currently most used technique for the detection of carbon dioxide however their use is limited by the high cost typically in a range of hundred pounds and can be too bulky for some applications. The performance of the sensor could be also affected by other gases or by high concentration of water vapour. The other disadvantage of NDIR sensors is represented by particulates (40).

GC-MS can be used for the detection of CO_2 however this approach is more expensive than NDIR sensors and cannot be used for real-time measurements.

2.1.4 Ammonia

Ammonia is one of the nutrients affecting the water quality and the chemical balance of the aquatic ecosystems.

Ammonia (NH_3) is a natural compound present in water environments taking involvement in nitrogen cycle and affects the biochemical processes such as a phytoplankton growth (43). The source of the naturally present NH_3 comes from sediments as the results of bacterial decomposition of organic matter (44). Higher concentrations can be affected by human activities, where ammonia is derived from wastes and fertilizers (44).

The lowest concentrations in the range of 10-100s of nM were observed in the open ocean and some unpolluted freshwater (45)(46), going to increase to single units µM level in coastal seawater and most continental water ecosystems. The concentration in mM levels could be found due to the anthropogenic pollution or due to the extreme biological activity (47)(48).

The increase of ammonia level associated with increase of bacteria population leads to the reduction of dissolved oxygen and subsequently causes decrease in species diversity (44). Ammonia at high levels is also directly toxic to fish species (49).

Ammonia level in water is measured by colorimetric technique, where the most of the methods use the spectrophotometric determination of the indophenol blue (IPB) complex formed by the reaction of ammonia with phenol and hypochlorite, in alkaline pH (50). The limit of detection (LOD) of this technique of 0.6 µM was presented with possible further improvement using a long-path liquid waveguide capillary cell (LWCC) (51). However the main disadvantages of this approach consist of the complicated operation and necessity to use chemical reagents (52).

2.1.5 Background information – Conclusions

This subsection described the importance of the some of the key parameters of air and water quality and summarize the commercially used techniques for their measurement, Table 2-1.

Table 2-1: Comparison of the currently used commercial techniques for the selected analytes.

M*	Technique	Sensitivity	Cost [£]	Size	Real Time	In-situ use	Ref
EtOH [g]	Electro-chemical/ IR absorption	Ppm range	10s-100s	≈10x15x5 cm	YES	YES	(53) (54)
CO_2 [g]	NDIR	≈10s ppm	100s	≈10x15x10 cm	YES	YES	(40)
VOCs [g]	PID/FID	Ppm range	100-10^3s	≈10x15x10 cm	YES	YES	(35)
NH_3 [l]	Colouri-metry	≈10s-100s nM	10^4 s	2x1x0.3 m	NO	Limit-ed	(50)
All [g] [l]	GC-MS / LC-MS	Ppb range	10^5-10^6 s	≈ 1x1x2 m	NO	NO	(55) (56) (57)

*M = measurand; [g] and [l] sign for gas and liquid phase of the measurand

The high demand for less expensive and real-time sensors was observed, which can be satisfied by the development of the novel optical fibre optic sensors.

2.2 Fibre optic sensors

2.2.1 Introduction

The optical fibre has a cylindrical shape and it contains the core with high refractive index (RI) and the cladding with lower RI. The whole fibre is commonly covered by plastic buffer (jacket) to enable the protection against any mechanical damage, Figure 2-1.

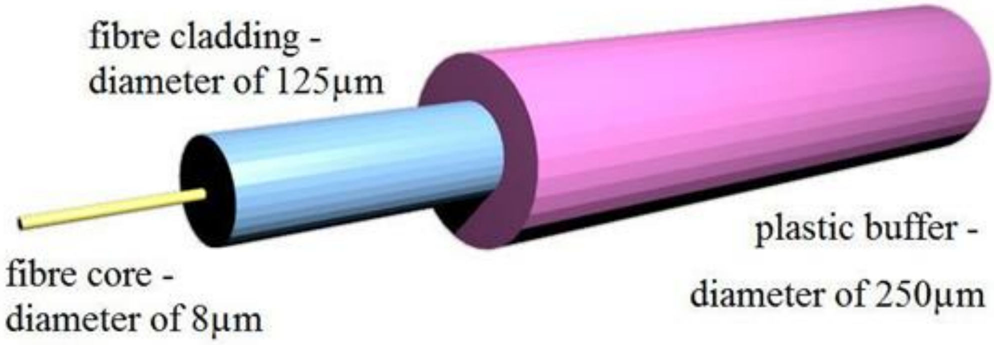

Figure 2-1: Scheme of typical single mode optical fibre.

The light propagates along the optical fibre via total internal reflection. Optical fibres can be single or multi-mode based on the number of the modes propagating in the fibre core. All of the fibres used in this work were single mode type.

It has been shown that optical fibres have unique properties which enable them to be highly suitable for the sensing applications (8).

In general, there are two approaches for FOS implementation: 1) intrinsic – the fibre itself is used as the transducer measuring a change in the ambient conditions, 2) extrinsic – the fibre enables only the transmission of light to and from the measurement region (7). When the light from the light source with appropriate wavelength range – associated with the material of the fibre and used sensor element is guided in optical fibre through the sensing area the transmission or reflection spectrum is measured by photo detector connected to the interrogation unit and the data are further evaluated using specialized software.

The possible applications for fibre optic sensors cover chemical and biological sensing, environmental monitoring or medical diagnosis. The key advantage of fibre optic sensors is their potential to produce highly sensitive and selective sensors (7)(10)(58). Chemically specific sensors can be fabricated by deposition of chemically sensitive nano-scale coatings onto the surface of the fibre (25)(59).

The optical fibres commonly used in telecommunications are not inherently sensitive to the physical or chemical factors in the surrounding environment (indeed any sensitivity is a confounding factor for them).

The fibre should be appropriately modified, for instance via fabrication of the fibre grating (11)(12), via tapering (60) or bending (61) the fibre and via etching the cladding (62) to obtain such sensitivity. Other option is to use of optical fibres to create an interferometer (26) (63) or deposit a coating over the fibre to create a sensor based on electro-magnetic resonance (64).

2.2.2 Sensing platforms used in fibre optic sensing

When the cladding is removed or etched or when both the fibre core and cladding are tapered then the evanescent field of the light propagating through the waveguide (fibre) interacts with the surrounding environment. When the specific sensitive coating is applied at this region the changes in the absorbance between this coating and the evanescent wave can be observed (7). The operation principle of an evanescent wave sensor based on tapered fibre is shown in Figure 2-2, where an example of transmission spectrum is shown in Figure 2-3.

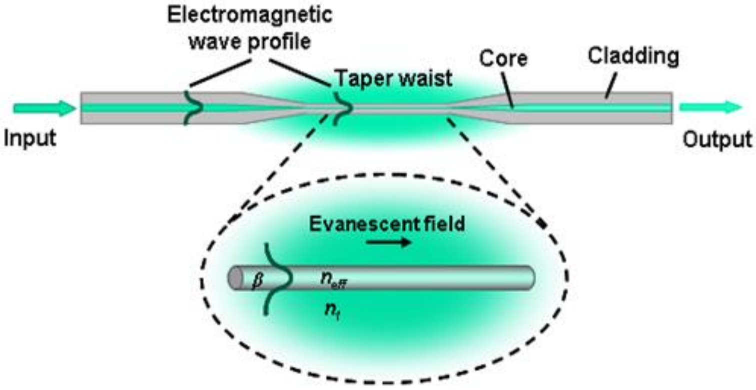

Figure 2-2: Schematic illustration of operation principle of the sensor based on the tapered optical fibre.

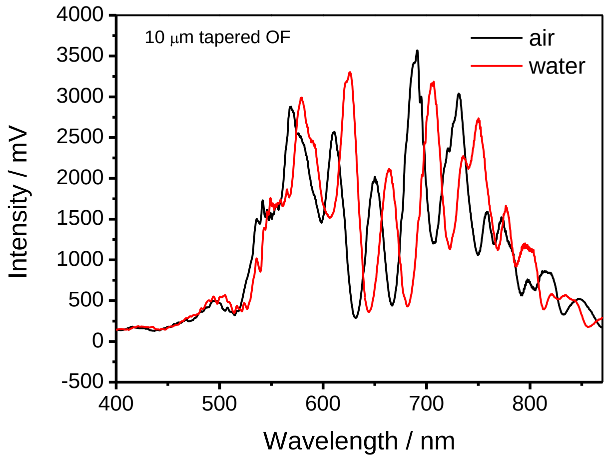

Figure 2-3: Example of the optical signal response of evanescent wave based tapered fibre-optic sensor (black and red line show the transmission spectra of the sensor in air and water).

The “U” shape bended fibre could be used to enhance the penetration depth of light transferred into the evanescent field and thus to enable the higher interaction between the evanescent wave and the coating/surrounding environment. As an example, “U” shape bended fibre optic sensors were developed for the detection of ammonia (61), methanol (65) or pH (66).

Changes within the interaction between the evanescent wave and the coating can be observed via surface plasmon resonance (SPR) or lossy mode resonance (LMR).

SPR technique has been considered as the gold standard in the field bio-sensing due its label free and real-time approach. The light propagates through the optical waveguide and then reacts with the functionalized usually gold substrate inducing the change in the optical signal. The amount of this change is relevant to the amount of the refractive index change induced by the binding of the analyte and thus indicates its concentration (67), Figure 2-4. On the other hand, it is necessary to use noble metal as the substrate for the sensitive layer and there is need to use a polarized light propagating through the waveguide (68).

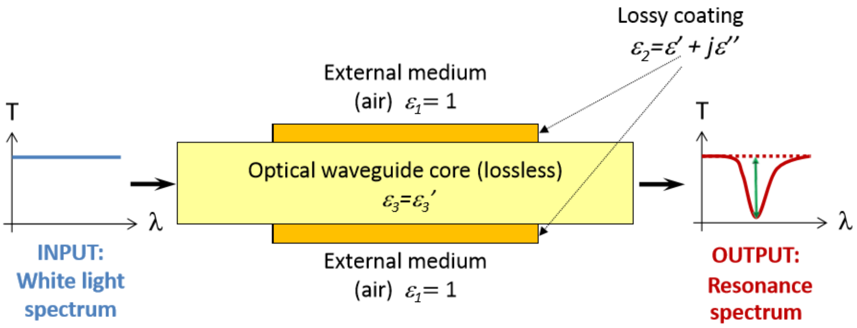

Figure 2-4: Schematic illustration of resonance based fibre optic sensor (68).

As an example, a sensor based on SPR and cladding removed plastic optical fibre had been used for the detection of uric acid (69) and SPR sensors have been reviewed in (67).

When a specific condition of the coating permittivity are fulfilled then the light is coupled into a different propagating medium and this loss of the transmitted light is referred as LMR. Semiconductor and polymers have been considered as useful coatings to enable a coupling between waveguide modes and a specific lossy mode of the thin film (68)(70).

Relative humidity and ammonia sensors were developed using LMR principle of operation, where the sensing platform was based on the etched cladding and tapered optical fibre respectively (62)(71).

Optical fiber interferometers represent the other type of fibre optic sensors. The principle of operation of any fiber optic interferometer is based on the interference between two beams that propagate through different optical paths of a single fiber or two different fibers (72). The following type of interferometers were used as fibre optic sensors: i) Fabry-Perot, ii) Mach-Zehnder, iii) Michelson and iv) Sagnac loop.

The Fabry-Perot-fibre optic interferometers can be developed via fabrication of an air gap or semi-reflecting mirror into the fibre (72)(73)(74) however the difficulties in the fabrication process have been considered as the main limitation for their applications (73). The easiest option is the deposition of the sensitive coating onto the tip of the fibre, as an example to fabricate an relative humidity sensor (26)(75). Two optical interfaces are represented with the fibre tip-coating and coating-environment each with characteristic Fresnel coefficients for reflection. The changes within the reflected optical signal are due to humidity induced changes of the coating (absorption of water vapour lead to the change of the refractive index) (26)(76). Similarly the carbon dioxide sensor has been presented with use of phenol as the sensitive material (77).

Mach-Zehnder interferometers in principle use two independent arms for the propagating light, the sensing arm and the reference arm. The sensing arm is exposed to the changes in the measurand of interest while the reference arm is isolated from the external variation (72). The effect of splitting and recombining of the incident light can be obtained by several ways in the fibre as schematically shown in Figure 2-5.

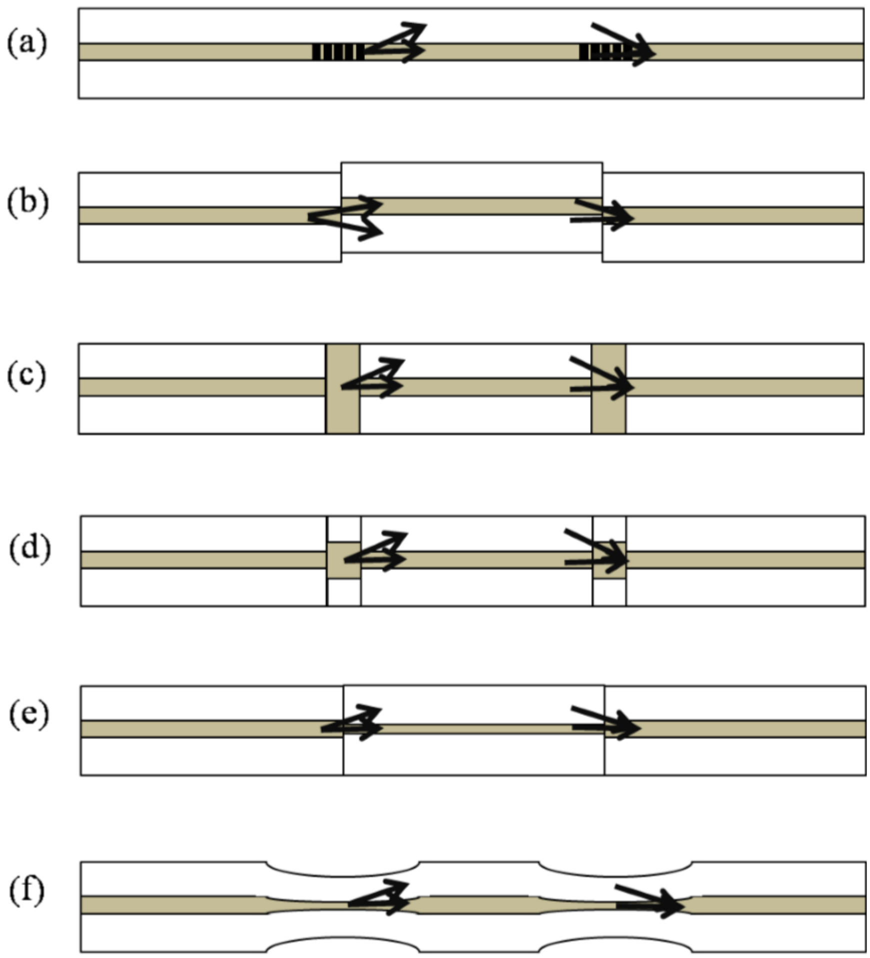

Figure 2-5: Examples of different types of Mach Zehnder interferometers using: a) pair of LPGs, b) core mismatch, c) air hole collapsing of photonic crystal fibre, d) segments of multi-mode fibre, e) segments of small core single mode fibre and f) fibre tapering (72).

Mach-Zehnder interferometer can be designed to be insensitive to temperature and bulk refractive index and response only to the changes of the selected chemical analyte. This is highly desirable for the use of the sensor in real environments, where both temperature and bulk RI represent the confounding factors for the chemical sensor performance (63).

Michelson interferometer acts as a half of Mach-Zehnder device. The light propagating through the fibre is split into two arms and then both of them are reflected with use of the mirror. The in-line Michelson interferometer is schematically shown in Figure 2-6. The coupling of the light from the fibre core can be done by the same methods as for Mach-Zehnder interferometer (72) and thus any LPG based sensor operating in reflection mode acts as Michelson interferometer. As an example, this arrangement had been demonstrated for a relative humidity sensor (78).

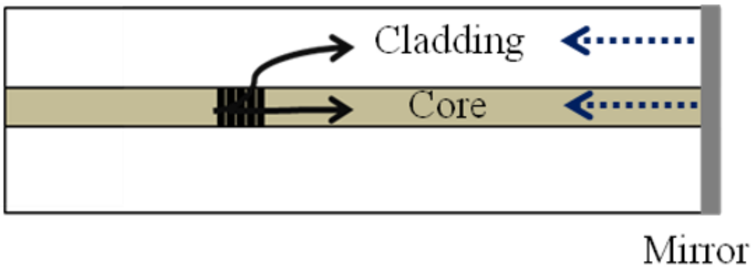

Figure 2-6: Schematic illustration of Michelson interferometer (72).

The principle of operation of Sagnac loop interferometer is based on the two beams propagating through the loop in counter directions with different polarization states (72), Figure 2-7. Optical path length difference is determined by the polarization dependent propagating speed of the mode guided along the loop (72).

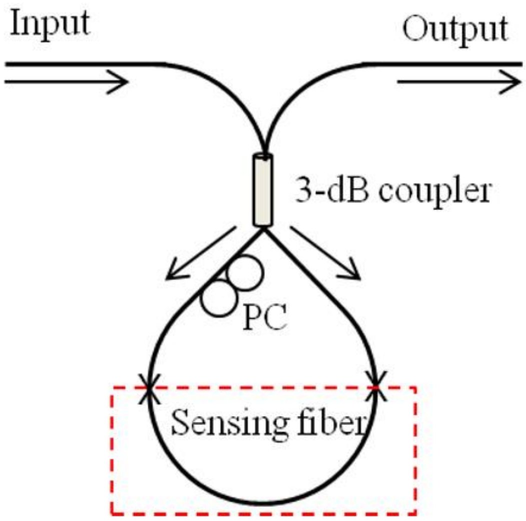

Figure 2-7: Schematic illustration of Sagnac loop interferometer (72).

High phase sensitivity is obtained using high birefringent or polarization maintaining fibres (72). Doping with germanium can increase thermal expansion coefficient inducing high birefringence variation and thus higher sensitivity can be obtained (79). On the other hand, the temperature sensitivity can be highly reduced using photonic crystal fibre to design a temperature insensitive strain sensor (80).

Inscription of the fibre grating into the setting with the Sagnac loop can lead to multi-parameter sensing, where simultaneous detection of strain and temperature (81) or refractive index and temperature (82) can be maintained.

Among the different types of fibre-optic sensors, those based on gratings, specifically long period gratings (LPGs), have been employed extensively for refractive index measurements (9) and for monitoring associated chemical processes (9), since they offer wavelength-encoded information, which overcomes the referencing issues associated with intensity based approaches.

Fibre grating consists of the periodic perturbation of the refractive index of the fibre core. There are two types of fibre gratings: i) fibre Bragg grating (FBG) (sometimes also called short period grating) and ii) long period grating (LPG). The principle of operation of both is schematically shown in Figure 2-8.

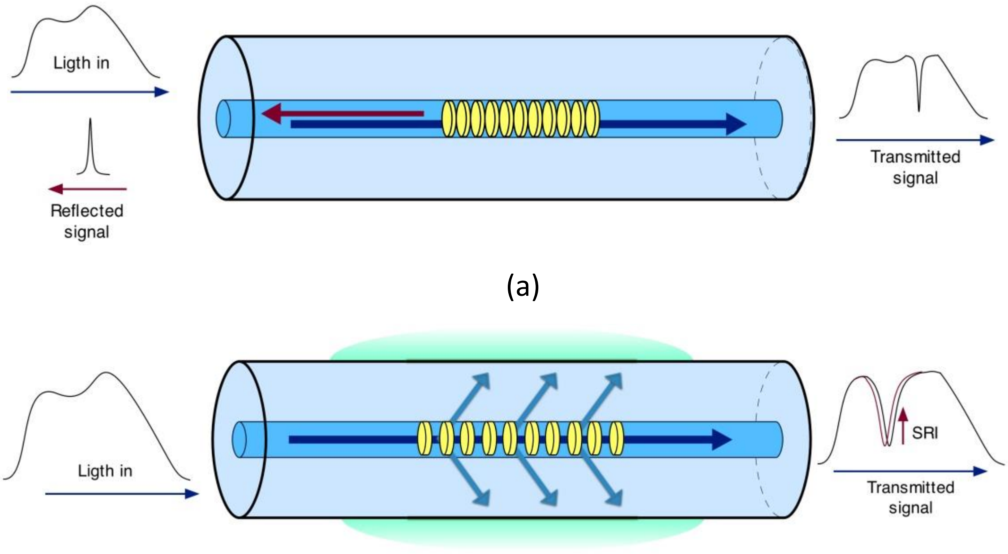

(a)

(b)

Figure 2-8: Scheme of a) the backward coupling of the light propagating through the FBG and b) the forward coupling of the light propagating through the LPG (83).

According to the coupled mode theory, the coupling of the propagating light could occur in the same or opposite directions (84). Contra-directorial (backward) coupling is observed for FBGs while the case of co-directorial (forward) coupling is represented by LPG (85).

However this classification can be used only where the grating is made at the right angle to the propagating light. The situation is much more complicated for both types of tilted gratings and the both cases of coupling can occur, which will not be covered in this work (85).

The FBGs are more suitable for measurement of physical parameters such as strain and temperature (11). The fibre with Bragg grating acts as a dichroic mirror and the wavelength with the highest reflectance is called Bragg wavelength and can be obtained using Equation 1.

$$\lambda_B = 2n_{eff}\Lambda$$

Equation 1

where Λ is the period of the grating, n_{eff} is the effective refractive index of the fibre core and λ_B is the reflected Bragg wavelength.

The principle of operation of FBG based fibre optic sensors is following: any external factor which can cause the change of Λ or n_{eff} can be measured as the function of the change of λ_B. This determines primary use of FBG for sensing the temperature and strain. A longitudinal deformation affects n_{eff} due to photo-elastic effect and Λ due to the increase of the grating pitch. Temperature affects n_{eff} due to thermal dilation and due to thermo-optic effect (86).

The grating period of an FBG is about 0.5 µm which is much smaller than grating period of an LPG which varies from tens to several hundred of micrometres (85).

This work focuses on the development of FOSs based on LPGs as they offer several advantages over the other (fibre-optic) sensing platforms: i) LPG shows a narrow bandwidth and, ii) high transmission loss of the attenuation bands; iii) the signal relies on the wavelength encoded information, iv) they offer structural stability and easy handling (in comparison to tapered and etched fibres).

The operation principle of an LPG based sensors is covered in the next subsection.

2.2.3 LPG based fibre optic sensors – principle of operation

LPG couples light between the fundamental core mode and the cladding of the fibre. The change of the transmission spectra can be observed due to this coupling and this change is shown as the series of loss or resonance bands (each correspond to one cladding mode). The cladding modes are sensitive to the surrounding environment and the change e.g. in temperature or refractive index causes the change in the transmitted spectrum (12). The principle of operation is shown in Figure 2-9.

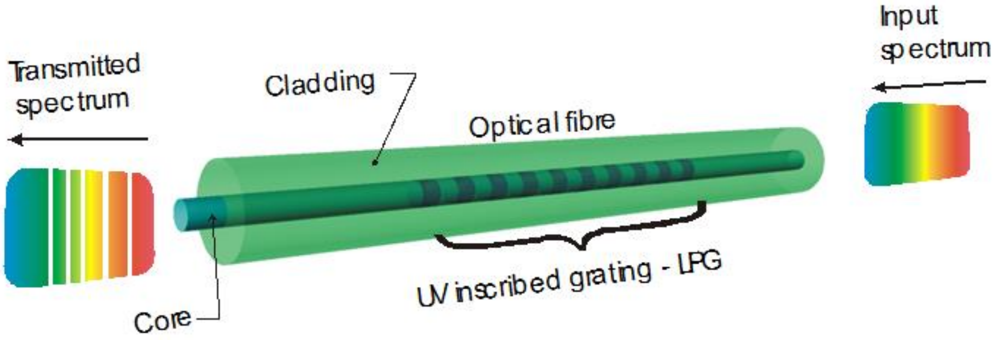

Figure 2-9: Scheme of LPG operation principle (7).

The large radius of the cladding makes it a multimode waveguide. Efficient coupling between the core and the cladding is achieved when both have a similar electric field. This limits the number of the coupling modes (87).

The cladding modes propagate along the fibre axis and decay rapidly due to scattering loses at the cladding-air interface. As the light is coupled to the discrete cladding modes, each associated with specific wavelength, LPG acts as a wavelength-dependent loss element (88)(89).

The series of attenuation bands occur in the transmission spectrum and the highest transmission loss is obtained at certain wavelengths (further referred as central wavelengths). The association between these wavelengths, the period of the grating and the effective refractive indices of the core and the *i*-th mode of the cladding can be theoretically expressed in phase matching condition. The central wavelength λ_{cw} of any LPG can be obtained according to Equation 2:

$$\lambda_{CW} = [n_{eff\,core} - n^{i}{}_{eff\,clad}]\,\Lambda$$

Equation 2

where $n_{eff\ core}$ and $n^{i}_{eff\ clad}$ are the effective refractive indices of the fibre core and i-th mode of the cladding, respectively (12)(89).

The phase matching curves can be obtained by fulfilling the Equation 2 where the central wavelength is plotted as the function of LPG period (12), Figure 2-10.

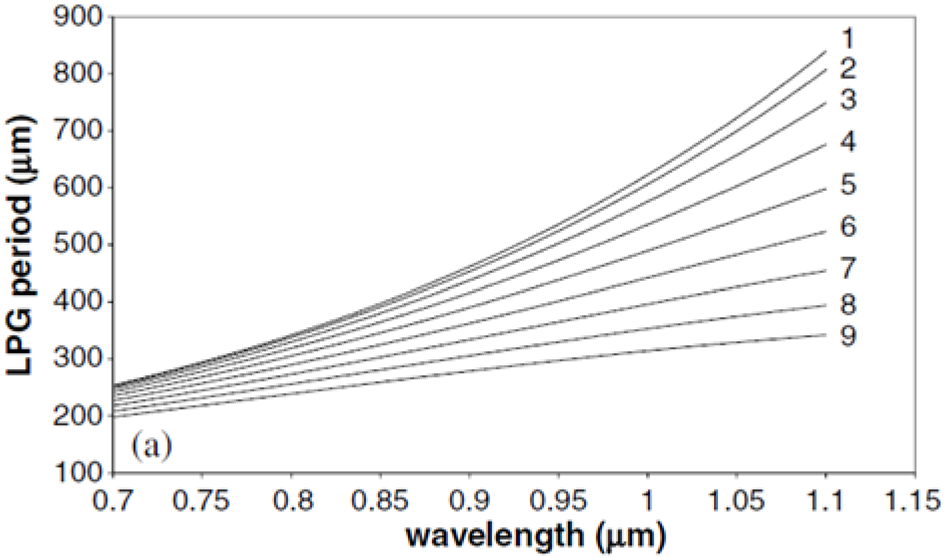

(a)

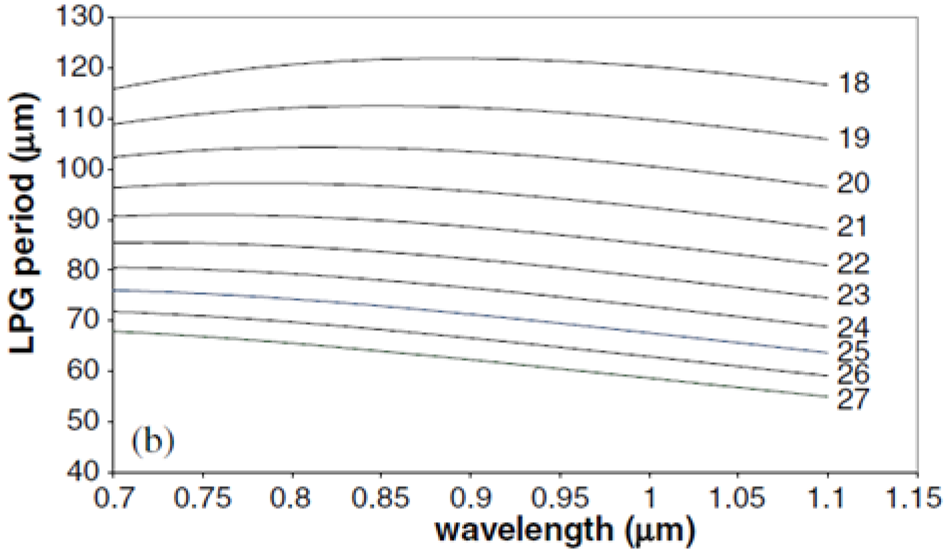

(b)

Figure 2-10: Phase matching curves a) of low order and b) high order cladding modes obtained with use of phase matching equitation (12).

The central wavelength of the attenuation band can be easily identified at the transmission spectrum as the wavelength with the lowest absolute transmittance which can be calculated using Equation 3:

$$T_i = 1 - \ sin^2 \ (K_i L)$$

Equation 3

where T_i indicates the transmission at *i-th* cladding mode, K_i is the coupling coefficient (constant) for the *i-th* cladding mode and L is the length of the LPG (12).

Each phase matching curve associated with the higher order cladding mode has its own phase matching turning point (PMTP), Figure 2-10b.

When the period of the LPG is close to PMTP then two attenuation bands occur in the same region but with different and independently recognized central wavelengths both associated with the same cladding mode and this phenomenon is called a dual resonance (90).

Fibre optic sensors operating close to the PMTP are the most sensitive to any environmental perturbations and the LPG based sensors using the dual resonance phenomenon have been presented e.g. for measurement of temperature, strain and refractive index (91).

The principle of any LPG based sensor is based on the modulation of the propagation of the core and the cladding modes by the change of the surrounding environment. This effect can be easily observed as the change of the central wavelength and detected in the transmitted spectrum. In general, LPG without selectively sensitive coating is sensitive to temperature, strain, bending and refractive index (88).

The calibration of the sensor can be done by exposing it to the known level of the factors of interest and by simultaneous noting the position of the central wavelength. Other possibility is to measure the change of the transmission amplitude at specific wavelength (12).

2.2.4 LPG fabrication

The periodic perturbation of the refractive index of the core of an optical fibre can be performed by photo-induction or by physical deformation of the fibre, that can be done mechanically (92), by periodic tapering of the fibre with CO_2 laser (93) or using electrical arc discharge as the heat source (94)(95).

The mechanical fabrication of LPG is based on the fibre pressed between a periodically grooved plate and a flat plate, Figure 2-11. The mechanically fabricated LPG is sensitive to polarization (92).

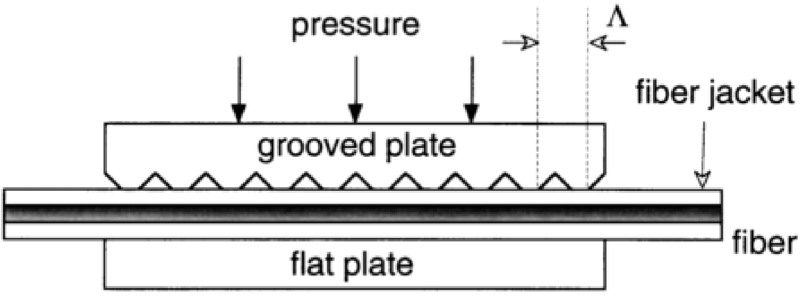

Figure 2-11: Side of the schematic setting for the mechanically induced LPG fabrication (92).

LPG fabrication using electric arc discharge represents the most common fabrication technique however the limited choice of the grating period is their biggest drawback, as fabrication of LPGs with shorter periods and thus operating at PMTP needs to use a high voltage power supply and still suffers from poor repeatability. In conclusion the electric arc fabrication technique provides an easy fabrication technique for LPGs with periods from 400 to 700 µm but suffers from the several issues highlighted above (95).

Exposure to electric arc discharge also induced the tapering of the fibre (95). The periodic tapering of the fibre allows the control over the grating period and LPG length however the tapering compromises the mechanical stability of the fibre as it achieves diameters of 10-15 µm (93), as shown in Figure 2-12.

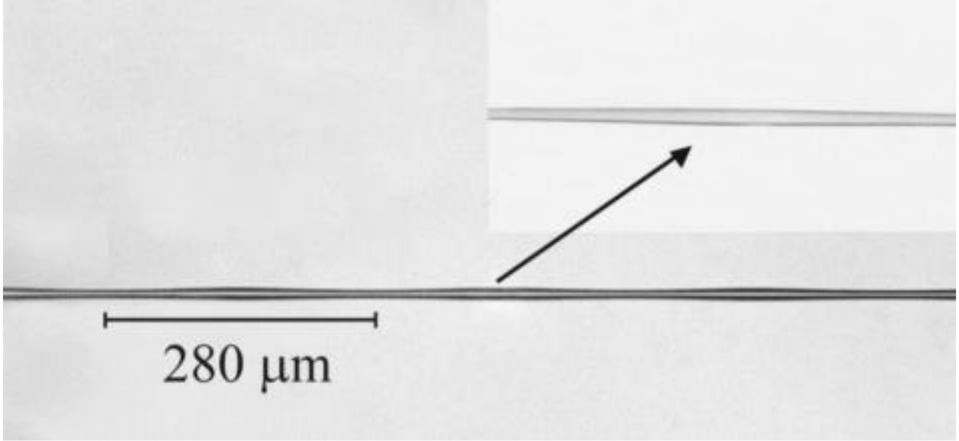

Figure 2-12: Optical micrograph of four periods of a micro- taper-based LPG. The inset shows a single bulge (93).

The photo-induction of the RI change can be done using the laser operating in UV (96), or infrared (IR) region (97)(98), or by ion implantation (99). Each individual part of the grating can be fabricated point-by-point (96)(98) or, in the case of UV irradiation, an extended section of the fibre can be exposed to the beam via an amplitude mask (100), that imposes a spatial modulation to the intensity of the laser beam.

LPG can be fabricated using irradiation in the near infrared (IR) region however LPGs fabricated by this approach suffer from the low transmission loss (less than 8 dB) (97). The set up for the LPG fabrication using femtosecond IR laser is shown in Figure 2-13.

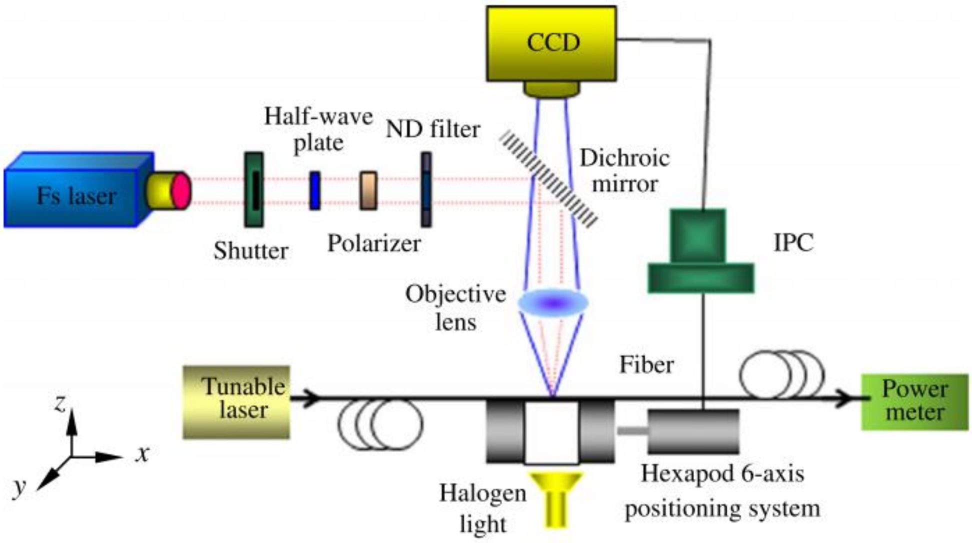

Figure 2-13: Schematic illustration of LPG fabrication using femtosecond laser operating in IR region at 800 nm (101).

The change of the refractive index of the fibre core is induced by the densification of the glass using IR technique. The advantage of this approach lays in high thermal stability of up to 1200 °C (12).

The technique using a laser beam in IR region is limited by the operating wavelength of the laser providing the ideal condition only for a single LPG period, in this case for 436 µm. The authors declared an inscription time of 55 min and LPG length of 40.11 mm. The improvement up to 20 dB transmission loss has been presented (101).

The fabrication of LPGs, particularly those of period shorter than 200 µm, via UV laser beam has been considered as the most promising approach to achieve satisfactory transmission loss, repeatability and relatively easy fabrication procedure. The mass production of LPGs with high reproducibility and low fabrication time is of importance for future commercial exploitation of the sensing platform. The fabrication of LPGs operating at PMTP with a high degree of repeatability was demonstrated recently (96). However the point-by-point fabrication is time consuming and fabrication of 40 mm long LPG with the period of ~ 110 µm can take approximately 3 hours (96). On the other hand the LPG fabrication using an amplitude mask can reduce the beam time considerably when the same energy density is used as in point-by-point approach.

2.2.5 LPG based fibre optic sensors – temperature sensitivity

The temperature sensitivity of the LPG can be theoretically explained using Equation 4:

$$\frac{d\lambda}{dT} = \frac{d\lambda}{d(n_{eff\,co} - n_{eff\,clad})}\left(\frac{dn_{eff\,co}}{dT} - \frac{d_{eff\,clad}}{dT}\right) + \Lambda\,\frac{d\lambda}{d\Lambda}\,\frac{1}{L}\,\frac{dL}{dT}$$

Equation 4

where λ is the central wavelength, T is the temperature, $n_{eff\ co}$ and $n_{eff\ clad}$ represent the effective refractive index of the fibre core and cladding respectively, L is the length of the LPG and Λ its period (102).

The first element of the Equation 4 on the right hand side takes into account the material effect (composition of the fibre and its contribution depends on the change of the effective refractive indices of the fibre core and cladding which is induced by the thermo-optic effect) and the order of the cladding mode. High order cladding modes associated with grating periods of ca. 100 µm show almost negligible material sensitivity for the standard Ge-Si fibre. On the other hand the material effect dominates for the low order cladding modes with periods higher than 100 µm (12)(102).

The strain sensitivity can be explained in the same manner as in the case of the temperature because there is also the contribution of the material effect and the cladding mode while LPG of low order cladding modes exhibit a negative material and positive waveguide effect (12).

According to the Equation 4 it is possible to conclude that by choosing appropriate material of the fibre and the LPG period a sensing array with high or almost no temperature sensitivity can be fabricated (103) and the same conclusion can be drawn for the strain (102). The linear dependence between the shift of the central wavelength and temperature change was observed within room temperature (104) and nonlinear change was observed at cryogenic temperature levels below 77K (105).

2.2.6 LPG based fibre optic sensors – refractive index sensitivity

The principle of the LPG sensitivity to refractive index is based on the change of the effective index of the cladding mode which is affected by the surrounding environment, Figure 2-14.

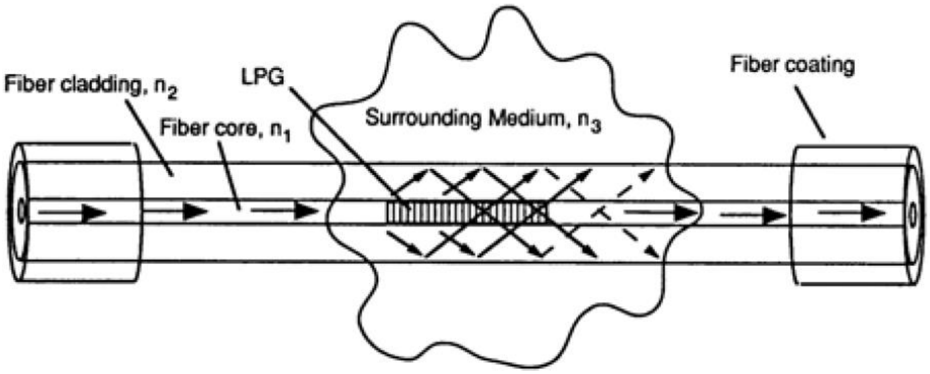

Figure 2-14: Schematic image of LPG as an refractive index sensor – light is coupled from the core in to the cladding in LPG region, the wavelength at which coupling occurs depends on refractive index of surrounding medium (n3) (89).

The relation between the refractive index of the surrounding medium and the effective index of the cladding mode results in the sensitivity of LPG to bulk RI as shown in Equation 5 (106).

$$\frac{2\pi}{\lambda_i} D_{clad} \left[(n_{clad})^2 - \left(n^{i}{}_{eff\ clad}\right)^2\right]^{1/2} - \left(i - \frac{3}{4}\right) 2\pi = 2\ cos^{-1} \left[\frac{n_{clad}{}^2 - n^{i}{}_{eff\ clad}{}^2}{n_{clad}{}^2 - n_{amb}{}^2}\right]^{1/2}$$

Equation 5

where D_{clad} is the diameter of the cladding, n_{clad} and n_{amb} represent the refractive index of the cladding and the ambient environment, $n_{\mathrm{eff}\ core}$ and $n^{i}{}_{eff\ clad}$ indicate the effective indices of the core and *i-th* mode of the cladding, while the order of the mode is *i*.

The central wavelength shifts to the shorter wavelength (blue shift) due to increase of the refractive index of the surrounding medium and then the attenuation band disappears when the refractive index of the cladding is reached. With further increase of the refractive index the attenuation band occurs again with the longer central wavelength (106).

The highest sensitivity was obtained for the higher order cladding modes and when the refractive index of the surrounding media is approaching the refractive index of the cladding Figure 2-15a (107).

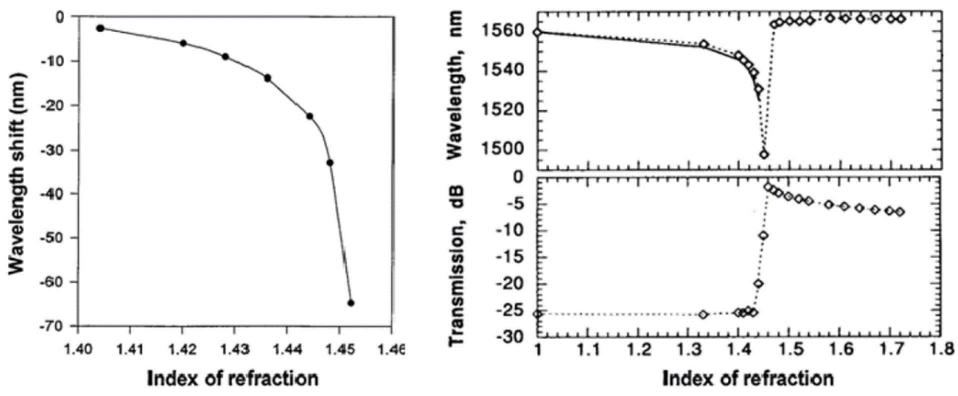

(a) (b)

Figure 2-15: a) The shift of the central wavelength of the LPG of 5th cladding mode due to the change of the refractive index of the surrounding environment (107) *and b) position of the central wavelength (up) and the transmission loss at this wavelength (down) of the LPG with the grating period of 275 µm for different levels of the refractive index of the surrounding environment* (89).

When these two refractive indices are equal then general decrease and no attenuation band is observed in transmission spectrum. There is no discrete cladding mode in this case and when the surrounding refractive index is higher than the refractive index of the cladding then reduced sensitivity is observed (89), Figure 2-15b, however the attenuation bands could occur due to Fresnel reflection in this case (106).

The practical use of refractive index sensor based on unmodified LPG is limited to a measurement of the RI range lower than the refractive index of the cladding with non-linear sensitivity (108). The RI sensors based on unmodified LPG were successfully used for online remote measurement of sodium chloride, calcium chloride and ethylene glycol aqueous solutions in the food quality sector (109) or for xylene concentration in paraffin solution, where the sensitivity of $6x10^{-5}$ of RI unit was obtained (110).

Better performance could be achieved when an additional film is deposited onto the LPG. This approach could induce the RI change which is selective to the compound of interest and enable the fabrication of highly selective and accurate chemical sensors (7)(59).

2.2.7 LPG based fibre optic chemical sensors – deposition of the sensitive element

The first such sensor based on coated LPG was presented in 2000 for immobilised antibody bio-sensing (111). The coating deposition can be also used for the increasing of the LPG sensitivity to chemically unspecific RI change, e.g. 400 nm thick film of SiO_2 nanoparticles was used to enhance the sensor's performance (112).

The refractive index of the deposited film affects the LPG performance. When a film has higher refractive than the cladding then the optical thickness of the film highly affects the change in the transmission spectrum (the position of the central wavelength). This trend was observed in a thickness range of a few hundred nanometres. On the other hand the coating with lower refractive index than the cladding shows much less sensitivity to the thickness (12). The thickness itself affects the change in the transmission spectrum as well. The shift of the central wavelength depends on the thickness of the film (113).

It can be concluded that the application of the nano-scale coating is highly beneficial for LPG based sensors. The proper choices of the material endow the LPG with the sensitivity to a desired measurand and the optimization of the thickness gives the highest level of this sensitivity (114). The specific cylindrical shape of the optical fibre represents an issue for the coating deposition. When all factors are considered then mainly three deposition techniques are used: the dip coating (DC) technique (115), the Langmuir-Blodgett (LB) technique (113) and the layer by layer (LbL) technique also known as electrostatic self-assembly (ESA) (15).

The dip coating technique was originally introduced for sol-gel or hydrogel coatings and is also suitable for the deposition on optical fibres. The main disadvantage of this approach is the limited thickness control in the nano-scale range (114), as an example, the LPG based sensor for chloroform detection in water was presented (115).

The principle of Langmuir-Blodgett technique can be explained as follows: the monolayer is prepared on the surface of a liquid and then deposited on the solid surface by the immersion of the solid substrate into the liquid and as this monolayer is in nanometre range it enables the precise control over the thickness of the film (59). The example of the deposition of the thin film on LPG was presented for calixarene molecules which endow the LPG with sensitivity to volatile organic compounds (VOCs) (20).

The layer by layer technique benefits from the thickness control and from a choice of using a wide range of coating materials. It is based on the deposition of the oppositely charged materials which can be added to the fibre on the molecular level to build up to the required thickness (15)(116).

There are two possibilities of working principle of such sensors: i) the entire coating can be made from the sensitive material and then it reacts with the compound of interest. This effect leads to a change of refractive index which is subsequently detected as the change of transmission spectra (112) and ii) the sensitive layer can be infused with the material that causes the chemical reaction which induces the refractive index change (15).

The sensitive material should fulfil the following criteria: appropriate morphology, porosity, flexibility, thickness for the sensing selectivity and matrix porosity for the speed of analyte diffusion (117).

As an example, LPG based sensor with functionalized film deposited by LbL technique was presented for ammonia sensing in water (15).

The next section will cover the recent progress in the field of fibre optic chemical and biochemical sensors using deposition techniques mentioned above.

2.2.8 LPG based fibre optic chemical and biochemical sensors – recent progress

2.2.8.1 Relative humidity sensors

Development of new relative humidity (RH) sensors is highly desired e.g. in the field of medical diagnostics (26). RH is also one of the key parameters of indoor air quality (3).

The sensitive coatings used for the RH measurement include PAH+/PAA- (polycation and polymer of acrylic acid) and Al_2O_3+/PSS- (118), TiO_2 (119), SnO (120), polyvinyl alcohol (19), polyimide (121) or gelatine and $CoCl_2$ (122).

LPG based RH sensors have been successfully tested to operate in high radiation environments (119)(120).

The summary of LPG based RH sensors is provided in Table 2-2.

Table 2-2: Summary of LPG based RH sensors

M*	Coating material	Sensitivity	Range	Resp. time	LPG Λ*	Ref
RH	10 bilayers of PAH+/PAA- and Al_2O_3+/PSS-	CW shift of 0.01 nm / RH %	20 to 90 %	No data	430 µm	(118)
RH	100 nm thin film of TiO_2	from 1.4 nm/RH % at low RH below 10 % dropping to 0.01 nm/RH % at high humidity levels	0-75 %	No data	404 µm	(119)
RH	300 nm of SnO	4.5 nm / 50 RH %	0-50 %	No data	410 µm	(120)
RH	polyvinyl alcohol	0.6 nm/RH % at 40 to 85 %; 0.025 nm/RH % at levels up to 40 %	20-85 %	No data	250 µm	(19)
RH	polyimide	0.1 nm/% RH and resolution limit of 0.8 % RH	20-80 %	No data	330 µm	(121)
RH	gelatine and $CoCl_2$	0.18 nm/RH %	35-90 %	24 s	525 µm	(122)

*M indicated measurand; Λ indicates period

2.2.8.2 H_2 sensors

Hydrogen plays an important part in various syntheses in chemical industry, even more it is considered as the energy source for the future. The monitoring of the hydrogen level is highly important due to the easily diffusion and possible explosion at concentrations over 4 % (123). LPG based H_2 gas sensors were successfully tested even at high temperature simulating conditions of coal or biomass gasification (18)(124). Two approached of the functional coating has been tested: i) palladium (123) and ii) zeolite (18)(124) based films. The properties of LPG based hydrogen sensors are summarized in Table 2-3.

Table 2-3: Summary of LPG based hydrogen sensors

M*	**Coating material**	**Sensitivity**	**Range**	**Resp. time**	**LPG Λ***	**Ref**
H_2	70 nm thin palladium	CW shift of 7.5 nm/4 %	4 %	3 min	400 µm	(123)
H_2	$SrCe_{0.8}Zr_{0.1}Y_{0.1}O_{2.95}$ (SCZY) – zeolite; thickness of 0.9 µm	1.9 nm / 10 % of H_2	10 %	No data	520 µm	(18)
H_2	$SrCe_{0.95}Tb_{0.05}O_3^{-\iota}$	0.2 nm CW shift /8 %	0.5 to 12 %	2 min	500 µm	(124)

*M = measurand; Λ = period; CW = central wavelength

2.2.8.3 Carbon dioxide LPG based sensors

LPG based carbon dioxide sensor had been reported with use of atactic polystyrene as sorbent for CO_2 molecules diffusing trough the polymer matrix (17). The sensor was used to measure carbon dioxide level at high-pressure aqueous solutions in conditions simulating the use of the sensor in subsurface monitoring in deep saline aquifers (125). The performance of LPG based CO_2 sensor is shown in Table 2-4.

Table 2-4: Summary of LPG base CO_2 sensors

M*	**Coating material**	**Sensitivity**	**Range**	**Resp. time**	**LPG Λ***	**Ref**
CO_2	365 nm atactic polystyrene	−1.23±0.08 pm/%CO_2; resolution of ±4.07 %	steps of 0, 25, 50, 75 and 100 %	No data	450 µm	(17)

*M = measurand; Λ = period

2.2.8.4 Ammonia LPG based sensors

Monitoring of ammonia in aquatic ecosystems is important and desired due its effect onto the biochemical processes. Ammonia either in gas and liquid phase is important for the health diagnostics as it was considered as biomarker for kidney, liver and physical disorders (126).

The ammonia detection in gas (126)(127)(128) or liquid phase (15) was reported using LPG based sensors and the results are summarised in Table 2-5.

Table 2-5: Summary of LPG based ammonia sensors

M*	**Coating material**	**Sensitivity**	**Range**	**Resp. time**	**LPG Λ***	**Ref**
NH_3 (g)	PDDA/TSPP	100 ppm induced CW shift of 10 nm; LOD = 0.67 ppm	3 to 1067 ppm	No data	100 µm	(126)
NH_3 (g)	PDDA/PAA	0.35 and 0.31 nm/ppm based on shift of 1st and 2nd CW	0.3 to 24 ppm	< 5 min	100 µm	(128)
NH_3 (g)	PAH/PAA	LOD = 10.7 ppm	3-348 ppm	< 5 min	100 µm	(127)
NH_3 (l)	PDDA/SiO_2 + TSPP or PAA	LOD = 140 ppb	0.1-100 ppm	< 100s	100 µm	(15)

*M = measurand; Λ = period; LOD = limit of detection; (g) and (l) indicate gas and liquid phase of the measured ammonia.

A practical example of LPG based ammonia sensor for the sea water quality monitoring will be shown in Chapter 6 with use of the methodology described in (15).

2.2.8.5 LPG based bio-chemical sensors

Development of new bio-chemical sensors is in high interest in the field of medical applications. The wide range of the analytes includes vancomycin (129), bacteria (16)(130)(131)(132)(133)(134)(135)(136), triacylglycerides (137), cholesterol (138), glucose (139) and streptavidin (140). Detection of antigens (anti-Igs) present in serum represent the recent challenge in bio-sensing field and prototypes of LPG based Ig sensors had been proposed already (141)(142)(143)(144). The performance of LPG based bio-chemical sensors is summarized in Table 2-6.

Table 2-6: Summary of LPG based bio-chemical sensors

Measurand	**Coating material**	**Sensitivity**	**Range**	**Resp time**	**LPG Λ^***	**Ref**
antigens	atactic polystyrene + Antibodies (Igs)		2-100 µg/mL	No data	460 µm	(144)
goat antigens in human serum	Eudragit L100 (polymer) + (Igs)	LOD = 70 µg/L (460 pM); 4.6 nm per 100 mg/L	up to 100 mg/L	15 min	165 µm	(143)
goat antigens in human serum	Eudragit L100 (polymer) + (Igs)	LOD = 7.6 mg/L and 0.5 mg/L		1 h	615 and 370 µm	(142)
antigens in human serum	120-160 nm thin titania−silica sol gel film + Igs	4.5 nm CW shift for 10 mg/L; LOD = 8 µg/L (5.3×10^{-11} M)	0.1 mg to 10 mg/L	40-60 min/serum	342 µm	(141)
vancomycin (glycol-peptide antibiotic)	molecularly imprinted polymer (MIP) nanoparticles		10 nM-700 µM (14 g/L - 1 g/L)	No data	111 µm	(129)

Francisella tularensis	bilayers of PAH or PDDA and PSS + antibodies (Igs)	Lowest detected dose of 10^5 colony forming units (CFU)		4 min	260 µm	(130)
methicillin-resistant *S. aureus* (MRSA)	five bi-layers of PAH/PCBS + mouse monoclonal antibody		10^2 - 10^6 CFU	No data	116 µm	(131)
E. coli	T4 bacteriophage	central wavelength shift of 1.3 nm was induced by 10^8 CFU		No data	169.7 µm	(133)
E. coli	APTES + T4 bacteriophage	CW shift 2 to 4 nm over the range	10^3 to 10^9 CFU	≈ 20 min	226.8 µm	(16)
lipopolysaccharide (LPS) on surface of *E. coli B*	70 nm TiO_2 film + *E. coli B* bacteriophage g37 adhesin	28.1 nm CW shift per 250 µg/mL of LPS		No data	226.8 µm	(136)
E. coli via membrane proteins	*E. coli* DNA aptamers	0.16 nm CW shift per decade	0.1 nM to 30 nM	No data	396 µm	(132)
Triacylglycerides (TGs) in human blood	APTES + Lipase enzyme	CW shift of 0.5 nm per mM at pH 7.4; LOD = 17.71 mg/dL	0.5-7 mM (44.27-620 mg/L)	≈ 1 min	581 µm	(137)
cholesterol in coconut oil	chitosan	CW shift of 25.12 nm per 5 mg/L	0.5-5 mg/L	No data	435 µm	(138)

glucose	APTES + glucose oxidase	0.8 nm / (mg/L)	0.1-3 mg/mL	30 s	550 µm	(139)
streptavidin	SiO_2:gold nanoparticles + biotin	6.9 nm/ (ng/mm^2) LOD of 19 pg/mm^2	19 nM-2.7 µM	Several s to > 15 min	110.7 µm	(140)

* Λ = period; LOD = limit of detection; CW = central wavelength

2.2.8.6 LPG based sensors for detection of organic compounds

Volatile organic compounds consist of a wide range of chemicals. Real-time VOCs monitoring is highly desired in the fields of air and environmental quality (145). Methane detection is at high interest in a wide range of applications including coal mines, landfills or in chemical industry (146). The chemical sensitivity of PAH in the mesoporous coating with SiO_2 NPs was used in a way to test and recognize different types of alcoholic beverages and to provide their quality assessment (147).

An LPG based methane sensors were proposed using cryptophane A as the sensitive element combined with styreneacrylonitrile (SAN) (148) or polycarbonate (146). The performance of LPG based methane sensors is summarized in Table 2-7.

Table 2-7: Summary of LPG based methane sensors

M*	**Coating material**	**Sensitivity**	**Range**	**Response time**	**LPG Λ**	**Ref**
CH_4	styreneacrylonitrile and cryptophane A	0.375 nm/CH_4 %	0.2-3.5 %	50 s	480 µm	(148)
CH_4	polycarbonate and cryptophane A	2.5 nm/ CH_4 %	0.2-3.5 %	No data	520 µm	(146)

* M indicates measurand; Λ indicates period

Calixarene molecules were used as the selective material to fabricate LPG based VOCs sensor (20)(145).

An LPG was coated with calix-4-resorcarene via Langmuir-Blodgett technique. Changes in transmission spectra were induced by the concentrated vapours of benzene and toluene, where much lower response was observed for aliphatic cyclohexane and hexane molecules (13 time higher response for toluene in comparison to hexane) (20). The same approach was used for the detection of toluene in water with the aim of demonstrating the feasibility of application of LPG based sensor to water quality tests (145).

An example of LPG based VOCs sensor in a practical application in the field of indoor air quality will be further explored in Chapter 6 using calixarene as the functional compound in the coating.

The properties of LPG based sensors used for the detection of organic compounds are summarized in Table 2-8.

Table 2-8: Summary of LPG based sensors for detection of organic compounds

M *	**Coating material**	**Sensitivity**	**Range**	**Resp time**	**LPG Λ**	**Ref**
ethanol (g)	ZnO nanorods	Change in transmission at CW	50 Torr	50 min	407 µm	(149)
aromatic carboxylic acids (ACAs)	10 layers of PAH/SIO_2	Response via CW shift and/or the intensity change at CW	1 µM to 1 mM	> 1500 s	100 µm	(150)
toluene (g)	calixarene	LOD of 231 ppm	3.7 to 73.4 kppm	15 s	180 µm	(20)
toluene (l)	calixarene	LOD of 41 ppm	1- 400 ppm	< 400 ms	97 µm	(145)

*M indicates measurand; Λ indicates period; CW indicates central wavelength; (g) and (l) indicate the gas and liquid phase of the measurand.

2.2.9 LPG based chemical sensors: conclusions

Optical fibre LPG has a high potential to provide the useful platform for the development of novel chemical sensors. The nano-scale coating represents the key element for chemical sensing. The range of different coating types and LPG based chemical sensors was demonstrated in the literature. The future development of new sensors is highly desired and depends on introduction of new materials as the sensitive layer.

2.3 Metal organic frameworks

2.3.1 Background information

Metal organic frameworks (MOFs) are crystalline materials with high stability, tuneable metrics, organic functionality and porosity (151). The stability is due to metal-oxygen-carbon strong bonds and the main advantages of MOFs consist of a huge surface area (∼7000 m^2/g) and the possibility of selective gas storage (21)(152).

The combination of MOFs with sensor transducers creates a prospect for the fabrication of highly sensitive and selective sensors. In this section, recent approaches to the development of MOF based sensors, advantages and characteristic features of each approach are discussed and examples of the sensitive and selective detection of various chemical analytes are provided.

MOFs consist of metal centres coordinated by organic linkers to construct porous structures, in which the porosity, internal surface area, chemical properties and organic functionality can be tuned. The ability to adjust the pore size and to perform post-synthesis functionalization enables the development of MOFs that offer specific reactions with an analyte of interest, where only certain molecules (treated by size or functional group) are allowed to enter into the MOF’s cavities. While MOFs are generally fabricated in the form of crystalline powders, the ability to deposit MOFs in the form of a thin film on a substrate that could act as a sensing platform, is crucial when considering the possible use of MOFs for (chemical) sensing purposes (22)(151)(153)(154). There are a number of challenges in the fabrication of thin films of MOFs, particularly in ensuring uniform coverage over the substrate and in providing control over the thickness and growth direction of the crystals (154).

The scientific concern had shifted during the last decade from the development and fabrication of new MOF materials into the field of their applications (23)(151)(155), where the main interests lie in selective hydrogen gas storage (156), selective gas adsorption (157) and separation (158) or catalysis (159). There have been limited reports of MOF based sensors, but these reports demonstrate their potential to become powerful analytical devices (153). The main advantage is the high chemical selectivity made possible by the ability to select a MOF with appropriate properties (23).

More than 20,000 different types of MOFs have been described over the last decade, which makes MOFs the most extensive group of porous materials (151). The variability of pore size and structure of MOFs is illustrated in Figure 2-16 (on the next page).

The main attraction of the use of MOFs in the development of sensors is the high chemical selectivity which could be provided by the appropriate selection of a MOF with desired properties matched to the analyte (153). The criteria for the evaluation of a sensor's performance include its sensitivity, selectivity, response time, material stability and re-usability. The following factors should be considered for the development of a MOF based sensor: i) identification of the desired MOF to obtain desired selectivity and sensitivity, ii) feasibility of the fabrication of the MOF in the form of a thin film on the selected substrate, iii) identify and apply means for signal transduction (153).

The selection of the appropriate MOF would consider the following material properties: the MOF structure because of the space conformation the number of pores and their size, as they represent a mechanical barrier for certain molecules to pass and the type of metal centres present, with a particular focus on open metal access sites, as they represent the key reactive part for the selective binding of the analyte (23).

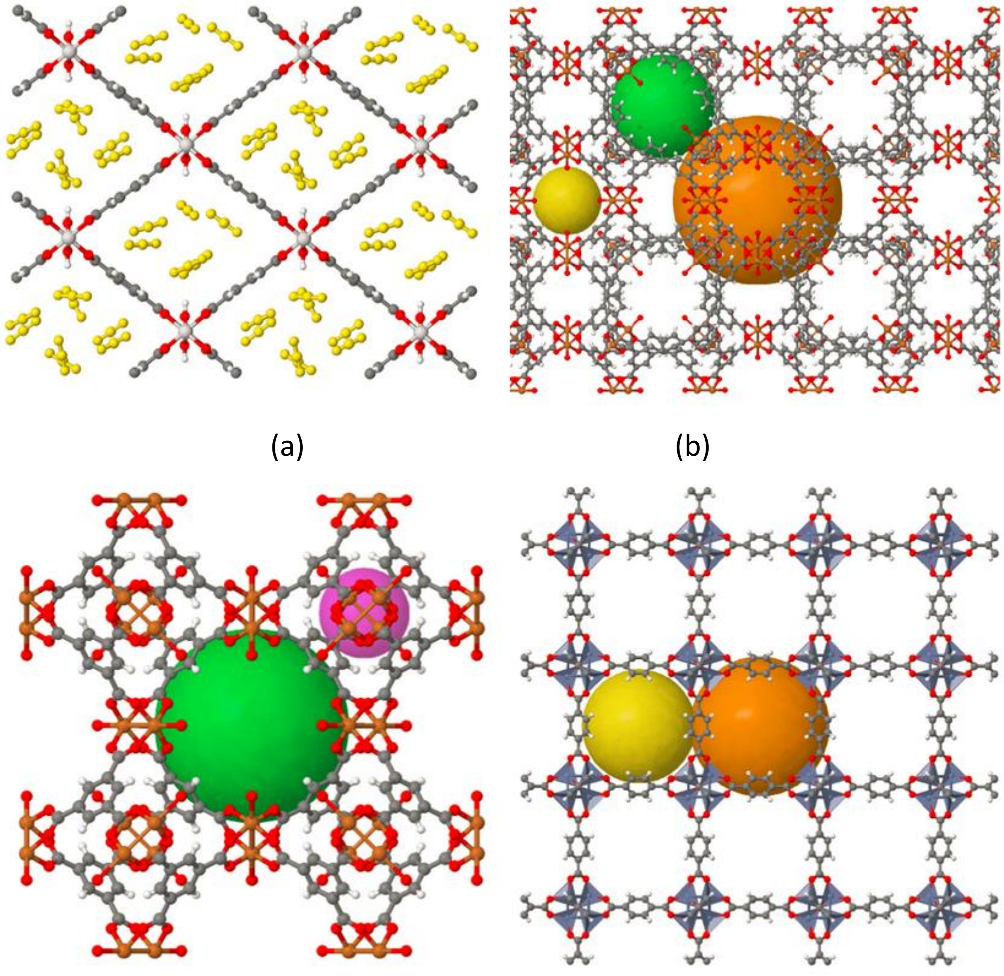

(a) (b)

(c) (d)

Figure 2-16: Examples of MOFs structures, represented by a) MIL-53, b) NOTT-112, c) HKUST-1 and d) MOF-5 (the colored balls represent the sizes of the pores in the frameworks). Figure taken in (160) *via creative common free licence (http://creativecommons.org/licenses/by/4.0/).*

The size of the pores of the MOF affects the fabrication of the film, as they are initially filled by the solvent. When the solvent molecules are removed there is a risk of collapse of the whole structure. This risk increases with the size of the pores. The MOF structure can be characterized by a permanent porosity only when the MOF retains its structure after the removal of the solvent molecules. This is more readily achieved for microporous structures (23).

Microporous MOF materials (pore size less than 20Å) can be used for gas storage and gas separation applications because of the strong interactions between the small gas molecule and the walls of the pores. Networks with larger pore size are advantageous for applications based on guest-host chemistry, for example catalysis (23).

A specific functional group can also be added after the synthesis to fit the desired purpose of the framework. This process is called post-synthetic modification (PSM) (161). PSM is useful for gas storage and catalytic applications where the surface properties and pore geometry are modified by the added functional groups. When PSM is designed and evaluated, the following factors should be taken into account: i) the substance which provides the functionality should be small enough to get into the cavities, ii) the reaction itself and its conditions don’t damage or even destroy the structure of the MOF (23).

In addition, much more specific molecular recognition could be achieved when the MOF is endowed with specific functions with following modifications: i) the change of the specific ligand or doping of metal ions into the framework – this approach is used mainly for lanthanide metals for their luminescent properties, ii) the use of post-synthesis modification by adding the desired functional groups or iii) the added functional groups could be directly entrapped in the cavities - this approach could also use the nanoparticles as such composites could enable the measurand recognition or could improve the signal transduction (162).

The strategies of functionalization of MOFs, the benefits of this approach and their possible use for a range of applications are also discussed by (163). As an example, surface-enhanced Raman scattering (SERS) can be used for chemical detection with enormous sensitivity and rapid response (164), which can be induced by metal nanostructures, in particular gold nanorods (AuNRs), deposited on the surface (165). The addition of AuNRs to the MOF structure enables use of SERS in a MOF based sensor (166).

The guest-host interactions can be specified by the size of the analyte. MOFs have been used as molecular sieves (167). Larger molecules cannot get into the cavities, but smaller molecules are allowed to pass (167). Other effects include a "gate opening effect" that has been observed where pore expansion or constrictions can occur due to the interactions between the network and guest molecules (adsorbate and adsorbent) (157). It has been demonstrated that size of the pores can expand from 3.8 to 28.8 Å in MOF-5 (168).

The level of water adsorption could be other important parameter to be considered during the MOF selection process (153). MOFs can be hydrophobic, for example the ZIF materials (24), while HKUST-1 can adsorb water (169). Following selection of the MOF with appropriate characteristics, it is necessary to find the most appropriate method for its fabrication in the form of thin film.

2.3.2 Thin film fabrication

From the practical point of view, the fabrication of MOF in the form of a thin film is considered to be crucial for the development of MOF based sensors. The development and the fabrication of MOF thin film has been reviewed in (154) (170). The uniformity of the film in terms of its structure, thickness and crystal orientation is desired, because these parameters influence drastically the performance of the sensor. The selected deposition technique plays an important role in MOF thin film fabrication as it can affect all of these crucial parameters.

The following methods have been reported for the fabrication of MOF films : i) liquid-phase epitaxy (LPE), ii) Langmuir-Blodgett / layer-by-layer deposition, iii) direct synthesis in situ, iv) seeded growth, v) electrochemical methods, vi) assembly of preformed MOF nanocrystals (154).

The following factors should be taken into account during the thin film synthesis: temperature, concentration of the solution of the reactants, the solubility of both in the solvent, the pH of the solution and the exact ligand and metal. The ligand properties such as bond angles, size and chirality influence significantly the final framework. The capability of the metal ions to adopt the requested geometry also affects the MOF structure (23).

The Langmuir-Blodgett technique was the first method used to demonstrate the controlled fabrication of a multi-layered film at nano-scale range with controllable thickness. This approach is advantageous due to the mild reaction conditions (room temperature, no highly toxic materials are involved) (154). LPE approach has been used for fabrication of MOF thin films (170)(171)(172)(173) and fabrication methodology is schematically shown in Figure 2-17.

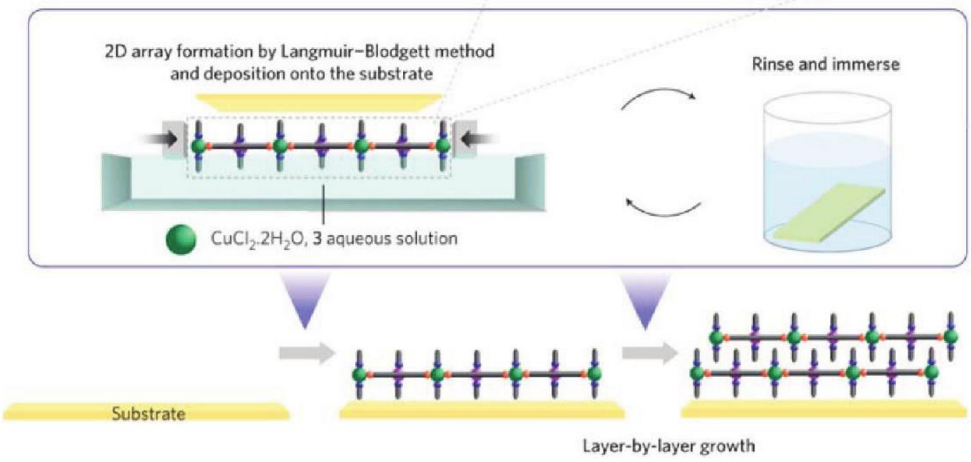

Figure 2-17: Schematic illustration of NAFS-1 thin film fabrication via Langmuir-Blodgett technique (173).

The layer-by-layer (LbL) technique consists of the deposition of oppositely charged materials that can be added to the substrate on the molecular level. This principle can enable control over the thickness of the film. In comparison to other techniques, LbL benefits from being a simple procedure that is conducted at room temperature. Other advantages include the rapid synthesis and minimal use of consumables. There are reports of the use of the LbL technique for MOFs thin film synthesis (174)(175)(176)(177), Figure 2-18.

Figure 2-18: Schematic illustration of MOF synthesis via LbL approach (177).

Direct synthesis represents the simplest way to form a film on a substrate which can be bare or be treated by organic molecules or self-assembled monolayers. The substrate is subsequently immersed in solution and the crystals grow attached to the substrate surface (154). The process of immersion in the mother solution for MOF creation is called in-situ crystallization and numerous crystalline, dense and homogenous films were fabricated using this approach (154). This technique enables the deposition of MOF films on a number of different substrate materials, including TiO_2 (178) or alumina (179). The in-situ growth of ZIF-8 film ceramic hollow fibres using a synthesis gel of high concentration has been reported (180).

The modification of the substrate including seeding and attachments of organic ligands has been suggested. The modification plays an important role and help to increase the growth rate of the film (154). In general, when the in-situ crystal synthesis approach is used, such promotion of the film growth seems to be essential to obtain a continuous film (181). This conclusion can be supported by several reports that show no film formation on bare substrates, while continuous films were obtained following the chemical modification of substrates (179)(182)(183)(184)(185).

The orientation of the film is also determined by the treatment of the substrates (183), which can be achieved using OH^- or $COOH^-$ groups (184). The same effect of surface preparation on crystal orientation was observed for HKUST-1 film deposited onto treated gold substrates (185).

The in-situ crystallization technique encompasses a wide range of conditions during film fabrication. The limiting factor of this approach is the ability of the crystals to nucleate on the liquid/solid interface of the substrate (154). For the development of MOF-based sensors, it is important to develop a procedure that allows the deposition of a thin film at room temperature with no requirement for substrate modification and that can be undertaken in a time period of a few hours (154).

The seeded growth method has been applied successfully for the synthesis of zeolite films (sometimes is referred as the secondary growth method) (186) but it is also of use the formation of MOF thin-films. The fabrication process consists of two stages: firstly, the seeds are prepared and deposited on the surface and then the film growth is initiated, often under solvothermal conditions (154), as indicated in Figure 2-19.

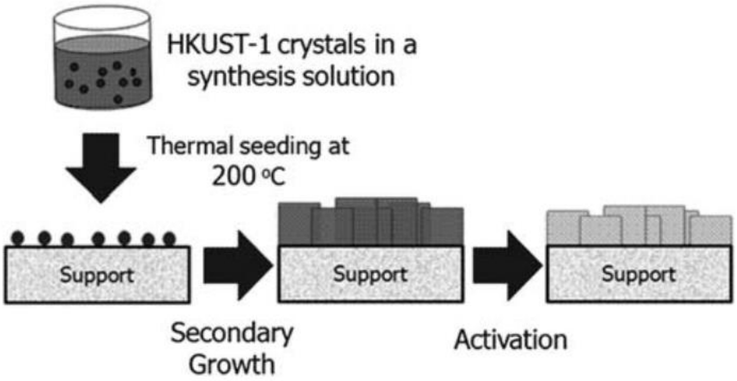

Figure 2-19: Schematic illustration of the seeded growth MOF thin film fabrication technique (187).

MOF nanocrystals with sizes in the range 20-100 nm can be used as the seeds. Firstly, single crystals are fabricated and then deposited on the substrate, either by dropping (188) or using the dip coating technique (189). The advantages of the seeded growth approach include its simplicity and possibility to use this technique as a transition step from fabrication of MOF in a form of single crystals to smooth thin films (154). On the other hand sometimes the seeds are not stable and dissolve or become dissociated from the substrate. This effect is due to the acidic properties of the organic linker, which can be solved by addition of a base (190). The lack of adhesion between the seeds and the substrate represents another issue (154). A further approach of secondary growth involves the use of microwave radiation, which enables the rapid synthesis of the film (190) or involves a thermal seeding at higher temperature (at 200 ^{o}C) (187).

A MOF film itself, when deposited on a substrate can also act as seed layer. It has been shown films obtained using this approach are more homogenous and continuous using than those fabricated by direct growth synthesis. By using such a seed layer, films of [$Cu_2(ndc)_2(dabco)$] of thickness in the range 500 to 700 nm could be formed on unmodified SiO_2 or Al_2O_3 substrates (191).

Electrochemical methods represent other promising approach for MOF film fabrication and they had been used to obtain Cu-MOF crystals. While to date only HKUST-1 films synthesis has been reported, the fabrication of films with other transition metals should be feasible (192).

The deposition of multiple layers with controllable thickness, sometimes even comprised from different materials, represent another challenge for MOF-based sensors, but the early trials of methods to achieve this have been presented (22)(24)(173)(176). The enhancement of the MOF thin film with other elements or the combination of different MOFs could lead to improvements in the sensor’s functionality (22).

While all of the discussed approaches could be used for the development of sensitive films for sensor applications, there is lack of generalization of these approaches to be more widely applied to fabricate films from other MOFs, as most of these materials are synthetized by solvothermal reactions at high temperatures (154).

2.3.3 MOF based sensors

The possibility of defining the chemical functionality as well as providing size selectivity makes MOFs interesting candidates for use as sensing materials. However, it is recognized that there is a need to identify the appropriate means for signal transduction to enable the use of the broad range of MOFs for chemical sensing (153). To date the development of MOF based sensors has been focused mainly on their luminescent properties (193) in combination with size/shape selective adsorption (23). However, the ability to tailor the properties of MOFs represents an important factor in sensor development. In theory, any change of the MOF properties could be measured to act as the sensing signal (162). Betard and Fisher (154) suggest four signal transduction approaches: luminescence of the material, changes in optical properties, changes in mass of the film (with use of quartz crystal microbalance and microcantilevers) and the changes in electrical properties. Lei et al. used similar groups of MOF sensors based on optical, electrochemical, mechanical and photo-electrochemical transduction (162).

The MOF itself can be used as both receptor and transducer in the case of solvatochromic or luminescent sensors (153)(162). However, this approach cannot be generalized because only a few MOFs and guests have been proven to show significant colour changes and most of MOFs show no evidence of such behaviour (153).

Solvatochromism is based on the shift of absorbed spectrum of the material due to the change of the solvent polarity, which induces a change of the dipole moment and enables the solvatochromic component to reach the excited state. Two effects can be observed with increasing solvent polarity: i) A red/bathochromic shift occurs when the dipole moment of the excited state is higher than the ground state, ii) a blue/hypsochromic shift occurs when the dipole moment of the excited state is smaller than that of the ground state (153).

The following sensors that exploit the luminescent properties MOFs have been reported: i) sensors for selective ion monitoring, ii) sensors for the presence/absence or type of the guest molecules and iii) sensors for stress-induced chemical detection (23). Luminescent materials can be obtained by using luminescent metal ions or clusters and organic ligand. Lanthanide metals are well-known for their luminescent properties and their use in MOFs synthesis has been reported (194). The incorporation of special host molecules can also be used to produce materials with luminescent properties (193).

Luminescent MOFs sensors have been described in a range of possible applications and have been reviewed in (195)(196)(197). Here the signal transduction is based on the incorporation of a lanthanide element in the framework of the MOF (198). The principles of operation of sensors exploiting such materials include measurement of changes in the inter-molecular distances between the metal ions and organic ligands, measurement of the level of the chemical binding between the analyte the metal part and host-guest chemistry interaction between the analyte and the framework (162). As an example, the detection of explosives represents an interesting application. Previously, Zn based MOFs were shown to exhibit an affinity to organic compounds such as pyridine, benzene and dodecane in liquid solutions (199). This behaviour was further examined and lead to the development of MOFs doped with luminescent elements used for the detection of dinitrotoluene and trinitrotoluene in vapour form (200**).** The detection principle is based on the induction of luminescence quenching by synergic effect of π-π stacking and hydrogen interaction that enables intermolecular electron transfer (201). The quenching effect was described also in a different study, where the detection of nitrobenzene with use of Cd based type of MOF had been shown (202).

A large group of MOF sensors is based on electrochemical changes and these were reviewed in (203)(204). Electrochemical sensors attract significant attention as they can enable the fabrication of versatile, reliable, attractive, highly sensitive and easy-to-use devices. However the electrochemical approach has two main issues: the conductivity of the MOF and the redox potential of the MOF (204). These issues could be overcome by the use of a mixture of MOF and a conductive material or by the attachment of a MOF film or coating to a substrate integrated with microelectronics. This provides the possibility of direct electron transfer between the film and substrate, with advantages such as control of film thickness, unobstructed access to pore cavities, and availability of active sites (203). The electrochemical approach has been successfully implemented in the development of MOF based sensors, where ZIF-70 was used as the key element for glucose measurement, where the principle relies on the measurement of dehydrogenase-based changes (NADH to NADH+) (205) or the use of a copper based MOF for the detection of H_2S inside cells.

Alternatively, quartz crystal microbalance (QCM) sensing, based on the measurement of the change of the oscillation frequency of the substrate due to the adsorption or desorption of molecules within the selected film, could be used (172)(206).

Sensors exploiting changes in optical properties are often based on the measurement of refractive index changes. The specific reaction between a MOF and a chemical vapour induces a change of the refractive index of the guest-host MOF based complex (24). For example, a 1 µm thick ZIF-8 film deposited on glass substrate to act as a Fabry-Perot interferometer was used for propane sensing. The concentration-specific changes in the light passing through the ZIF-8 film were observed by monitoring the UV-VIS transmission spectrum. The wavelength shifts in the features of the channelled spectrum that is characteristic of such interferometers exhibited an almost linear dependence on propane concentration (24).

Thin film of UiO-66 (zirconium based MOF) had been deposited on the tip of optical fibre and the changes in the fringes of the reflected light were used for the detection of Rhodamine-B in water (207).

One-dimensional photonic crystals (Bragg stacks), with use of a microporous metal-organic framework material and mesoporous titanium dioxide, have been used as a MOF based optical sensing platform, where device including ZIF-8 (208) and HKUST-1 (171) show the selective response for different organic vapours measured as a shift of photonic bandgap.

The sensor for detection of Cu^{2+} ions in aqueous solutions had been shown. The sensing approach was based on the changes in absorbance at 430 nm evaluated with use of UV–vis spectrophotometric and digital image-based colorimetric analysis. The sensor responded linearly in a range of 1.57 – 157.37 nM followed by non-linear response up to approximately 32 µM of Cu^{2+}. The colour change of the substrate was presented to be visible also with naked eye at higher concentration (approximately over 700 nM). Authors declared the LOD of 7.8 nM and 3.2 nM with use of of UV–vis spectrophotometric and Digital Image-based Colorimetric analysis, respectively. The sensitivity is enough to be possible to detect CU^{2+} ions to fulfil the WHO criteria for drinking water. The sensor also could determine the Cu^{2+} concentration in biological samples like blood or serum (209).

The proposed CO_2 sensor measures changes in NIR absorption of thin film consisting of HKUST-1 deposited in the etched region of optical fibre. The proof of concept had been presented with multimode optical fibre with the coated region of 8 cm and the film thickness of 100 nm and authors declared a limit of detection of 500 ppm of CO_2 gas in mixture with argon with use of high resolution NIR spectroscopy (210). The higher sensitivity was then obtained using the same film but coated onto the etched single mode fibre over the region of 5 cm. The improved LOD of 50 ppm of CO_2 mixed with argon was reported (211).

Kelvin probe setup had been used of gas measurements, where MOF-74 and Zn3(btc)2·12H2O (Zn-btc) MOF showed the sensitivity towards CO_2 and short-chain alcohols respectively (212)(213).

MOF films can be also used to improve the selectivity of existing gas sensors. The accumulation of specific gas molecules around the nanoparticles causes a small change in refractive index. When an HKUST-1 film was deposited on silver nanoparticles, it caused 14-fold signal improvement for CO_2 sensing with use of localized surface plasmon resonance spectroscopy (214).

There is a need to establish a suitable means of signal transduction to enable the use of MOFs for chemical sensing (22)(24). The pores for all MOF structures are scaled in Angstroms, which makes it extremely difficult to measure the individual response from each pore and crystal. The most promising approach appears to be the adoption of macroscopic perspective and to analyse changes in the properties of the whole film. This can be achieved by the use of optical transduction techniques, which require the fabrication of a film, ideally with controllable thickness, on an optical sensing platform such as optical fibre sensors.

2.4 Conclusions

In this chapter, the overview of the commercially used techniques for the detection of VOCs, carbon dioxide and ammonia were provided and the high demand for real-time sensors in the field of IAQ and water quality was discovered.

The concept and use of fibre optic sensors was introduced. The literature review focused on the recent progress in the field of LPG based chemical sensors. LPG provides an ideal platform among the fibre optic sensors as it benefits from the wavelength encoded information and enable the deposition of the sensitive coating, the key element for chemical sensing.

Materials from MOFs family was described and it can be concluded that the combination of the diversity, specific selectivity and sensitivity of different materials seems to be highly promising in the field of the development of precise and reliable chemical sensors, especially in combination with optical fibres as sensing platform, while optical fibres solve the problem with the signal transduction.

The literature review in the second part focused on the fabrication of MOF thin films in respect with the potential deposition of MOF thin films on the surface of optical fibre LPG.

Both fibre optic LPG sensors and metal organic frameworks represent a hot research topic and both these areas noticed a rapid increase in the publications, with various range of suggested applications however long period grating fibre optic sensor with MOF functional coating has not been presented yet, the closest material applied on LPG was zeolite.

The information obtained from the literature review suggested that it should be possible to fabricate LPG based MOF coated sensor with high selectivity and sensitivity and this concept taken into practice is shown in Chapter 4 and Chapter 5.

Deposition of nanoparticles to functionalize LPG has been considered as the useful platform for the development of LPG based chemical sensors. The further functionalization of the sensitive layer broadens this concept even further and creates a possibility to measure a wide range of analytes. This approach was decided to be tested further in the real environments and it is demonstrated on two LPG based sensors for the detection of VOCs and ammonia in Chapter 6 and as a part of multi-parameter array used for IAQ monitoring in Chapter 7.

Chapter 3: Fabrication of LPGs using UV laser beam

3.1 Introduction

The fabrication of LPGs operating at phase match turning point with use of UV laser is presented. Two techniques, fabrication point-by-point and via the amplitude masks are compared.

All LPGs used in the project and presented in this thesis were fabricated by UV laser exposure using techniques described here. The purpose of this chapter is to summarize methodology, so the LPG fabrication details won't be repeated again in the following chapters.

3.2 Methodology

LPGs were fabricated using UV laser in a photosensitive boron–germanium co-doped optical fibre (Fibercore PS750). This type of the fibre provides the high photosensitivity to UV light due to the co-doped germanium into the fibre core enabling the fabrication of an LPG and doesn't require pre-treatment (such as hydrogen loading). The mode field diameter of 4.4 - 5.9 µm at 780 nm and cut-off wavelength in a range of 610 – 750 nm are stated by the manufacturer. For comparison, the standard telecommunication fibres are not sensitive to UV light and are set to operate around 1550 nm (third telecommunication window based on the absorption of commonly present chemicals in the environment) and thus their cut-off wavelength is in the near IR region.

The selected grating period facilitates coupling to a higher order cladding mode (LP_{019}) at the PMTP, where its response to external refractive index is largest (215). The use of optical fibre with a short cut-off wavelength ensures that resonance bands at their PMTP lie towards the red end of the visible spectrum, allowing the transmission spectrum of the LPG to be monitored using an inexpensive light source, halogen lamp, and a low-cost CCD spectrometer.

The combination of the wavelength range based on the properties of the fibre and the spectrometer together with the application of the phase matching curves (shown in Figure 2-10) gives the desired region of the LPG grating period close to 110.0 µm to provide sensors operating at PMTP (occurring by coupling to LP_{019} cladding mode) and thus to fabricate LPGs with the highest sensitivity with the attenuation bands in visible-near infrared spectrum. All the LPGs fabricated and used in this project fulfil those criteria.

The cladding modes associated with the attenuation bands have been calculated through numerical modelling using the phase matching equation and weakly guided approximation to determine the effective refractive indices of the core and cladding modes and the known values of the central wavelengths and the grating period (89).

Prior to the LPG fabrication and thus the exposure to the output from the laser, the polyacrylate jacket of the fibre was mechanically removed (using a specialized stripping tool) over the section of the proposed grating and the fibre was wiped using 2-propanol. The fibre was fixed using V-groves mounts on a translation stage. The fibre was fixed such that it was kept taut, with a constant strain, for the duration of the fabrication process.

The laser used to side-illumination of the optical fibre was a frequency quadrupled Nd:YAG laser emitting at 266 nm (Continuum minilite I). The output power of the laser was 5 mW and the beam diameter was 3 mm. A cylindrical lens with a focal length of 100 mm was used to focus the 3 mm diameter beam.

The fabrication set-up is shown schematically in Figure 3-1.

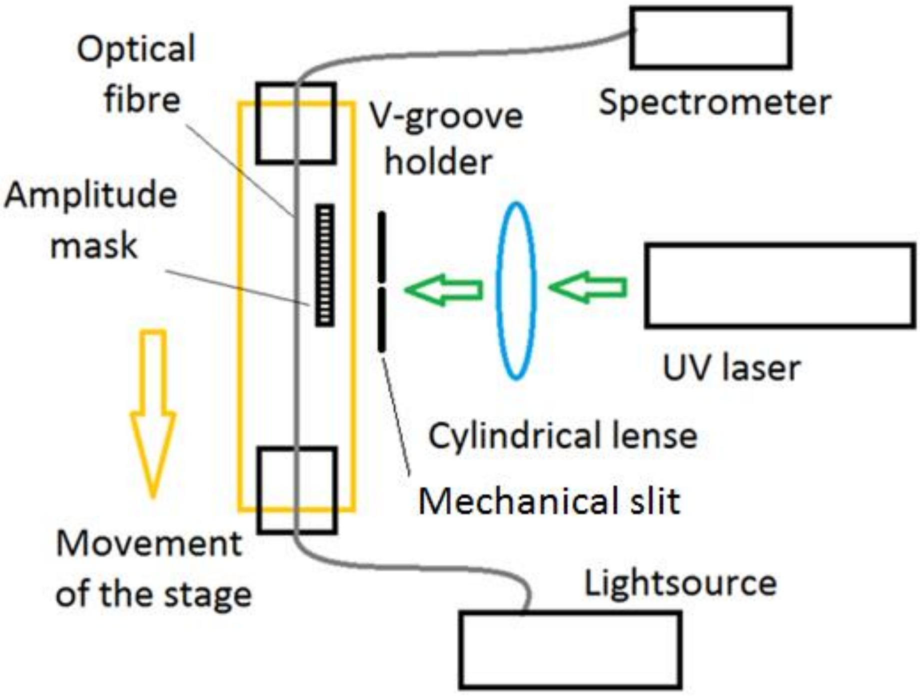

Figure 3-1: Scheme of the LPG fabrication using UV laser beam using point by point technique or via amplitude mask.

The point by point technique used mechanical metal slit to obtain the beam width of approximately 55 µm. Each part of the grating has been written separately with one spot exposure time of 30 s with followed by shift of the translation stage according to the desired grating period. The process was repeated until the grating length reached 30 mm.

The fabrication system is shown in Figure 3-2.

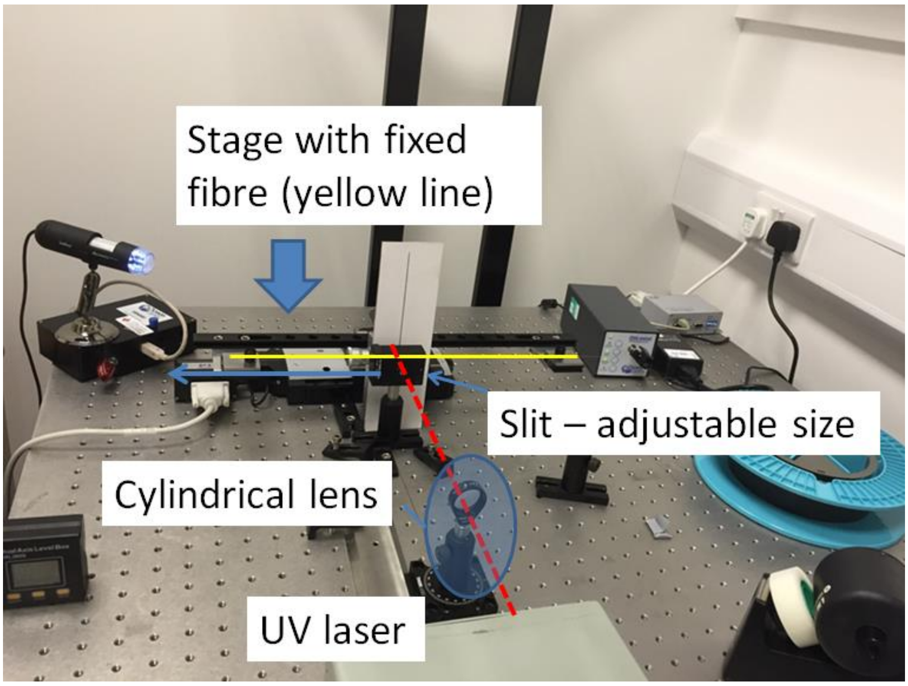

Figure 3-2: Setting of LPG fabrication system using UV laser via point by point approach.

Alternatively, the fibre can be exposed to the laser beam through custom made (Suzhou Sunshine Laser Technology Co., Ltd., China) amplitude masks of 1Cr18Ni9Ti steel alloy (the mechanical slit was removed from the system in this case). The beam propagates onto the amplitude mask, producing a 3 mm long line focus aligned with the axis of the fibre. The beam waist along the axis of the fibre was calculated to be 1 mm. The fibre was fixed in the proximity of the amplitude mask. During exposure, the optical fibre and amplitude mask were moved across the laser beam as shown schematically in Figure 3-1. The dimensions of the amplitude mask are 90x15x0.15-0.2 mm with a grating size of 70x6 mm in the central region, Figure 3-3.

Figure 3-3: Amplitude mask used for the fabrication of LPGs, custom made of 1Cr18Ni9Ti steel alloy (Suzhou Sunshine Laser Technology Co., Ltd., China); the dimensions of the whole mask are 90x15x0.15-0.2 mm (width-height-thickness with the grating itself of 70x6 mm (width-height).

LPGs with grating periods of 109.0, 108.8 and 108.6 µm or 109.0 and 109.5 µm have been fabricated using point by point approach and via amplitude masks respectively. The grating period has been chosen in such a way that LPG can operate at phase match turning point of LP_{019} cladding mode. The duty cycle of the fabricated LPGs was kept to be approximately 50:50.

The transmission spectrum of the optical fibre was recorded by coupling the output from a tungsten-halogen lamp (Ocean Optics HL-2000) into the fibre, analysing the transmitted light using a fibre coupled CCD spectrometer (Ocean Optics HR4000). Two different configurations were used. The spectrometer operates over the range of 200 to 1100 nm or 600 to 1100 nm with the resolution of 0.24 and 0.13 nm respectively. This light source was selected that it can provide enough light intensity at the desired wavelength range. The same setting has been used for all other experiments presented in further chapters.

The transmission spectra were recorded with an acquisition interval of 10 s during the LPGs fabrication. This sampling frequency is fast enough to monitor the changes in the transmission spectra associated with the LPG fabrication. The complete fabrication process takes 2.5 hours when fabricated using point-by-point method and 20 min when grating is inscribed via amplitude mask.

The Ocean Optics SpectraSuite software has been used for the displaying and saving the transmission spectra. The time average of three transmission spectra and the “boxcar width” function has been used to reduce the noise.

The positions of the central wavelengths have been determined using Spectra Interrogation Routine, the specialized home-made Labview based software (216), developed by Matthew Partridge, Cranfield University. The moving average function using 5 points was employed to detect central wavelengths position.

The same central wavelength tracking approach was applied throughout the entire work.

The transmission spectra of the fabricated LPGs, were measured in air and water or methanol (refractive index of 1.33 and 1.36 at 589.29 nm respectively) to demonstrate the repeatability of the fabrication procedure and to determine the sensitivity to the refractive index change.

The LPG arrays with the periods of individual LPG of 109.0 and 110.5 µm have been fabricated using amplitude masks to demonstrate the feasibility of LPG based multi-parameter sensing. The length of the individual LPGs was chosen to be 1, 2 and 3 cm.

The transmission loss increases with the increase of the LPG length. 1 cm represents the minimum for the detection of the attenuation band (≈10 %) at the transmission spectrum when using the fabrication system described above, while 3 cm provides the attenuation loss of about 40 %, at PMTP that is commonly used for the LPG based sensors (15)(140)(150). The increase of the LPG length to ≈4 cm does not provide the further increase in transmission loss due to the over-coupling (101). The decrease of the LPG length up to 1 cm can be beneficial in health monitoring applications, e.g. for in-situ measurement in endotracheal tube (217)(218) where as short as possible sensors are desirable.

3.3 Results and discussion

3.3.1 Fabrication via point by point approach

The point by point technique enables a precise control over the transmission spectrum by choosing the grating period, especially when the LPG operates close to or at the phase match turning point. As an example the change in the grating period of 0.2 µm enhances the rapid changes in the transmission spectra as demonstrated for LPGs with grating periods of 109.0, 108.8 and 108.6 µm, Figure 3-4.

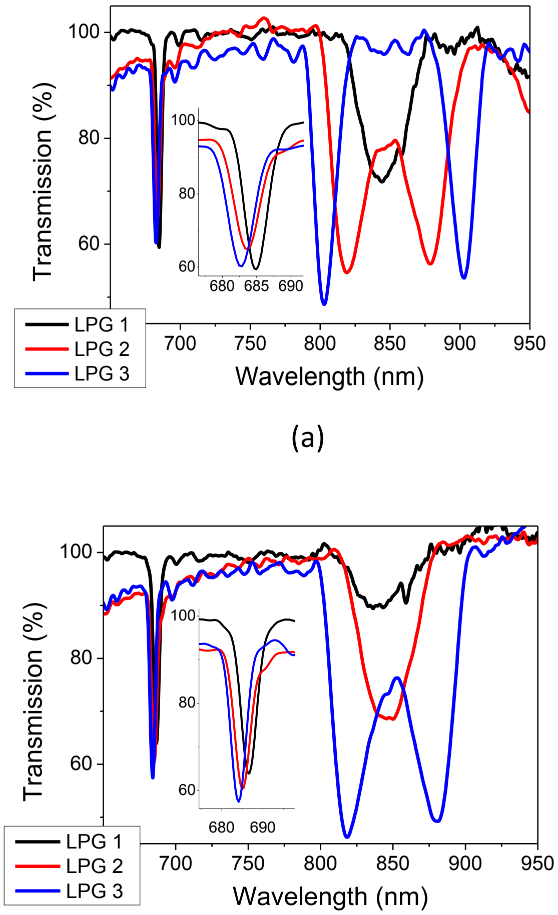

(a)

(b)

Figure 3-4: Transmission spectrum of LPGs fabricated using point by point approach with the LPG period of 109.0 (black), 108.8 (red) and 108.6 µm (blue) taken in a) air and b) water.

LPGs operating at PMTP have been successfully fabricated using point by point approach with similar results published in (96). The following LPGs had been fabricated with use of amplitude masks in order to fabricate LPGs faster, with similar transmission loss, width of the attenuation band and repeatability as with use of point by point approach.

3.3.2 Fabrication via amplitude masks

Absence of the control over the amount of refractive index change of the fibre core induced by the laser beam during the LPG fabrication has been mentioned as one of the disadvantages when LPG is fabricated using a UV laser beam via an amplitude mask (96). The amplitude of the refractive index can be controlled via speed of the translation stage, which determines the exposure time of each section of the fibre. Usually, the transmission loss of about 40 % is used for LPG based sensors (15)(20) and for this reason the speed of the movement of the stage was optimized to obtain 40 % transmission loss at LP_{018} and LP_{019}. The transmission loss is also proportional to the LPG length. LPGs with 40 % attenuation loss can be obtained at 30 mm length, with beam exposure time of 20 min that corresponds to the stage movement speed of 0.025 $mm.s^{-1}$.

The evolution of the transmission spectra during the LPG fabrication is shown in Figure 3-5a (on the next page). The attenuation band of LP_{018} cladding mode started to appear within 3 min from the beginning of the fabrication and from that moment the amount of transmission loss started to increase linearly until it reached 40 % loss after the 20 min of exposure to laser beam, Figure 3-5b. Similarly the evolution of the second resonance band (LP_{019}) working at PMTP was detected, where the shallow u-shape attenuation band occur after 5 min with further increasing of the transmission loss, Figure 3-5a. The length of the LPG was increasing linearly with time as the stage was moving, reaching 30 mm after 20 min.

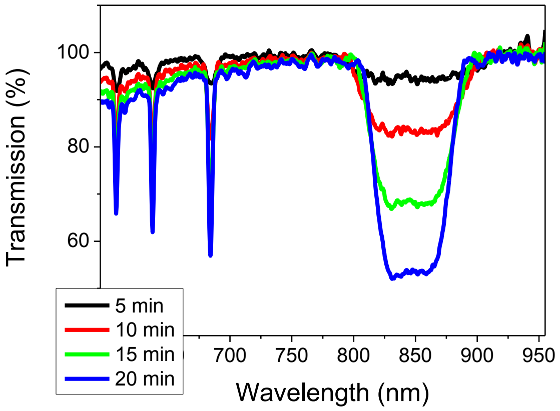

(a)

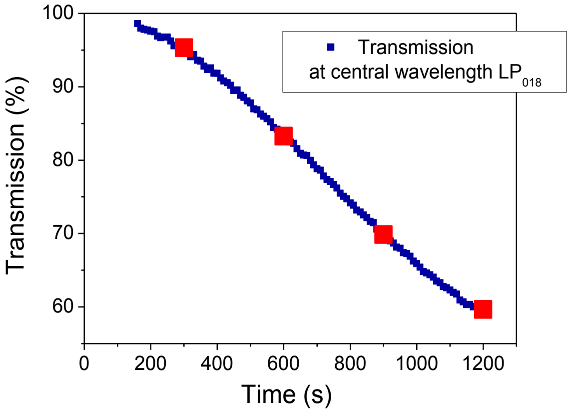

(b)

Figure 3-5: Transmission spectra of LPG with period of 109.0 µm after 5 (black line), 10 (red), 15 (green) and 20 min (blue) from the beginning of the beam exposure and b) Change in the transmission at the central wavelength of LP_{018} *cladding mode during the LPG fabrication (blue) (red squares determine the position of the selected transmission spectra shown in Figure 3-5a).*

Repeatability of the fabrication procedure is one of the important requirements for mass production of LPG based sensors and it is highly challenging to achieve this especially when the LPG operates close to or at the

PMTP. In order to demonstrate the feasibility of the reproducibility, three LPGs with same period of 109.0 µm that operate at PMTP were fabricated. Changes in the transmission spectra were recorded in air and methanol, with the results shown in Figure 3-6.

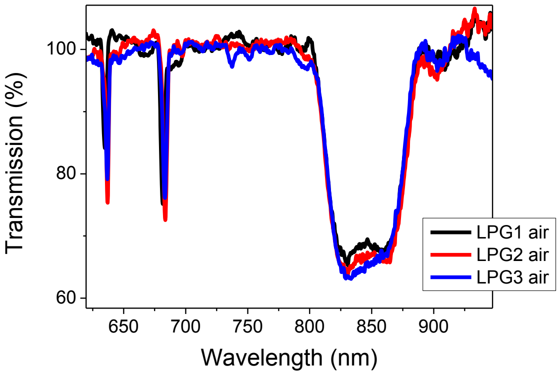

(a)

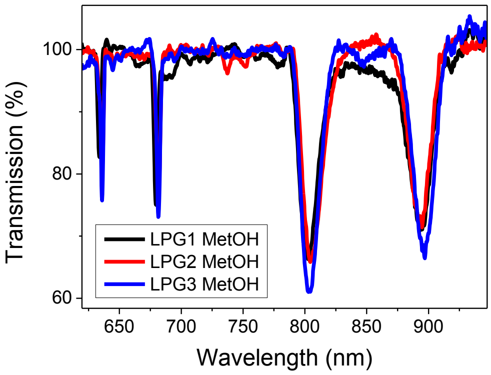

(b)

Figure 3-6: Transmission spectra of LPGs with period of 109.0 µm measured in a) air and b) methanol corresponding to LPG1 (black), LPG2 (red) and LPG3 (blue).

The difference in the transmission loss of the LP_{019} attenuation band was less than 3 % and the difference between the separations of the attenuation bands corresponding to the same LP_{019} cladding mode was observed to be less than 2 % in methanol. Similar results were observed for LPGs with period of 109.5 µm, Figure 3-7b.

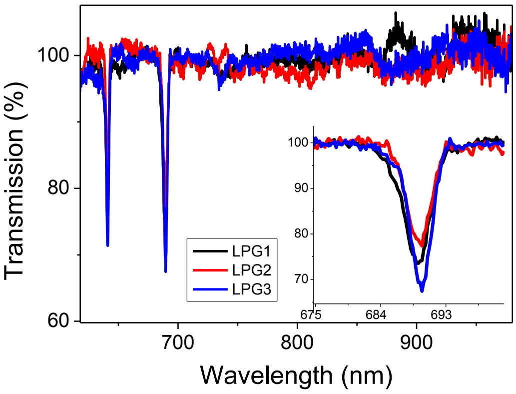

(a)

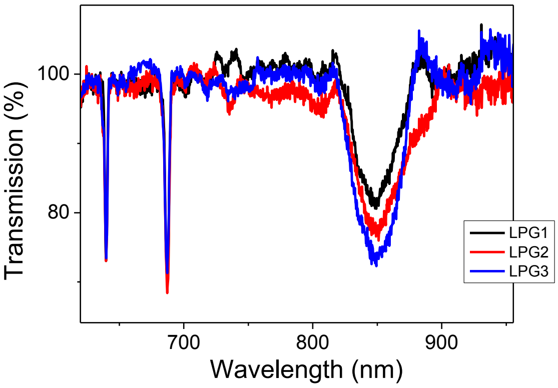

(b)

Figure 3-7: Transmission spectra of LPGs with period of 109.5 µm measured in a) air and b) methanol corresponding to LPG1 (black), LPG2 (red) and LPG3 (blue), the inset shows the attenuation bands corresponding to LP_{018} cladding mode.

These results show similar repeatability as the previously presented LPGs fabricated by UV laser with point by point technique (96).

The possibility to multiplex LPGs is demonstrated with the fabrication of the array containing two LPGs with period of 109 and 110.5 µm. It is possible to distinguish clearly each individual LPG in the transmission spectrum. The proportion of transmission loss to LPG length is demonstrated as the arrays consist of LPGs with length of 1, 2 and 3 cm, Figure 3-8, where even the length of 1 cm enables the recognition of the attenuation bands of the LPGs.

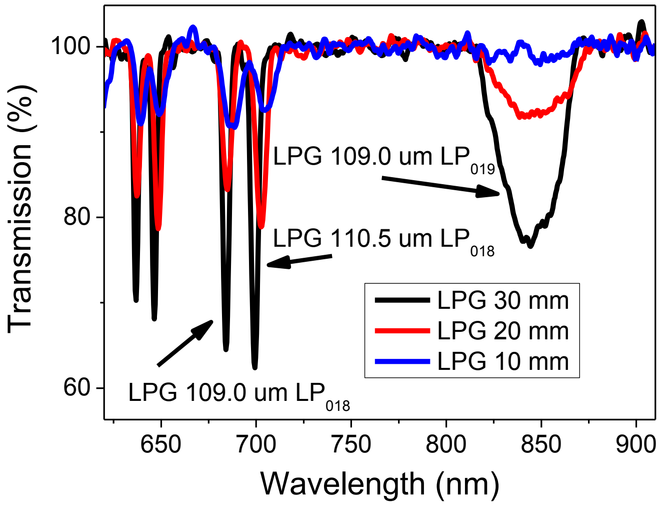

Figure 3-8: Transmission spectra of array consisting of LPGs with period of 109 and 110.5 µm and length of 3 cm (black), 2 cm (red) and 1 cm (blue) measured in air.

3.5 Conclusions

Fabrication of LPGs using UV laser irradiation point by point or via the amplitude masks has been shown. For the first time to the best to author's knowledge, the fabrication of LPGs operating at the PMTP using amplitude masks has been presented. Fabrication technique via an amplitude mask produces LPGs at PMTP with high transmission loss and narrow attenuation bands. High repeatability of the fabrication process that can produce LPGs with highly similar transmission spectra was presented using an inexpensive custom made amplitude mask.

Chapter 4: Organic vapour sensor based on LPG modified with ZIF-8

4.1 Introduction

In this chapter, an LPG based chemical vapour sensor coated with ZIF-8 functional coating is presented. The ZIF-8 film was characterized by scanning electron microscopy (SEM) and the thickness and refractive index of the 1,2,3,5 and 10 growth cycles thick films were determined using an ellipsometer. The crystallinity of the films was examined by x-ray diffraction pattern (XRD). The performance of an LPG coated with a ZIF-8 thin film exposed to methanol, ethanol, 2-propanol and acetone vapours is discussed, revealing a concentration specific response to methanol, ethanol and acetone.

4.2 Background information

The fabrication of low-cost, portable, accurate and real-time sensors for VOCs is of considerable interest as the gas chromatography – mass spectroscopy (GC-MS) approach used commonly for total VOCs detection is expensive and needs experienced personnel (35). The key element of any portable chemical sensor is the sensitive layer that captures the analyte.

Chapter 4: Organic vapour sensor based on LPG modified with ZIF-8

It has been shown in Chapter 2 that metal organic frameworks (MOFs), because of their unique properties, offer an ideal platform for the development of the sensitive layer.

Among the variety of MOFs, zeolitic imidazole framework (ZIF) - ZIF-8 possesses properties that show promise for sensor development, such as its chemical robustness and thermal stability due to the sodalite (SOD) type of structure. The structure of ZIF-8 comprises zinc ions coordinated by four imidazolate rings with large cavities (11.6 Å) and small pore apertures (3.4 Å) (199), Figure 4-1.

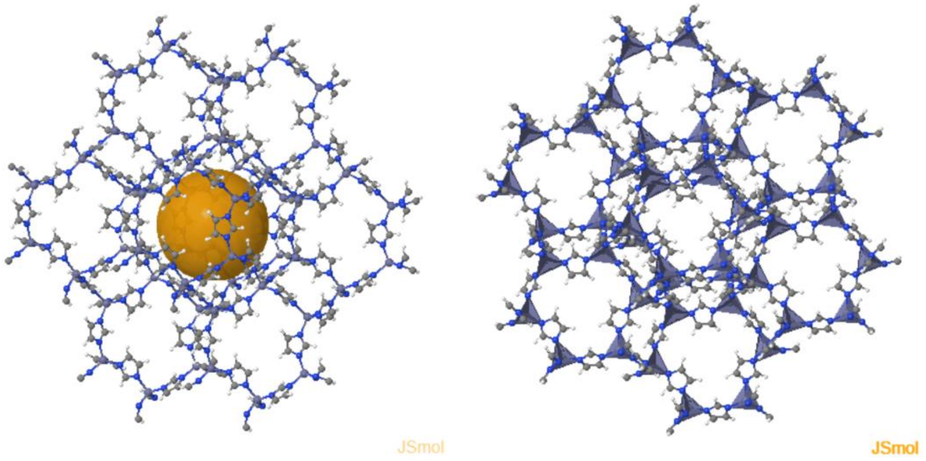

Figure 4-1: ZIF-8 3D structure (The tetrahedra show the zinc-nitrogen bonds; The sphere represents the pore size within the framework which can be used for gas storage; Both figures represent the same ZIF-8 structure) (160).

ZIFs have been considered to behave as adsorbents with molecular sieving properties. An investigation of a ZIF-8 film demonstrated the adsorption of isopropanol in a selective manner versus water (219). A ZIF-8 based Fabry-Perot interferometer exhibited a concentration-specific reaction to a mixture of propane and nitrogen (24). ZIF-8 film fabrication involves no substrate modification. The procedure works at room temperature and facilitates control over the thickness with one growth cycle that takes less than an hour (22)(24).

4.3 Methodology

4.3.1 Materials

Zinc nitrate hexahydrate, 2-metyl-imidazole, methanol, ethanol, 2-propanol and acetone were purchased from Sigma-Aldrich. All of the chemicals were analytical grade reagents and used without further purification.

4.3.2 Characterization of ZIF-8 film

SEM was used to evaluate the structure and the thickness of the films deposited on glass substrates. Measurements were undertaken by Philips XL30 FEG ESEM electron microscope with 10 kV beam voltage. Glass slides of dimensions 1x1 cm^2 and 2x2 cm^2 were cut from standard microscope glass slides and then coated with ZIF-8 thin films, following the procedure described in section 4.2.3. Samples coated with films consisting of 1,2,3,5 and 10 growth cycles of ZIF-8 were characterized by SEM.

Thin Pt layers were sputtered on all samples before the SEM analysis. The sputter was set to 0.8 kV voltage and 0.7 mA current. The glass slides were sputtered by two layers of the Pt coating, with a deposition interval of 90 seconds.

The thicknesses of the films on the glass substrates were further evaluated using an ellipsometer. The measurements were undertaken using an Alpha-SE Ellipsometer (J.A Woolan) and the data processed using a model assuming a transparent film on a glass substrate. Data were collected at a spectral resolution of 1 nm and measured in the wavelength range of 380–900 nm; for simplicity the RI value of the mesoporous film was determined at one wavelength (632.8 nm). The refractive index measurement has been taken at 632.8 nm. The changes in the refractive index over the wavelength range of 400-800 nm are negligible (220) and cannot influence the LPG sensor performance or the comparison with other films/fabrication techniques.

X-ray diffraction patterns were collected using a Bruker-AXS D8 Advance diffractometer, using θ/θ goniometer geometry, a Cu-anode line-focus x-ray tube (powered at 40 kV & 35 mA), a Göbel mirror (producing a parallel CuKα beam) with a 0.6 mm exit slit, a diffracted beam 0.12º Soller-slit collimator and a scintillation counter x-ray detector. The samples were scanned with a fixed glancing incident angle of 2.140 and 1.140º, over a 2θ range of 5º to 40º, with a 2θ step size of 0.02º and a step time of 32 s. (The x-ray analysis had been done by Dr Nigel Neate, an expert in this field from the University of Nottingham).

4.3.3 Sensor fabrication and modification

LPG with grating period of 110.7 µm and of length 40 mm, was fabricated in a point-by-point fashion. The results obtained using this LPG are shown in sections 4.4.3 and 4.4.4. LPGs with grating periods of 109.0 and 109.5 µm and of length 30 mm, were fabricated using an amplitude mask and the results are shown in section 4.4.5. The fabrication procedure followed the methodology described in details in Chapter 3.

The set-up of the sensing system is schematically shown in Figure 4-2.

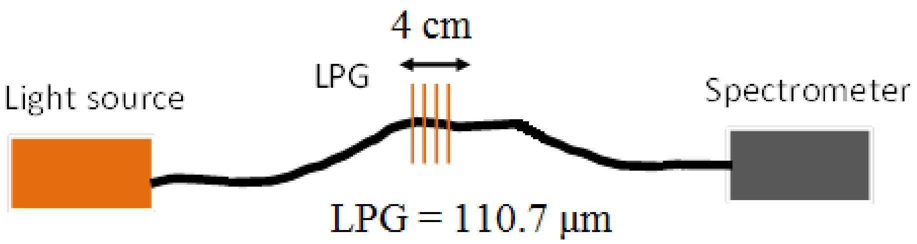

Figure 4-2: Schematic illustration of the LPG sensor.

LPG was coated with ZIF-8 by an in-situ crystallization technique, Figure 4-3 (22)(24).

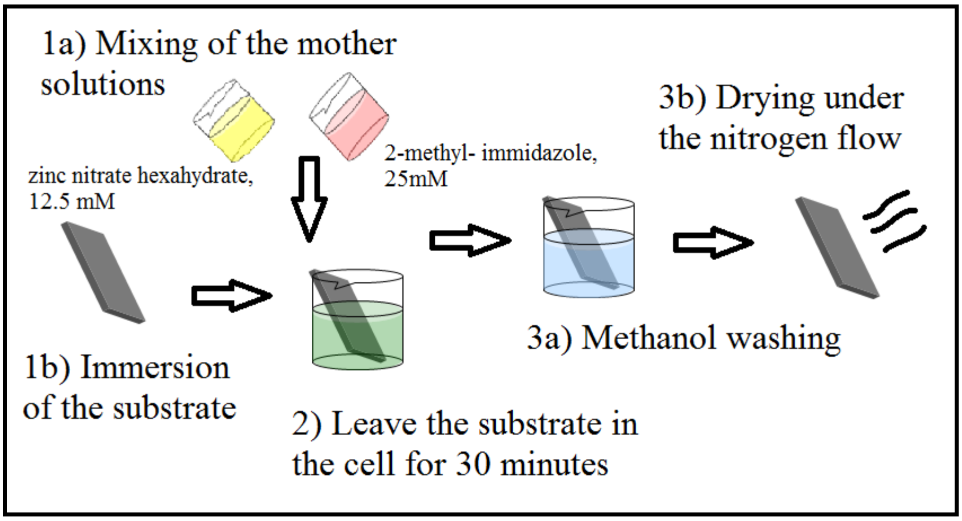

Figure 4-3: ZIF-8 fabrication methodology (24).

Briefly, solutions of 15 ml of 12.5 mM zinc nitrate hexahydrate and 15 ml of 25 mM 2-metyl-imidazole in methanol were mixed in a Petri dish. The LPG was fixed in a specially designed holder to keep the LPG taut and straight. The LPG was placed inside the Petri dish and immersed into the film forming solution for a period of 30 min. Then the LPG was washed by methanol and dried under nitrogen flow. The process was repeated to obtain thicker films consisting of 2 and 5 growth cycles. The transmission spectrum of the LPG was monitored during each deposition step.

4.3.4 Sensor performance

The performance of the coated LPG as a chemical sensor was investigated by monitoring the central wavelengths of the resonance bands while exposing the sensor to methanol, ethanol, 2-propanol and acetone vapours. VOCs samples of volume of 200 µl were injected by a pipette into a container containing the LPG, Figure 4-4. The transmission spectra were monitored with acquisition interval of 10 seconds. A water droplet was also injected for comparison, with the aim of investigating the response to relative humidity, a potential interfering factor.

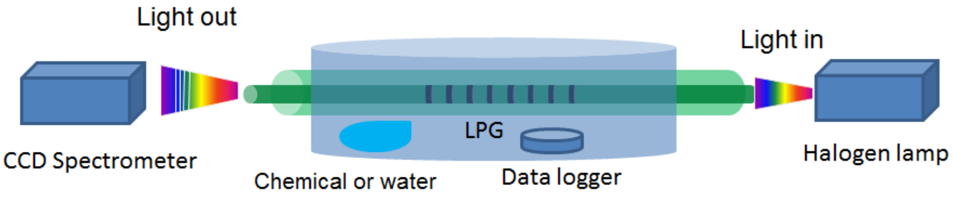

(a)

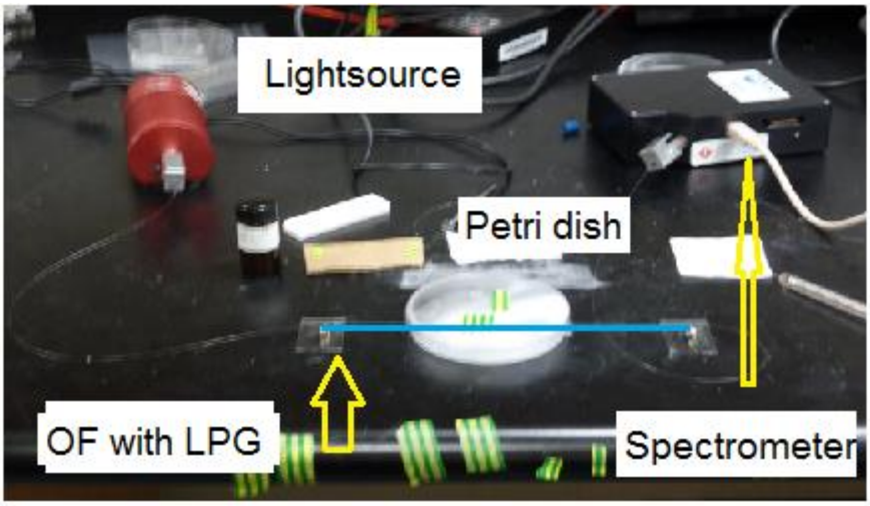

(b)

Figure 4-4: Set-up for chemical sensitivity experiments: a) scheme and b) photo of the experiments conducted in Petri dish.

The response of the LPG to methanol, ethanol, 2-propanol and acetone was investigated with the fibre positioned in an environmental chamber composed of closed polytetrafluoroethylene (PTFE) box (15x15x15 cm with a total volume of 3.375 L), Figure 4-5. The LPG was fixed 5 cm above the base. The chemical of interest (volume of 10 and 50 µl or 0.5 and 2 µl for experiments presented in section 4.4.4 and 4.4.5 respectively) was injected from the top of the box by a pipette and the transmission spectrum was monitored and recorded. The concentration was calculated according to the amount of the analyte injected and the volume of the box.

Figure 4-5: PTFE box used for the chemical sensing.

Temperature and relative humidity were also recorded during all experiments with logging interval of 10 seconds by data logger (iButton® Hygrochron Temperature/Humidity Logger, part number DS1923, from Maxim Integrated^{TM} with precision of +/-0.5 ^{o}C and +/- 0.6 RH %) and a temperature resolution of 0.5 ^{o}C.

The chemical concentration of the organic gases in the closed chamber has been calculated as follows. The concentration in ppm is given as the portion of the volume of the organic compound in gas form ($V_{VOC[g]}$) divided by the volume of the whole chamber ($V_{chamber}$), Equation 6.

$$\mathrm{C}\ [\mathrm{ppm}] = \frac{V_{VOC[g]}}{V_{chamber}}$$

Equation 6

The volume of the injected VOC in the gas form can be calculated via the following equation based on the ideal gas law, Equation 7.

$$V_{VOC[g]} = 22.4 * \frac{T_1}{T_{std}} * n = 22.4 * \frac{T_1}{T_{std}} * \frac{m}{M} = 22.4 * \frac{T_1}{T_{std}} * \frac{\rho V_{VOC[l]}}{M}$$

Equation 7

Where $V_{VOC[l]}$ is the injected volume of the chemical in the liquid form, *22.4* is the volume of 1 mol of the ideal gas at standard conditions (pressure of 1 atmosphere and temperature of 0^oC), T_1 is the actual temperature when the experiment was conducted, the whole fraction T_1/T_{std} is the correction for any temperature deviation from the standard conditions, *n* is the amount of molls, *m* is the mass of the VOC compound, *M* is the molecular weight and *ρ* signs the density. The substitutions for number of molls (*n*) has been calculated using basic chemical formula n = m/M and m=ρ.V.

4.4 Results and discussion

4.4.1 Film morphology

The SEM images allow to assess the coverage of the glass-slide substrate, Figure 4-6, and the thickness of the deposited ZIF-8 film, Figure 4-7. The density of the crystals over the substrates is affected by the concentration of the film forming solution. The optimal in terms of the uniform crystal cover over the surface of the substrates was found to be 12.5 mM for Zn source and 25 mM for methyl-imidazole (22).

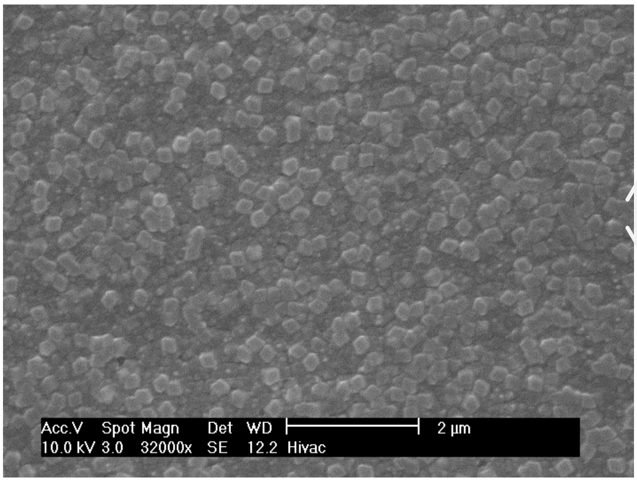

Figure 4-6: Top view SEM image of ZIF-8 film grown on glass substrate with 5 growth cycles.

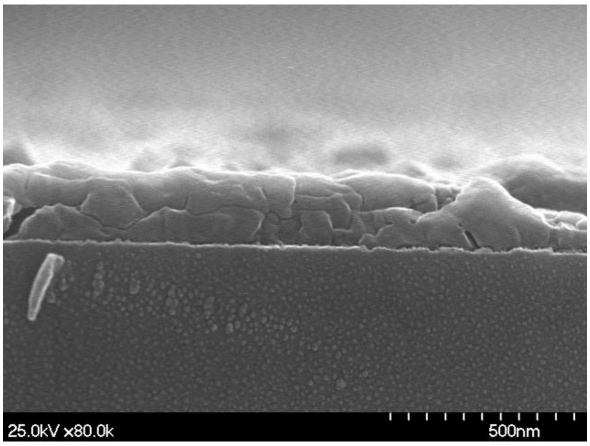

Figure 4-7: Cross sectional SEM image of ZIF-8 film grown on glass substrate with 10 growth cycles.

The horizontal size of the crystals in the ZIF-8 film was observed to increase as a function of growth cycle, starting at approximately 100 nm and ending at

400 nm, in films of 1 and 10 growth cycles respectively. This effect was observed through substrates coated with 1, 3, 5 and 10 growth cycles, Figure 4-8 and Figure 4-9 respectively.

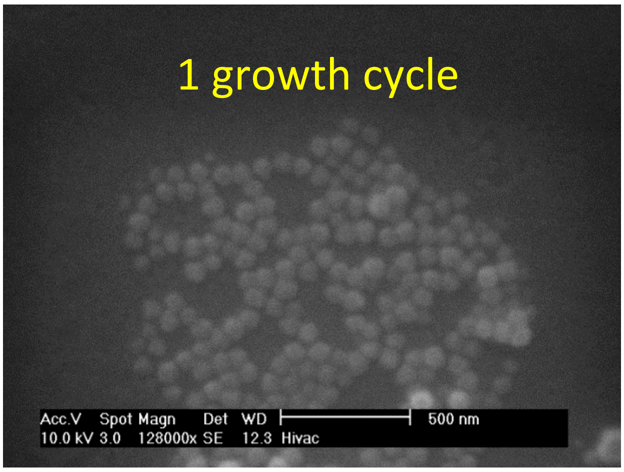

(a)

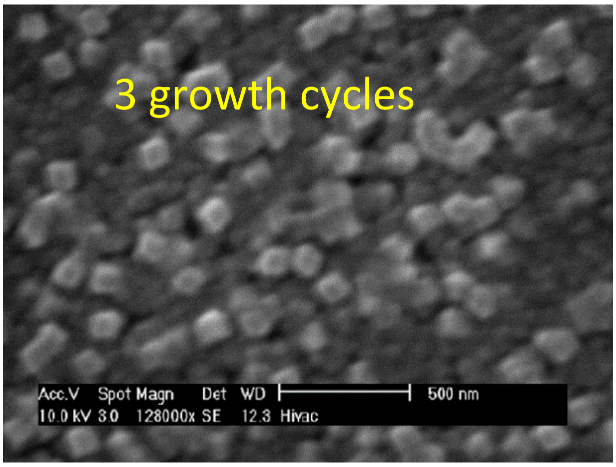

(b)

Figure 4-8: SEM images of ZIF-8 film comprised of a) one and b) three growth cycles (the white line at the bottom corresponds to 500 nm).

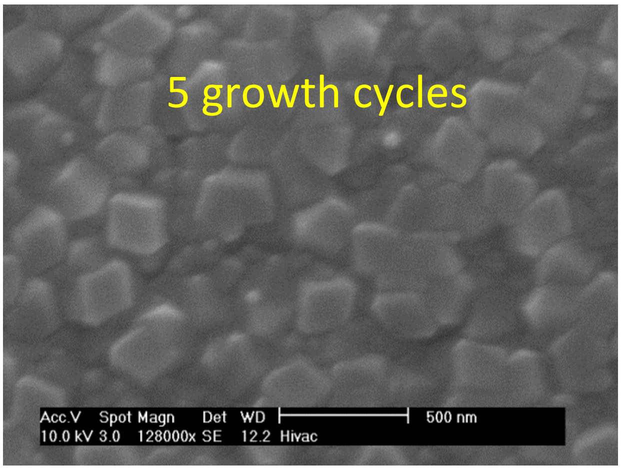

(a)

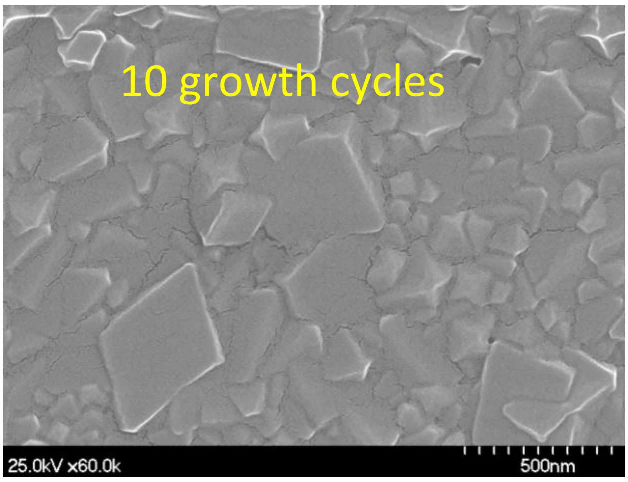

(b)

Figure 4-9: SEM images of ZIF-8 film comprised of a) five and b) ten growth cycles (the white line at the bottom corresponds to 500 nm).

This could be explained by the agglomeration of the freshly crystalized ZIF-8 units onto the surface of the previously formed ones, similarly to that described for the seeded growth fabrication technique (154). The increase of the crystal sizes with increasing number of growth cycles has been observed previously for substrates comprised of 1, 10 and 40 growth cycles (24).

Lu and Hupp characterized the surface area by applying the Brunauer-Emmett-Teller equation and obtained surface value S_{BET} = 1530 m^2/g and the micropore volume V_{micro} = 0.59 cm^3/g (estimated by Saito and Foley (SF) method) (24). As the same fabrication procedure has been followed here, similar characteristics are expected.

The film thickness was evaluated using cross-sectional SEM imaging. A film consisting of 10 growth cycles has a thickness of about 400 nm, Figure 4-7, which is approximately about half of the value presented earlier obtained using the same deposition method (24). The smaller thickness of the film in comparison to the work presented by Lu and Hupp (24) could well be due to the differences in the nitrogen flow rate or the exact vertical position of substrates in the Petri dish during the crystallization process in the film forming solution.

The SEM images were taken on the glass slides following the same procedure as conducted for the deposition on the optical fibre LPG. It was assume that properties of the obtained thin films are similar. In addition, advantage of using glass substrates instead of optical fibres is in the simpler experimental procedure for SEM measurements. Monitoring of the properties of the film directly on the fibre surface or the tip of the optical fibre should be done in the further work.

Ellipsometry measurements were conducted to investigate further the thickness of the substrates coated with 1, 2, 3, 5 and 10 growth cycles. A linear dependence of the MOFs film thickness on number of the deposited cycles was obtained with the slope of approximately 50 nm per growth cycle, Figure 4-10. These results correspond well with the data obtained using SEM images, Figure 4-7.

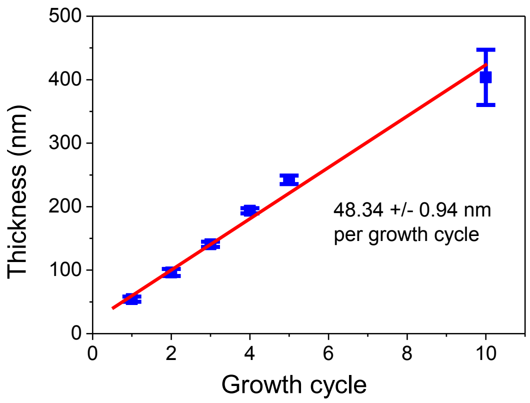

Figure 4-10: Ellipsometry measurement: thickness of the ZIF-8 film as a function of growth cycle (average value is shown and error bars were calculated as the standard deviation from the measurement over the 3 samples).

The refractive index (RI) of the coating was measured by ellipsometry and a nonlinear relation between growth cycle and RI was observed. RI values varied from 1.48 to 1.40 for a film composed of 1 and 10 growth cycles respectively, Figure 4-11. Interestingly, this change corresponds to the size of the crystals, Figure 4-8 and Figure 4-9. Larger crystals were observed on the substrates at the higher number of growth cycles which could denote presence of larger mesopores in the film structure (221). Refractive index of ZIF-8 films depends strongly on the selected crystallization method and conditions during fabrication. As an example, crystallization can be conducted in the nitrogen atmosphere, or under the N_2 flow with different rate or time or it can be conducted at the liquid-air interface in the capillary regime (24)(221). Large variations in RI values have been reported previously. Demessence et al. reported ZIF-8 films with RI ranging from 1.18 and 1.23 (219). On the other hand, Cookney et al. obtained ZIF-8 films with much higher RI ranging from 1.54 to 1.58, which was related to the low porosity of these films (221).

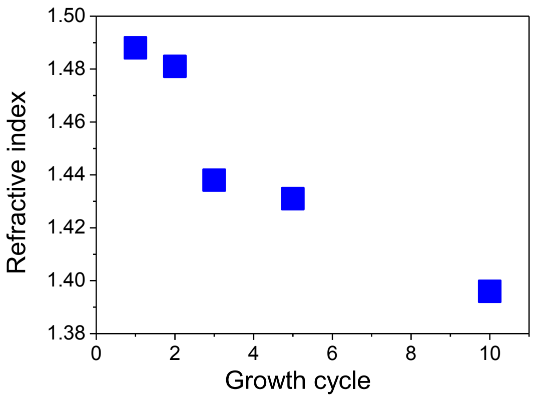

Figure 4-11: Ellipsometry measurement: refractive index of the ZIF-8 film as a function of growth cycle (RI was measured at 632.8 nm).

4.4.2 Film structure

X-ray diffraction patterns establish that the films comprised of ZIF-8 crystals, Figure 4-12. The positions of the peaks {110}, {200}, {211}, {220}, {310} and {322} indicate a crystalline ZIF-8 structure. The highest intensity, at the {110} reflection peak, suggests that the orientation of the crystals is perpendicular to the substrate. The elevated plateau from 15 to 40 θ° relates to the amorphous structure of the glass substrate. The position and the intensity of the peaks in Figure 4-12 are in a good agreement with the X-ray diffraction patterns presented in the literature and as well with the modelled diffraction pattern for ZIF-8 (24)(179).

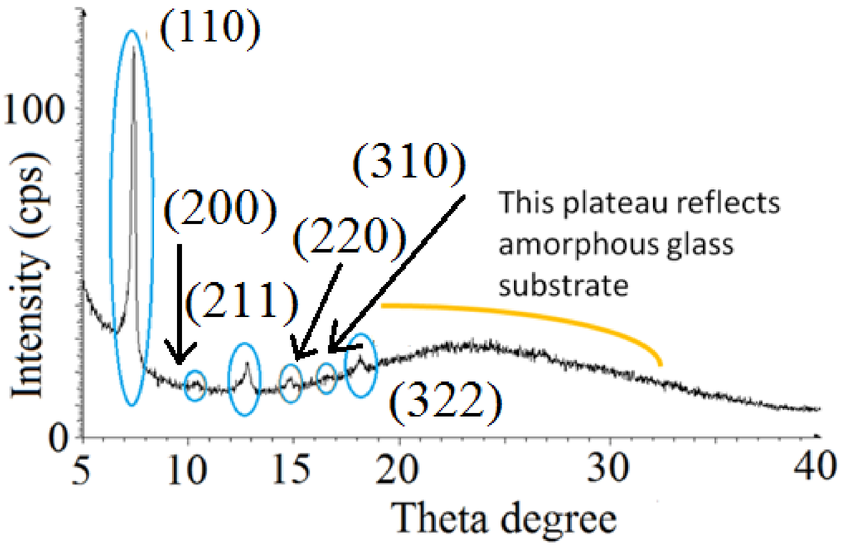

Figure 4-12: In-plane X-Ray diffraction patterns of 20 growth cycles of ZIF-8 film on glass substrate, recorded at room temperature.

4.4.3 LPG modification

The transmission spectrum of an unmodified LPG with period of 110.7 µm is shown in Figure 4-13. Attenuation bands in the region of 775 and 900 nm correspond to the LP_{019} cladding mode and operate near the PMTP, while the other bands (region of 625 and 670 nm) correspond to lower order cladding modes and are less sensitive for this LPG period.

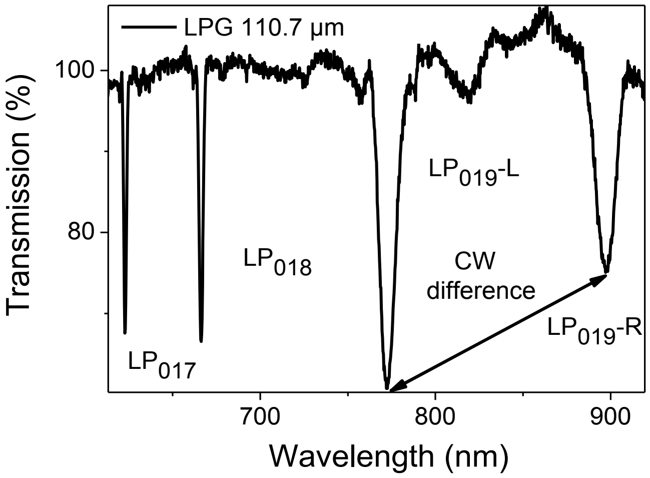

Figure 4-13: Transmission spectrum of an uncoated LPG with period of 110.7 µm measured in air, with attenuation bands at 670 nm and 775 and 900 nm corresponding to the LP_{018} and LP_{019} cladding modes (the dual resonance was observed for the LP_{019} cladding mode denoted as LP_{019}-L (775 nm) and LP_{019}-R (900 nm)); CW, central wavelength.

Changes in the transmission spectra of the LPG when immersed into the film forming solution were monitored. The transmission spectra recorded 30 min after the immersion are compared in Figure 4-14.

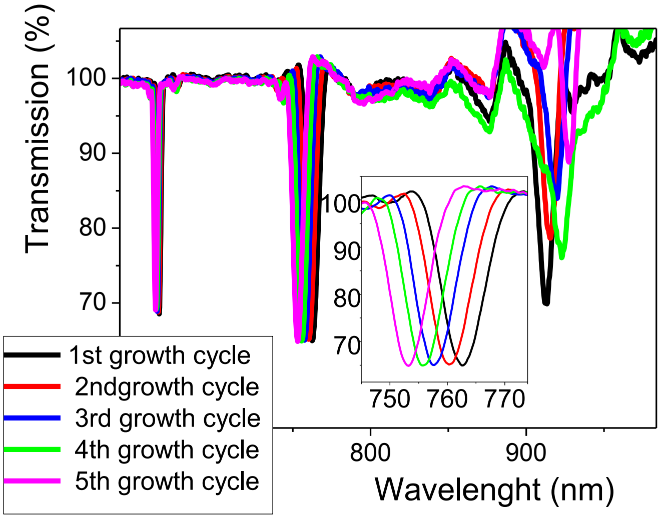

Figure 4-14: Transmission spectrum of LPG sensor measured in solution a) after 30 min of immersion to the film forming solution for 1st (black line), 2nd (red), 3rd green, 4th (blue) and 5th (magenta) growth cycle of ZIF-8, the inset shows the attenuation bands corresponding to LP_{018} *cladding mode in detail.*

The shifts of the central wavelengths of the LP_{019}-L, LP_{019}-R and LP_{018} resonance bands recorded in the film forming solution over the 1st to 5th growth cycles were observed to be of order nanometres, with the highest value for LP_{019}-R. Larger shifts of the central wavelengths of the attenuation bands were observed when the LPG was immersed in the solution than when the LPG was in air. This was expected, since the attenuation bands are known to show a dependence on the refractive index of the medium surrounding the fibre, with the response being larger for higher surrounding refractive indices (89) and previous work has also shown that the presence of a thin coating on the fibre can influence the sensitivity to surrounding refractive index (112)(222).

Changes in the central wavelengths of all of the attenuation bands were observed in air after the deposition of each of 1st to 5th growth cycle of ZIF-8,

Figure 4-15. The largest shift of the central wavelength during the deposition was observed for LP$_{019}$-R. The difference in the sensitivities of LP$_{019}$-R and LP$_{019}$-L to the film thickness can be explained by asymmetry in the phase matching curve around the PMTP (20)(91). The increasing separation of the attenuation bands corresponding to LP$_{019}$-L and LP$_{019}$-R can be expressed as the change of the difference between the central wavelengths and this change ranged from 150.61 to 174.19 nm for 5 growth cycles. The enhanced sensitivity that is achieved by operating at the PMPT is highlighted by the comparison of the response of the resonance band corresponding to coupling to LP$_{018}$ with those of LP$_{019}$-L and LP$_{019}$-R in Figure 4-16. A linear dependence of the change in the separation of the central wavelengths of LP$_{019}$-L and LP$_{019}$-R on the number of growth cycles indicates the uniform growth of the ZIF-8 film, Figure 4-16.

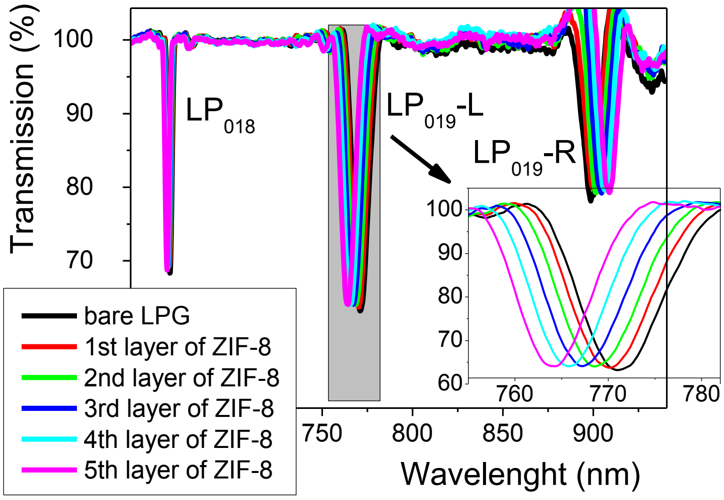

Figure 4-15: Transmission spectra of the LPG measured in air; black line, bare LPG and red, green, blue, cyan and magenta lines after the deposition of 1st to 5th growth cycle of ZIF-8.

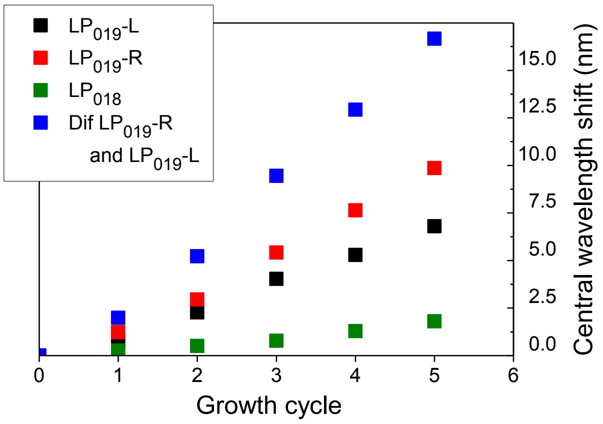

Figure 4-16 Change in the position of the central wavelength corresponding to LP_{018}, LP_{019}-L, LP_{019}-R cladding modes and the change in the difference between the central wavelengths corresponding to LP_{019} cladding mode (blue) during the deposition of 1st to 5th growth cycle of ZIF-8.

The smaller response of the central wavelengths of the attenuation bands for the first growth cycle agrees with the observations of Lu and Hupp when depositing ZIF-8 on silica substrates (24), where they reported that the thickness of the coating deposited on the first growth cycle was less that the thicknesses of the layers deposited after subsequent growth cycles.

The linear relationship between the change of the separation between the central wavelengths and the number of growth cycles correlates well with the thickness measurements taken by the ellipsometer. The change in the central wavelength difference are plotted as a function of the optical thickness, i.e. the product of RI and thickness of the ZIF-8 film determined from the ellipsometer in Figure 4-17, showing a linear relationship with a gradient of 4.7 nm wavelength shift /100 nm film thickness.

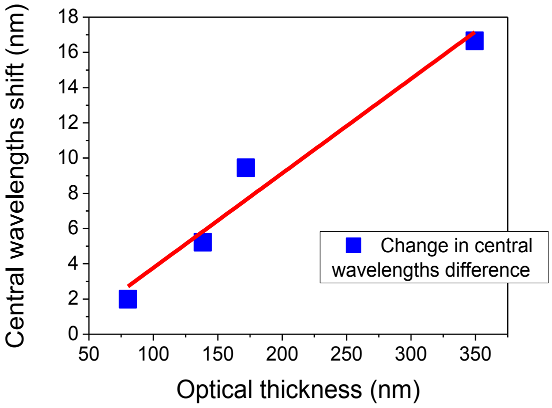

Figure 4-17: The change in the separation of central wavelengths (LP_{019}-R minus LP_{019}-L) corresponding to LP_{019} cladding mode induced by the deposition of ZIF-8 as a function of optical thickness.

The transmission spectrum was monitored and recorded throughout the deposition process, and the separation between the LP_{019}-L and LP_{019}-R bands are plotted as a function of time in Figure 4-18. The plots show a number of interesting features. Firstly, as indicated by the black lines, which are a guide to the eye, the central wavelengths of the resonance bands show a higher sensitivity to coating thickness when the LPGs is immersed in the growth solution than they do when the LPG is in air. Secondly, when the LPG is immersed in the growth solution, following the initial large step change in the central wavelengths in response to the increased surrounding refractive index, there is a continuous change as the ZIF-8 crystallises onto the optical fibre.

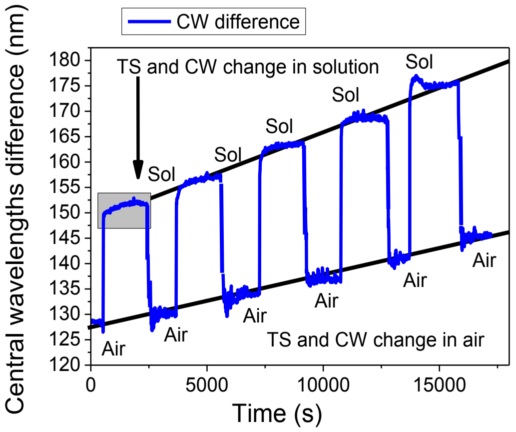

Figure 4-18: The dynamic shift of the central wavelength during the deposition of 1st to 5th growth cycle onto a surface of LPG.

The oscillation of the central wavelength that occurred after the immersion process is likely due to the nitrogen flow that affects the spectra in two ways. Firstly, the central wavelength change is caused only by the mechanical response of the LPG to the flow, which causes slight movement and bending. Secondly, the chemical process is taking a place in the freshly crystallized ZIF-8 film, where methanol is being replaced by nitrogen and then subsequently replaced by air in the ZIF-8 pores until the final crystalline ZIF-8 structure is reached on the surface of LPG.

The rapid decrease of the central wavelength that can be seen to occur immediately after the immersion in the film forming solution indicates that the crystallization process starts rapidly and a high efficiency was observed within the first 10 minutes. The evolution of the transmission spectrum while the LPG was in the film forming solution (for the 1st growth cycle, labelled with the grey box in Figure 4-18, was used for the evaluation of the film fabrication process, Figure 4-19.

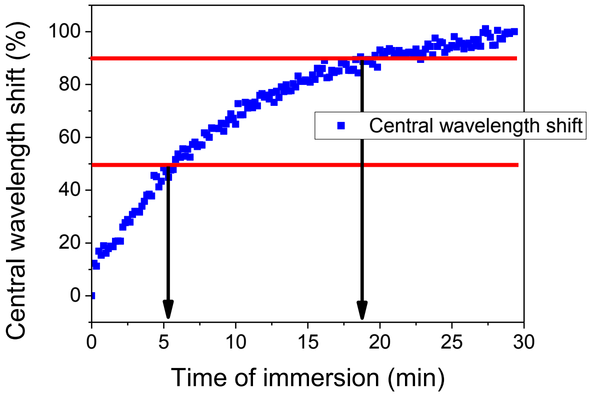

Figure 4-19: The relative shift of the central wavelength during the immersion in the film forming solution over the deposition of 1^{st} growth cycle of ZIF-8 (red lines indicated 50 and 90 % of the deposition process).

The measurement of the change in the difference between central wavelengths in real time provides an opportunity to observe the efficiency of the crystallization during the deposition in real time. It is possible to identify that the crystallization process starts rapidly, with a 50 % and 90 % of the central wavelength change reached within ~5 and ~20 min respectively. The central wavelengths of the attenuation bands were determined in real time using the peak detection routine in LabVIEW to process the spectra recorded by the Ocean Optics spectrometer.

This finding is in a good agreement with real time measurements during the film deposition reported with the use of Quartz Crystal Microbalance (QCM) measurement of ZIF-8 film growth where changes in frequency and mass were measured for 2 hours and the 90 % mass change taken a place within 30 minutes (24). For this reason authors decided to set the growth cycle immersion for 30 min. Both the QCM and LPG data indicate that 50 % crystallization is achieved within ~5 min following immersion in the solution.

4.4.4 VOCs sensing

The LPG sensor response to the injection of each of the tested VOCs to the Petri dish was within 30 s. The shift of the central wavelengths of the bands reached the saturation in less than 60 s for methanol and acetone and about 180 s for ethanol and 2-propanol. The response time correlates well with differences in volatility (based on the differences in boiling points), of the solvents where the highest value is expected for acetone, then methanol, ethanol and 2-propanol, respectively (223). The evaporation rate is affected by the functional group, partial pressure of the saturated vapour, molecular weight, surface of the spill and air flow over the spill.

The highest response was observed for methanol, where the change in the bands' separation due to the concentrated vapours of 4.23 nm was obtained in comparison to 2.4 nm change induced by exposure to ethanol, for the sensor coated by 5 growth cycles, Figure 4-20. The inset shows the LP_{019}-L attenuation band in detail, where central wavelength shifts of 2.7 and 1 nm were observed for methanol and ethanol, respectively.

A decrease of the transmission amplitude of the LP_{019}-L band caused by the RI change due to the exposure to the chemical vapours was observed. Similar to the central wavelength, the highest intensity change was observed for methanol.

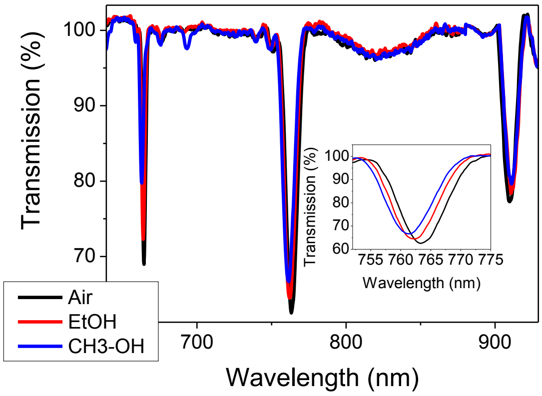

Figure 4-20: Transmission spectra of the LPG sensor with 5 growth cycles of ZIF-8 film measured in: black line, air and after exposure to: blue line, methanol and red line, ethanol.

Similarly, the transmission spectra are shown for acetone and 2-propanol, where the maximal change in the band separation reached 3.64 and 2.65 nm, respectively Figure 4-21 and Figure 4-22 (again, inset shows the detail of the LP$_{019}$-L attenuation band).

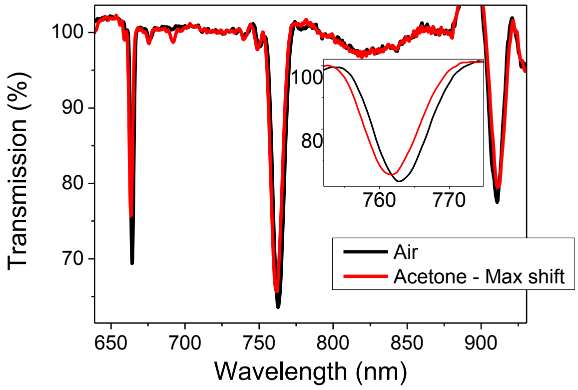

Figure 4-21: Transmission spectra of the LPG sensor with 5 growth cycles of ZIF-8 film exposed to acetone.

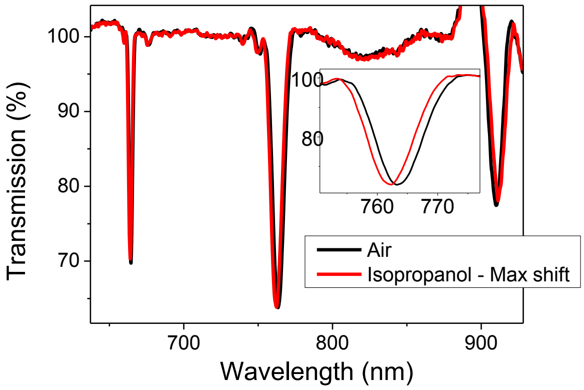

Figure 4-22: Transmission spectra of the LPG sensor with 5 growth cycles of ZIF-8 film exposed to 2-propanol.

The sensor coated with 2 growth cycles of ZIF-8 showed the highest response to methanol, followed by acetone and with significantly smaller values for ethanol and 2-propanol, Figure 4-23. Similarly to the changes in transmission spectra during the deposition, the bigger shift of the central wavelengths was observed for LP_{019} in comparison to LP_{018} cladding mode. The minimal response was observed for water corresponding to relative humidity increase from ≈40 to ≈70 %) revealing high selectivity of the sensor towards VOCs over humidity.

The sensor response was reversible, as the transmission spectra returned to their initial positions within 10 minutes after the maximum shift of the central wavelength was observed and complete evaporation of the chemicals. The differences between the recovery times corresponded to the differences in volatility of the VOC in the same way as for the response time (the recovery time was observed to be less than 3 minutes for acetone, about 5 minutes for methanol and about 10 minutes for 2-propanol and ethanol). It should be noted that the temperature difference was less than 1 ^{o}C during the all experiments, Figure 4-23.

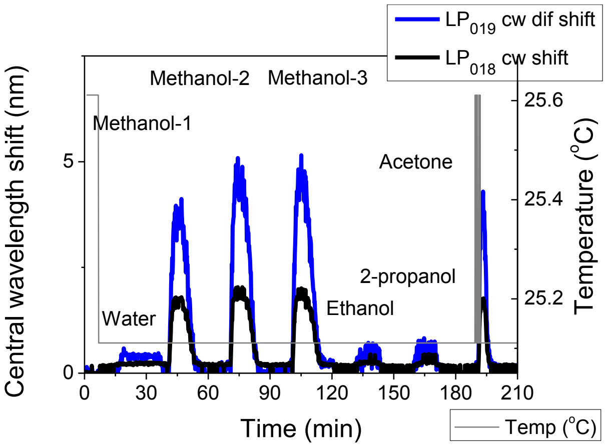

Figure 4-23: The dynamic shift of the central wavelength of the LPG sensor coated with 2 growth cycles of ZIF-8 at the exposure to different organic vapours and water (for comparison); black line, LP_{018} cladding mode and blue line, LP_{019} cladding mode; grey line, temperature.

The actual position, surface area and the local airflow in the Petri dish may affect the actual concentration of the injected VOC and thus the response of the LPG which leads to slightly different central wavelength shifts at the LPG exposure to methanol three times, Figure 4-23.

The monitoring of changes in the central wavelengths of the resonance bands takes advantage of the wavelength encoded nature of LPG-based sensors. While it would be possible to monitor changes in intensity at the mid-point of the resonance band edge as the central wavelength changes, this would introduce the need for intensity reference correct for fluctuations in source intensity, in down lead losses, etc. While, using the current interrogation system, a wavelength lying outside the resonance bands could be used as a reference, care would need to be taken as the reference wavelength might be separated from the centre of the band by 10s of nm, making the measurement susceptible to changes in the spectrum of the broadband light source.

While the experiments in the Petri dish showed qualitative response of the LPG to different organic vapours, they don't allow proper comparison of the effect of the number of growth cycles (thickness) on the sensitivity and don't enable to show concentration specific and quantitative response. Methanol, for its highest response in these experiments, was chosen to examine the response of the sensor over the range of concentrations. The experiments conducted in the environmental chamber (at the conditions close to the saturated atmosphere) showed the effect of the thickness of the film on the sensitivity. The all following results were obtained from the experiments conducted in the closed box (described in Figure 4-5). Higher sensitivity was observed for the sensor coated with 5 growth cycles. Small changes of ≈ 2% in the transmission at the central wavelength were also observed. The transmission spectra of the LPG modified with the 5 growth cycles of ZIF-8 film measured in air and methanol is shown in Figure 4-24.

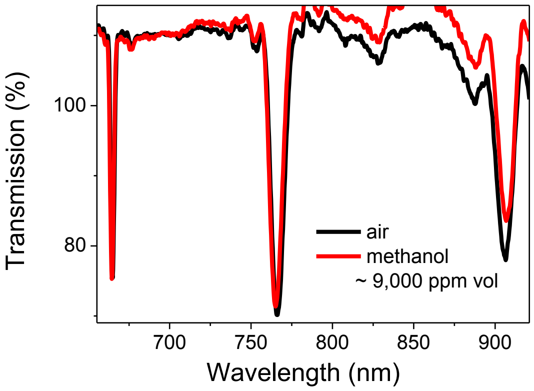

Figure 4-24: LPG sensor with 5 growth cycles of ZIF-8: a) shift in transmission spectrum corresponding to approximately 9,000 ppm of methanol.

The sensor coated with 5 growth cycles was exposed to methanol concentrations ranging from 1,790 to 27,900 ppm, the central wavelength shift was measured and the calibration curve plotted, Figure 4-25.

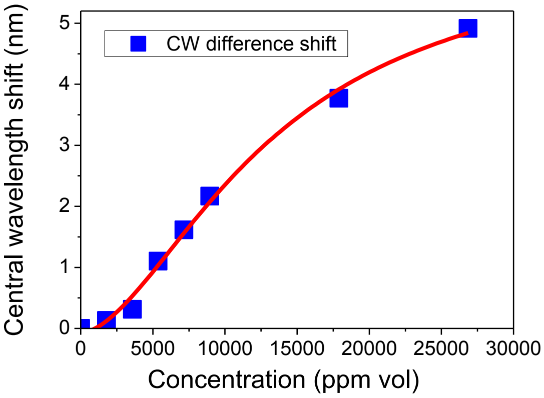

Figure 4-25: LPG sensor coated with 5 growth cycles of ZIF-8 - methanol calibration curve.

Similar experiment had been conducted for the sensor coated with 2 growth cycles however the wavelength shift for the concentrations up to 9,000 ppm is shown, Figure 4-26.

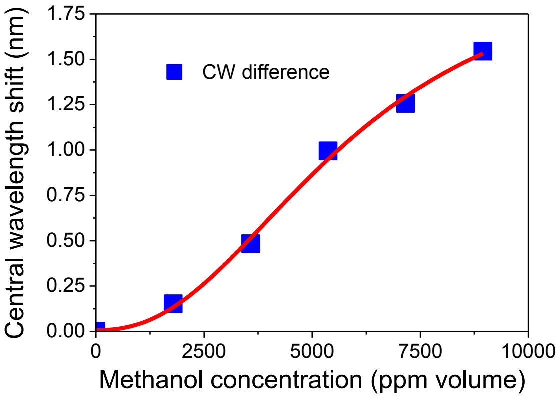

Figure 4-26: LPG sensor coated with 2 growth cycles of ZIF-8 - methanol calibration curve.

The limit of detection (LOD) of 1454 ppm was calculated using concentration from the calibration curve in Figure 4-25 for the sensor coated with 5 growth cycles and this value corresponds to 0.065 nm shift of central wavelength. This LOD is 1.5 times lower as compared with 2 growth cycles film.

LPGs coated with 2 and 5 growth cycles of ZIF-8 exhibited sensitivity to methanol, ethanol, 2-propanol and acetone vapours. The highest sensitivity was to methanol. This can be explained by the use of methanol in the film forming solution and by the fact that the size of the pores matched well the size of the methanol molecule (199).

The measurement of the response times of the sensor was limited by the time taken for the solvents to evaporate (with an upper limit of three minutes).

A higher sensitivity was observed for the sensor coated with 5 growth cycles, which suggests that the sensitivity will increase with further increases in coating thickness. Issues associated with the decrease of attenuation of the resonance bands of the LPG at the deposition of the thicker films can be resolved by optimisation of the grating period. The lowest limit of detection for the given LPG sensor configuration was found to be 1454 ppm. This value can be decreased by optimising sensor parameters such as grating period, length of the grating and film thickness.

4.4.5 Sensitivity improvements

Although the obtained limit of detection is currently too high for the direct real-world application, the results confirmed the feasibility of sensors based upon LPGs coated with MOF thin films. In order to increase sensitivity and bring sensor closer to the potential real-world application, different LPGs, operating more closely to the PMTP, were coated with 5 growth cycles and their sensitivities were tested over the same analytes. All results presented in this section are based on the experiments conducted in the closed PTFE box.

The LPGs have been coated with 5 growth cycles of ZIF-8: i) LPG with period of 109.0 µm, where “U” shape band of LP_{019} cladding mode split into two attenuation bands after the deposition, Figure 4-27a, further referred as sensor A and ii) LPG with period of 109.5 µm, where no attenuation band corresponding to the LP_{019} cladding mode has been observed before the coating process and developed only after the deposition of ZIF-8 to provide the highest possible sensitivity, Figure 4-27b, further referred as sensor B.

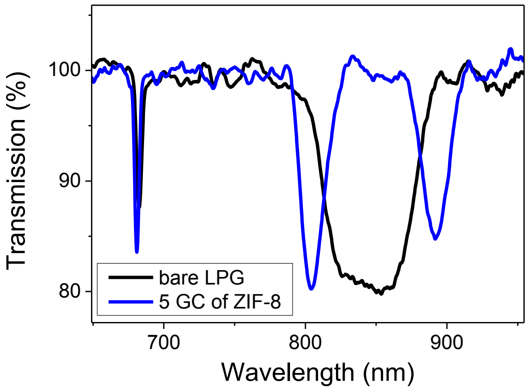

(a)

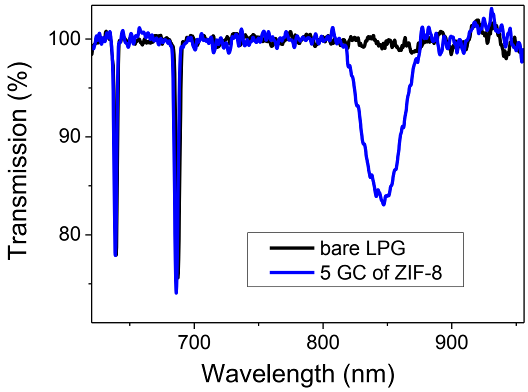

(b)

Figure 4-27: Transmission spectrum of an LPG with period of a) 109.0 – Sensor A and b) 109.5 µm – Sensor B measured in air: uncoated (black) and coated with 5 growth cycles of ZIF-8 (blue), GC, growth cycle.

The sensor A was exposed to methanol, ethanol and acetone concentrations ranging from 1,790 to 27,900, 1,240 to 24,800 and 987 to 19,700 ppm, respectively. The higher sensitivity to all tested analytes has been observed in comparison to the results presented in previous section. For example, the change in the central wavelength difference induced by ~9,000 ppm of methanol vapour was measured to be 8.37 nm in comparison to 2.17 nm obtained when using first sensor (results shown in Figure 4-24), Figure 4-28.

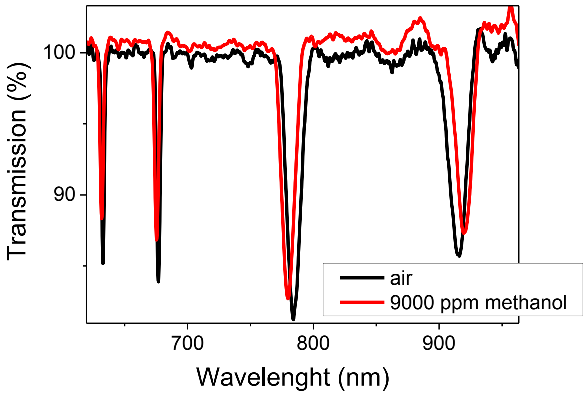

Figure 4-28: Sensor A (LPG coated with 5 growth cycles of ZIF-8): shift in transmission spectrum corresponding to approximately 9,000 ppm of methanol.

The sensor A was calibrated via three independent measurements and its performance was evaluated. The sensitivity to ethanol and acetone was observed to be higher than for methanol, Figure 4-29.

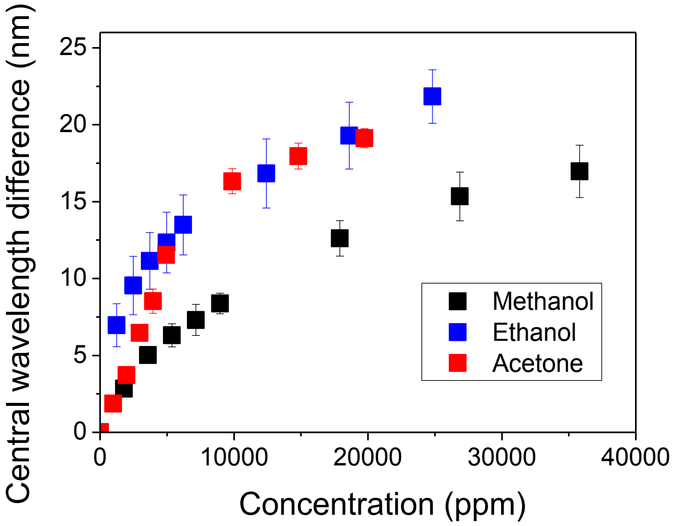

Figure 4-29: Sensor A: calibration curves for methanol (black), ethanol (blue) and acetone (red).

The difference to the results obtained from the Petri dish experiments could be related to a different concentration caused by the same amount of the measurand (200 µl had been used for all chemicals in Petri dish resulting in the concentration in a range of 100s thousands of ppm). The sensor can saturate at lower concentrations in the case of ethanol and acetone and for that reason the methanol induced higher central wavelength shift at conditions close to the saturation point. The other option is represented by the different temperature level of the experiments, as those used for the calibration curve have been conducted at ~15 °C (in comparison to ~25 °C for Petri dish experiment). The temperature could affect the reaction kinetic between the analyte and ZIF-8 structure in a different way for each chemical.

The LODs of 14.74, 37.78 and 9.57 ppm for acetone, methanol and ethanol respectively were calculated using concentration from the calibration curve in Figure 4-29 for the A sensor and these values correspond to 0.065 nm shift of the central wavelength.

The high sensitivity of the sensor A towards the ethanol and acetone vapours lead to the further investigation of the possibilities of the improvement of the LOD. The sensor B was exposed to acetone and ethanol vapours in a range of 49 to 543 and 61 to 666 ppm respectively. The ethanol solution of 0.5, 0.5, 0.5, 2 and 2 µl was injected to PTFE box (described in Figure 4-5).

The sensor's performance can be tracked via the shift of the central wavelength of LP_{018} cladding mode. As an example, the sensor B responded even to the lowest concentration of 61 ppm of ethanol and showed the further shift of the central wavelength up to highest concentration of 666 ppm of ethanol, inducing the shift of the central wavelength of 0.60 nm, Figure 4-30.

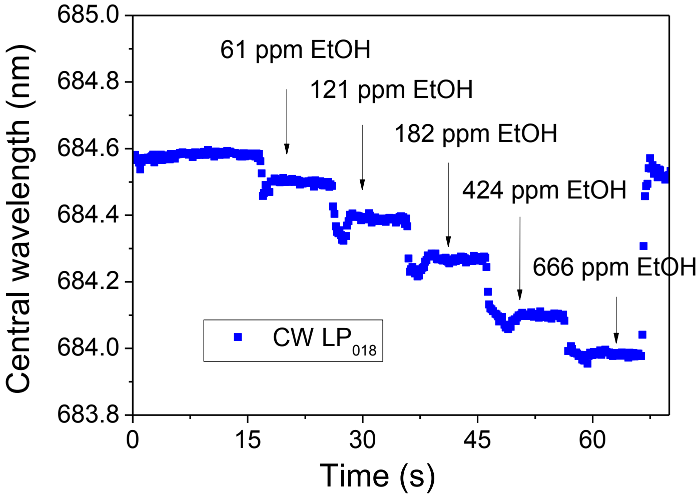

Figure 4-30: The dynamic shift of the central wavelength of the sensor B (coated with 5 growth cycles of ZIF-8) at the exposure to ethanol vapours at concentration range from 61 to 666 ppm.

The higher sensitivity can be obtained via the evaluation of the changes in the attenuation band operating at PMTP. Two different approaches have been used i) changes in transmission at the central wavelength and ii) changes in band width at selected transmission level.

The change in the bandwidth represents the novel approach in the field of the evaluation of LPG based sensors. It can reduce the noise level in comparison with the detection of the central wavelength and provides the higher sensitivity via the wavelength encoded information, especially when the single “U” shape attenuation band is observed in the transmission spectrum.

For instance, concentration of 543 ppm of acetone vapour induced a change of approximately 2 % in transmission at the central wavelength of Sensor B, Figure 4-31. Similarly, a concentration of 666 ppm of EtOH caused approximately 3 % change in transmission, Figure 4-32.

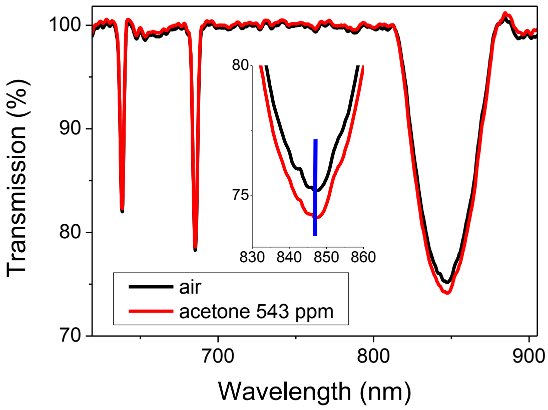

Figure 4-31: Sensor B: change of the attenuation loss in the transmission spectrum corresponding to 543 ppm of acetone; the blue line indicates the wavelength where the transmission level was measured.

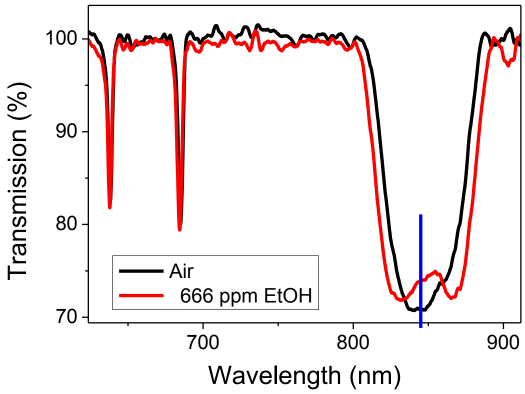

Figure 4-32: Sensor B: change of the attenuation loss in the transmission spectrum corresponding to 666 ppm of ethanol; the blue line indicates the wavelength where the transmission level was measured.

The Sensor B was exposed to acetone vapours in a range from 49 to 543 ppm and the changes in the transmission at the central wavelength are shown in Figure 4-33.

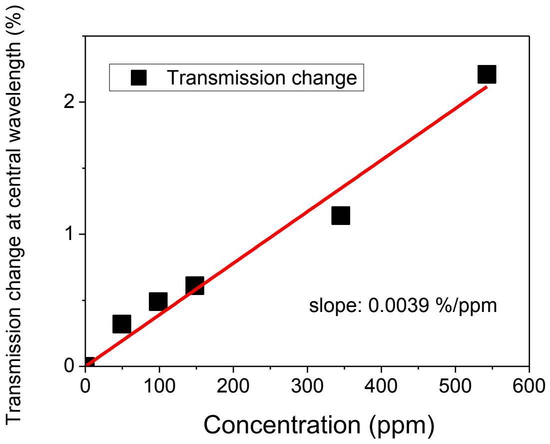

Figure 4-33: Sensor B: acetone calibration curve based on the change in transmission loss.

In theory, transmission value is calculated from the intensity measured directly in the transmission spectrum with range in thousands of mV and precision of 0.01 mV leading to the theoretical limit of measurement of 0.0001 % change in transmission loss. However in practical measurement the intensity values are continuously changing. The standard deviation of 5 mV was calculated based on these changes and for this reason the adequate change of 0.05 % in transmission has been used for the calculation of LOD.

The LOD of 12.82 and 10.64 ppm have been calculated for acetone and ethanol respectively for Sensor B based on the change in transmission at the central wavelength of the attenuation band corresponding to LP_{019} cladding mode.

The evolution of the differences in the width of the attenuation band corresponding to LP_{019} cladding mode has been demonstrated in response to ethanol vapours in the range of 61 to 666 ppm, Figure 4-34a. The band width has been measured at the wavelengths corresponding to 85 % of transmission, as shown in detail for the left section of the attenuation band in Figure 4-34b.

As an example, the band width increased from 54.68 to 66.27 nm as a response to 666 ppm of ethanol, Figure 4-34.

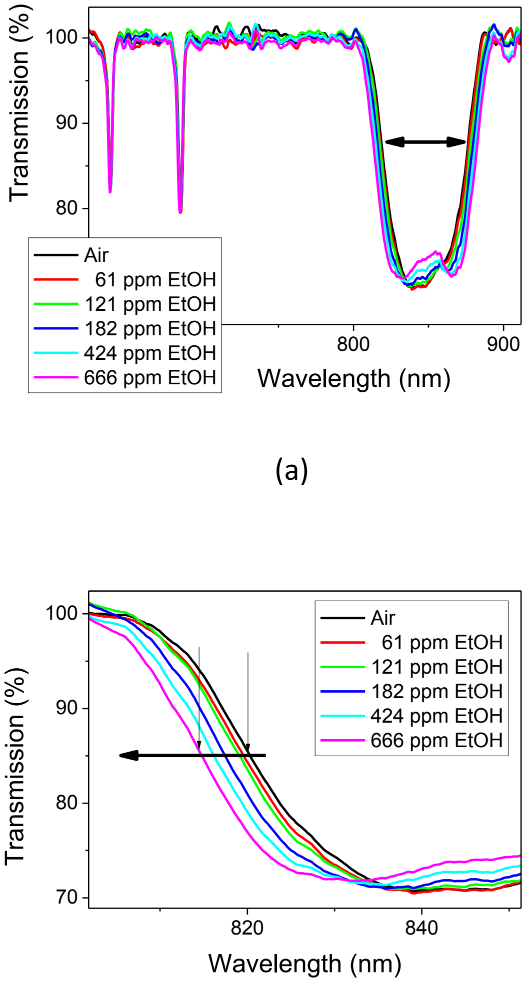

(a)

(b)

Figure 4-34: Sensor B: a) Transmission spectra and b) left section of the attenuation band corresponding to LP_{019} *cladding mode in detail, measured in air (black), in response to 61 (red), 121 (green), 181 (blue), 424 (cyan) and 666 ppm of ethanol (magenta).*

The calibration curve has been calculated based on the change of band width via the results of three independent measurements. The slope of 0.018±0.0015 nm/ppm has been obtained for ethanol, Figure 4-35.

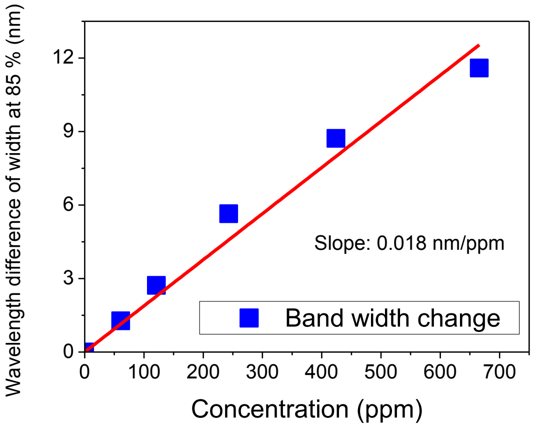

Figure 4-35: Sensor B: ethanol calibration curve based on the changes in band width.

Similarly, the response of the Sensor B has been evaluated for acetone over the range of 49 to 543 ppm with a slope of width difference of 0.015±0.001 nm/ppm.

The similar results for both ethanol and acetone were obtained when the different transmission levels were set, e.g. ½ of the attenuation or 80 and 90 % of transmission.

The LOD of the sensor has been calculated in relation to the average standard deviation of 0.1 nm obtained over the values measured in stable conditions (at each concentration level) over the 2 min period using the slopes of width differences. The LOD of 5.56 and 6.67 ppm is presented for ethanol and acetone respectively for Sensor B.

The sensitivity of the Sensor A and Sensor B with use of the different data evaluation techniques over the range of analytes is compared in Table 4-1.

Table 4-1: Comparison of the performance of Sensor A and Sensor B towards organic vapours across the different evaluation techniques.

Sensor	Analyte	Conc. range [ppm]	Data evaluation technique	Sensitivity [nm/1000 ppm]	LOD [ppm]
Sensor A	MetOH	1,790 to 27,900	CW shift	0.83 ± 0.08	37.78
Sensor A	EtOH	1,240 to 24,800	CW shift	2.58 ± 0.28	14.74
Sensor B	EtOH	61 to 666	Δ Bandwidth	18 ± 1.5	5.56
Sensor B	EtOH	61 to 666	Δ Transmission	4.5 ± 0.2**	10.64
Sensor A	Acetone	987 to 19,700	CW shift	1.46 ± 0.06	9.57
Sensor B	Acetone	49 to 543	Δ Bandwidth	15 ± 1	6.67
Sensor B	Acetone	49 to 543	Δ Transmission	3.9 ± 0.2**	12.82

* The linear response approximation has been done for the sensitivity calculation.

** The units are in the transmission percent loss per 1000 ppm.

The obtained sensitivity for the ethanol vapour measurement fulfils the criteria for ethanol limit values for drivers in the range of 0.1-0.5 mg.L^{-1} (the values differ across the countries). The conversion of those limits into the amount of ethanol in gas phase will give the range of 30-130 ppm (224).

The obtained sensitivity for the detection of acetone is sufficient to monitor occupational exposure in workspace. Health and Safety Executive in UK states the exposure limits of 500 and 1500 ppm of acetone as a weighted average over 8 hours and 15 min respectively (225). Electrochemical based sensor represent the competing developing technology in a field of new acetone gas sensors, the

LODs vary from 0.4 to 500 ppm however they suffer from high operating temperature (200-500 °C) and sometimes were tested only in N_2 atmosphere (226). When the sensitivity of the LPG sensor is further improved, e.g. using different data evaluation technique (based on the area change of the attenuation band) the LPG based sensor can be used as a non-invasive technique in health diagnostic. The concentration ranges from 1.7 ppm to 3.7 ppm could be detected in breath of people with diagnosed diabetic conditions in comparison to 0.8 ppm measured in breath of healthy people (227). Furthermore, the LPG based sensors with current design can be used for measurement of acetone in breath for the monitoring of ketogenic diet and associated weight loss (range of 2-40 ppm) or diabetic ketoacidosis (75-1250 ppm) (228).

4.4 Conclusions

ZIF-8 films with controllable thickness have been deposited successfully onto the surface of an optical fibre LPG and the response of the transmission spectra has been characterized. X-ray diffraction patterns allowed the crystal structure of the film to be assessed and ellipsometry measurements revealed the direct relationship between the crystallization growth cycle and the film thickness, corresponding to a slope of approximately 50 nm per growth cycle. The change of the central wavelengths of the LPG resonance bands have been shown to be dependent upon the optical thickness of ZIF-8 film deposited onto the surface of LPG.

The obtained LOD in a range of units of ppm for ethanol and acetone suggests the potential of the sensor for real world applications. The further improvement could be done using higher resolution of the spectrometer and combined approach of data analysis (including the transmission, central wavelength and width change). The sub ppm level will be highly desired in health monitoring applications, e.g. breath analysis.

The higher sensitivity could be also achieved using the thicker film.

The novel concept of the LPG based gas organic compounds sensor coated with a MOF material has been demonstrated. The thorough study on cross-sensitivity and the response of the sensor to the mixtures of gases can be included in the further work.

Chapter 5: LPG based carbon dioxide sensor coated with HKUST-1

5.1 Introduction

In this chapter, an LPG based carbon dioxide sensor coated with HKUST-1 functional coating is presented.

Within the various MOF thin film fabrication techniques, there are two approaches highly suitable for the deposition of the sensitive film on the surface of LPG: i) in situ crystallization technique and ii) layer by layer (LbL) technique. The procedures following these approaches were identified for the HKUST-1 thin film synthesis. The both of them were compared in terms of the feasibility of the deposition procedure (time and cost efficiency) and the sensitivity of the film to carbon dioxide. The aim of these experiments is the development of HKUST-1 LPG based carbon dioxide sensor.

The HKUST-1 film was characterized by scanning electron microscopy (SEM) and the thickness and refractive index (RI) of the 10, 20 and 40 cycles thick films were determined using an ellipsometer. The crystallinity of the films was examined by x-ray diffraction pattern (XRD).

The response of the resonance bands in the transmission spectrum of an LPG modified with in situ growth thin film and 10, 20 and 40 layers of HKUST-1 film upon exposure to carbon dioxide is shown.

The sensing mechanism is based on the measurement of the change of the refractive index (RI) of the coating that is induced by the penetration of CO_2 molecules into the HKUST-1 pores.

5.2 Background information

It has been shown (in Chapter 2) that metal organic frameworks (MOFs) offer an ideal platform for the development of sensitive films with responses to specific analytes. Among the variety of MOFs, thin film of HKUST-1 is considered to be highly selective for carbon dioxide sensing due to the presence of unsaturated copper$^{(II)}$ metal centres and its structure, which consists of two large central cavities (9 Å) surrounded by smaller 5 Å cavities (229).

The structure of HKUST-1 film is schematically shown in Figure 5-1.

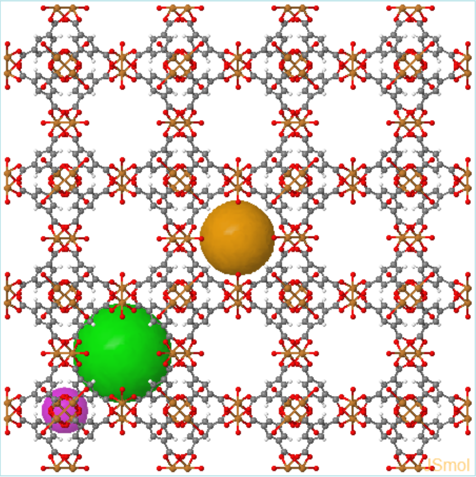

Figure 5-1: HKUST-1 3D structure (The sphere represents the pore size within the framework which can be used for gas storage) (160).

In situ crystallization technique represents the simplest technique for the fabrication of MOF films however the fabrication time can range from hours to days (154). Rapid thermal deposition technique can significantly decrease the crystallization time due to the rapid solvent evaporation at elevated temperature at the time enabling the synthesis of well inter-grown MOF film (230).

The layer by layer deposition has been used previously for the fabrication of MOF films (174)(176) and its use is desired due to the simplicity of the procedure, which is conducted at room temperature, requires less time and involves minimal use of consumables in comparison to other techniques. In particular, the LbL approach for HKUST-1 crystallization leads to the fabrication of films with higher crystal density, conforming into homogenous films with preferred {222} orientation (176).

5.3 Methodology

5.3.1 Materials

Copper nitrate hemi(pentahydrate) ([Cu(NO3)2·2.5H2O]), 1,3,5-benzene tricarboxylic acid (BTC), dimethylformamide (DMF), copper acetate ($Cu(CH_3COO)_2$), potassium hydroxide (KOH) and ethanol were bought from Sigma Aldrich. All of the chemicals were analytical grade reagents and used without further purification. Deionized water (18.3 MΩ cm) was obtained by reverse osmosis followed by ion exchange and filtration (Millipore, Direct-QTM).

5.3.2 Characterization of HKUST-1 films

SEM, X-Ray diffraction patterns and ellipsometry measurements have been conducted to evaluate the properties of the HKUST-1 thin films. The procedures followed the ones described in the previous chapter for ZIF-8 films (section 4.3.2).

5.3.3 Sensor fabrication and functionalization

LPGs with a grating period of 109.2 and 109.5 µm and length of 30 mm have been functionalized using in situ crystallization technique. Single LPGs with periods of 109.0 µm and 108.8 and LPG array consisting of LPGs with the period of 109.5 and 110.5 µm and length of 30 mm (for all) have been functionalized with use of layer by layer technique. All the fabrication procedures followed the methodology described in Chapter 3.

The system used for the deposition of the sensitive coating is identical to the one already described in the previous chapter (4.3.3).

The surface of LPG was functionalized with OH^- groups prior to the fabrication of HKUST-1 film. The optical fibre was rinsed with deionized water and immersed in a 1 wt% KOH in ethanol/water = 3:2, v/v solution for 20 min.

5.3.3.1 In-situ crystallization technique

The LPG was coated with HKUST-1 via in situ crystallization technique using rapid thermal deposition (230), Figure 5-2.

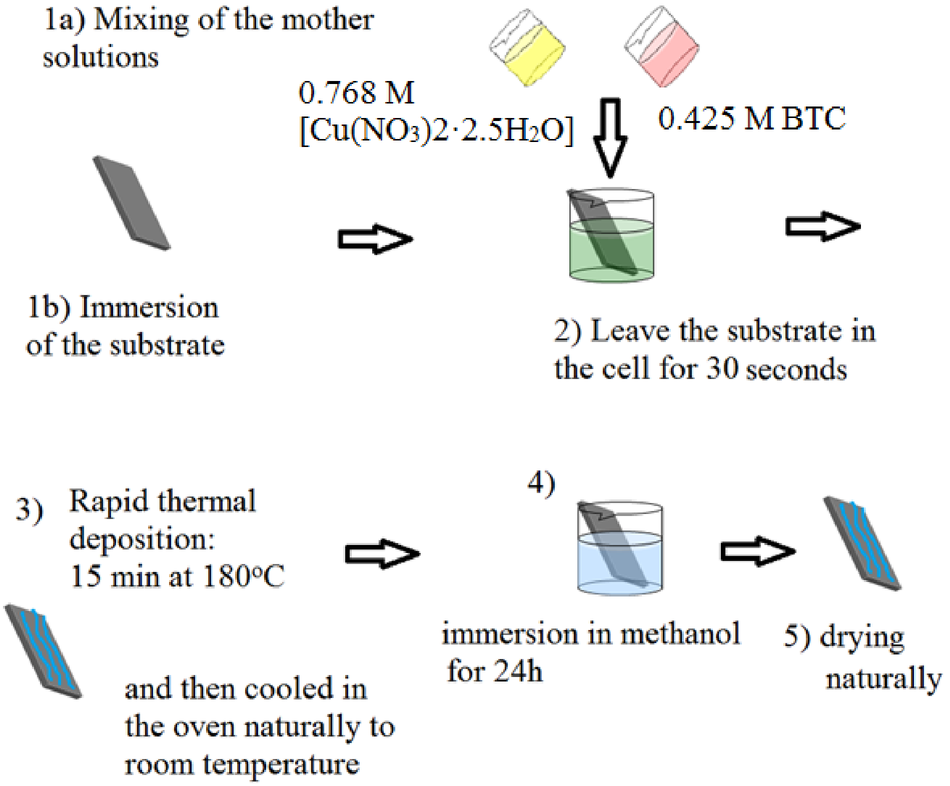

Figure 5-2: HKUST-1 film fabrication methodology using in situ crystallization technique (230).

The mother solutions of 0.768 M copper nitrate hemi(pentahydrate) (metal solution) and 0.425 M BTC (ligand solution) in DMF have been prepared and stirred for 10 min. The ligand solution (20 mL) was then added to the metal solution (20 mL) dropwise (with use of a pipette) and the mixture was stirred until the clear solution was obtained. 14 mL of the mixed solution has been injected to the Petri dish.

The LPG was placed inside the Petri dish and immersed into the film forming solution for a period of 30 s and then the excess of the solution has been carefully wiped.

The LPG was subsequently placed into the oven preheated to 180 ^{o}C. The oven was switched off after 15 min and the LPG was left there to cool down naturally. When the temperature was close to the ambient level, the LPG was immersed in methanol for 24 hours to remove DMF from the HKUST-1 cavities and replace it with methanol and then left to dry under the ambient conditions (to release methanol from the cavities to make the porous structure of the film).

5.3.3.2 Layer by layer technique

Alternatively, the LPG was coated with HKUST-1 using a layer by layer technique (176). Briefly, solutions of 1 mM BTC and 0.2 mM copper acetate in ethanol were prepared. The optical fibre was immersed into a $Cu_2(AcO_4)$ solution and an BTC solution for 5 min each, resulting in the alternate deposition of Cu^{2+} and BTC^{-}, forming an HKUST-1 film on the surface of LPG. Between each of these steps the LPG was immersed in ethanol for 10 min to remove all unreacted parts of film forming solutions. The process was repeated to obtain a thicker film consisting of 10, 20 or 40 growth cycles. Transmission spectra were recorded continuously during the deposition process. The HKUST-1 layer by layer deposition is schematically shown in Figure 5-3.

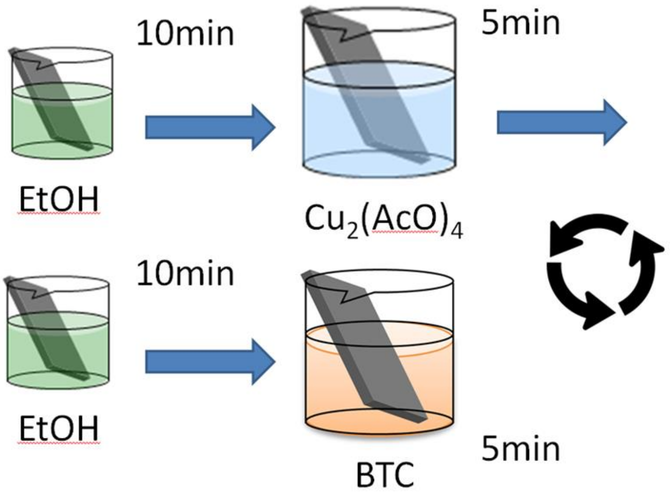

Figure 5-3: HKUST-1 film fabrication methodology using layer by layer technique (176).

The effect of the immersion into pure ethanol (for 10 min at the beginning and then as an intermediate step between the immersions to metal and ligand solutions) on the quality of the film has been tested. Two approaches of the layer by layer method were used: i) following procedure published in (176) and shown in Figure 5-3 and ii) replace the immersion to ethanol step by rinsing with ethanol (conducted three times with a plastic pipette).

5.3.4 Sensor performance

The performance of the LPG as a chemical sensor was investigated by exposure the coated device to elevated concentration of carbon dioxide. The response of the LPG was investigated with the fibre positioned in an environmental chamber composed of closed polytetrafluoroethylene (PTFE) box (15x15x15 cm). The LPG was fixed 5 cm above the base of the chamber.

The setting of the experiment is schematically shown in Figure 5-4.

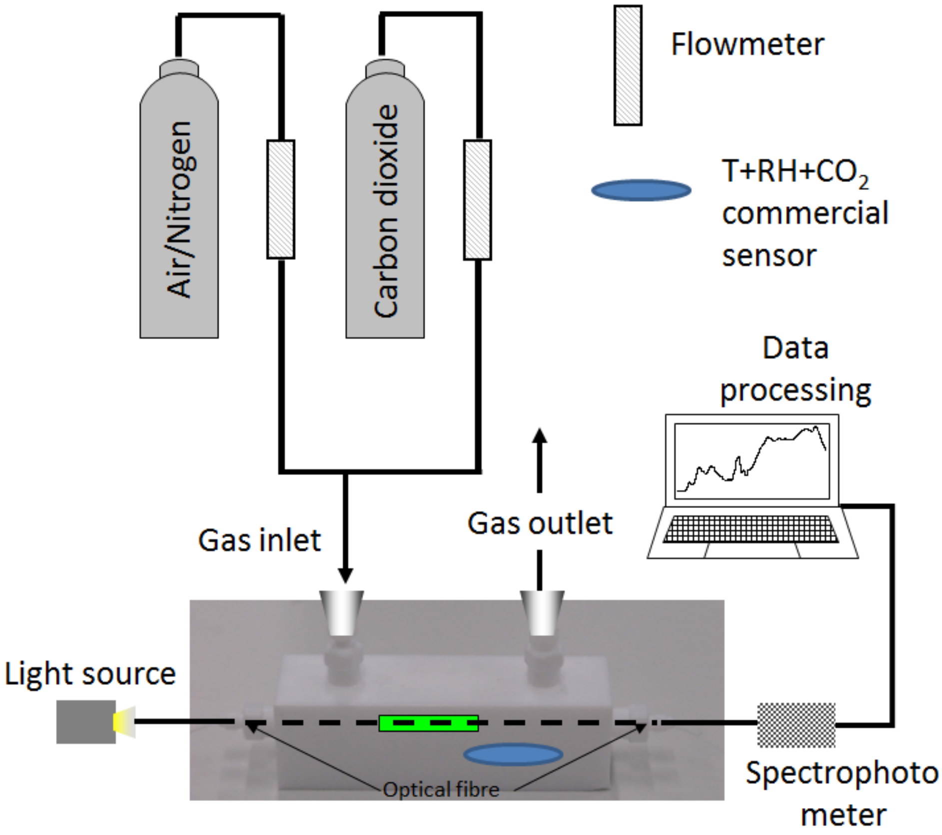

Figure 5-4: Schematic illustration of the experimental set-up used for CO_2 sensitivity experiments.

The chamber was initially filled with nitrogen and then the concentration of CO_2 gas was increased up to 40,000 ppm by infusion of the mixture of CO_2 and argon.

The central wavelengths of the resonance bands in the LPG's transmission spectra were recorded and sensor response to the presence of carbon dioxide was evaluated. The concentration of carbon dioxide, the temperature and the relative humidity (RH) were measured by a commercial data logger (K-33 ICB 30% CO_2 sensor from CO2meter, Inc.) An acquisition interval of 20 s was set for all experiments (it represents the minimal interval of a commercial data logger).

5.4 Results and discussion

5.4.1 Film morphology

Three different approaches of the deposition techniques were examined; deposition: i) via in-situ crystallization technique, ii) layer by layer with 10 min crystallization in ethanol and iii) layer by layer with ethanol rinsing.

Homogenous crystalline film, uniformly covering the substrate was observed for in-situ crystallization technique (Figure 5-5) and layer-by-layer approach following the procedure with immersion to ethanol (Figure 5-6). Homogenous film was observed also for the layer by layer procedure with ethanol rinsing however the single crystals were not identified (Figure 5-7).

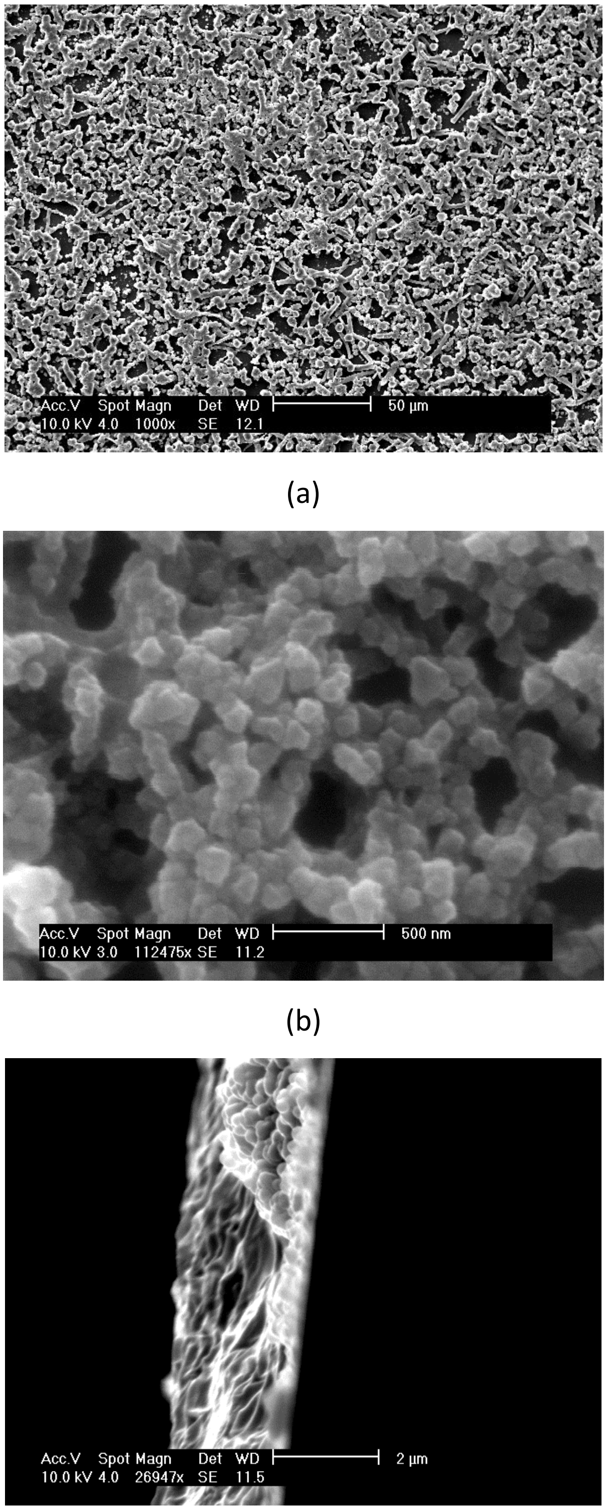

(a)

(b)

(c)

Figure 5-5: a), b) Top view and c) cross sectional SEM images of HKUST-1 film grown on class substrate via the in-situ crystallization technique.

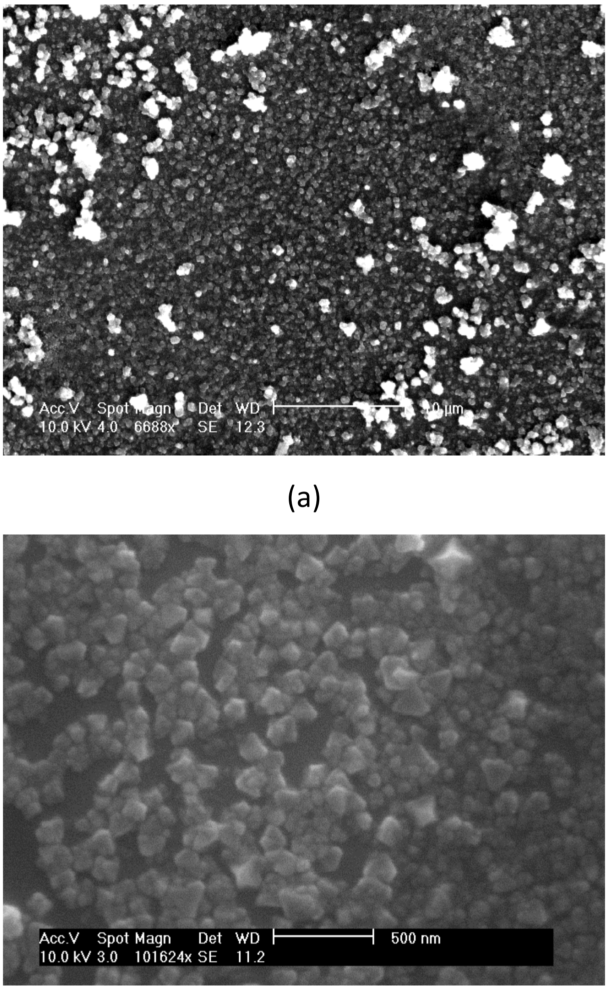

(a)

(b)

Figure 5-6: a) Top view SEM images of 40 layers of HKUST-1 film grown on class substrate via the layer by layer technique following the ethanol immersion step.

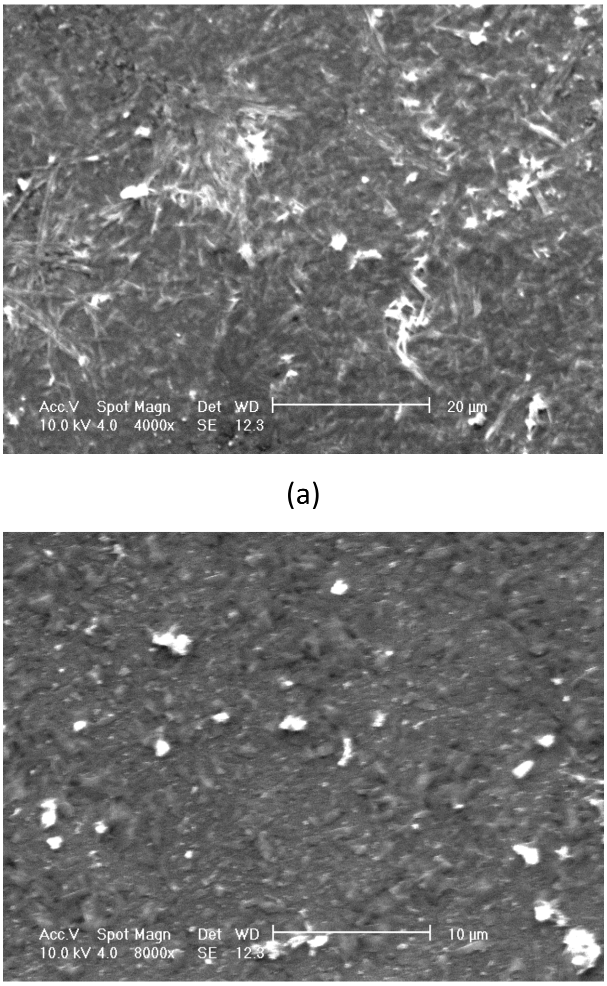

(a)

(b)

Figure 5-7: a), b) Top view SEM images of 40 layers of HKUST-1 film grown on class substrate via the layer by layer technique with use of ethanol washing.

The skipping of the ethanol immersion step in the layer by layer deposition technique leads to the development of much smaller crystals. This finding supports the hypothesis that the 10 min of immersion in ethanol plays a similar role for the HKUST-1 crystallization as the Phase 2, rapid thermal development, for the in-situ crystallization technique. Although the individual crystals could not be detected the difference in the structure between deposited film and precursors suggested the sufficient building process of HKUST-1.

This hypothesis is in a good agreement with the previously reported study characterizing the HKUST-1 film deposited using the layer by layer approach onto the quartz microbalance electrodes. No change in mass frequency during the deposition while the substrates were immersed in ethanol was observed (176).

The immersion step in ethanol affected the size and quality of the crystals however the deposition of the HKUST-1 film on the surface of the substrate was observed. As this change in the procedure rapidly reduced the deposition time (from 30 min to 10 min per layer), it has been decided to follow this adjusted deposition procedure.

The film thickness obtained via the in situ crystallization technique was estimated to be 2 µm based on the cross-section SEM image, Figure 5-5c. On the other hand the thickness of the film fabricated via layer by layer technique was expected to be in a range of 10s of nm (176) and for this reason the thickness measurement were conducted using the ellipsometer, where the results indicated the film thickness of ≈ 55, 20 and 10 nm for 40, 20 and 10 layered film respectively. No significant difference in film thickness was observed within procedures with and without the immersion in methanol step.

5.4.2 Film structure

X-ray diffraction patterns establish that the films comprised HKUST-1 crystals. The positions of the peaks {200}, {220}, {311}, {222}, {400}, {331}, {420}, {333} and {440} indicate a crystalline HKUST-1 structure. The highest intensity, at the {222} reflection peak, suggests that the orientation of the crystals is preferred to be out of plane orientation along the {222} crystallographic direction. The elevated plateau from 15 to 40 θ° relates to the amorphous structure of the glass substrate. The position and the intensity of the peaks in Figure 5-8 are in a good agreement with the X-ray diffraction patterns reported in the literature and with the modelled diffraction pattern for HKUST-1 (230).

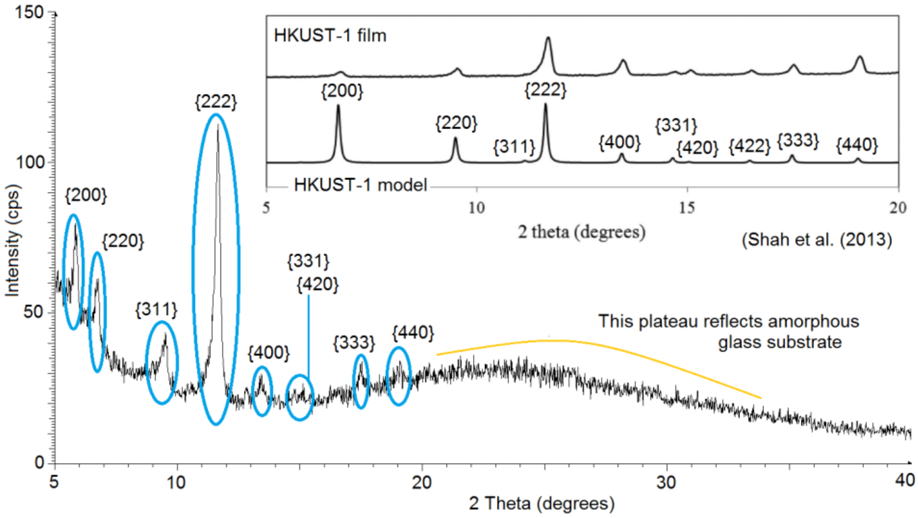

Figure 5-8: In-plane X-Ray diffraction patterns of HKUST-1 film on glass substrate, recorded at room temperature; inset on the right top shows the results obtained in (230) *and modelled values.*

5.4.3 LPG modification using in-situ crystallization technique

The evolution of the transmission spectrum of LPG with period of 110.0 µm during the HKUST-1 deposition process is shown in Figure 5-9.

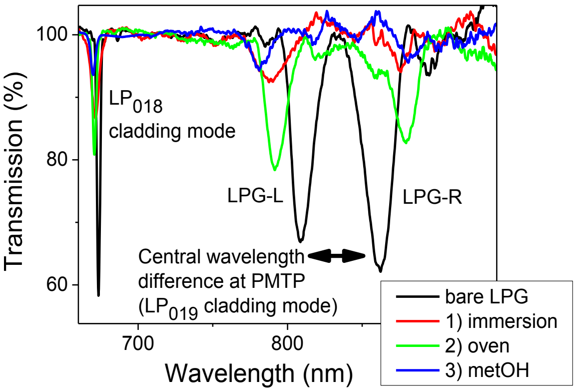

(a)

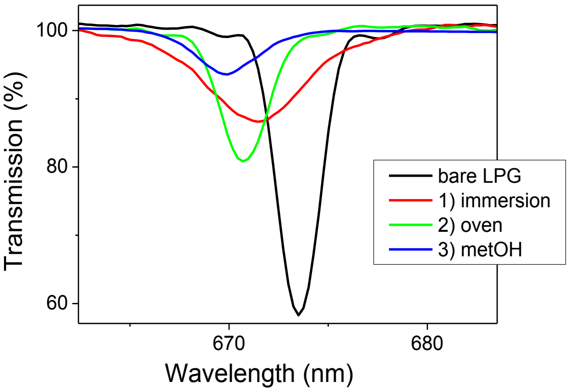

(b)

Figure 5-9: Deposition of HKUST-1 via in situ crystallization technique: bare LPG (black) and after the end of Phase 1 – immersion into mother solution (red), after the end of Phase 2 – rapid thermal development in the oven (green) and after the end of Phase 3 – immersion in methanol with further evaporation (blue); a) Transmission spectrum of LPG with period of 110.0 µm taken in air and b) attenuation band corresponding to LP_{018} *cladding mode.*

The massive change of 33.35 nm of the difference in central wavelengths operating at PMTP and of 32.15 % in the transmission loss (for LPG-R) was observed after the immersion of LPG into the mother solution (Phase 1), with the attenuation bands operating at PMTP almost disappearing, Figure 5-9 (red line).

The evaporation of the solvent took place in the oven during Phase 2, associated with the increase of the transmission loss that can be observed for attenuation bands operating at PMTP in Figure 5-9a (green) and for LP_{018} cladding mode in Figure 5-9b (green). Rapid thermal deposition induced the crystallization of HKUST-1 structure, where DMF was still present in the cavities (230). This structural change can explain the further shift (separation) of the central wavelengths operating at PMTP and LP_{018} cladding mode.

DMF was replaced in the cavities by methanol that was subsequently evaporated. The further shift of the central wavelengths and decrease in transmission loss was observed, with LPG-R disappearing and LPG-L with a very weak transmission loss, Figure 5-9a (blue). Same trend was observed over the change of central wavelength corresponding to LP_{018} cladding mode, Figure 5-9b (blue).

Changes in the transmission spectra during the whole Phase 1 and Phase 3 were monitored at the central wavelength corresponding to LP_{018} cladding mode, Figure 5-10a and Figure 5-11, respectively.

The evolution of the transmission spectrum while the LPG was in the film forming solution showed the continuous shift of the central wavelength in the first 30 s after the immersion followed by saturation, Figure 5-10b.

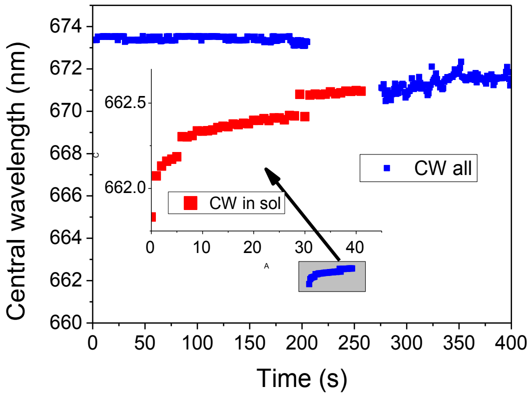

(a)

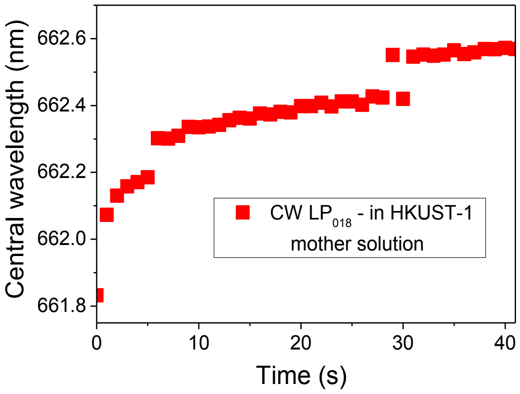

(b)

Figure 5-10: The dynamic shift of the central wavelength during the deposition of HKUST-1 via in situ crystallization technique: a) Phase 1, immersion in the mother solution, inset shows the interval while LPG was immersed in detail and b) the interval while LPG was immersed in detail (data from the grey box from Figure 5-10a).

Minimal shift of the central wavelength was observed within the first 10 h while the LPG was immersed in methanol during the Phase 3 followed by the continuous change that saturated approximately after 20 h, Figure 5-11. These changes are expected to be associated with the replacement of DMF by methanol in HKUST-1 cavities.

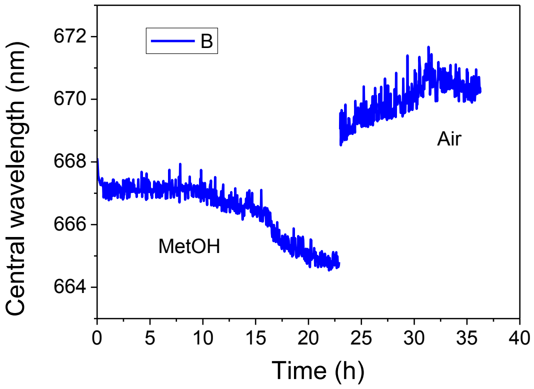

Figure 5-11: The dynamic shift of the central wavelength during the deposition of HKUST-1 via in situ crystallization technique: Phase 3, immersion in methanol with further evaporation.

5.4.4 CO_2 sensing using in-situ crystallization technique

When exposed to carbon dioxide, no measurable change of the central wavelength was observed, as the response to the high concentration of carbon dioxide in the range from 500 to 5,500 ppm, Figure 5-12. The continuous shift in the position of the central wavelength matched the continuous shift in the temperature, where no steps according to the levels of CO_2 were observed.

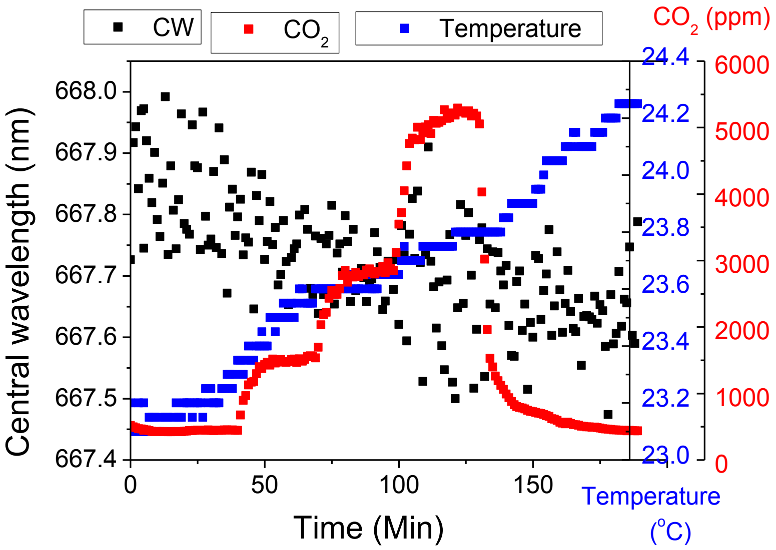

Figure 5-12: The sensor coated with HKUST-1 via in situ crystallization technique exposed to carbon dioxide in mixture with air: dynamic shift of the central wavelength corresponding to the LP_{018} cladding mode (black), concentration of carbon dioxide (red) and temperature (blue).

This observation could be due to the influence of the ambient humidity present in air. While the sensitivity of HKUST-1 to carbon dioxide was demonstrated previously as the gas partial pressure in vacuum (176), it is known that water vapour can react with the open copper sites in the HKUST-1 structure and then block their specific affinity to carbon dioxide molecules. This effect was previously accounted for the degradation of the film properties with time of a HKUST-1 film stored under elevated relative humidity levels (176).

To further test this hypothesis another LPG with period of 109.5 µm was coated by HKUST-1 film using in-situ crystallization technique and exposed to the mixture of nitrogen and carbon dioxide up to the CO_2 concentration of 42,000 ppm. The transmission spectra before and after the deposition of HKUST-1 are shown in Figure 5-13.

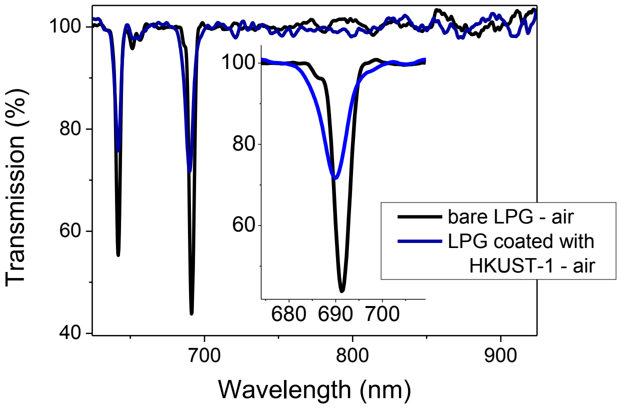

Figure 5-13: Transmission spectrum of LPG with period of 109.5 µm taken in air before (black) and after (blue) the deposition of HKUST-1 film via in-situ crystallization technique.

When the LPG was exposed to carbon dioxide the position of the central wavelength responded again to temperature only and no observable shift was observed as the response to CO_2, Figure 5-14. The drop of the central wavelength at 100 min was probably caused by the relaxation of the fibre due to the nitrogen flow (the whole transmission spectrum dropped in the intensity values at this time).

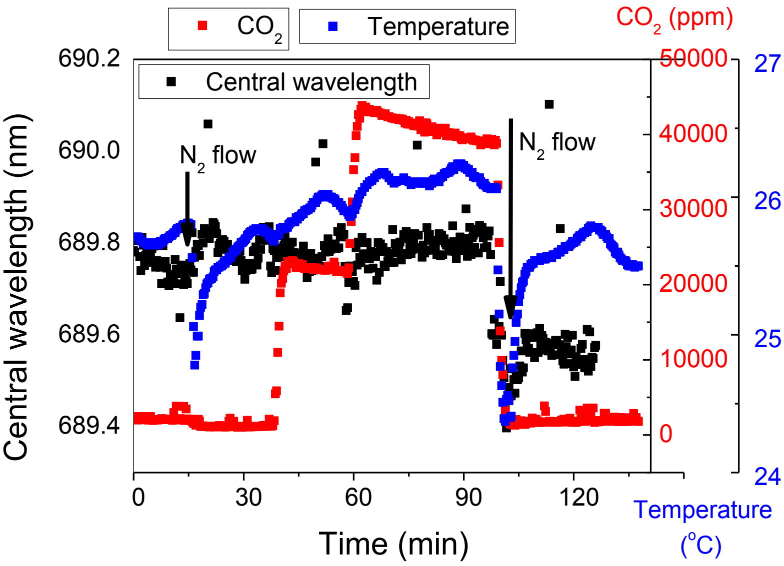

Figure 5-14: The sensor coated with HKUST-1 via in situ crystallization technique exposed to carbon dioxide in mixture with nitrogen: dynamic shift of the central wavelength corresponding to the LP_{018} cladding mode (black), concentration of carbon dioxide (red) and temperature (blue).

Absence of the response of the LPG based sensors coated with HKUST-1 film with use of in-situ crystallization technique to carbon dioxide could be explained by the high film thickness, estimated to be ≈ 2 µm (Figure 5-5b), exceeding highly the optimum region for sensitive coating in a range of hundreds of nm (112).

The experiments with the LPG sensors modified by layer by layer technique has been undertaken using mixtures of nitrogen and CO_2 to investigate further the sensitivity of deposited HKUST-1 films to carbon dioxide.

5.4.5 LPG modification using layer by layer technique

Since LPG is also sensitive to the temperature, an array containing LPG1 and LPG2 with periods of 109.5 and 110.5 µm respectively was fabricated and LPG1 was coated with 40 layers of HKUST-1. This array is further referred as Array A. The performance of Array A as the carbon dioxide sensor was evaluated via the changes in the central wavelength difference associated with the attenuation bands of bare and coated LPGs. The bare LPG2 works as a reference to subtract the effect of temperature and any other perturbation from the surrounding environment (e.g. the flow effect of the gas that could possibly cause the relaxation of the LPG). The transmission spectrum of the array taken in air before and after the deposition of HKUST-1 on LPG1 is shown in Figure 5-15.

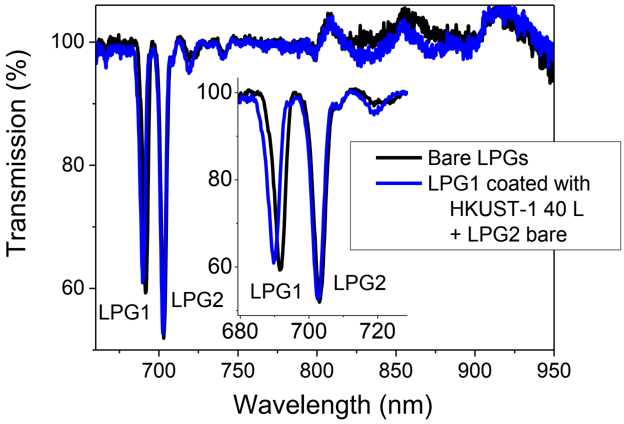

Figure 5-15: Transmission spectrum of Array A before (black) and after the deposition of 40 layers of HKUST-1 onto LPG1 (blue), inset show the attenuation band of LPG1 in detail.

The shift of the attenuation band corresponding to LPG1 induced by the deposition of HKUST-1 film can be observed, while the attenuation band corresponding to the bare LPG2 remained in the same position, Figure 5-15.

Changes in the transmission spectra of the LPG when immersed into the film forming solutions (metal and ligand) were monitored. The total change of the central wavelength of LPG1 associated with attenuation band corresponding to LP_{018} cladding mode induced by the deposition of 40 layers of HKUST-1 was measured to be 5.5 and 6.7 nm in air and solution respectively, Figure 5-16.

The black lines, which are a guide to the eye, indicate the central wavelengths of the resonance bands. Higher sensitivity to coating thickness when the LPGs is immersed in the growth solution than in air was observed. The "spikes" in the figure represent the short period of time, while LPG was in air when the metal solution was replaced with the ligand solution, Figure 5-16.

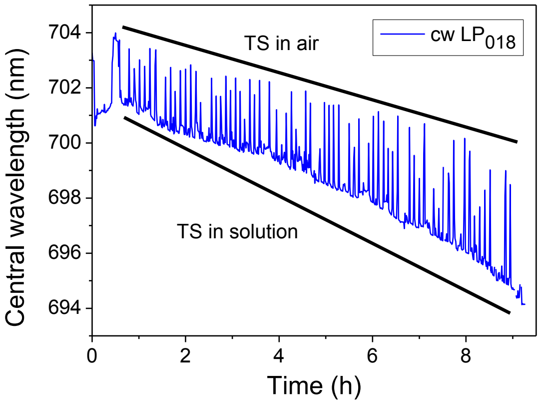

Figure 5-16: The dynamic shift of the central wavelength of LPG 1, Array A, corresponding to the LP_{018} cladding mode during the deposition of 1st to 40th layer of HKUST-1 onto a surface of LPG.

5.4.5 CO_2 sensing using LPG coated via layer by layer technique

The both LPGs are sensitive to the temperature, while only LPG1 is sensitive to carbon dioxide and so any changes in the difference of the position of the central wavelengths are due to response to carbon dioxide only.

The changes in the transmission spectrum of Array A as the response to carbon dioxide levels in a range of 2,000 – 40,000 ppm are shown in Figure 5-17. The highest concentration of 40,000 ppm caused the 0.72 nm change in the position of the central wavelength of coated LPG1 (Figure 5-18a) corresponding to LP_{018} cladding mode, higher change can be expected when the sensor will operate at PMTP. The bare LPG2 stayed in the same position (Figure 5-18b).

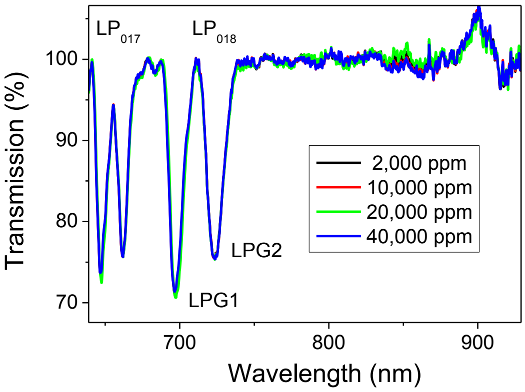

Figure 5-17: Transmission spectrum of a) Array A (LPG 1 coated with 40 layers of HKUST-1 at exposure to 2,000 (black), 10,000 (red), 20,000 (green) and 40,000 (blue) ppm of carbon dioxide.

.

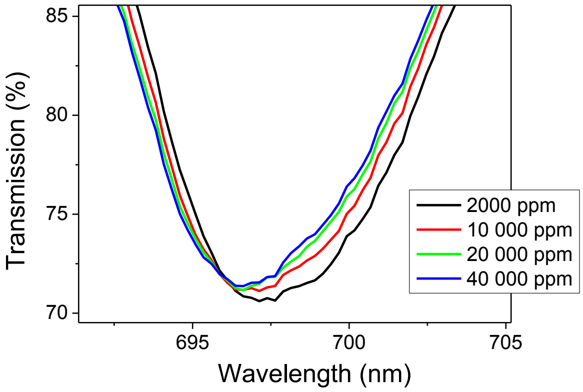

(a)

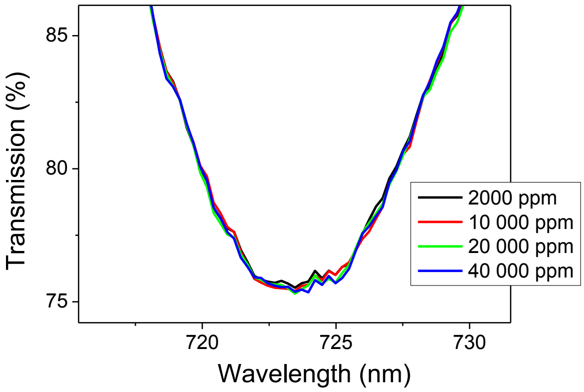

(b)

Figure 5-18: Transmission spectrum of a) Array A (LPG 1 coated with 40 layers of HKUST-1); b) LPG1 and c) LPG2 in detail at exposure to 2,000 (black), 10,000 (red), 20,000 (green) and 40,000 (blue) ppm of carbon dioxide.

The sensor's performance can be tracked via the shift of the central wavelength of LP_{018} cladding mode of LPG1, as no detectable shift of the bare LPG2 was observed, Figure 5-18b.

The dynamic shift of the central wavelength of LPG1 was tracked during the carbon dioxide sensitivity experiment, Figure 5-19. The position of the central wavelength of LPG1 is possible to distinguish between the each CO_2 concentration step up to 40,000 ppm, Figure 5-19.

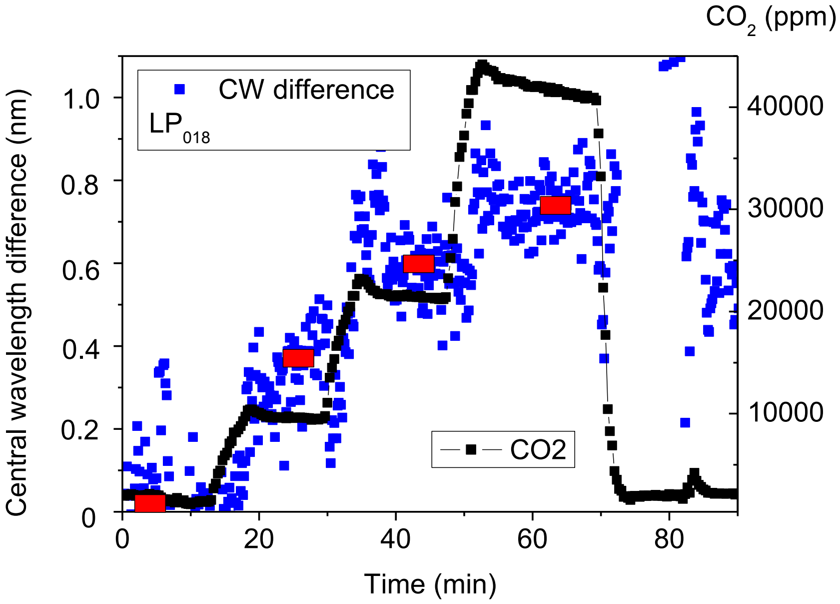

Figure 5-19: Array A (LPG1 coated with 40 layers of HKUST-1+bare LPG2) during the exposure to carbon dioxide in the range up to 40,000 ppm: dynamic change of the central wavelengths difference corresponding to the LP_{018} cladding mode of LPG1 and LPG2 (blue) and carbon dioxide concentration (black); red boxes indicate the intervals used for the calibration curve presented in Figure 5-20.

The changes in the differences of central wavelengths corresponding to LP_{018} cladding mode were monitored and the calibration curve has been obtained, Figure 5-20.

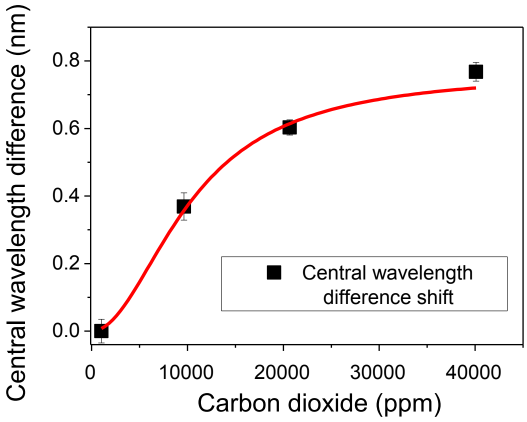

Figure 5-20: Array A: Carbon dioxide calibration curve.

The LOD has been calculated using the average standard deviation of 0.07 nm obtained over the values measured in stable conditions (at each concentration level) over the 3 min period and using calibration curve, Figure 5-20. The LOD of 1184 ppm was identified for the range of CO_2 concentration of up to 10,000 ppm.

The increase of the sensitivity could be achieved with increase the thickness of the film however it has been reported that film consisting of 80 layers lost the preferred {222} crystal orientation enabling the optimal conditions of CO_2 adsorption (176). The higher sensitivity can also be achieved via optimisation of the LPG period to operate at PMTP.

5.4.6 Sensitivity improvements

Although the obtained limit of detection is currently too high for the direct real-world application, the results confirmed the feasibility of carbon dioxide detection based upon LPGs coated with HKUST-1 thin films.

In order to increase sensitivity and bring sensor closer to the potential real-world application, different LPGs, operating at the PMTP, were fabricated. HKUST-1 films consisting of 10, 20 and 40 layers have been deposited on the surface of the single LPG with period of 108.8 (10 layers) and 109 µm (20 and 40 layers).

The changes in the transmission spectra in air before and after the deposition have been monitored, Figure 5-21.

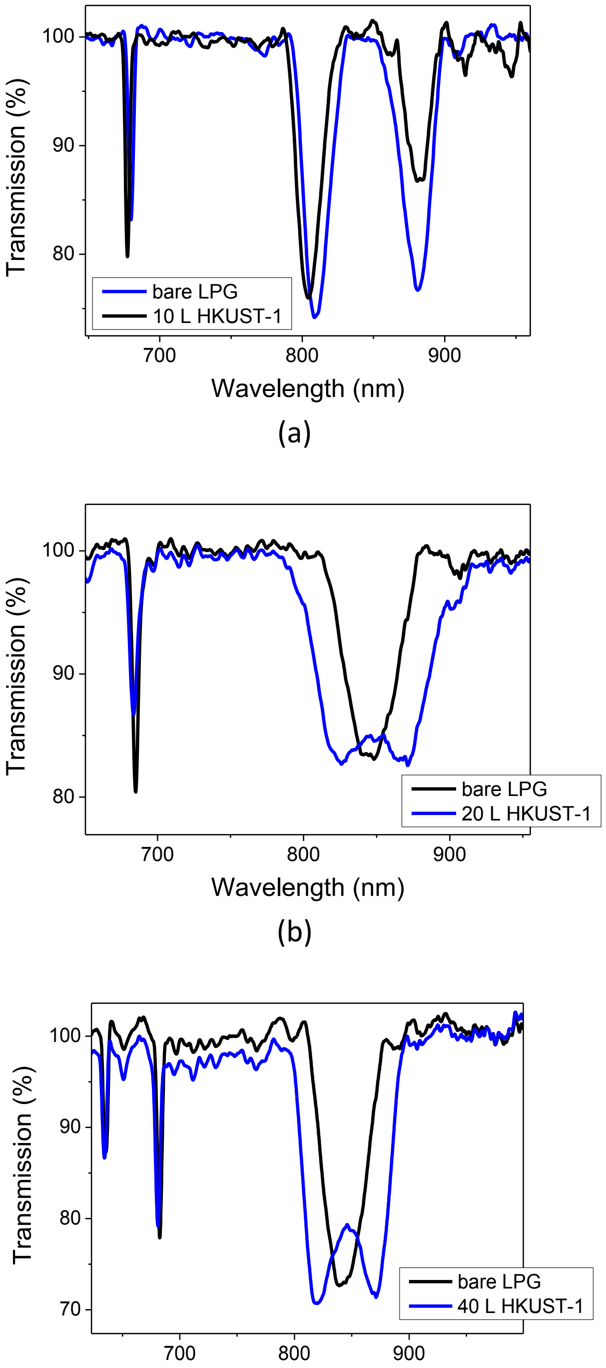

(a)

(b)

(c)

Figure 5-21: Transmission spectrum of LPG with the period of 109 μm taken in air before (black) and after the deposition of a) 10, b) 20 and c) 40 layers of HKUST-1 (blue).

Changes in the transmission spectra of the LPG when immersed into the film forming solutions (ligand) were also monitored. The linear increase of the difference between the central wavelengths operating at PMTP was observed over the deposition of 40 layers of HKUST-1, Figure 5-22. The average increase of 1.2 nm in the band separation was calculated based on the position of the central wavelengths after 5 min of immersion to ligand solution of each deposited layer. The smaller observed slope at the beginning where the film started to grow on the substrate is in agreement with previous study (176). The small plateau around 20th layer was caused by the break in the fabrication process, where the LPG was immersed into ethanol for ≈ 1 hour.

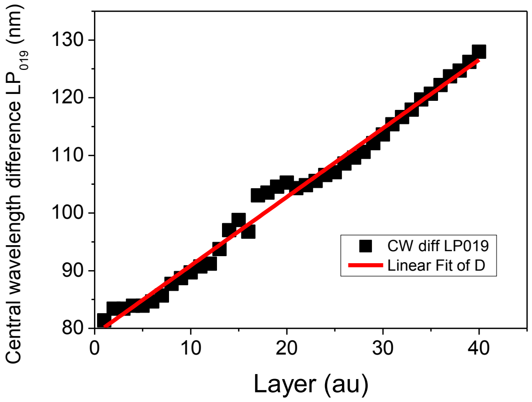

Figure 5-22: Difference between the central wavelengths corresponding to LP_{019} cladding mode during the deposition of 1st to 40th layer of HKUST-1 (taken in ligand solution).

The sensors coated with 10, 20 and 40 layers of HKUST-1 were exposed to carbon dioxide concentrations ranging from 1,450 to 41,200 ppm and the shift of the central wavelengths was recorded, Table 5-1.

Table 5-1: LPG sensor coated with 10, 20 and 40 layers of HKUST-1 – Carbon dioxide sensitivity

Sensor	Δ CW* LP_{019} ≈ 10k ppm CO_2	Δ CW* LP_{019} ≈ 20k ppm CO_2	Δ CW* LP_{019} ≈ 40k ppm CO_2	Δ Temperature
10 layers	1 nm	saturated	saturated	0.92 °C
20 layers	4.45 nm	saturated	saturated	0.93 °C
40 layers	7.2 nm	8.44 nm	10.58 nm	0.37; 0.59; 0.85 °C

* CW = central wavelength

The sensor coated with 10 layers showed the smallest response of 1 nm change in the central wavelength difference of the attenuation bands operating at PMTP (ΔCW_{LP019}). The slight temperature increase was observed in the chamber after the each injection of carbon dioxide. The temperature sensitivity measured as the change in the difference of the central wavelengths corresponding to LP_{019} cladding mode was calculated to be ≈ 0.92 nm/°C. When this temperature induced change is subtracted then ΔCW_{LP019} of 0.15 nm was calculated to be caused by CO_2. No further changes in the transmission spectrum were observed with increasing the carbon dioxide concentration to 20,000 ppm.

Concentration of ≈ 10,000 ppm of carbon dioxide induced the change in the central wavelength difference of 4.45 nm for the sensor coated with 20 layers. The ΔCW_{LP019} after the subtraction of the temperature effect was calculated to be 3.3 nm. This change definitely proved the response of the sensor to carbon dioxide. However no further shift of the central wavelengths were observed with increase the carbon dioxide concentration up to 40,000 ppm.

The sensor coated with 40 layers showed the largest response towards the exposure to carbon dioxide. The continuous shift of the central wavelength difference was observed over the whole concentration range up to 41,200 ppm, where it reached 10.58 nm (9.64 nm after the temperature effect subtraction). The change in the transmission spectrum is shown in Figure 5-23.

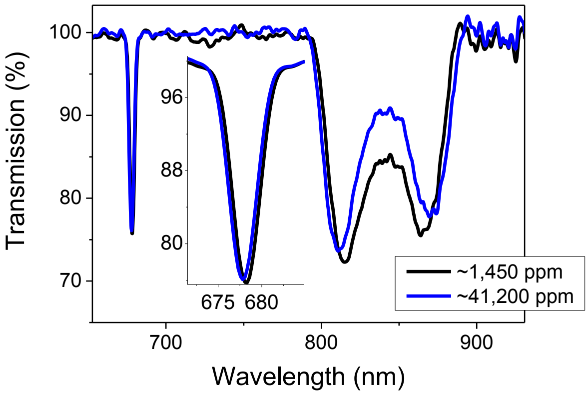

Figure 5-23: LPG sensor coated with 40 layers of HKUST-1: a) Transmission spectra at exposure to 1,450 (black) and 41,200 ppm of carbon dioxide (blue); the inset shows the attenuation band corresponding to the LP_{018} cladding mode in detail.

The difference between the central wavelengths of the attenuation bands operating at PMTP was monitored over time during the exposure of the sensor to carbon dioxide, Figure 5-24.

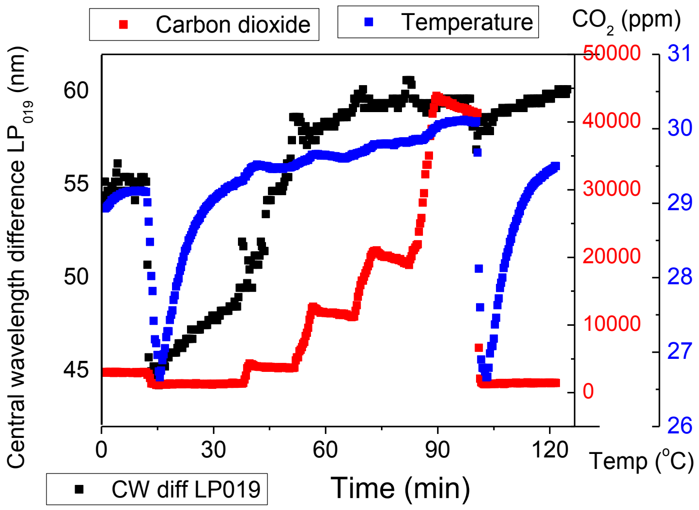

Figure 5-24: The sensor coated with 40 layers of HKUST-1 exposed to carbon dioxide in mixture with nitrogen: dynamic shift of the central wavelengths difference corresponding to the LP$_{019}$ cladding mode (black), concentration of carbon dioxide (red) and temperature (blue).

Initial (after 15 min) rapid response associated with the nitrogen flowing inside the chamber and rapid decrease in temperature was observed. The carbon dioxide level reached concentration ~1,300 ppm at this stage.

The moderate increase from 45 to 50 nm in the difference of the central wavelengths between 15 and 30 min of the experiment is fully induced by the increasing temperature from 26.5 to 29.3 °C, where the CO$_2$ level was stable at 1300 ± 50 ppm. This region was used for the temperature calibration of the sensor with calculated sensitivity of 1.22 nm.°C^{-1}.

The rapid increase of ΔCW$_{LP019}$ was observed (more than 5 nm) when the CO$_2$ was introduced into the chamber followed by the small increase of temperature (~0.4 °C). The further increase in the band separation was observed associated with CO$_2$ concentration increase up to 40,000 ppm.

The response of the sensor was observed to be irreversible as no change in the transmission spectrum was detected when the chamber was fluxed with nitrogen and the carbon dioxide reached back levels close to 1,300 ppm.

The temperature effect was subtracted based on the temperature calibration and the ΔCW_{LP019} associated to temperature was removed, Figure 5-25. Minimal shift (less than 0.5 nm) was observed then between 20,000 and 40,000 ppm carbon dioxide concentration levels indicating the saturation of the sensor.

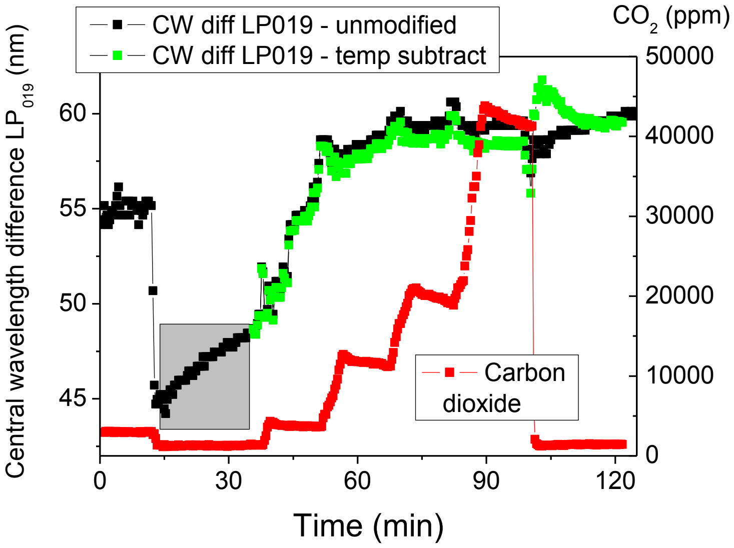

Figure 5-25: The sensor coated with 40 layers of HKUST-1 exposed to carbon dioxide in mixture with nitrogen: dynamic shift of the central wavelengths difference corresponding to the LP_{019} cladding mode before (black) and after subtraction of the temperature effect (green); concentration of carbon dioxide (red); the grey box indicates the values used for the temperature calibration.

The LPG sensor started to response immediately (in 20s) after the exposure to carbon dioxide. The response time of 6 min was calculated for the step change between the different levels of carbon dioxide concentration and based on the time when the central wavelength shift reached 90% of the total change. However the continuous temperature effect and acquisition interval of 20 s of commercial device make it difficult to determine the response time more accurately and thus this value is only indicative. More static condition measurements are necessary for the clarification of the response time and better evaluation of the sensitivity.

The changes in the central wavelength difference of the attenuation bands operating at PMTP were plotted as function of carbon dioxide and the calibration curve was obtained, Figure 5-26.

It has been mentioned that the position of the central wavelength was affected by temperature. The subtraction of this temperature effect from the change in the position of the central wavelengths was applied to the calibration curve, Figure 5-26 (blue spots).

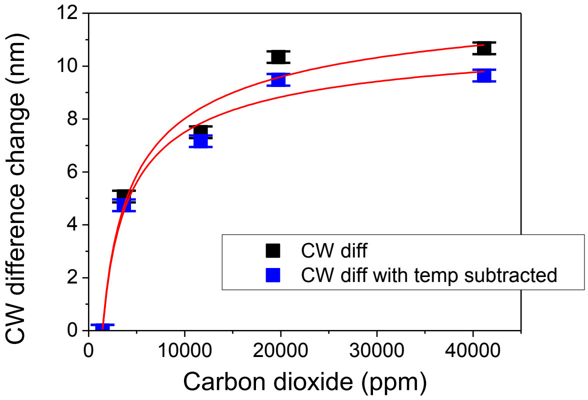

Figure 5-26: LPG sensor coated with 40 layers of HKUST-1: Carbon dioxide calibration curve before (black) and after the temperature level was subtracted (blue).

The limit of detection (LOD) (the smallest detectable difference in CO_2 concentration) has been calculated using the average standard deviation of 0.28 nm obtained over the values measured in stable conditions (at each concentration level) over the 3 min period and from the calibration curve (after the subtraction of temperature). The LOD of 401 ppm was identified for the region up to 10,000 ppm.

The sensor provides sufficient sensitivity for the detection of carbon dioxide for indoor air quality, where the target range of ≈400-10,000 ppm is required (3)(231). The practical use of the sensor in the real environment is compromised by the effect of the ambient relative humidity. The further work should target the development of the protective layer for separation of the water molecules. However the sensor can be still used in the field of food industry, e.g. for monitoring of the food packaging processes (40), where only the mixture of oxygen, nitrogen and carbon dioxide is used (232).

5.5 Conclusions

An HKUST-1 film has been deposited successfully onto the surface of an optical fibre LPG using the in-situ crystallization and the layer-by layer technique and the response of the transmission spectra has been characterized. The linear shift of the central wavelength during the deposition indicates the uniform growth of the HKUST-1 film with the increasing number of layers.

HKUST-1 thin film had been characterized using SEM, XRD and ellipsometer. The x-ray diffraction pattern obtained with use of XRD matches well with the previously reported data and proved the deposition of HKKUST-1 film with desired {222} orientation. The thickness of the film of 2 µm and 55 nm was established for the film deposited with use of in-situ crystallization and layer by layer (40 layers) approach respectively. LbL technique enabled much better control over the thickness of the film.

The LPG coated via in situ crystallization technique did not show chemical sensitivity to carbon dioxide. This could be explained by exceeding thickness of the sensing layer. The LPG coated with 40 layers HKUST-1 responded to carbon dioxide concentrations in the range of ≈2,000-40,000 ppm and the LOD of 401 ppm was obtained. The thinner films showed the smaller response to CO_2 concentrations up to 10,000 ppm with further saturation of the sensor.

The obtained LOD in a range of 100s ppm of carbon dioxide suggests the potential of the sensor for real world applications. The further improvement could be done by using higher resolution spectrometer and combined approach of data analysis (including the transmission, central wavelength and width change).

Chapter 5: LPG based carbon dioxide sensor coated with HKUST-1

The novel concept of the LPG based carbon dioxide sensor coated with a MOF material has been demonstrated. The thorough study on cross-sensitivity, deformation of the film by ambient RH and the implementation of the sensor into a multi-parameter sensing array can be included in the further work.

Chapter 6: Chemical sensors based on LPG coated with silica nanoparticles

6.1 Introduction

In this chapter, two practical applications of LPG based sensors are demonstrated for detection of i) volatile organic compounds emitted from paints and ii) ammonia in seawater samples. The principle of operation of both sensors is based on the deposition of silica nanoparticles on the surface of the LPG and their further functionalization with calixarene and tetrakis porphyrin dye (TSPP) towards VOCs and ammonia respectively.

The indoor air and seawater quality have been chosen for the demonstration of real-world application of LPG based sensor.

6.2 The sensor operation principle

Silica nanoparticles have been previously used as the sensitive material for FOSs as they enhance the sensitivity to bulk refractive index (112) or relative humidity (26). Calixarene or TSPP can be infused into the coating to endow the LPG with sensitivity to VOCs (27) or ammonia (15).

6.2.1 Detection of ammonia

TSPP represents a tetrakis(4-sulfophenyl) porphine, a compound that changes its optical properties (absorbance and refractive index) in response to exposure to ammonia. These changes are chemically induced by the deprotonation of TSPP and its returning to monomeric state and cause the decrease in the refractive index of the film (126). The sensor operation principle is schematically shown in Figure 6-1.

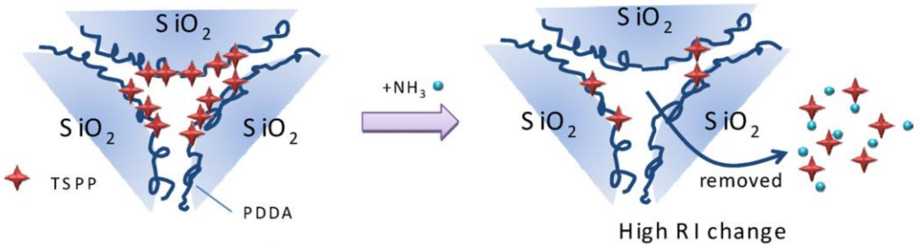

Figure 6-1: Operation principle of LPG based TSPP ammonia sensor (126).

The re-charge of TSPP by hydrogenation can be done, when the sensor is exposed to highly acidic environment, e.g. to vapours of strong (0.1 M) aqueous solution of HCl. The refractive index of the film is increased back to its initial value and this change is associated with the change in the transmission spectrum (126). However this re-charge is not possible to be done when TSPP compound is actually removed from the film as a response to ammonia binding.

6.2.2 Detection of VOCs

Calixarene molecules contain a number of phenol or resorcinol aromatic rings connected together to a larger ring and the whole molecule looks like a bowl (233). The analyte of the interest reacts with calixarene and becomes temporarily entrapped, however only the weak interactions occur (no covalent bond is created) which enable easy liberation from the cavity and this effect causes the reversibility of the sensor. The sensitivity of the reaction depends on the size and shape of the molecule of interest and for this reason the specific reactions to different VOCs is expected (20).

6.3 Methodology

6.3.1 Materials

Poly(allylamine hydrochloride) PAH (M_w: 75,000), Poly(diallyldimethylammonium chloride) (PDDA) (M_w 200,000–350,000, 20 wt% in H_2O), KOH, NH_3, TSPP, benzene, toluene, chloroform and acetone were purchased from Sigma-Aldrich. SiO_2 NPs (SNOWTEX 20L) was purchased from Nissan Chemical. Calix-[8]-arene (CA[8]) and calix-[4]-arene (CA[4]) 1 mM solutions were synthetized in the lab by Frank Davis, Cranfield University. All of the chemicals were analytical grade reagents and used without further purification. Deionized water (18.3 MΩ cm) was obtained by reverse osmosis followed by ion exchange and filtration (Millipore, Direct-QTM).

6.3.2 Sensor fabrication

LPGs were fabricated following the procedure described in Chapter 3 using same single mode optical fibre. The grating period was selected such that the LPG operated at or near the phase matching turning point.

A single LPG with period of 109.0 µm was fabricated using point by point approach and it was further used for the detection of VOCs. The concept of ammonia detection in seawater was tested using two LPG arrays consisting of LPG1 and LPG2 with periods of 109.0 and 109.5 µm respectively, where the LPG one was coated with the sensitive element, Figure 6-2. These arrays will be further referred as Array 1 and Array 2. They were used for tap water and seawater samples experiments respectively.

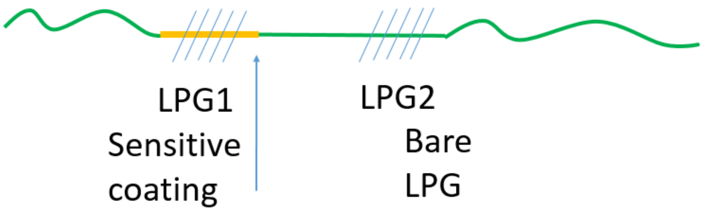

Figure 6-2: Scheme of the proposed LPG based TSPP ammonia sensor.

6.3.3 Thin film deposition

A mesoporous thin film of SiO_2 nanoparticles (NPs) was deposited onto the LPG using an electrostatic self-assembly approach as previously described (15) (112) (150).

Briefly, the region of the optical fibre with the LPG was rinsed with deionized water and immersed in a 1 wt% ethanolic KOH (ethanol/water = 3:2, v/v) solution for 20 min, leading to a negatively charged surface. The optical fibre was then sequentially immersed into a solution containing a positively charged polymer, PAH (used further for VOCs sensing) or PDDA (used for NH_3 sensing), and a solution containing negatively charged SiO_2 NPs for 15 min each, resulting in the alternate deposition of PAH or PDDA and SiO_2 NPs layers on the surface of the fibre. The fibre was rinsed with distilled water, and dried by flushing with nitrogen gas after each deposition step. The immersion in the PAH and SiO_2 nanoparticles was repeated until the desired number of layers were deposited (5 for VOCs, and 8 or 5 for NH_3 sensor of Array 1 and Array 2 respectively). The transmission spectrum of the LPG was measured after each deposition step.

CA[8] and CA[4] were used as the functional materials to provide sensor with the sensitivity to VOCs and TSPP was used for the sensitivity to NH_3. The LPG modified with the $(PAH/SiO_2)_5$ was immersed into a 1 mM of CA[8] aqueous solution for 2 hours followed by washing and drying and LPG sensor is referred as CA[8]. After all experiments (VOCs measurements) were completed with CA[8] sensor, the LPG was immersed into NH_3 solution for 2 hours to remove the CA[8] molecules. The LPG was then dried and immersed into CA[4] solution (the procedure was the same as for CA[8]). LPG modified with CA[4] is referred as CA[4] sensor. Similarly, the LPG modified with $(PDDA/SiO_2)_{5\text{ or }8}$ was immersed to 1 mM of TSPP aqueous solution for 2 hours followed by washing and drying. The whole deposition procedure is schematically shown in Figure 6-3.

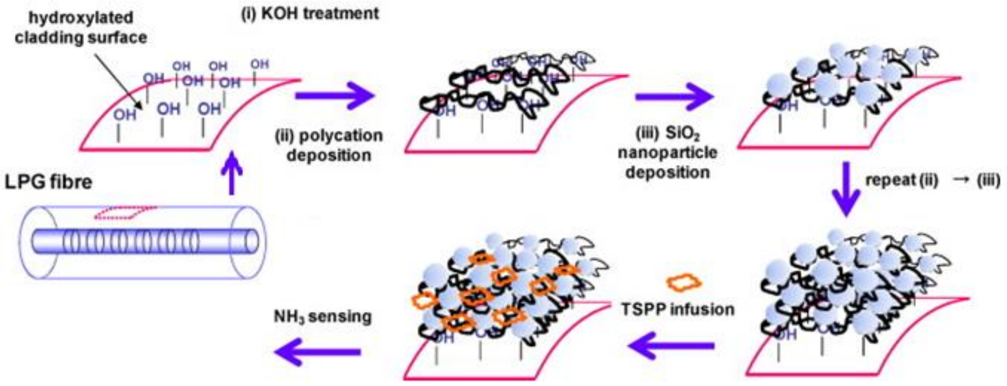

Figure 6-3: Schematic illustration of the layer by layer deposition process (15).

Transmission spectra of the LPG at the CA[8] and CA[4] or TSPP infusion were measured along with the dynamic change at the particular wavelength and the process was terminated when the dynamic change saturated.

6.3.4 Ammonia experiments

Array 1 was tested for the sensitivity to ammonia in tap water samples. The aquatic solutions of 0.1, 0.25, 0.5 and 1 mg.L^{-1} of ammonia were prepared via the dilution of original solution (concentration of 28%).

The LPG was fixed in the Teflon holder used for the deposition and then exposed to tap water and to all ammonia solutions for 10 min. The sample was pumped out after the each test and the LPG was washed by distilled water three times and the sample with higher concentration was injected subsequently.

Array 2 was tested for the sensitivity to ammonia in seawater samples. Seawater sample was taken at Plymouth Marine Centre. The LPG was tested to the sample with no modification and then to samples with added ammonia with concentrations of 0.5, 1, 2, 4 and 10 µM.

The transmission spectra were recorded every 10 s and the position of the central wavelength of the attenuation bands were noted.

6.3.5 Volatile organic compounds experiments

The LPG modified with the CA[8] and CA[4] was tested for VOCs sensitivity in the lab and then during paint leakage test simulation as follows.

The LPG was fixed in the closed cell and the solution of the VOC of interest (benzene, toluene, acetone and chloroform), of volume of 10, 30, 50, 100 µl (according to the saturation level), was injected in the cell (standard Petri dish with volume of 100 cm^3) and then was left until saturation. The cell was opened shortly before adding each volume. The LPG was kept in a straight position to avoid any bending which can affect its performance.

The temperature and relative humidity (RH) were simultaneously recorded as both of them are interfering factors (LPG itself is sensitive to temperature and SiO_2 NPs thin film causes the sensitivity to RH). One Wire sensor was used to control temperature and RH during the all experiments (sensor specifications are described in Chapter 4).

The simulation of ISO standard test involved exposure of the LPG sensor to the mixture of VOCs emitted from paints within a chamber consisting of a desiccator base and a stainless steel emission cell, as shown in Figure 6-4. The LPG was fixed in a glass desiccator (with estimated volume of 7.5 L) for 4.5 hours; a piece of a cardboard box of surface area 100 cm^2 freshly painted by commercially available paints was placed inside the desiccator. The paint source was: Plasti-kote project paint, 143S Antique gold (further referred as spray paint) and Wickes Master universal multi-surface primer (can paint).

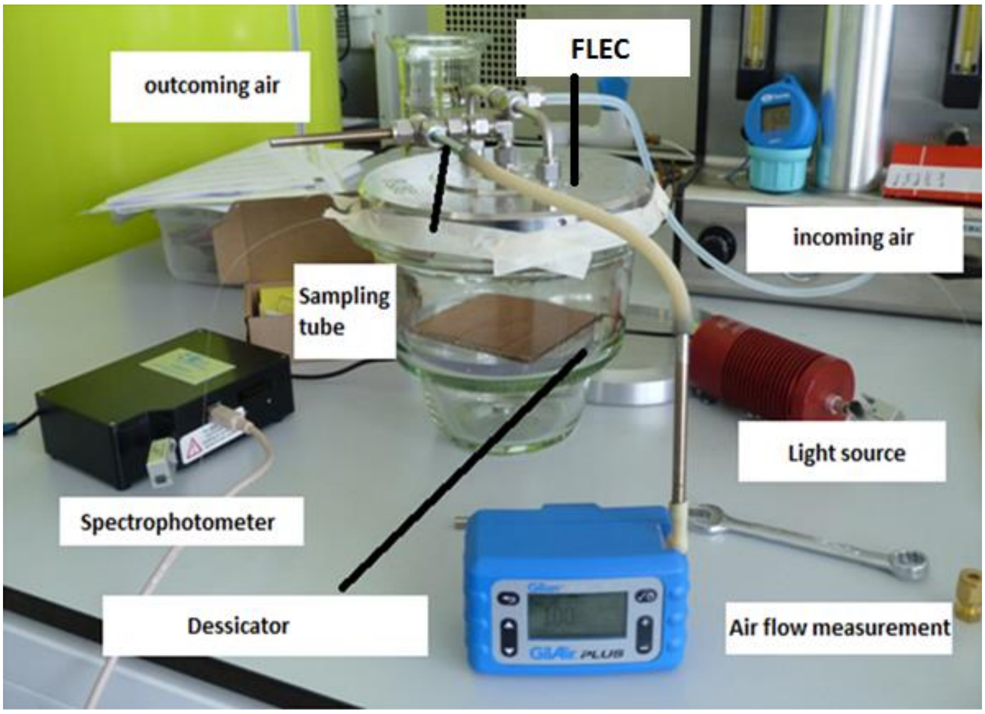

Figure 6-4: The scheme of the paint leakage test.

Transmission spectra were recorded every 1 min during all experiments. The central wavelengths of the attenuation bands were obtained using Spectrum Interrogation Routine Software and Origin was used for further data analysis.

The temperature and relative humidity were kept at the same level during the experiments and simultaneously measured using OneWire device.

A constant airflow was maintained during the whole experiment. The incoming air was controlled to be a 1:1 mixture of dry and humid air (initial RH in the cell was measured around 60 %). An emission cell, stainless steel enclosure designed for the testing of emissions of VOCs from materials, (FLEC®, Chematec) was placed on the top of the desiccator base. Air provided to the device enters the enclosure from the perimeter and exits centrally where there is the facility to sample the air to determine the presence of VOCs. The FLEC® is further described in the international standard ISO 16000-10, which concerns determination of the emission of VOCs from construction products.

The air was constantly leaving the measuring system through an air sampling tube on the outlet. The sorbent tubes (packed with Tenax TA) were used to collect the mixture of VOCs in the air. The air flow rate was 100 mL per minute and samples were collected for 2.5 minutes with the final total volume of 0.25 L and used as follows.

The air samples leaking from both paints were evaluated using TD/GC/MS (thermal desorption/gas chromatography/mass spectrometry). The VOCs were identified using special software according to peak area and expected retention time according to a library of previously analysed pure compounds.

The thermal desorption technique was used to desorb VOCs from the tubes and a DB5 gas chromatography column and a mass spectrometer (quadropole) was used for the VOCs analysis.

D8-toluene (C6D5CD3) (IS), retention time (RT) = 15.48 min was used as internal standard for GC-MS analysis. Its solution in methanol was injected to all tubes prior to analysis.

Details of this type of analysis method are in ISO 16000-6 (*Indoor air part 6 - Determination of volatile organic compounds in indoor and test chamber air by active sampling on Tenax TA sorbent, thermal desorption and gas chromatography using MS or MS-FID*).

6.4 Results and discussion

6.4.1 Detection of ammonia in seawater

Deposition of the $(PAH/SiO_2)_8$ film with further infusion of TSPP lead to the changes in the transmission spectrum of LPG1 of Array 1 and Array 2, Figure 6-5, which agree well with the previous observation (15). The changes in the transmission induced by the deposition of the silica nanoparticles will be also described in more details in Chapter 7.

The "U" shape attenuation band corresponding to LP_{019} cladding mode of LPG1 evolved during the deposition process providing the sensor with the highest sensitivity, while the other bands (in region of 670 nm) correspond to lower order cladding mode of both LPG1 and LPG2 and show the lower sensitivity, Figure 6-5a.

Similar change of the transmission spectrum with evolution of the "U" shape attenuation band at PMTP was observed for Array 2, Figure 6-5b (blue line). The further changes in the transmission spectrum were observed after the immersion in water (due to the increase of the RI), Figure 6-5b (red line). "U" shape attenuation band at PMTP observed in air split into two after the immersion in water and it becomes possible to distinguish two attenuation bands of LPG1 and LPG2 corresponding to LP_{018} cladding mode, Figure 6-5b.

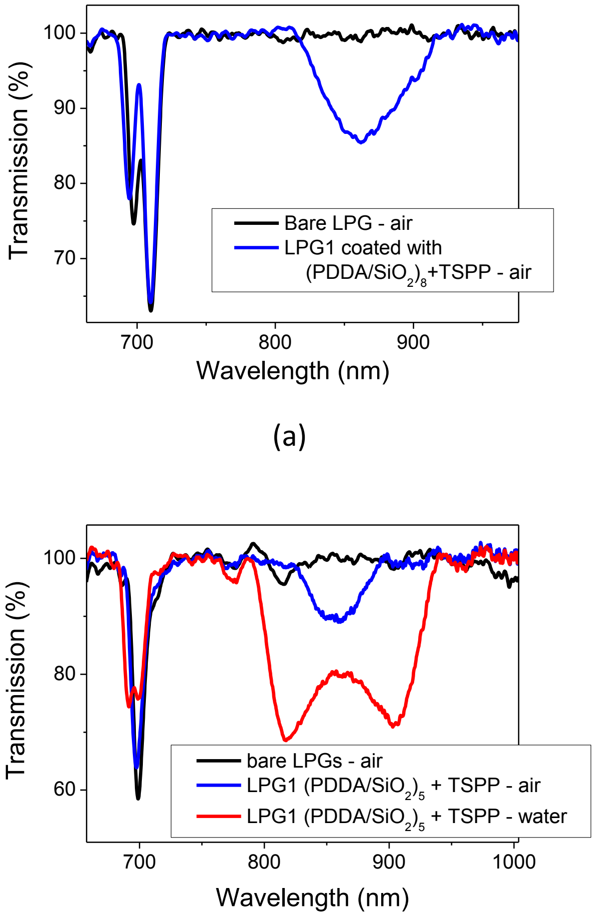

(a)

(b)

Figure 6-5: Transmission spectra taken in air of a) Array 1 and b) Array 2 before (black) and after the deposition of the sensitive coating consisting of SiO_2 NPs infused with TSPP taken in air (blue) and water (red).

The Array 1 has been exposed to ammonia in tap water. The transmission spectrum of LPG1 responded to NH_3 concentration levels of 0.1, 0.25, 0.5 and 1 mg.L^{-1}, Figure 6-6. The performance of the sensor was evaluated via the changes in the transmission at the central wavelength of the "U" shape band corresponding to LP_{019} cladding mode and the changes in the width of this band (in the same way as described in Chapter 4). For example, ammonia concentration of 1 mg.L^{-1} induced the change in the transmission at 855 nm (as indicated by black line in Figure 6-6Figure 6-1b) of 4.88 % and bandwidth change of 22.4 nm (at 95 % transmission level), Figure 6-6b.

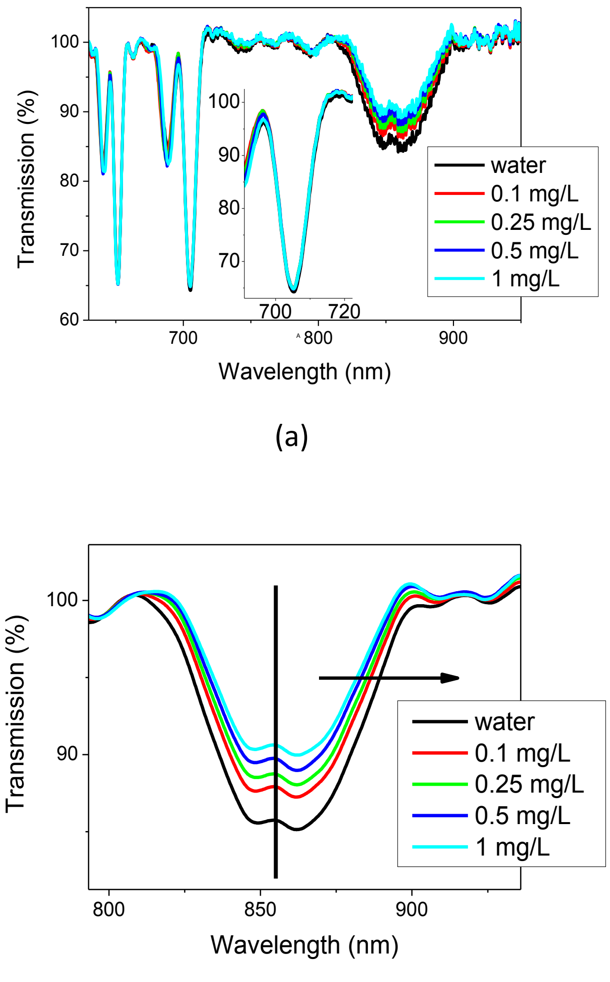

(a)

(b)

Figure 6-6: Transmission spectra of a) Array 1 with inset of LPG2 in detail and b) LPG1 in detail exposed to tap water (black) and 0.1 (red), 0.25 (green), 0.5 blue and 1 mg.L^{-1} aqueous solutions of ammonia.

No changes in the transmission spectra were observed at the LP_{018} attenuation band associated to the bare LPG2 as shown in inset of Figure 6-6a.

The calibration plot has been calculated over the tested range of 0.1 to 1 mg.L^{-1} of ammonia based on the measurement of changes in transmission, Figure 6-7a, and bandwidth, Figure 6-7b.

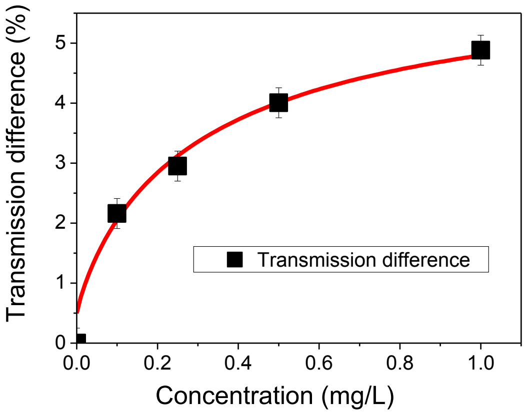

(a)

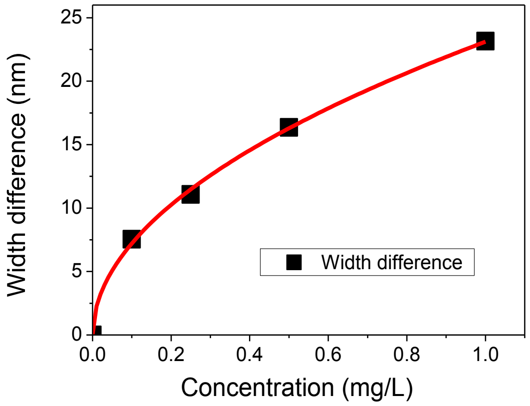

(b)

Figure 6-7: Array 1: ammonia calibration curve based on the changes in a) the transmission at central wavelength and b) the bandwidth associated with the attenuation band corresponding to LP_{019} *cladding mode.*

The results indicated that LPG should be able to detect the ammonia even at lower concentration than the smallest tested dose of 0.1 mg.L^{-1} (equivalent of 5.88 µM). The performance of array 2 was tested in real seawater samples over the range of 0.5 to 10 µM reaching the environmental levels (µM were used as they are more common units for chemical detection in seawater).

Firstly, the sensor was exposed to deionized water and sea water (2 times) and minimal difference in the transmission spectrum was observed, Figure 6-8. This finding indicates that the sensor can respond to ammonia in seawater as it was shown for tap water samples.

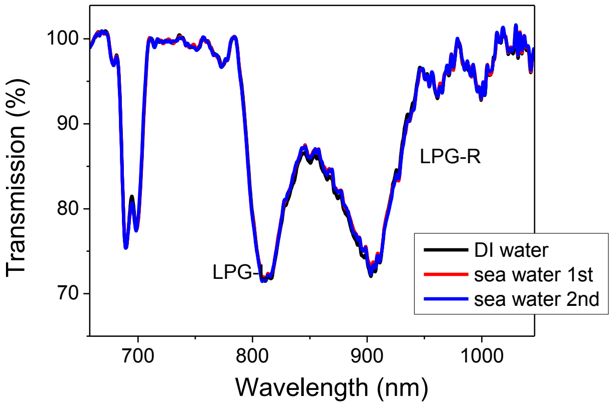

(a)

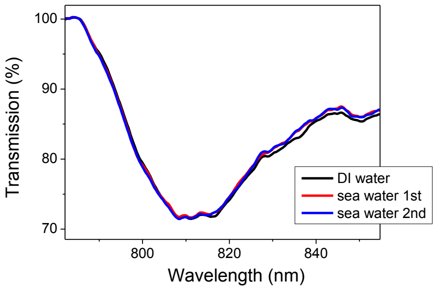

(b)

Figure 6-8: a) Transmission spectrum of Array 2 and b) attenuation band of LPG-L in detail immersed in DI water (black) and two times in seawater (red) and (blue).

The Array 2 was subsequently exposed to ammonia dissolved in seawater and the changes in the transmission spectrum were observed, Figure 6-9.

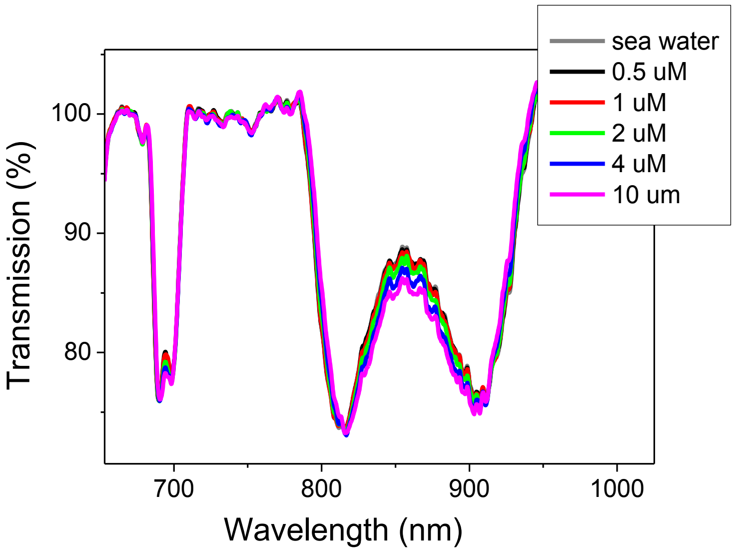

Figure 6-9: Array 2: transmission spectrum in response to sea water (grey), 0.5 (black), 1 (red), 2 (green), 4 (blue) and 10 µM (pink) of ammonia dissolved in sea water sample.

The LPG transmission spectrum responded within 30 s to the injection of each of the tested ammonia concentration. The continuous shift of the central wavelengths has been observed, where the saturation started approximately after 5 min. The central wavelength difference of the attenuation band as a function of time is shown in Figure 6-10.

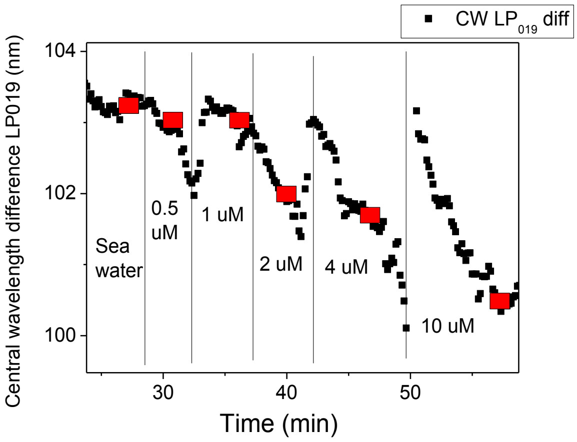

Figure 6-10: Array 2: The dynamic change of the central wavelength difference as a response to ammonia in seawater over the concentration range up to 10 µM.

The changes in the difference of central wavelengths of the attenuation bands corresponding to LP_{019} cladding mode and the changes in the band width at 90 % transmission level were plotted as a function of ammonia concentration and the calibration curves were obtained, Figure 6-11a and Figure 6-11b respectively. The results clearly showed that even the lowest tested concentration of 0.5 µM induced the changes of 0.36 and 0.26 nm in the central wavelengths difference and bandwidth respectively.

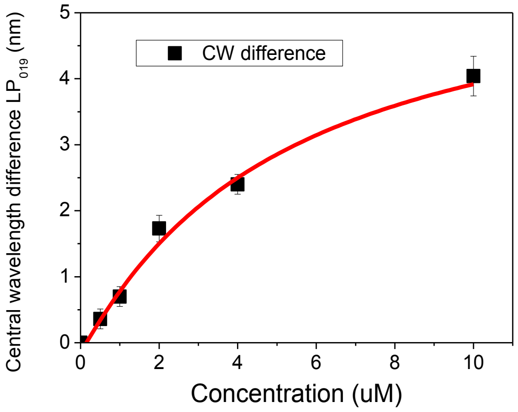

(a)

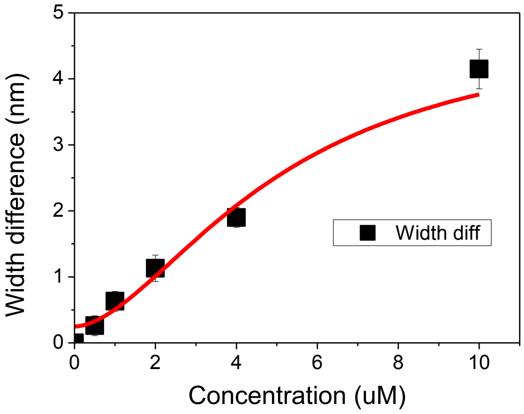

(b)

Figure 6-11: Array 2: ammonia calibration curve based on the changes in the difference a) between the central wavelengths and b) bandwidth of the attenuation band corresponding to the LP_{019} *cladding mode.*

The error bars in Figure 6-11 were calculated based on the standard deviation of the values taken from the 5 transmission spectra covering the same concentration level and the saturated response of the sensor (indicated by the red boxes in Figure 6-10).

The central wavelength difference has been used for the calculation of the LOD, as it has higher slope of the calibration curve. The minimal detectable change of 0.15 nm had been stated based on the average standard deviation of 0.15 nm obtained over the values measured in stable conditions (at each concentration level) over the 1 min period.

The LOD of 303 nM has been calculated using the calibration curve and the central wavelength shift of 0.15 nm in Figure 6-11a using the following Equation 8:

$$LOD = \frac{\sigma}{k}$$

Equation 8

Where σ is the standard deviation (0.154 nm) and k is the slope the calibration curve (0.509 nm/µM).

The obtained sensitivity enables the use of the sensor in the water environment, especially for non-saline waters, where the concentration in single units of µM and higher is expected (47) (48). The main drawback is represented by the absence of the sensor’s recovery, because the functional compound is removed from the coating in the presence of ammonia and thus the sensor works only on the one-time basis.

The sensor’s performance in the presence of other nutrients and chemicals naturally present in the environment should be examined to determine any cross-sensitivity.

6.4.2 Detection of VOCs emitted from paints

In order to endow the sensor with sensitivity to VOCs LPG was initially modified by applying 5 layers of SiO_2 NPs. The observed change in the transmission spectrum was in a good agreement with previously reported (15) (112). Comparison of the transmission spectra of the LPG measured after its immersion into CA[8] and CA[4] solutions is shown in Figure 6-12a. The CA[4] causes the larger wavelength shift of the central wavelengths (ΔCW at LP_{019} = 17.96 nm) than CA[8] where only the small change was observed (2.75 nm). This effect can be explained by the molecule size of calixarene molecules indicating that smaller CA[4] was deposited more effectively on the SiO_2 film surface.

Evolution of the transmission spectrum of the LPG immersed in CA[4] solution during the modification process is shown in Figure 6-12b. The largest shift of the central wavelength as well as the absolute transmittance at the central wavelength was observed in first 15 minutes and small or nor change observed after an hour.

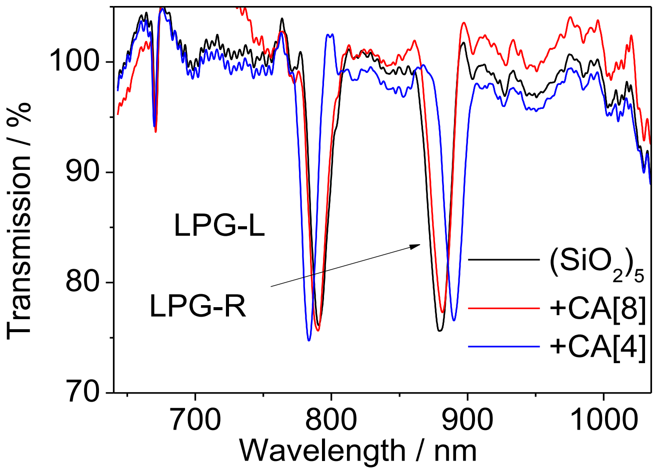

(a)

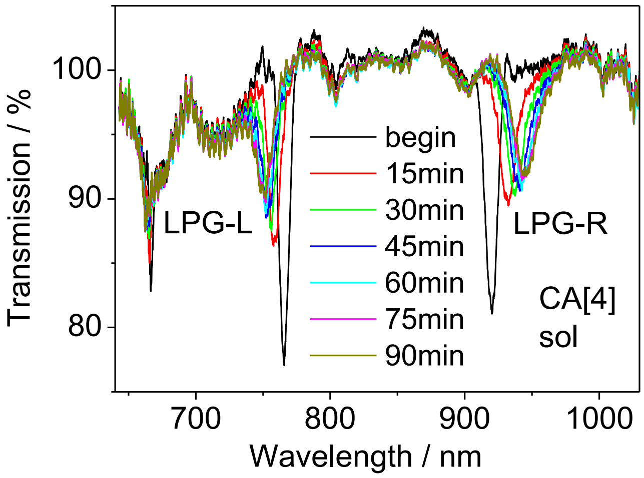

(b)

Figure 6-12: (a) TS after $(SiO_2)_5$ *NPs deposition (black) with infused CA[8] (red) or CA[4] (blue) and (b) TS of LPG at the infusion of CA[8] into* $(PAH/SiO_2)_8$ *film deposited over LPG in solution at different time intervals.*

The characterization of the response of the LPG to VOCs showed that the optical fibre can respond to the high concentrations of a range of different VOCs. The results from the exposure of the sensor to individual VOCs are summarized in Table 6-1.

Table 6-1: Sensitivity of CA[4] and CA[8] to individual VOCs

Slope of the calibration curve [nm/ppm]		
Type of calixarene	CA[4]	CA[8]
VOC	Δ CW$_{019}$ difference	
acetone	7.2 E-05	1.0 E-05
benzene	5.4 E-05	1.8 E-05
chloroform	2.5 E-05	0.7 E-05
toluene	5.4 E-05	2.0 E-05

A measurable response to VOCs was observed for LPG modified with CA[4] and CA[8] almost immediately even at the 10 µL of the injected solution, corresponding approximately to VOCs vapour concentrations of 18,000, 23,700, 19,800 and 26,000 ppm for toluene, chloroform, benzene and acetone respectively. The biggest shift was observed for acetone and the lowest for chloroform.

With increasing amount of VOC injected the sensor response saturated at 28,000, 210,000, 125,000 and 298,000 ppm for toluene, chloroform, benzene and acetone respectively.

CA[8] sensor demonstrated smaller response than CA[4] almost in all cases. No differences or ones at the edge of the resolution of the spectrometer were observed between individual VOCs for CA[8] sensor. The highest response which indicates the highest sensitivity was observed for CA[4] sensor and with LPG-R attenuation band and for this reason these data were used for further analysis.

The transmission spectra with maximum observed shift was noted for each volume injected and the position of the central wavelength was obtained. As an example acetone vapour at the concentration close to the saturation point (~298,000 ppm) induced the change in the central wavelengths difference of 2.65 nm for CA[4] sensor, Figure 6-13.

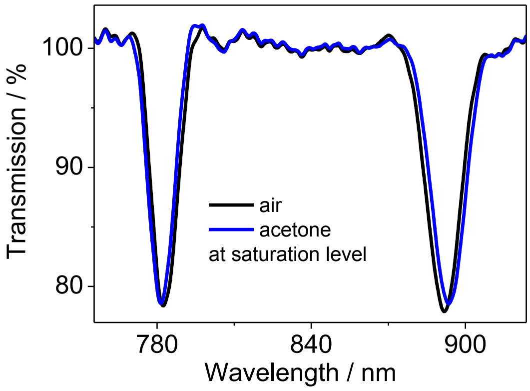

(a)

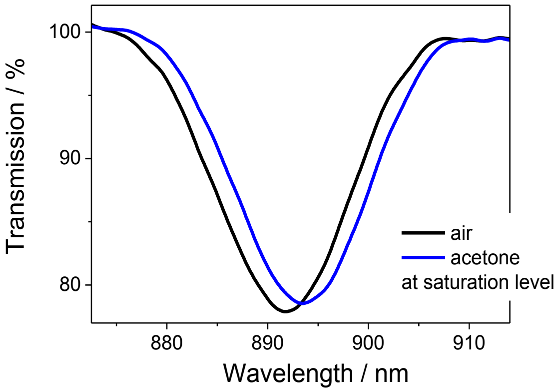

(b)

Figure 6-13: Transmission spectrum of a) CA[4] sensor and b) LPG-R in detail in air (black) and exposed to high concentration of acetone (blue).

The highest absolute shift of the central wavelength was observed for acetone; however the same volume of the injected VOC doesn't reflect the same concentration. The shift of the central wavelength of LPG-R of CA[4] sensor was used for the recalculation to enabled the comparison of the sensor's sensitivity to individual VOCs. The recalculation has been done for 10 µl injected volume. The concentration was divided by the absolute shift of the central wavelength (in nm) and multiplied by 0.13(nm) as the resolution of the spectrometer. The theoretical limit of detection was stated at 2841, 3626, 6550 and 3961 ppm for acetone, benzene, chloroform and toluene respectively.

Nearly same LOD to acetone, benzene and toluene and 2 times larger LOD to chloroform could be probably explained by the smaller size of chloroform molecules which leads to less occurrence of interaction between them and the calixarene film.

However, stable conditions during the experiments cannot be reached because the chamber was not hermetically sealed and no validated measuring technique has been done to measure VOC concentration simultaneously. According to these factors affecting the experiment the calibration curve cannot be made properly and all the concentrations are approximate.

The sensitivity achieved to date does not meet the criteria for the 8 hours exposure given by Health and Safety Executive (HSE), stated as 500, 50, 2 and 1 ppm for acetone, toluene, chloroform and benzene respectively and neither the 15 min exposure limit of 1500 and 100 ppm for acetone and toluene respectively. Further work is required to optimise the sensitivity of the sensor.

As the CA[4] sensor showed higher sensitivity to individual VOCs, it has been decided to expose it to both spray and can paint, while CA[8] sensor was exposed to spray paint only, to compare the performance of different types of calixarenes over the mixture of VOCs. The positions of the central wavelength for selected transmission spectra-time intervals are shown in

Table **6-2**.

Table 6-2: Absolute shift of the central wavelength difference during the paint experiments

paint	spray		can
sensor	CA[8]	CA[4]	
min	Δ CW_{019} difference (nm)		
0	0	0	0
5	0.96	3.57	0.57
30	3.25	3.53	2.62
120	3.13	3.93	2.63
final	0.23	0.12	0.13

LPG CA[8] sensor was exposed to the mixture of VOCs leaked from the spray paint in the desiccator. The visible change of the transmission spectrum was observed 5 min after the paint was installed. The shift of the central wavelength continued until 30 min of the experiments and then saturated. The LPG responded immediately to the paint removal from the desiccator while the rapid change of the central wavelength was observed. The final transmission spectrum was taken three minutes after the paint removal and similar position of the central wavelength was observed in comparison to the initial ones, indicating good reversibility of the sensor response,

Table **6-2**.

CA[4] sensor was exposed to the same paint at the same conditions and similar results were obtained in comparison to CA[8] sensor. The dynamic response of CA[4] sensor presented via the position of the central wavelength of LPG-L and LPG-R is shown in Figure 6-14a.

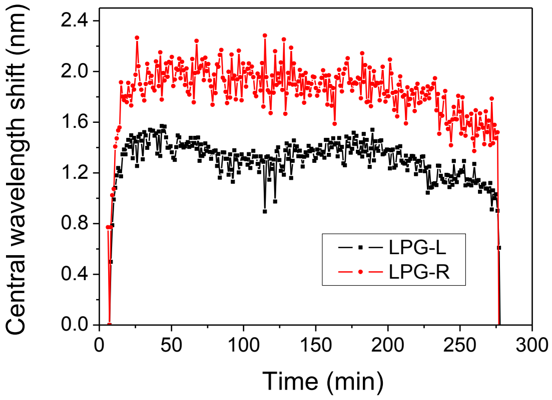

(a)

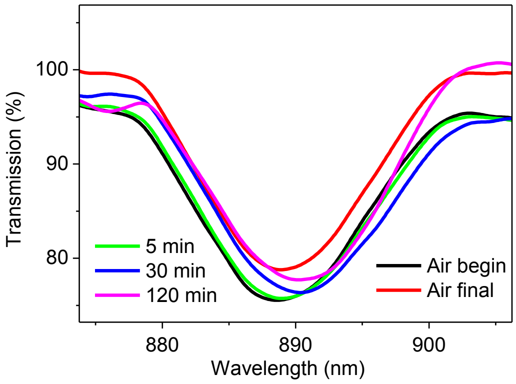

(b)

Figure 6-14: a) Dynamic change of CA[4] sensor central wavelengths corresponding to LPG-L (black) and LPR-R (red) during the spray paint experiment and b) Transmission spectra of CA[4] sensor of LPG-R in detail at selected times during the can paint experiment – initial one (black), final one (red) and 5 (green), 30 (blue) and 120 min (pink) after the paint placement.

CA[4] sensor was finally exposed to the can paint and transmission spectra at time intervals presented in

Table **6-2** (the detail of the attenuation band of LPG-R) is shown in Figure 6-14b. The slower initial response was observed in this case while almost no change in the position of the central wavelength was observed 5 minutes after the paint installation.

The experiments showed higher response of CA[4] sensor as compared to CA[8] to the spray paint and the higher response of LPG-R to LPG-L was observed for both sensors. This finding is in agreement with laboratory experiments. LPG CA[4] sensor responses differently to two types of paints, most likely because of different VOCs composition they have. The less pronounced response of LPG was observed mainly during the first 30 min during the experiment with the can paint. These observations support the hypothesis of the different response to individual VOCs concluded during the experiments in the lab.

The GC-MS analysis proved the different chemical composition of two different paints used in this work. More than 250 different compounds were identified in both paints. This finding indicates that the VOCs with higher molecular weight are present in a can paint. Although it is difficult to get the exact list of chemicals present because the individual peaks are overlapping which causes biases in chemical detection, some of the VOCs were classified. The following VOCs (5 with the highest abundance) were identified for each paint: spray - n-octane, o-xylene, n-nonane, Propan-2-ol, n-decane; can - o-xylene, n-decane, n-nonane, n-undecane, etylbenzene.

Even these five examples are similar, Figure 6-15 shows the presence of different VOCs in both paints and it can be clearly stated that different kinds of mixtures were presented there.

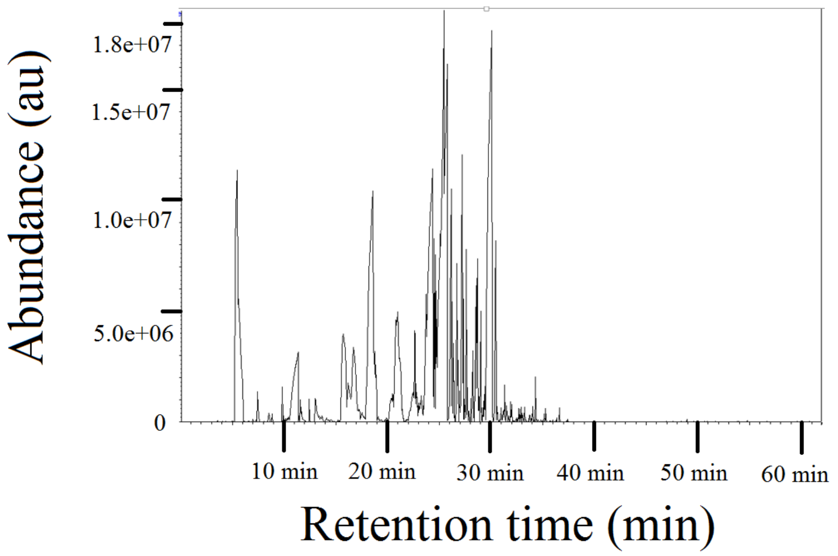

(a)

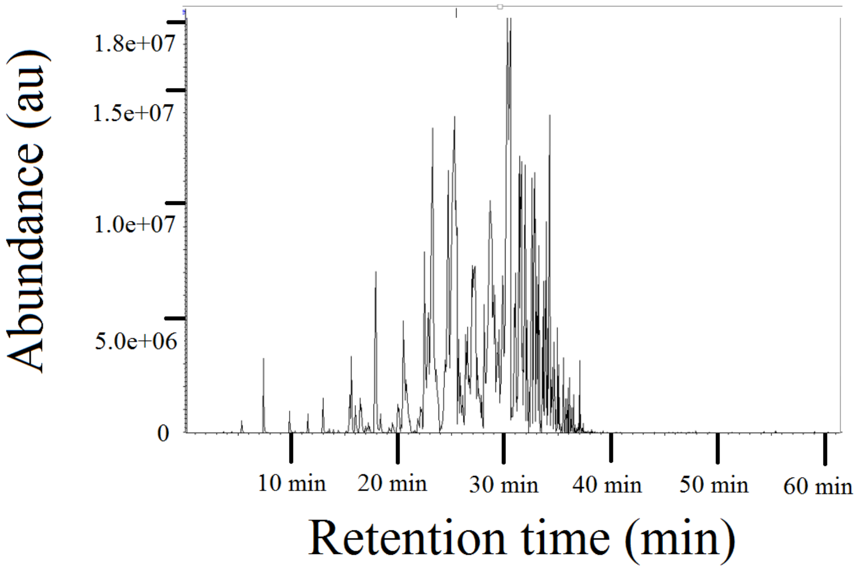

(b)

Figure 6-15: Results from GC-MS (a) spray paint (b) can paint.

Different response of the sensor to paint in a spray and in a can could be explained as follows. There were higher amount of aromatic compounds in the spray paint, and higher amount of aliphatic compounds were found in a can paint. This conclusion correlates well with the higher response of the optical fibre sensor to spray paint, because the higher sensitivity was obtained for aromatic VOCs in comparison to aliphatic ones as mentioned in (20).

The sensor with infused CA[4] was observed to be more sensitive than that infused with CA[8]. This could well be due to the fact that calix[4]arenes usually form much more definite geometries and have better defined cavities than calix[8]arenes which tend to be flatter and more flexible structures.

The experiments with the paints had been done in conditions which are similar to that used for tests which determine the emission of VOCs from building products and furnishing that are covered in British standards and international ISO norms. This kind of testing of VOC emission from different materials could be a further target for the application of fibre optic sensors after optimization of the sensor performance.

The experiments also showed the potential of measuring total or selected VOCs with use of optical fibres technology, however its use at the low concentrations (ppb range) is highly questionable at this stage, but still can be used for measuring occupational exposure or for measuring at places with higher concentrations (in hundreds or thousands of ppm). When all the issues will be managed, then the sensor can possibly work on a similar preciseness as other real time VOC sensors such as PID detectors.

6.5 Conclusions

Two practical applications of LPG based chemical sensors were presented.

The sensor based on TSPP was successfully tested over the measurement of ammonia in tap water and seawater samples. It has been proved that the optical fibre LPG can operate in seawater.

The sensor responded to the smallest dose of 0.5 µM showing a strong potential to have enough sensitivity to be used for real-time ammonia monitoring even on the open ocean.

Further work will target the possible repeatability of the measurement via the re-charge of the sensor, stronger embedment of TSPP into the sensitive coating (to measure the changes in the TSPP structure instead of remove of the film) or via the finding of the different sensitive element. The re-charge of the sensor could be done with HCl, where the low pH environment enables the re-hydrogenation of TSPP. The implementation of TSPP into the sensitive film directly instead of infusion into the existing coating can also improve the sensor’s performance. Testing of polyacrylic acid (PAA), as the functional coating, represents the other possible direction for the further research.

The optimisation of the sensor’s performance could be done via changes in the LPG period and film thickness.

The long-term target in this field will be real-time measurement of ammonia and the other chemicals affecting the seawater quality in-situ, e.g. as part of the buoy.

The performance of an LPG sensor based on CA[8] or CA[4] to VOCs has been assessed. The experiment was performed under conditions similar to that used in British Standard and ISO norms that determine the emission of VOCs from building products.

The ability to sense VOCs using functionalized LPGs has been demonstrated, but further work is required to improve the sensitivity, by optimization of the grating period and coating thickness. Based on the experiments presented here, and with improved calibration, it is anticipated that a limit of detection lower than of 1000s of ppm could be achieved.

It can be concluded that the LPG reacts to the high concentrations of different types of VOCs in the lab as well as in the real environment however the more precise conditions during the lab experiments are needed to be possible to obtain the more precise calibration curves.

Although the sensor cannot discriminate between individual VOCs, a different response was observed to two different commercial paint products, suggesting that the sensor can distinguish between the different mixtures and thus the sensor can be used for the detection of TVOCs.

Further work should target proper conditions during calibration. The use of hermetically sealed chamber with controllable temperature and relative humidity and simultaneous measurement of validated technique will be highly desired. The performance of the sensor to lower concentrations starting at ppm to tens ppm level should be also tested.

The use of the different functional coating can lead to the development of more sensitive sensors. It has been shown in Chapter 4 on the example of ZIF-8, where it could be possible to detect ethanol and acetone in a range of 10s ppm. The deposition of other materials from MOF family can lead to the fabrication of highly selective and sensitive VOCs sensors.

Chapter 7: Multi-parameter sensing using an LPG array

7.1 Introduction

In this chapter, a sensor array consisting of 3 LPGs with different grating periods written in a single optical fibre used for simultaneous measurements of temperature, relative humidity and concentration of volatile organic compounds is presented.

The design of the RH and VOCs sensors is based on the sensitive coating of silica nanoparticles and with further infusion of calixarene respectively, where both materials were introduced in Chapter 6.

Each LPG sensor was designed with optimised response to a particular measurand. The sensors were calibrated in the laboratory and the simultaneous measurement of the key indoor air quality parameters was undertaken in laboratory and office environments.

7.2 Sensor design and operation principle

One of the key advantages of fibre optic sensors is the ability to multiplex an array of sensors, sensitive to the same or to different parameters. This can be of significant benefit in real environments, where the influence of interfering factors such as temperature or relative humidity should be reduced. Simultaneous detection of several parameters at the same location using a single optical fibre offers additional information that allows correction for changes of the interfering parameters (12).

The LPGs have periods selected such that they all operate near the phase matching turning point and that differ by up to 1 µm to facilitate wavelength division multiplexing. A mesoporous coating of silica nanospsheres was deposited onto LPG1, such that it was sensitive to RH. The surface of LPG2 was left unmodified and was used to measure temperature. A functional material, Calixarene, was infused into a mesoporous silica nanospshere coating deposited onto LPG3 to sensitise the LPG to VOCs (20)(27).

The sensor array is illustrated in Figure 7-1.

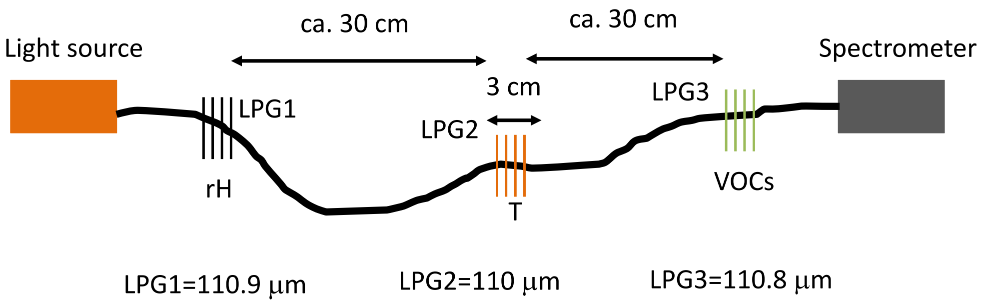

Figure 7-1: Schematic illustration of the LPG sensor array; the individual LPGs were used to measure: LPG1 relative humidity (RH); LPG2 temperature; and LPG3 volatile organic compounds (VOCs).

7.3 Methodology

7.3.1 Materials

Poly(allylamine hydrochloride) (PAH) (M_w: 75,000), NaOH 1 M aqueous solution, benzene, toluene, chloroform and acetone were purchased from Sigma-Aldrich. SiO_2 nanoparticles (NPs) (SNOWTEX 20L) were purchased from Nissan Chemical. P-sulphanatocalix[8]arene (CA[8]) 1mM solution was synthetized in the laboratory by Frank Davis, Cranfield University, following the procedure described in (20). All of the chemicals were analytical grade reagents and used without further purification. Deionized water (18.3 MΩ cm) was obtained by reverse osmosis followed by ion exchange and filtration (Millipore, Direct-QTM).

7.3.2 Fabrication of the array

LPGs with grating periods of 110.0, 110.9 and 110.8 µm, all of length 40 mm, were fabricated with use of point by point method following the procedure described in Chapter 3. The sensing array was fabricated by splicing together the 3 individual LPGs, with adjacent LPGs separated by a length of 30 cm of optical fibre with its buffer coating intact, which avoids the creation of in-fibre Mach-Zehnder interferometers (234). The grating period was selected such that the LPGs operated at or near the phase matching turning point, which, for coupling to a particular cladding mode (in this case LP_{019}), ensured optimized sensitivity.

The transmission spectrum of the optical fibre was recorded in a same way already described in the previous chapters.

The periods of LPGs were selected in such a way that each of them can be associated with distinct and uniquely identifiable resonance band in the spectrum, which allowed multi-parameter measurements where each LPG was measuring temperature, relative humidity or VOCs (see Section 3 for more details). In particular, LPG1, of period 110.9 µm, was modified with 5 layers of SiO_2 NPs and used for RH measurements. LPG2, of period 110.0 µm was used for temperature measurement and was left uncoated. LPG3, of period 110.8 µm, was coated with 8 layers of the SiO_2 NPs thin film that was subsequently infused with calixarene molecules and used for VOCs measurements.

7.3.3. Thin film deposition

Mesoporous thin films of SiO_2 NPs were deposited onto LPG1 and LPG3 using an electrostatic self-assembly technique. To sensitize LPG3 to VOCs, the $(PAH/SiO_2)_8$ coated LPG was infused with calixarane molecules. The deposition has been undertaken following the procedure described in Chapter 6.

7.3.4 Sensor calibration

The temperature responses of the LPGs were characterised over a range from 10 ^oC to 85 ^oC by placing the LPGs in an environmental chamber equipped with fibre-optic feed-through. This characterisation process was undertaken for each LPG individually, before splicing and coating, and was repeated after the LPGs had been spliced to form the array and after LPGs 2 and 3 had been coated with the silica nanospheres. The transmission spectra were saved at each temperature, 3 min after thermal equilibrium was reached. A temperature data logger (iButton® already described in Chapter 4), was placed in close proximity to the LPGs. The central wavelengths of the resonance bands were determined from the recorded transmission spectrum.

Similarly to the calibration of the temperature sensitivity of the LPGs, the response to RH was characterised for each LPG individually, before splicing and coating, and was repeated after the LPGs had been spliced to form the array and after LPGs 2 and 3 had been coated with the silica nanospheres.

The LPGs (individual and array) were fixed inside a small cell (Petri dish, volume 100 cm^3), into which a water droplet was injected. The LPGs were maintained straight and taut to avoid bend-induced distortion of the spectrum. The increase of the RH in the cell was monitored using the RH data logger. The transmission spectrum and data logger values were recorded every 10 s.

The performance of LPG3 as a VOC sensor was assessed by exposing it to high concentrations of chloroform, toluene, benzene and acetone vapours. LPG3 was coated with $(PAH/SiO_2)_5$ and infused with CA[8] and the central wavelength of the LPG3-R resonance band (identified in the spectrum shown in Figure 7-2) was monitored.

The LPGs were fixed in the same cell that was used for RH calibration and a solution of the particular VOC was injected by syringe using the following volumes: 10 µl of toluene, 50 µl of benzene and chloroform and 100 µl of acetone.

7.3.5 Experiments in the real environment

To investigate the performance of the sensor array in real environments, the system was deployed in two offices and in a laboratory:

1) in an open-plan office area with mechanical ventilation (Vincent Building, Cranfield University) over a 24 h period (sampling rate 10min), further referred as Vincent Building experiment;
2) in a research laboratory (Whittle building, Cranfield University) over a period of 60 h (sampling rate 5min), further referred as Whittle Building lab experiment;
3) in an office with natural ventilation (Whittle Building, Cranfield University) over a 60 h period (sampling rate 5min), further referred as Whittle Building office experiment.

Since there is no reliable and sensitive portable sensor for VOCs measurements that can be used for the benchmarking and the VOCs levels in the ambient environment are relatively low and lower that the limit of detection of the LPG VOC sensor, the studies of performance in real environments focussed on measurements of RH and temperature in different building areas, using the temperature and humidity data logger for benchmarking.

7.4 Results and discussion

7.4.1 Sensor fabrication

The transmission spectra of the individual LPGs measured before splicing into the array are shown in Figure 7-2b. The periods of the LPGs were chosen such that, when the 3 LPGs were combined, the resonance bands corresponding to the individual LPGs could be resolved. Consequently, the period of LPG1 is such that it couples light from the core to the (LP_{019}) mode near the phase matching turning point, just before band splits (Figure 7-2b, red line). The deposition of the coating leads to the splitting of the resonance band (these bands were labelled LPG1-L and LPG1-R, indicating short and long wavelength), as shown in Figure 7-2 and in (96). The transmission spectrum of the LPG array after splicing, but before LPG1 and LPG3 were coated, is shown in Figure 7-2a, where distinct resonance bands corresponding to each of the LPGs are observed clearly.

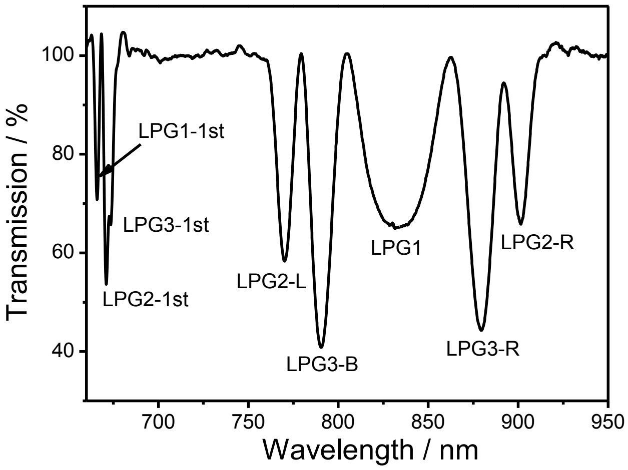

(a)

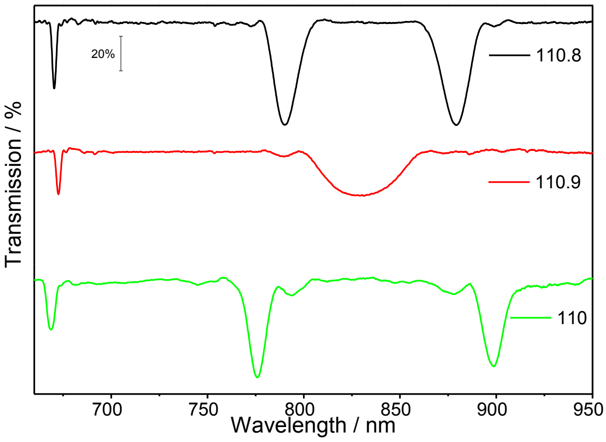

(b)

Figure 7-2: a) Transmission spectrum of the optical fibre LPG sensor array containing 3 LPGs, of period 110.9 (LPG1), 110.0 (LPG2) and 110.8μm (LPG3) (L and R labels indicate short and long wavelength, respectively, positions of the resonance bands corresponding to the coupling of the same cladding mode, 1st indicates the positions of first resonance bands) and b) Transmission spectra of the individual LPG grating with the period of: green line, 110 μm, black line, 110.8 μm; and red line, 110.9 μm.

7.4.2 Functional coating deposition

Deposition of the (PAH/SiO_2)$_5$ film leads to the changes in the transmission spectrum of LPG1, Figure 7-3, which agrees with previous observation (220).

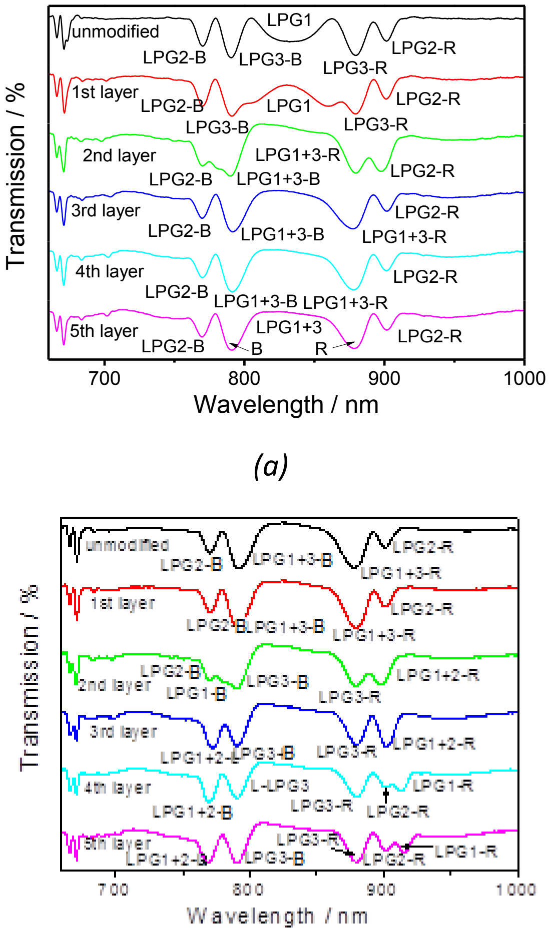

(a)

(b)

Figure 7-3: Transmission spectra of the sensor array at the deposition of (PAH/SiO_2)$_5$ on LPG1 measured in (a) air and (b) LPG1 in solution, LPG2 and LPG3 in air taken with bare LPG1 (black) and after the deposition of 1st (red), 2nd (green), 3rd (blue), 4th (cyan) and 5th (pink) layer.

In particular, the deposition of the first layer was observed to cause the attenuation band of LPG1 to split into two (labelled LPG1-L and LPG1-R), showing a dual resonance. Further increase of the film thickness resulted in changes of the central wavelengths of the attenuation bands until they merged with the attenuation bands of LPG2 and LPG3.

The evolution of the transmission spectrum during the deposition of the $(PAH/SiO_2)_8$ film onto LPG3 is shown in Figure 7-4 and Figure 7-5. A continuous linear shift of attenuation bands' central wavelengths was observed when LPG3 was immersed into the SiO_2 solution – decrease for LPG3-L, increase for LPG3-R, Figure 7-5b. The resonance bands corresponding to LPGs 2 and 3 merged after deposition of the 2nd layer (labelled as LPG2+3-R). Due to the overlap of the resonance bands of LPG1 and LPG3, it was difficult to observe their wavelength shift when LPG transmission spectra were measured in air, Figure 7-5a. It should be noted that overlap of the resonance bands could limit sensor performance, introducing cross-talk between sensors and ambiguity if the peaks merge or cross-over. The modification of the senor surface was conducted in such a way that this cross-talk was avoided and bands were clearly distinguishable.

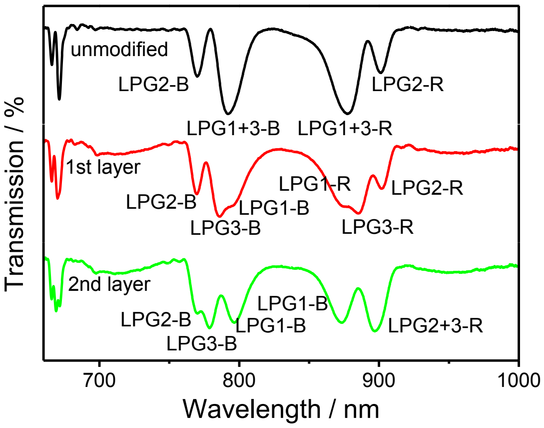

Figure 7-4: Transmission spectra of the sensor array at the deposition of $(PAH/SiO_2)_8$ on LPG3 measured in (a) air (black), 1st (red) and 2nd (green) layer.

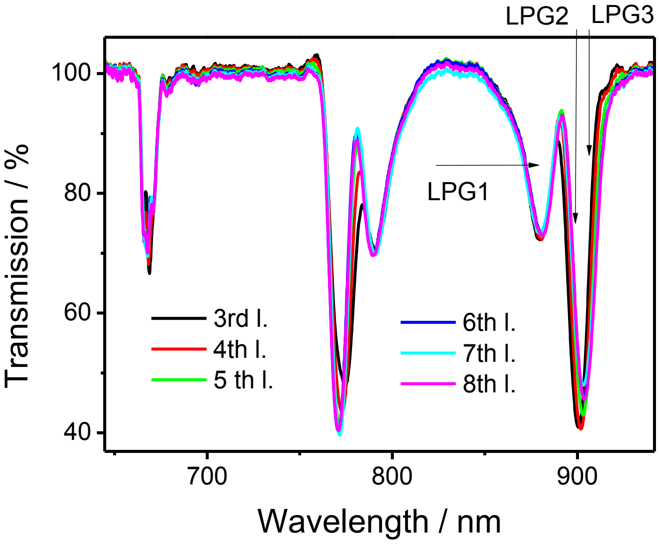

(a)

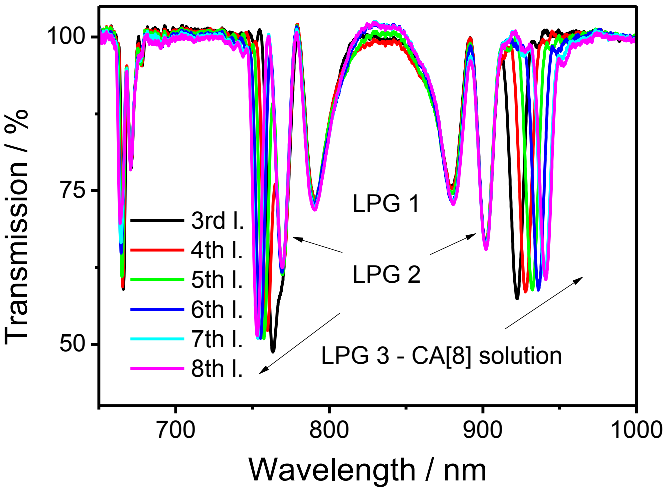

(b)

Figure 7-5: Transmission spectra of the sensor array at the deposition of (PAH/SiO$_2$*)*$_8$ *on LPG3 measured a) in air and b) in solution after the deposition of 3*rd *(black), 4*th *(red), 5*th *(green), 6*th *(blue), 7*th *(cyan) and 8*th *layer (pink).*

The central wavelengths of the dual resonance bands of LPG3 were observed to change as the CA[8] infused into the coating and changed the coating's refractive index. The evolution of the resonance bands is shown in Figure 7-6. This shift of the resonance bands in response the change in the coating's RI enables the discrimination of the LPG2-R and LPG3-R when the LPGs were in air.

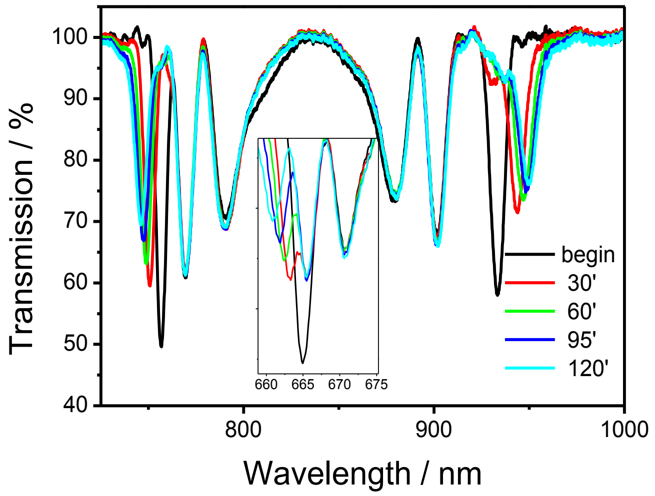

Figure 7-6: Transmission spectrum of the LPG sensor array measured in solution during the infusion of CA[8] into the $(PAH/SiO_2)_8$ film deposited on LPG3; the inset shows evolution of the 1^{st} resonance band.

The corresponding changes of the transmission spectrum are shown in Figure 7-7a. The process was terminated after no further shift in the attenuation bands was observed, which took approximately two hours. It should be also noted that the resonance bands associated with LPG1 and LPG2 remained unchanged. Figure 7-7b compares the transmission spectrum of the sensor array before and after deposition of the $(PAH/SiO_2)_8$ film and after infusion of CA[8] into the $(PAH/SiO_2)_8$ film. The transmission spectrum of the modified sensor array shows distinct resonance bands, allowing the multiplexing of the sensors in the wavelength domain.

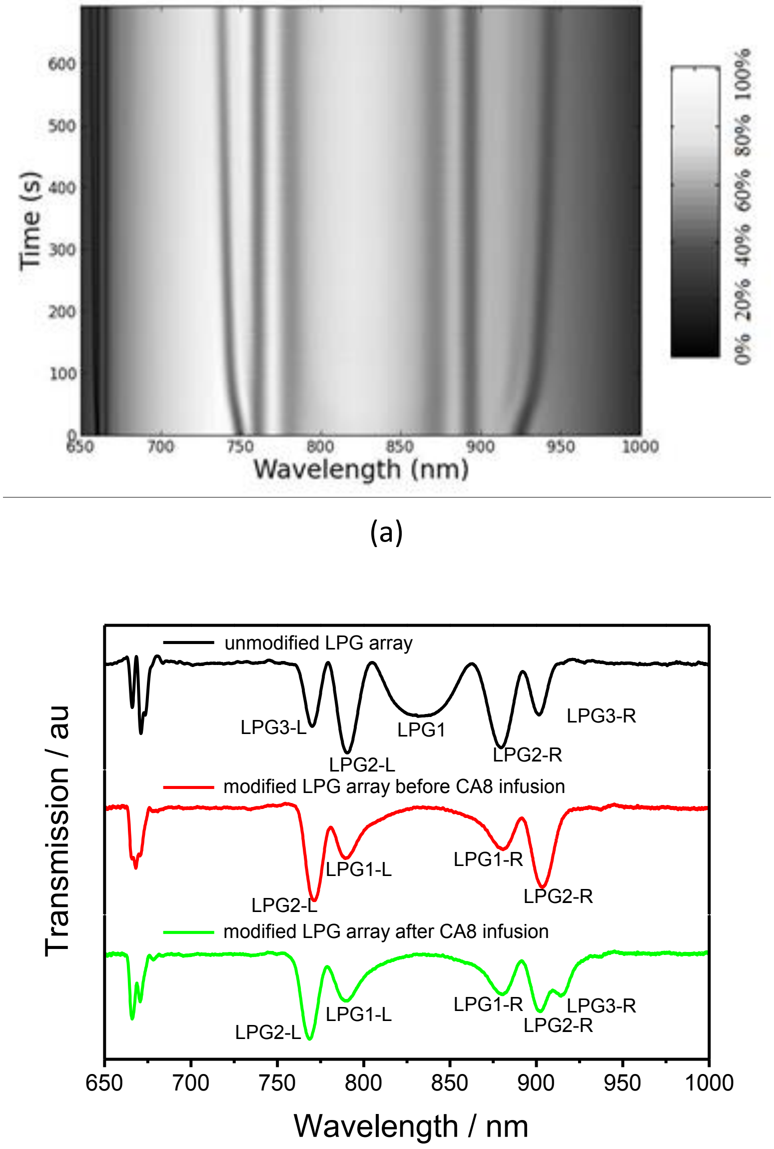

(a)

(b)

Figure 7-7: a) Evolution of the attenuation bands for LPG array during the infusion of CA[8] into the (PAH/SiO$_2$)$_8$ film deposited onto LPG3; and b) transmission spectra of the LPG array measured in air: black line, all LPGs are unmodified; red line, LPG1 modified with (PAH/SiO$_2$)$_5$ film, LPG3 (PAH/SiO$_2$)$_8$ film before CA[8] infusion and unmodified LPG2; and green line, same as red line but infused with CA[8].

7.4.3 Temperature calibration

Figure 7-8 shows the shift of the central wavelength of the single unmodified LPG3 (before splicing) induced by the temperature change. A linear response of the change in the central wavelengths was observed over the tested range of 25-85 ^{o}C.

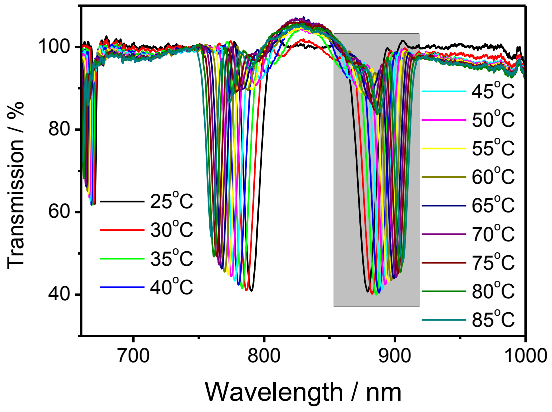

(a)

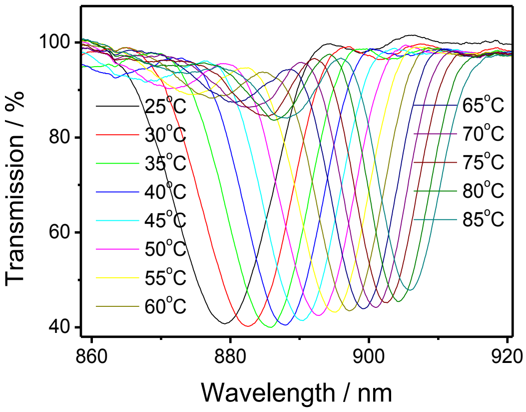

(b)

Figure 7-8: a) Evolution of the transmission spectra of the unmodified LPG3 prior the splicing of the array and b) attenuation band of LPG-R in detail at the temperature increase from 25 to 85 ^{o}C.

Figure 7-9a shows transmission spectra of all 3 spliced LPGs recorded at different temperatures. The resonance bands of all of the LPGs can be resolved throughout the measurement range. Figure 7-9b shows the calibration plot of the central wavelength *vs* temperature for the longer wavelength (labelled R) of attenuation bands of LPG1, LPG2 and LPG3.

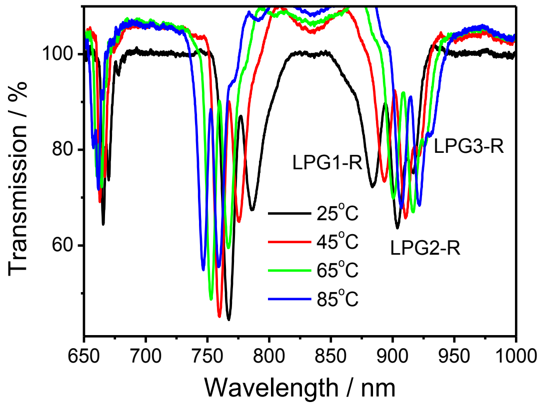

(a)

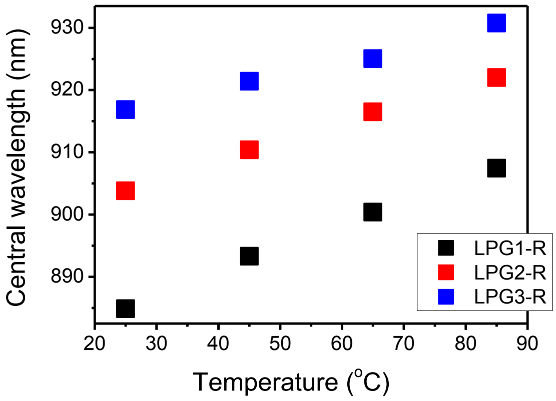

(b)

Figure 7-9: Transmission spectra of the sensor array at different temperatures and b) central wavelengths of LPG1-R (black), LPG2-R (red) and LPG-3 (blue) at selected temperature levels (data taken from Fig 4a, the error bars of each point are 0.065 (half of the resolution of the spectrometer) and are not visible as they are smaller than the data points.

The temperature response of LPG2-R, recorded during three calibration tests, is shown in Figure 7-10a. The small offsets in the central wavelength recorded at the same temperature during the three experiments may be associated with a difference in the strain applied to the fibre when it was mounted, which was to ensure that the fibre was not bent. It is known that an LPG sensor operating at the phase matching turning point is extremely sensitive to temperature, strain, surrounding refractive index and bending (20)(91). To take this into account, the temperature response was measured several times and the weighted average value of the calibration curve was used when determining the temperature during the subsequent experiments undertaken in real environments.

The temperature response was also measured after deposition of the PAH/SiO_2 film onto LPG3. The presence of the coating reduced the temperature sensitivity of the LPG3-R resonance band from 0.45±0.02 to 0.25±0.01 nm.$^{o}C^{-1}$, Figure 7-10b. There are two factors that can change the sensor's response to temperature after modification with PAH/SiO_2 film: a change in the RH with temperature (since the mesoporous film is sensitive to RH) and the thermo-optical properties of the PAH/SiO_2 film (a change of the RI of the film with temperature). Relative humidity decreases with increasing temperature is suggested to be the main cause of the reduced gradient.

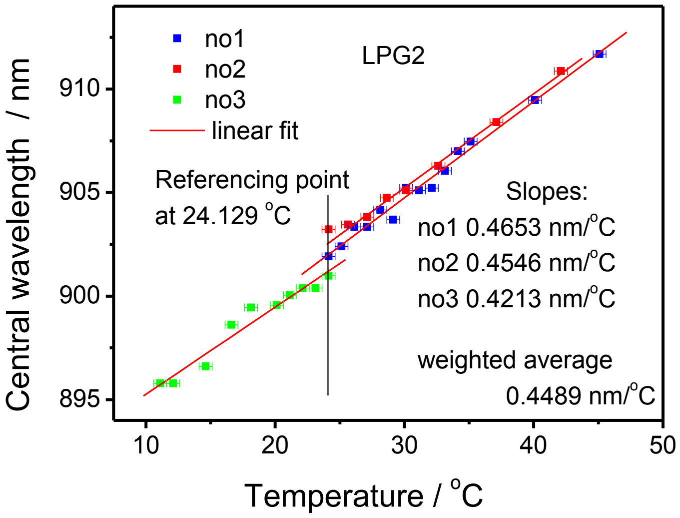

(a)

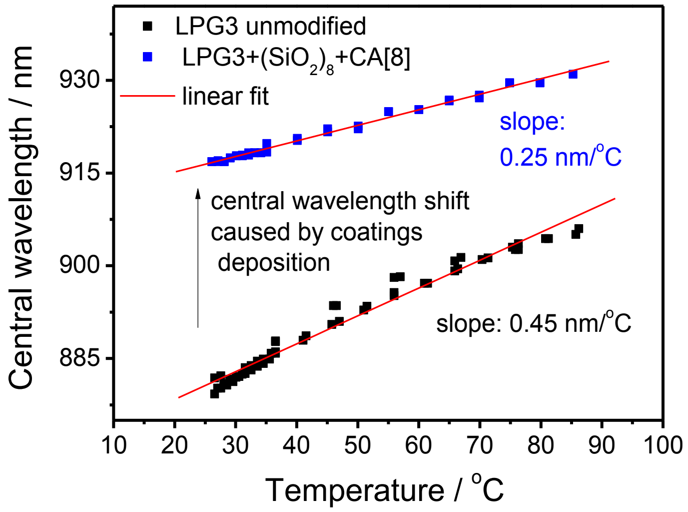

(b)

Figure 7-10: Temperature calibration curves: (a) no1 (blue spots): only LPG2 was exhibited to T change, no2 (red) and no3 (green): all LPGs were exhibited to temperature change and (b) comparison of the calibration curves of LPG3 measured: before (black) and after modification (8l SiO_2 NP's + CA[8]) (blue).

In order to obtain the real temperature sensitivity of the LPG modified with PAH/SiO_2 film and to take into account the effect of the RH, the gradient of the temperature response was recalculated using the following Equation 9:

$$\Delta\lambda_{total} = \Delta\lambda_T + \Delta\lambda_{RH}$$

Equation 9

where $\Delta\lambda_{total}$ is the measured total temperature induced wavelength shift of the resonance band of the LPG modified with the PAH/SiO_2 film, $\Delta\lambda_T$ is the wavelength shift caused by temperature only (this was plotted as a calibration curve); and $\Delta\lambda_{RH}$ is the wavelength shift caused by RH only (determined from the RH calibration curve of the LPG modified with the PAH/SiO_2 film).

This process revealed that the temperature sensitivities of the coated LPG were similar to that measured before the coating deposition. This recalculation was also used when processing the data from the measurements undertaken in laboratory and office environments.

The temperature sensitivities of resonance bands LPG1-R, LPG2-R and LPG3-R (after all modifications) were determined to be 0.45±0.02 nm.$^{o}C^{-1}$, 0.45±0.02 nm.$^{o}C^{-1}$ and 0.25±0.01 nm.$^{o}C^{-1}$ respectively and are summarized in Table 7-1. The detection limit of the LPG array was calculated to be 0.29±0.01 ^{o}C, determined from the LPG2-R calibration curve (Figure 7-10a), taking into account the spectral resolution of the spectrometer used (0.13 nm). It should be noted that the differences between the slopes for individual LPGs arises from the different LPG period and the thickness and type of the coating (discussed earlier).

Table 7-1: Individual LPG sensitivity to temperature: comparison based on the shift of the central wavelength of the attenuation band operating at PMTP.

LPG	Sensitivity [nm.$^{o}C^{-1}$]
LPG1-L modified with $(PAH/SiO_2)_5$	0.40±0.02[a]
LPG1-R modified with $(PAH/SiO_2)_5$	0.45±0.02[a]
LPG2-L unmodified	-0.50±0.02[a]
LPG2-R-unmodified	0.45±0.02[a]
LPG3-R modified with $(PAH/SiO_2)_8$ + infused with CA[8]	0.25±0.01[a]

[a]The error indicates the standard deviation of 3 separate experiments.

7.4.4 RH calibration

No change in the transmission spectrum of LPG2-R (without coating) was observed when the array was exposed to RH changes in the range from 40 to 70 %. Single, unmodified LPG1 and LPG3 were examined in the same way and it has been shown that, within the measurement resolution, uncoated LPGs are not sensitive to RH. The sensitivity of the modified LPG sensors arises from the changes in the RI of the mesoporous coating when water molecules infuse into the coating. Interestingly, when LPG3, modified with $(PAH/SiO_2)_8$ and infused with CA[8], was exposed to humidity, the sensitivity was much smaller than that of LPG1 with the $(PAH/SiO_2)_5$ coating but without CA[8]. Most plausibly this is a result of the hydrophobicity of the CA[8] and hence, when infused into the PAH/SiO_2 film, it suppress water adsorption.

RH calibration curves of 3 separate measurements conducted for LPG1-R modified with the (PAH/SiO_2) film are shown in Figure 7-11. Similar to the temperature measurements, the central wavelength of the resonance band at the start of the individual calibration experiments (initial) was different (explained earlier). Differences in the ambient temperature will also influence the initial position of the central wavelength as well. The average slope was used to determine the values of RH during experiments undertaken in the laboratories and offices. The detection limit of the LPG array was 1.39 RH %, determined from weighted average of the slopes (0.09 ± 0.01 nm per 1% RH change) obtained from the calibration curves (Figure 7-11) and spectral resolution of the spectrometer (0.13 nm). The shift of the central wavelengths in response to a change in RH for LPG1-R is shown in Figure 7-12a. By monitoring the transmission at a fixed wavelength, selected to midway up the slope of the resonance band of LPG1-R, the response to the RH change can also be observed, Figure 7-12b.

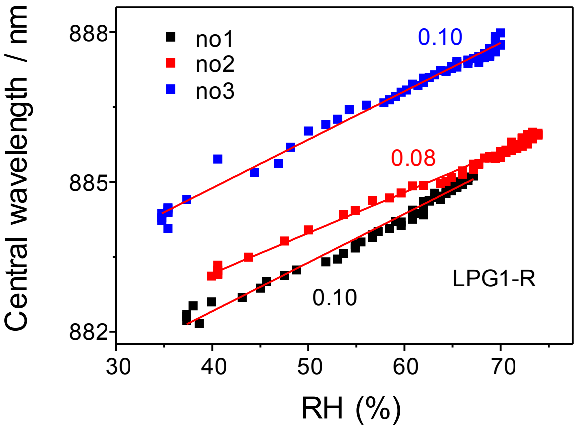

Figure 7-11: RH calibration curve for LPG1-R modified with the $(PAH/SIO_2)_5$ film; for three separate set of calibrations (no1, no2 and no3); the values near the calibration curves indicate the slope of the curve (nm RH $\%^{-1}$), the error bars of each point are 0.065 (half of the resolution of the spectrometer) and are not visible as they are smaller than the data points.

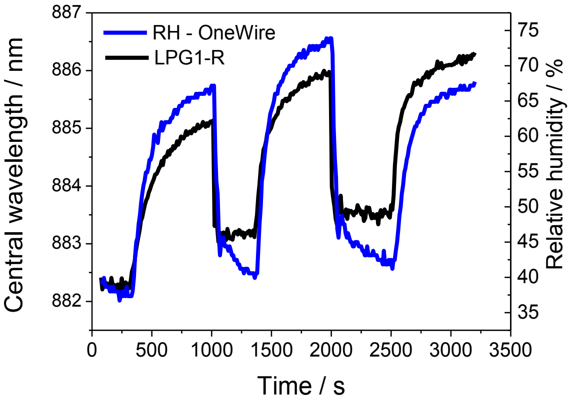

(a)

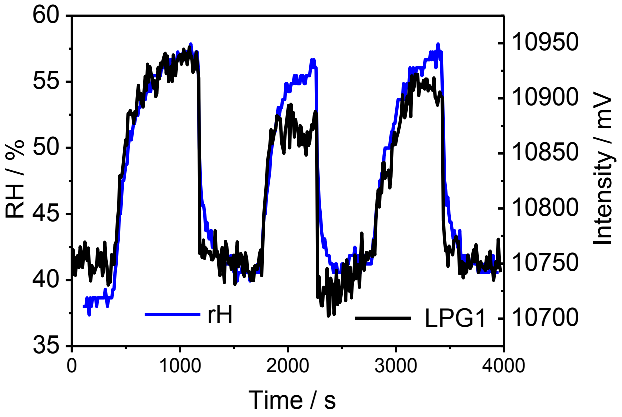

(b)

Figure 7-12: RH calibration experiment: a) Black line, wavelength shift of the resonance band of LPG1-R modified with the (PAH/SiO$_2$)$_5$ film; blue line, RH values measured using the humidity data logger and c) Intensity value taken at the ~882 nm (associated with the LPG1-R attenuation band) (black) and RH values measured using the data logger (blue).

7.4.5 VOCs calibration

No changes in the central wavelengths of the resonance bands corresponding to LPG1, modified with the $(PAH/SiO_2)_5$ film, and unmodified LPG2 were observed when the sensor array was exposed to chloroform, as can been seen in Figure 7-13a (on the next page). A small, but measurable shift of the resonance band corresponding to LPG3, modified with the $(PAH/SiO_2)_8$ infused with CA[8], was observed at high VOCs concentrations, as can be seen on example of acetone in Figure 7-13b.

The results for all VOCs experiments are summarized in Table 7-.

Table 7-2: LPG3 performance during VOCs experiments

VOC	Amount of solution	Estimated concentration	Central wavelength shift
Acetone	100 µl	298,000 ppm	0.35±0.065* nm
Benzene	50 µl	125,000 ppm	0.23±0.065* nm
Chloroform	50 µl	210,000 ppm	0.58±0.065* nm
Toluene	10 µl	28,000 ppm	0.24±0.065* nm

*Error bars represent the half of the resolution of the spectrometer

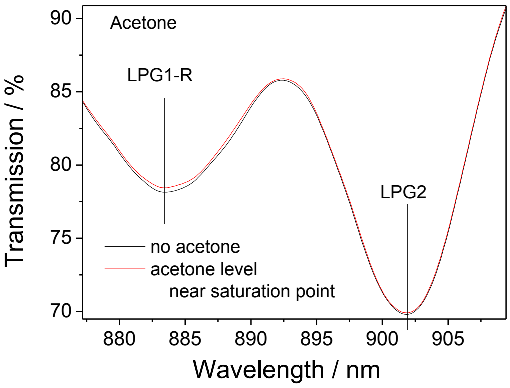

(a)

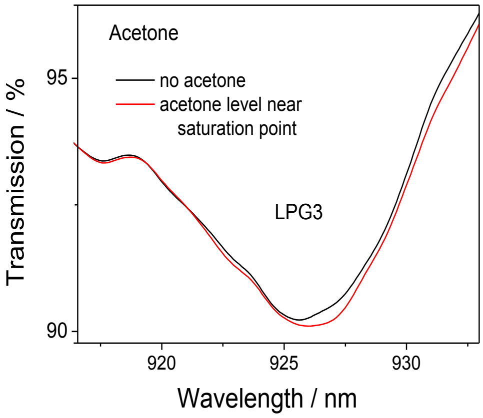

(b)

Figure 7-13: Changes in the transmission spectra of the LPG array, (a) LPG1-R, LPG2 and (b) LPG3, in response to exposure to a high concentration of acetone.

The low sensitivity to VOCs was, most plausibly, a result of non-optimal grating period and film thickness. In this case, we have demonstrated the potential for the use of the LPG for VOCs detection at high concentration as part of the sensing array. Future work will focus on studying this issue in more detail. The factors of interest include the increase of the transmission loss after the deposition of the functional film that can be achieved by change of the grating period and/or thickness of the film, as well as use of different types of calixarene molecules as different geometries with different cavities may lead to more definite geometries that will cause improved interaction of VOCs with the coating.

7.4.6 Experiments undertaken in real environments

During the experiment in the Vincent Building, the temperature and RH values ranged from 23.1 to 24.6 ^{o}C and 32.1 to 53.7 %, respectively. The unmodified LPG2 and LPG1 modified with the (PAH/SiO$_2$)$_5$ film were used to measure temperature and RH. Using the calibration curves described in sections 7.4.3 (Figure 7-10a) and 7.4.4 Figure 7-12a, the RH and temperature measured using the sensor array and data logger were compared, as shown in Figure 7-14a and Figure 7-14b, respectively.

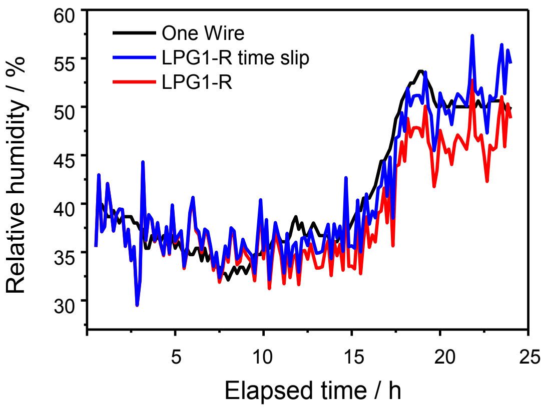

(a)

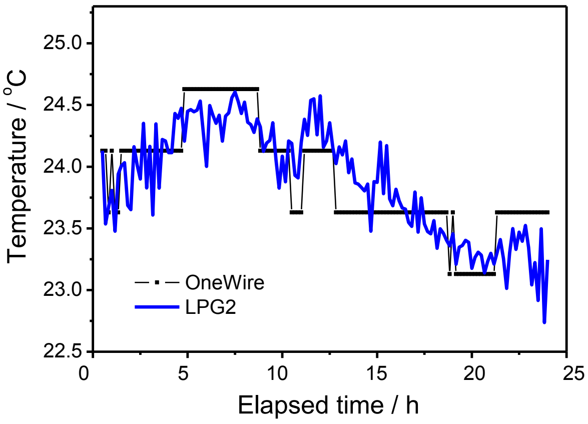

(b)

Figure 7-14: Vincent Building office area: Dynamic change of a) RH measured using LPG sensor array; RH values were calculated from wavelength shift using calibration curves (use LPG1-R, Figure 7-12a): black line, RH measured using humidity and temperature data logger; blue line, with and red line, without use of time slip correction; and (b) temperature measured using LPG sensor array (blue); temperature values were calculated from wavelength shift using calibration curves (use LPG2, Figure 7-10a); black line, temperature measured using humidity and temperature data logger.

Although extra care had been taken to anchor the LPGs firmly to keep them taut and straight during the measurements, it was found that they relaxed over the extended measurement period (>24 h). This relaxation caused a slight shift of the central wavelength with elapsed time. To take this into account a correction coefficient (time slip) was introduced. It takes into account the wavelength shift caused by bending as the result of the LPG relaxation and its total value, where the total difference caused by bending was divided with duration of the experiment, resulting in the time slip coefficient value of 0.0067 nm.h^{-1}, that was applied to the evaluation of temperature during the Whittle Building office experiment and RH during experiment in Vincent Building, Figure 7-18a and Figure 7-14a respectively. The effect of time slip coefficient was negligible in all other cases due to the small range of the measured values. This effect was not observed during the calibration experiments, as their duration was typically 4h.

The Figure 7-14a shows the effect of the time slip coefficient onto RH evaluation. The comparison of the RH calculated values before and after adding the correction coefficient is presented for LPG1-R. The slight relaxation of the LPG causes the shift of the central wavelength to the higher wavelengths, resulting in lower RH values, with the increasing difference over time, red line in Figure 7-14a.

In further work, the LPG should be fixed using the resin or glue, when the long-time (over 24 hours) experiments are conducted or otherwise the LPG region should be prevented from the airflow to minimalize the occurrence of the bending over time.

To investigate the correlation between the measurements performed by the data logger and the LPG sensor array, the temperature and RH values measured using the data logger were plotted against the LPG sensor array. The slope of the linear fit within these values was higher than 0.99 which indicates strong correlation between the sensing array and the data logger for all experiments. As an example the correlation is shown in Figure 7-15 for experiments undertaken in Vincent Building.

The LPG based sensor shows the higher sensitivity than the commercial OneWire sensor with the resolution of 0.5 °C and thus different type of the commercial device should be used in the future for more precise calibration of the LPG and comparison, e.g. use the thermo-couplers.

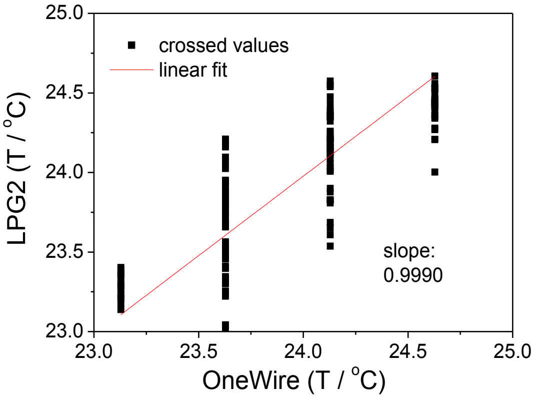

(a)

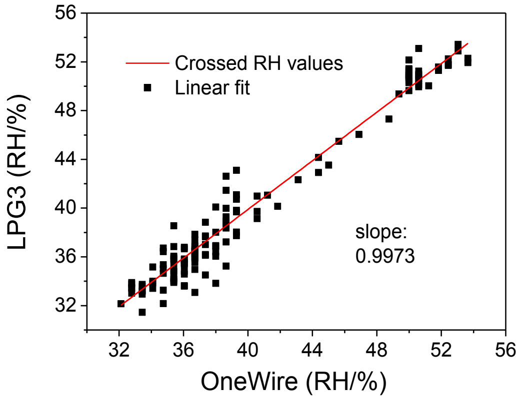

(b)

Figure 7-15: Vincent building office area: a) Temperature and b) RH values measured by data logger and LPG2 and LPG3, respectively.

The data recorded by the system during the Whittle building lab experiment are shown in Figure 7-16 and Figure 7-17, respectively.

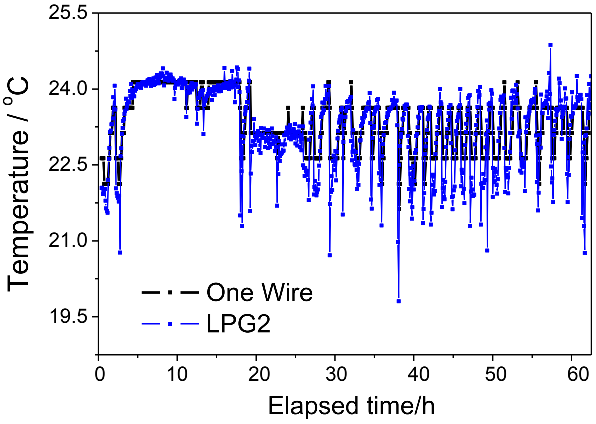

(a)

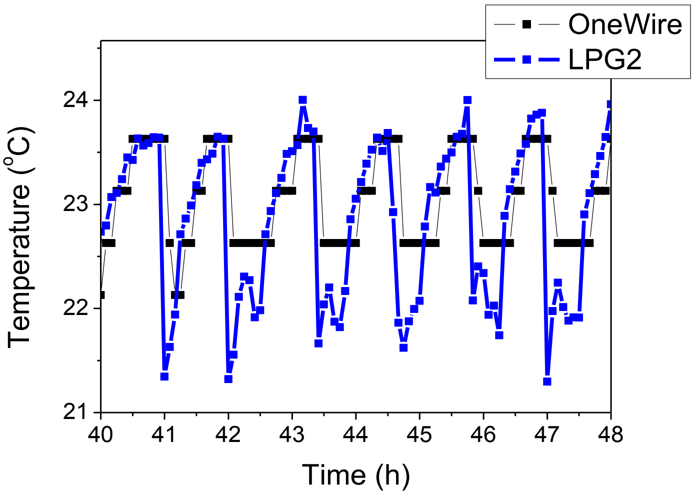

(b)

Figure 7-16: Whittle building lab area: Dynamic change of temperature measured using LPG sensor array (blue); temperature values were calculated from wavelength shift using calibration curves; temperature measured using humidity and temperature data logger (black); a) during the whole experiment and b) over the 8 hours in detail.

In the Whittle building lab experiment, the temperature and RH values ranged from 21.6 to 24.1 °C and 42.5 to 61.4 % respectively and the data measured by the LPG sensor array and the data logger were in a good agreement.

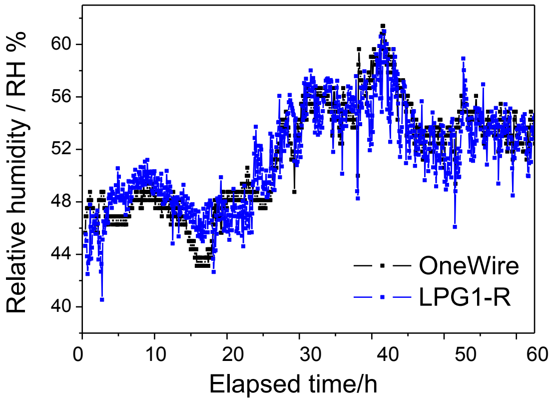

(a)

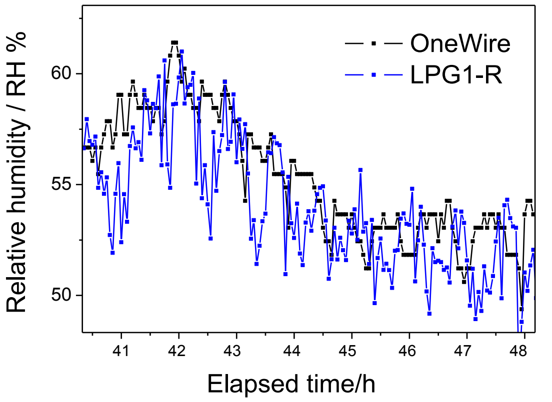

(b)

Figure 7-17: Whittle building lab area: Dynamic change of RH measured using LPG sensor array (blue); RH values were calculated from wavelength shift using calibration curves; RH measured using humidity and temperature data logger (black); a) during the whole experiment and b) over the 8 hours in detail.

The response time of the LPG based sensor was faster than for the commercial device, Figure *7-16*b. Similar trend was observed of RH values, where the LPG based sensor responded even to the small and short-term fluctuations probably caused by the air flow periodically coming from the air ventilation system, Figure 7-17b.

The values for temperature and RH ranged from 22.1 to 28.6 ^{o}C and 34.8 to 57.3 % respectively in Whittle building office area, Figure 7-18 and Figure 7-19 respectively. The time slip correction was used for temperature values calculation in this case, Figure 7-18.

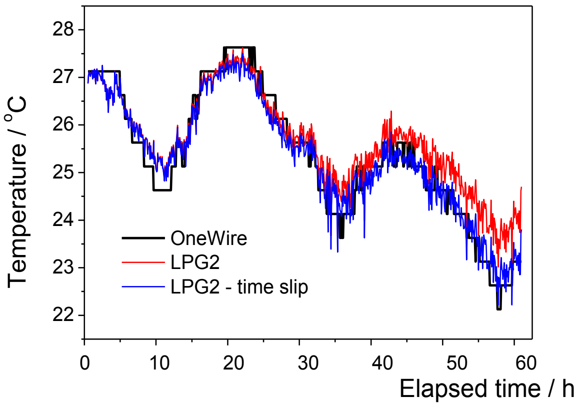

Figure 7-18: Whittle building office area: Dynamic change of temperature measured using LPG sensor array before (red) and after (blue) time slip correction; temperature values were calculated from wavelength shift using calibration curves; temperature measured using humidity and temperature data logger (black).

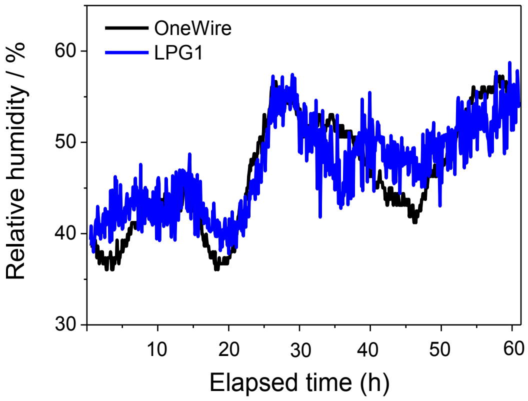

Figure 7-19: Whittle building office area: Dynamic change of RH measured using LPG sensor array (blue); RH values were calculated from wavelength shift using calibration curves; RH measured using humidity and temperature data logger (black).

The average difference between the values measured by data logger and the values calculated based on performance of the array was below 0.5 ^{o}C and 5 % of RH. The achieved accuracy fulfils the guidelines and recommendations for temperature and RH indoor given in the units of ^{o}C (235) or tens of RH percent respectively (32).

As expected, the concentration of VOCs in real environment was lower that the detection limit of the LPG, such that the resonance bands of LPG3 showed no response. The concentration of VOCs in real environment can increase significantly when new carpets are installed or after painting the walls. As was shown in Chapter 6 the LPG sensor modified with a $(PAH/SiO_2)_8$ coating infused with CA[8] can be used successfully to measure VOCs emitted from the paint.

7.5 Conclusions

An array of three long period gratings fabricated in a single optical fibre and multiplexed in the wavelength domain was used to measure simultaneously temperature, relative humidity and volatile organic compounds, which are key indoor air quality indicators. It was demonstrated successfully that the data produced by the LPG sensor array under real conditions was in a good agreement with that produced by commercially available sensors. The average differences between values obtained by the optical fibre sensor and standard temperature and RH sensors were better than 0.5^{o}C and 5% respectively. Further, the potential application of fibre optic sensors for VOC detection at high levels has been demonstrated.

Although there is a range of sensors developed for IAQ monitoring, the fibre optic sensor offers the ability to perform multi-parameter measurements that allows the increase the efficiency of the IAQ monitoring and the building energy performance.

The feasibility of measuring three different parameters have been demonstrated. Measurement of other IAQ factors such as carbon monoxide or dioxide together with temperature and RH are possible using the same principle. Other advantages of the fibre optic sensors include multipoint sensing with only one evaluation point.

Chapter 8: Conclusions

The complete cycle of the development of LPG based fibre optic chemical sensors have been explained and demonstrated.

The process of LPG fabrication has been shown using two different techniques based on UV irradiation inducing the periodical change of the refractive index of the fibre core: i) LPG fabrication via point-by-point fashion and ii) via amplitude masks.

The LPG fabrication via amplitude masks represents fast, effective and reproducible approach, with the reduction of fabrication time to 20 min in comparison to 150 min when using point-by-point technique.

The design and fabrication of LPG arrays enabled the development of multi-parameter sensing platforms and provided a step from the lab based to real-world applications, where the series of LPGs written in a single optical fibre can deal with the confounding factors such as temperature or relative humidity.

The development of novel chemical sensors has been demonstrated via the use of MOFs as the sensitive coating, where the possibility for detection of organic vapours and carbon dioxide was demonstrated using ZIF-8 and HKUST-1, respectively.

ZIF-8 based sensors show huge potential for ethanol and acetone sensing, where the limit of detection in range of single units of ppm in vapour phase was obtained. Promising results were presented also towards detection of methanol vapours.

The proof of concept was demonstrated using HKUST-1 based carbon dioxide sensor. Two different deposition techniques were compared: i) in-situ crystallization and ii) layer by layer. The latter approach enables the detection of carbon dioxide in the wide concentration range of up to 40,000 ppm with the minimum resolution of 400 ppm.

Two examples of the practical applications have been demonstrated, where the LPG based sensors were employed to detect VOCs emitted from the paints and ammonia in seawater. These examples proved the applicability of the LPG based chemical sensor not only in the labs based settings, but also in the challenging real world environment.

Alternative approach based on the functional coating has been used consisting of deposition of mesoporous film of silica nanoparticles via layer by layer technique onto the surface of the optical fibre with the subsequent infusion of the functional material – calixarene or porphyrin based dye into the pores of the SiO_2 coating to provide the sensitivity and selectivity to volatile organic compounds and ammonia, respectively.

The simultaneous measurement of temperature and relative humidity conducted in the real environment for indoor air quality monitoring was successfully demonstrated. The LPG based sensors were proved to measure the temperature and relative humidity with the similar precision as the commercial devices. The feasibility of multi-parameter measurement in real environment with the use of an LPG array has been shown.

Operation principle of all proposed LPG based sensors relies on the evaluation of the changes in the transmission spectrum. These changes are induced by the changes in the functional coating, such as refractive index, when the sensitive film is exposed to the analyte of interest. The most common and most widely used approaches for the sensor calibration are: i) monitoring of the change in the central wavelength or ii) transmission change at specific wavelength (region). In this work these approaches were broadened to include the measurement of the changes in the width of the attenuation band at selected transmission level. This new approach of data analysis can improve the sensitivity of the sensor, as it has been demonstrated on ethanol and acetone vapour sensing with the use of ZIF-8.

The performance of the sensors developed and described in this thesis is summarized in Table 8-1 for LPGs coated with MOFs and in Table 8-2 for LPGs coated with silica nanoparticles.

Table 8-1: Comparison of the developed sensors based on metal organic frameworks

Sensitive coating	MOFs	
	ZIF-8	HKUST-1
Measurand	VOCs (g)	CO_2
Readiness	Proof of concept	Proof of concept
Sensitivity	1.8 nm / 100 ppm of EtOH; should be tested in real environment; resolution in range of 10s ppm	~0.72 nm/1000 ppm; need to be optimized; currently resolution of 400 ppm
Selectivity	Tested against water vapour	Tested against N_2
Response time	~ 1 min – affected by the evaporation rate	~ 1 min

Table 8-2: Comparison of the developed sensors based on silica nanoparticles

Sensitive coating	SiO_2 NPs		
	NPs only	+ calixarene	+ TSPP
Measurand	RH	VOCs (g)	NH_3 (l)
Readiness	Real environment experiments	Real environment experiments	Real environment experiments
Sensitivity	0.09 nm/RH %; Resolution of 1.4 % In agreement with commercial techniques	2.5-7.5 E-05 nm/ppm resolution in a range of 1000s ppm	~ 0.7 nm/µM Optimization needed for use in unpolluted aquatic environment
Selectivity	Tested against VOCs	Tested against hexane & decane	Tested against Met-OH & Et-OH
Response time	< 10 s	~ 1 min – affected by the evaporation rate	~ 10 min

The further work in the field of fibre optic chemical sensors and their use for multi-parameter measurement, preferably in-situ, could target the following areas: i) primary research: investigating application of the new suitable materials such as MOFs for selective chemical detection and the methods of their deposition onto the surface of LPG; ii) identifying the field of practical implementation of the sensors already tested in the lab, such as use of silica nanoparticles for RH or TSPP for ammonia and pH sensing; do the experiments in real environment; combining of the currently working sensors into arrays; iii) work on sensor prototype that could be used in industry: work on sensor design and reducing the costs for the used equipment and iv) work on data analysis, the use of different approaches for the evaluation of the sensor performance, associated software and hardware development.

The MOFs family offers a wide range of materials that could be further used as the sensitive coating for LPG based sensors. MOFs application however is currently limited by the challenges in fabrication of these materials in the form of a thin film (154). There are several approaches that might help to overcome this challenge. For example, the use of microwave radiation can provide an interesting option in this field to broad the range of suitable MOFs as sensitive coatings (190). Alternative approach could be entrapment of the prepared MOFs crystals as powders into the host matrix, for instance sol-gel (154). For instance, seeding out the MOF crystals into polystyrene coating could be advantageous in this case (163).

Various fibre optic and LPG based sensors have been proposed already however a small number of them was tested in the real environment. ZIF-8 based sensor could be potentially used in biomedical applications. For example, it can be tested for the detection of alcohol or acetone in breath, where limit values for drivers in European countries range between 0.1 and 0.5 mg.L^{-1} in blood, adequate to 30-130 ppm of ethanol in breath (224). Similarly HKUST-1 based sensor could be tested for indoor air quality applications (3), however in this case the negative effect of relative humidity onto the structure of the film should be solved.

The current application of the LPG based sensors is rather limited to predominant application in laboratory settings. The further research can target the development of “blue box” with the sensor (9). The high resolution spectrometer and halogen light source can be replaced by LED and photodetector, this setting will benefit of smaller size and cost. The LPG could also work in the reflection mode, where the light will go through the fibre with LPG region and then will be reflected by the mirror layer (gold or silver) on the tip of the fibre. The reflected light then goes through the grating again and then is transmitted to the detector (19). The whole sensor could be designed and fabricated in a size of a pen, with a possible reading of the results on a screen of mobile phone.

Improvement in the data analysis represents the last area of the proposed further research. Currently some steps of the signal processing are still performed manually by a specialized personnel. Development of the software for the analyte recalculation, automatization of the signal processing and evaluation of the sensor performance will enable the use of LPG based sensors directly in industrial applications.

References

1. Hancke GP, de Silva B de C, Hancke GP. The role of advanced sensing in smart cities. Vol. 13, Sensors (Switzerland). 2013. 393-425 p.
2. Leech JA, Nelson WC, Burnett RT, Aaron S, Raizenne ME. It’s about time: A comparison of Canadian and American time-activity patterns. J Expo Anal Environ Epidemiol. 2002;12(6):427–32.
3. Crump D. Investigating indoor air quality problems: best practice and case studies. Proc ICE - Forensic Eng [Internet]. 2013;166(2):94–103. Available from: http://www.icevirtuallibrary.com/content/article/10.1680/feng.13.00001
4. Carpenter SR, Caraco NF, Correll DL, Howarth RW, Sharpley AN, Smith VH. Nonpoint pollution of surface waters with phosphorus and nitrogen. 1998 Aug;8(3):559–68.
5. Diaz RJ, Rosenberg R. Spreading dead zones and consequences for marine ecosystems. Vol. 321. 2008. p. 926–9.
6. Hestir EL, Brando VE, Bresciani M, Giardino C, Matta E, Villa P, et al. Measuring freshwater aquatic ecosystems: The need for a hyperspectral global mapping satellite mission. Remote Sens Environ [Internet]. 2015;167:181–95. Available from: http://dx.doi.org/10.1016/j.rse.2015.05.023
7. Korposh S, James S, Tatam R, Lee S. Fibre-Optic Chemical Sensor Approaches Based on Nanoassembled Thin Films : A Challenge to Future Sensor Technology. Curr Dev Opt Fiber Technol. 2013;585.
8. Kersey AD. A Review of Recent Developments in Fiber Optic Sensor Technology. Opt Fiber Technol [Internet]. 1996;2:291–317. Available from: http://www.sciencedirect.com/science/article/pii/S106852009690036X

9. Rego G. A review of refractometric sensors based on long period fibre gratings. Sci World J. 2013;2013.

10. Wang XD, Wolfbeis OS. Fiber-Optic Chemical Sensors and Biosensors (2013-2015). Anal Chem. 2016;88(1):203–27.

11. Rao Y. In-fibre Bragg grating sensors. Meas Sci Technol. 1997;8:355–75.

12. James SW, Tatam RP. Optical fibre long-period grating sensors: characteristics and application. Meas Sci Technol. 2003;14(5):R49–61.

13. Lim D V. Detection of microorganisms and toxins with evanescent wave fiber-optic biosensors. Proc IEEE. 2003;91(6):902–7.

14. Gupta BD, Verma RK. Surface plasmon resonance-based fiber optic sensors: Principle, probe designs, and some applications. J Sensors. 2009;2009.

15. Korposh S, Selyanchyn R, Yasukochi W, Lee SW, James SW, Tatam RP. Optical fibre long period grating with a nanoporous coating formed from silica nanoparticles for ammonia sensing in water. Mater Chem Phys [Internet]. 2012;133(2–3):784–92. Available from: http://dx.doi.org/10.1016/j.matchemphys.2012.01.094

16. Tripathi SM, Bock WJ, Mikulic P, Chinnappan R, Ng A, Tolba M, et al. Long period grating based biosensor for the detection of Escherichia coli bacteria. Biosens Bioelectron [Internet]. 2012;35(1):308–12. Available from: http://dx.doi.org/10.1016/j.bios.2012.03.006

17. Melo L, Burton G, Davies B, Risk D, Wild P. Highly sensitive coated long period grating sensor for CO2 detection at atmospheric pressure. Sensors Actuators, B Chem [Internet]. 2014;202:294–300. Available from: http://dx.doi.org/10.1016/j.snb.2014.05.062

18. Jiang H, Yang R, Tang X, Burnett A, Lan X, Xiao H, et al. Multilayer fiber optic sensors for in situ gas monitoring in harsh environments. Sensors Actuators, B Chem [Internet]. 2013;177:205–12. Available from: http://dx.doi.org/10.1016/j.snb.2012.10.122

19. Alwis L, Sun T, Grattan KT V. Fibre optic long period grating-based humidity sensor probe using a Michelson interferometric arrangement. Sensors Actuators, B Chem [Internet]. 2012;178:694–9. Available from: http://dx.doi.org/10.1016/j.snb.2012.11.062

20. Topliss SM, James SW, Davis F, Higson SPJ, Tatam RP. Optical fibre long period grating based selective vapour sensing of volatile organic compounds. Sensors Actuators, B Chem. 2010;143(2):629–34.

21. Yaghi OM, O'Keeffe M, Ockwig NW, Chae HK, Eddaoudi M, Kim J. Reticular synthesis and the design of new materials. Nature. 2003;423(6941):705–14.

22. Lu G, Farha OK, Zhang W, Huo F, Hupp JT. Engineering ZIF-8 Thin Films for Hybrid MOF-Based Devices. Adv Mater. 2012;24:3970–4.

23. Kuppler RJ, Timmons DJ, Fang Q-R, Li J-R, Makal TA, Young MD, et al. Potential applications of metal-organic frameworks. Coord Chem Rev [Internet]. 2009 Dec [cited 2016 Apr 20];253(23–24):3042–66. Available from: http://www.sciencedirect.com/science/article/pii/S0010854509001271

24. Lu G, Hupp JT. Metal Organic Franeworks as Sensors A ZIF (Based Fabry Perot Device as a Selective Sensor for Chemical Vapours and Gases.pdf. 2010;7832–3.

25. Urrutia A, Goicoechea J, Arregui FJ. Optical fiber sensors based on nanoparticle-embedded coatings. J Sensors. 2015;2015.

26. Hernandez FU, Morgan SP, Hayes-gill BR, Harvey D, Kinnear W, Norris A, et al. Characterization and Use of a Fiber Optic Sensor Based on PAH / SiO 2 Film for Humidity Sensing in Ventilator Care Equipment. 2016;63(9):1985–92.

27. Korposh S, Davis F, James SW, Wang T, Lee S-W, Higson S, et al. Detection of volatile organic compounds (VOCs) using an optical fibre long period grating with a calixarene anchored mesoporous thin film. Proc SPIE - Int Soc Opt Eng [Internet]. 2013;8794(1):87941I. Available from: http://www.scopus.com/inward/record.url?eid=2-s2.0-84884314640&partnerID=tZOtx3y1

28. Ekmekcioglu D, Keskin SS. Characterization of Indoor Air Particulate Matter in Selected Elementary Schools in Istanbul, Turkey. Indoor Built Environ [Internet]. 2007;16(2):169–76. Available from: http://search.ebscohost.com/login.aspx?direct=true&AuthType=ip,uid&db=eih&AN=25163144&site=ehost-live

29. Scientific Committee on Health and Environmental Risks S. Opinion on risk assessment on indoor air quality (SCHER). 2007;(29 May):33.

30. Rudge J, Gilchrist R. Excess winter morbidity among older people at risk of cold homes: A population-based study in a London borough. J Public Health (Bangkok). 2005;27(4):353–8.

31. NHS. Heatwave Plan for England. 2013;(May):21.

32. Arundel A V., Sterling EM, Biggin JH, Sterling TD. Indirect health effects of relative humidity in indoor environments. Environ Health Perspect. 1986;VOL. 65(3):351–61.

33. Husman T. Health effects of indoor-air microorganisms. Scand J Work Environ Heal. 1996;22(1):5–13.

34. Chua KJ, Chou SK, Yang WM, Yan J. Achieving better energy-efficient air conditioning - A review of technologies and strategies. Appl Energy [Internet]. 2013;104:87–104. Available from: http://dx.doi.org/10.1016/j.apenergy.2012.10.037

35. Federal-Provincial Advisory Committe on Environmental and Occupational Health. Indoor Air Quality in Office Buildings : A Technical Guide. 1995. 1-57 p.

36. Jones a. P. Indoor air quality and health. Atmos Environ. 1999;33(28):4535–64.

37. Yu C, Crump D. A review of the emission of VOCs from polymeric materials used in buildings. Build Environ. 1998;33(6):357–74.

38. Marć M, Zabiegała B, Namieśnik J. Testing and sampling devices for monitoring volatile and semi-volatile organic compounds in indoor air. TrAC - Trends Anal Chem. 2012;32:76–86.

39. Pekey, Hakan, Arslanbas D. Peksey and Arslanbas (2008) VOCs - schools - active pump - personal conc.pdf. 2008;

40. Neethirajan S, Jayas DS, Sadistap S. Carbon dioxide (CO 2) sensors for the agri-food industry-A review. Food Bioprocess Technol. 2009;2(2):115–21.

41. Liu X, Byrne RH, Adornato L, Yates KK, Kaltenbacher E, Ding X, et al. In situ spectrophotometric measurement of dissolved inorganic carbon in seawater. Environ Sci Technol. 2013;47(19):11106–14.

42. Hanson PJ, Edwards NT, Garten CT, Andrews JA. Separating root and soil microbial contributions to soil respiration: A review of methods and observations. 2000;48(1):115–46.

43. Domingues RB, Barbosa AB, Sommer U, Galv??o HM. Ammonium, nitrate and phytoplankton interactions in a freshwater tidal estuarine zone: Potential effects of cultural eutrophication. Aquat Sci. 2011;73(3):331–43.

44. U.S. EPA. Ammonia [Internet]. Contact Us CADDIS Volume 2: Sources, Stressors & Responses. [cited 2016 Jul 18]. Available from: https://www3.epa.gov/caddis/ssr_amm_int.html

45. Hu H, Liang Y, Li S, Guo Q, Wu C. A modified o -phthalaldehyde fluorometric analytical method for ultratrace ammonium in natural waters using edta-naoh as buffer. J Anal Methods Chem. 2014;2014.

46. Brzezinski MA. Vertical distribution of ammonium in stratified waters. Limnol Ocean. 1988;33(5):1176–82.

47. Eddy FB. Ammonia in estuaries and effects on fish. J Fish Biol. 2005;67(6):1495–513.

48. Hinkle SR, Böhlke JK, Duff JH, Morgan DS, Weick RJ. Aquifer-scale controls on the distribution of nitrate and ammonium in ground water near La Pine, Oregon, USA. J Hydrol. 2007;333(2–4):486–503.

49. Milne I, Seager J, Mallett M. Effects of short-term pulsed ammonia exposure on fish. Environ Toxicol Chem. 2000;19(12):2929–36.

50. Mantoura RFC, Woodward EMS. Optimization of the indophenol blue method for the automated determination of ammonia in estuarine waters. Estuar Coast Shelf Sci. 1983;17(2):219–24.

51. Li QP, Zhang JZ, Millero FJ, Hansell DA. Continuous colorimetric determination of trace ammonium in seawater with a long-path liquid waveguide capillary cell. Mar Chem. 2005;96(1–2):73–85.

52. Liang Y, Pan Y, Guo Q, Hu H, Wu C, Zhang Q. A novel analytical method for trace ammonium in freshwater and seawater using 4-methoxyphthalaldehyde as fluorescent reagent. J Anal Methods Chem. 2015;2015.

53. Berger a. How does it work?: Alcohol breath testing. Bmj. 2002;325(7377):1403–1403.

54. Gibb KA, Yee AS, Johnston CC, Martin SD, Nowak RM. Accuracy and usefulness of a breath alcohol analyzer. Ann Emerg Med. 1984;13(7):516–20.

55. Stein SE. An integrated method for spectrum extraction and compound identification from gas chromatography/mass spectrometry data. J Am Soc Mass Spectrom. 1999;10(8):770–81.

56. Selyanchyn R, Korposh S, Matsui T, Matsui H, Lee S-W. Purge and Trap Sampling Coupled to Curie Point Thermal Desorption for the Detection of Parts per Trillion 2,4,6-Trichloroanisole in Water. Chromatographia [Internet]. 2009 Feb 4 [cited 2016 Nov 23];71(611):317–21. Available from: http://www.scopus.com/inward/record.url?eid=2-s2.0-77949263586&partnerID=tZOtx3y1

57. Hussain SZ, Maqbool K. GC-MS : Principle , Technique and its application in Food Science. Int J Curr Sci. 2014;13:116–26.

58. Elosua C, Matias IR, Bariain C, Arregui FJ. Volatile Organic Compound Optical Fiber Sensors: A Review. Sensors. 2006;6(11):1440–65.

59. James SW, Tatam RP. Fibre Optic Sensors with Nano-Structured Coatings. J Opt A Pure Appl Opt [Internet]. 2006;8(7):S430–44. Available from: http://dx.doi.org/10.1088/1464-4258/8/7/S19

60. Tiwari D, Mullaney K, Korposh S, James SW, Lee S-W, Tatam RP. Ammonia sensing using lossy mode resonances in a tapered optical fibre coated with porphyrin-incorporated titanium dioxide. 2016;9916:99161H.

61. Korposh S, Okuda H, Wang T, James SW, Lee SW. U-shaped evanescent wave optical fibre sensor based on a porphyrin anchored nanoassembled thin film for high sensitivity ammonia detection. In SPIE; 2015.

62. Ascorbe J, Corres JM, Matias IR, Arregui FJ. High sensitivity humidity sensor based on cladding-etched optical fiber and lossy mode resonances. Sensors Actuators, B Chem [Internet]. 2016;233:7–16. Available from: http://dx.doi.org/10.1016/j.snb.2016.04.045

63. James SW, Korposh S, Lee S-W, Tatam RP. A long period grating-based chemical sensor insensitive to the influence of interfering parameters. Opt Express. 2014;22(7):8012–8023.

64. Sharma A, Jha R, Gupta B. Fiber-Optic Sensors Based on Surface Plasmon Resonance: A Comprehensive Review. Sensors Journal, IEEE [Internet]. 2007;7(8):1118–29. Available from: http://ieeexplore.ieee.org/search/srchabstract.jsp?arnumber=4260987&isnumber=4214860&punumber=7361&k2dockey=4260987@ieeejrns

65. Wang T, Okuda H, Lee SW. Methanol selective fibre-optic gas sensor with a nanoporous thin film of organic-inorganic hybrid multilayers. In SPIE; 2015.

66. Raoufi N, Surre F, Rajarajan M, Sun T, Grattan KT V. Fiber optic pH sensor using optimized layer-by-layer coating approach. IEEE Sens J. 2014;14(1):47–54.

67. Homola J. Surface plasmon resonance sensors for detection of chemical and biological species. Vol. 108. 2008. p. 462–93.

68. Arregui FJ, Del Villar I, Corres JM, Goicoechea J, Zamarreño CR, Elosua C, et al. Fiber-optic lossy mode resonance sensors. Procedia Eng. 2014;87(September):3–8.

69. Kant R, Tabassum R, Gupta BD. Fiber Optic SPR-Based Uric Acid Biosensor Using Uricase Entrapped Polyacrylamide Gel. IEEE PHOTONICS Technol Lett. 2016;28(19):2050–3.

70. Del Villar I, Zamarreño CR, Hernaez M, Arregui FJ, Matias IR. Generation of lossy mode resonances with absorbing thin-films. 2010;28(23):3351–7.

71. Tiwari D, Mullaney K, Korposh S, James SW, Lee S-W, Tatam RP. Ammonia sensing using lossy mode resonances in a tapered optical fibre coated with porphyrin-incorporated titanium dioxide. 2016;9916:99161H. Available from: http://proceedings.spiedigitallibrary.org/proceeding.aspx?doi=10.1117/12.2236926

72. Lee BH, Kim YH, Park KS, Eom JB, Kim MJ, Rho BS, et al. Interferometric fiber optic sensors. Sensors. 2012;12(3):2467–86.

73. Rajibul Islam M, Mahmood Ali M, Lai MH, Lim KS, Ahmad H. Chronology of fabry-perot interferometer fiber-optic sensors and their applications: A review. Sensors (Switzerland). 2014;14(4):7451–88.

74. Huang Y, Tao J, Huang X. Research Progress on F-P Interference—Based Fiber-Optic Sensors. Sensors 2016, Vol 16, Page 1424. 2016;16(9):1424.

75. Huang C, Xie W, Yang M, Dai J, Zhang B, Member S. Optical Fiber Fabry – Perot Humidity Sensor Based on Porous Al 2 O 3 Film. 2015;27(20):2127–30.

76. Huang C, Xie W, Lee D, Qi C, Yang M, Wang M, et al. Optical Fiber Humidity Sensor With Porous TiO 2 / SiO 2 / TiO 2 Coatings on Fiber Tip. 2015;27(14):1495–8.

77. Gouveia C, Markovics A, Baptista JM, Kovacs B, Jorge PAS. Measurement of CO 2 using refractometric fiber optic sensors 2 Experimental Results. In: Proceedings of the 3rd WSEAS International Conference on Advances in Sensors, Signals and Materials. Stevens Point, WI, USA; 2010. p. 169–73.

78. Alwis L, Sun T, Grattan KTV. Fibre optic long period grating-based humidity sensor probe using a Michelson interferometric arrangement. Sensors Actuators B Chem [Internet]. 2013 Mar [cited 2016 May 21];178:694–9. Available from: http://www.sciencedirect.com/science/article/pii/S0925400512012580

79. Moon DS, Kim BH, Lin A, Sun G, Han YG, Han WT, et al. The temperature sensitivity of Sagnac loop interferometer based on polarization maintaining side-hole fiber. 2007 Jun 25;15(13):7962–7.

80. Dong X, Tam HY, Shum P. Temperature-insensitive strain sensor with polarization-maintaining photonic crystal fiber based Sagnac interferometer. 2007;90(15).

81. Kang J, Dong X, Zhao C, Qian W, Li M. Simultaneous measurement of strain and temperature with a long-period fiber grating inscribed Sagnac interferometer. Opt Commun [Internet]. 2011;284(8):2145–8. Available from: http://dx.doi.org/10.1016/j.optcom.2011.01.002

82. Yuan J, Zhao C-L, Zhou Y, Yu X, Kang J, Wang J, et al. Reflective long-period fiber grating-based sensor with Sagnac fiber loop mirror for simultaneous measurement of refractive index and temperature. Appl Opt [Internet]. 2014;53(29):H85. Available from: http://ao.osa.org/abstract.cfm?URI=ao-53-29-H85

83. Gouveia C a J, Baptista JM, Jorge P a S. Refractometric Optical Fiber Platforms for Label Free Sensing. In: Current Developments in Optical Fiber Technology and. 2013. p. 345–73.

84. Yariv A. Coupled-Mode theory for guided-wave optics. IEEE J Quantum Electron. 1973;9(9):919–33.

85. Chen X. Optical Fibre Gratings for Chemical and Bio-Sensing. 2013; Available from: http://cdn.intechopen.com/pdfs/45044/InTech-Optical_fibre_gratings_for_chemical_and_bio_sensing.pdf

86. Werneck MM, Allil RCSB, Ribeiro B a, Nazaré FVB De. A Guide to Fiber Bragg Grating Sensors. 2013;1–24.

87. Erdogan T. Fiber grating spectra. J Light Technol. 1997;15(8):1277–94.

88. Vengsarkar AM, Lemaire PJ, Judkins JB, Bhatia V, Erdogan T, Sipe JE. Long-period fiber gratings as band-rejection filters. J Light Technol. 1996;14(1):58–64.

89. Patrick HJ, Kersey AD, Bucholtz F. Analysis of the response of long period fiber gratings to external index of refraction. J Light Technol. 1998;16(9):1606–12.

90. Cheung CS, Topliss SM, James SW, Tatam RP. Response of fibre optic long period gratings operating near the phase matching turning point to the deposition of nanostructured coatings. 2008;25(6):897–902. Available from: http://dx.doi.org/10.1364/JOSAB.25.000897

91. Shu X, Zhang L, Bennion I. Sensitivity characteristics of long-period fiber gratings. J Light Technol. 2002;20(2):255–66.

92. Savin S, Digonnet MJ, Kino GS, Shaw HJ. Tunable mechanically induced long-period fiber gratings. Opt Lett. 2000;25(10):710–2.

93. Kakarantzas G, Dimmick TE, Birks T a, Le Roux R, Russell PS. Miniature all-fiber devices based on CO(2) laser microstructuring of tapered fibers. Opt Lett. 2001;26(15):1137–9.

94. Rego G, Okhotnikov O, Dianov E, Sulimov V. High-Temperature Stability of Long-Period Fiber Gratings Produced Using an Electric Arc. 2001;19(10):1574–9.

95. Rego G. Arc-Induced Long Period Fiber Gratings. J Sensors [Internet]. 2016;2016:1–14. Available from: http://www.hindawi.com/journals/js/2016/3598634/

96. Wong RYN, Chehura E, Staines SE, James SW, Tatam RP. Fabrication of fiber optic long period gratings operating at the phase matching turning point using an ultraviolet laser. Appl Opt [Internet]. 2014;53(21):4669–74. Available from: http://www.ncbi.nlm.nih.gov/pubmed/25090202

97. Kondo Y, Nouchi K, Mitsuyu T, Watanabe M, Kazansky PG, Hirao K. Fabrication of long-period fiber gratings by focused irradiation of infrared femtosecond laser pulses. Opt Lett. 1999;24(10):646–8.

98. Lan X, Han Q, Wei T, Huang J, Xiao H. Turn-around-point long-period fiber gratings fabricated by CO 2 Laser point-by-point irradiations. IEEE Photonics Technol Lett. 2011;23(22):1664–6.

99. Fujimaki M, Ohki Y, Brebner JL, Roorda S. Fabrication of long-period optical fiber gratings by. Opt Lett. 2000;25(2):88–9.

100. Li X, Yue C, Xia L, Chen X, Xie S. Novel technique for long period gratings fabrication using broad spectrum ultraviolet source. Microw Opt Technol Lett. 2002;33(5):368–70.

101. Li B, Jiang L, Wang S, Tsai HL, Xiao H. Femtosecond laser fabrication of long period fiber gratings and applications in refractive index sensing. Opt Laser Technol [Internet]. 2011;43(8):1420–3. Available from: http://dx.doi.org/10.1016/j.optlastec.2011.04.011

102. Bhatia V. Temperature-insensitive and strain-insensitive long-period grating sensors for smart structures. Opt Eng. 1997;36(7):1872.

103. Ng MN, Chiang KS. Thermal effects on the transmission spectra of long-period fiber gratings. 2002;208(July):321–7.

104. Bhatia V. Applications of long-period gratings to single and multi-parameter sensing. Opt Express [Internet]. 1999;4(11):457–66. Available from: http://www.osapublishing.org/abstract.cfm?uri=oe-4-11-457%5Cnhttps://www.osapublishing.org/oe/abstract.cfm?uri=oe-4-11-457

105. James SW, Tatam RP, Twin A, Bateman R, Noonan P. Cryogenic temperature response of fibre optic long period gratings. Meas Sci Technol [Internet]. 2003;14(8):1409. Available from: http://stacks.iop.org/0957-0233/14/i=8/a=329

106. Lee BH, Liu Y, Lee SB, Choi SS, Jang JN. Displacements of the resonant peaks of a long-period fiber grating induced by a change of ambient refractive index. Opt Lett. 1997;22(23):1769–71.

107. Bhatia V, Vengsarkar a M. Optical fiber long-period grating sensors. Opt Lett. 1996;21(9):692–4.

108. Pilla P, Manzillo PF, Malachovska V, Buosciolo a, Campopiano S, Cutolo a, et al. Long period grating working in transition mode as promising technological platform for label-free biosensing. Opt Express. 2009;17(22):20039–50.

109. Falciai R, Mignani AG, Vannini A. Long period gratings as solution concentration sensors. Sensors Actuators, B Chem. 2001;74(1–3):74–7.

110. Allsop T, Zhang L, Bennion I. Detection of organic aromatic compounds in paraffin by a long-period fiber grating optical sensor with optimized sensitivity. Opt Commun. 2001;191(3–6):181–90.

111. DeLisa MP, Zhang Z, Shiloach M, Pilevar S, Davis CC, Sirkis JS, et al. Evanescent wave long-period fiber bragg grating as an immobilized antibody biosensor. Anal Chem. 2000;72(13):2895–900.

112. Korposh S, Lee S-W, James SW, Tatam RP. Refractive index sensitivity of fibre optic long period gratings with SiO2 nanoparticle based mesoporous coatings. 2011;7753:19–22. Available from: http://dx.doi.org/10.1117/12.884777

113. Rees ND, James SW, Tatam RP, Ashwell GJ. Optical fiber long-period gratings with Langmuir – Blodgett thin-film overlays. Opt Lett. 2002;27(9):686–8.

114. Arregui FJ, Matias IR, Corres JM, Del Villar I, Goicoechea J, Zamarreño CR, et al. Optical fiber sensors based on Layer-by-Layer nanostructured films. Procedia Eng [Internet]. 2010;5:1087–90. Available from: http://www.scopus.com/inward/record.url?eid=2-s2.0-78650589671&partnerID=tZOtx3y1

115. Cusano A, Pilla P, Contessa L, Iadicicco A, Campopiano S, Cutolo A, et al. High-sensitivity optical chemosensor based on coated long-period gratings for sub-ppm chemical detection in water. Appl Phys Lett. 2005;87(23):1–3.

116. Urrutia A, Goicoechea J, Ricchiuti AL, Barrera D, Sales S, Arregui FJ. Simultaneous measurement of humidity and temperature based on a partially coated optical fiber long period grating. Sensors Actuators, B Chem [Internet]. 2016;227:135–41. Available from: http://dx.doi.org/10.1016/j.snb.2015.12.031

117. Korposh S, Kodaira S, Lee SW, Batty WJ, James SW, Tatam RP. Deposition of SiO2/Polymer Nanoporous thin films on long-period grating (LPG) optical fibres and dramatic Enhancement of the resonance bands. Proc 3rd Int Conf Sens Technol ICST 2008. 2008;666–9.

118. Zheng S. Long-period fiber grating moisture sensor with nano-structured coatings for structural health monitoring. Struct Heal Monit [Internet]. 2014;14(2):148–57. Available from: http://shm.sagepub.com/content/14/2/148.abstract

119. Consales M, Berruti G, Borriello A, Giordano M, Buontempo S, Breglio G, et al. Nanoscale TiO_2-coated LPGs as radiation-tolerant humidity sensors for high-energy physics applications. Opt Lett [Internet]. 2014;39(14):4128. Available from: https://www.osapublishing.org/abstract.cfm?URI=ol-39-14-4128

120. Berruti G, Consales M, Borriello A, Giordano M, Buontempo S, Makovec A, et al. A Comparative Study of Radiation-Tolerant Fiber Optic Sensors for Relative Humidity Monitoring in High-Radiation Environments at CERN. IEEE Photonics J [Internet]. 2014;6(6):1–15. Available from: http://ieeexplore.ieee.org/lpdocs/epic03/wrapper.htm?arnumber=6909002

121. Alwis L, Sun T, Grattan Kenneth V. Analysis of Polyimide-Coated Optical Relative Humidity Sensor. IEEE Sens J. 2013;13(2):767–71.

122. Nidhi, Tiwari U, Panwar N, Kaler RS, Bhatnagar R, Kapur P. Long period fiber grating humidity sensor with gelatin/cobalt chloride coating. IEEE Sens J. 2013;13(11):4139–40.

123. Kim YH, Kim MJ, Rho BS, Park MS, Jang JH, Lee BH. Ultra sensitive fiber-optic hydrogen sensor based on high order cladding mode. IEEE Sens J. 2011;11(6):1423–6.

124. Wei XT, Wei T, Xiao H, Lin YS. Terbium doped strontium cerate enabled long period fiber gratings for high temperature sensing of hydrogen. Sensors Actuators, B Chem [Internet]. 2011;152(2):214–9. Available from: http://dx.doi.org/10.1016/j.snb.2010.12.009

125. Melo L, Burton G, Warwick S, Wild PM. Experimental Investigation of Long-Period Grating Transition Modes to Monitor CO 2 in High-Pressure Aqueous Solutions. J Light Technol. 2015;33(12):2554–60.

126. Wang T, Yasukochi W, Korposh S, James SW, Tatam RP, Lee S-W. A long period grating optical fiber sensor with nano-assembled porphyrin layers for detecting ammonia gas. Sensors Actuators B Chem [Internet]. 2016;228:573–80. Available from: http://linkinghub.elsevier.com/retrieve/pii/S0925400516300594

127. Wang T, Korposh S, James S, Tatam R, Lee SW. Optical fiber long period grating sensor with a polyelectrolyte alternate thin film for gas sensing of amine odors. Sensors Actuators, B Chem [Internet]. 2013;185:117–24. Available from: http://dx.doi.org/10.1016/j.snb.2013.04.034

128. Wang T, Korposh S, Wong R, James S, Tatam R, Lee S-W. A Novel Ammonia Gas Sensor Using a Nanoassembled Polyelectrolyte Thin Film on Fiber-optic Long-period Gratings. Chem Lett [Internet]. 2012;41(10):1297–9. Available from: http://www.scopus.com/inward/record.url?eid=2-s2.0-84868268827&partnerID=tZOtx3y1

129. Korposh S, Chianella I, Guerreiro A, Caygill S, Piletsky S, James SW, et al. Selective vancomycin detection using optical fibre long period gratings functionalised with molecularly imprinted polymer nanoparticles. Analyst [Internet]. 2014;139(9):2229–36. Available from: http://www.ncbi.nlm.nih.gov/pubmed/24634909

130. Cooper KL, Bandara AB, Wang Y, Wang A, Inzana TJ. Photonic biosensor assays to detect and distinguish subspecies of Francisella tularensis. Sensors. 2011;11(3):3004–19.

131. Bandara AB, Zuo Z, Ramachandran S, Ritter A, Heflin JR, Inzana TJ. Detection of methicillin-resistant staphylococci by biosensor assay consisting of nanoscale films on optical fiber long-period gratings. Biosens Bioelectron. 2015;70:433–40.

132. Queiros RB, Gouveia C, Fernandes JRA, Jorge PAS. Evanescent wave DNA-aptamer biosensor based on long period gratings for the specific recognition of E. coli outer membrane proteins. Biosens Bioelectron [Internet]. 2014;62:227–33. Available from: http://dx.doi.org/10.1016/j.bios.2014.06.062

133. Smietana M, Bock WJ, Mikulic P, Ng A, Chinnappan R, Zourob M. Detection of bacteria using bacteriophages as recognition elements immobilized on long-period fiber gratings. Opt Express. 2011;19(9):7971–8.

134. Brzozowska E, Smietana M, Koba M, G??rska S, Pawlik K, Gamian A, et al. Recognition of bacterial lipopolysaccharide using bacteriophage-adhesin-coated long-period gratings. Biosens Bioelectron. 2015;67:93–9.

135. Koba M, Smietana M, Brzozowska E, Gorska S, Mikulic P, Bock WJ. Reusable Bacteriophage Adhesin-Coated Long-Period Grating Sensor for Bacterial Lipopolysaccharide Recognition. J Light Technol [Internet]. 2015;33(12):2518–23. Available from: http://ieeexplore.ieee.org/lpdocs/epic03/wrapper.htm?arnumber=6930716

136. Smietana M, Koba M, Brzozowska E, Krogulski K, Nakonieczny J, Wachnicki L, et al. Label-free sensitivity of long-period gratings enhanced by atomic layer deposited TiO_2 nano-overlays. Opt Express [Internet]. 2015;23(7):8441. Available from: http://www.opticsinfobase.org/abstract.cfm?URI=oe-23-7-8441

137. Baliyan A, Sital S, Tiwari U, Gupta R, Sharma EK. Long period fiber grating based sensor for the detection of triacylglycerides. Biosens Bioelectron [Internet]. 2016;79:693–700. Available from: http://dx.doi.org/10.1016/j.bios.2015.12.089

138. Mathews CB, Libish TM, Kaushalkumar B, Vivek V, Prabhu R, Radhakrishnan P. A fiber optic biosensor for the detection of cholesterol levels based on chitosan coated long period grating. Optoelectron Lett [Internet]. 2016;12(1):23–6. Available from: http://link.springer.com/10.1007/s11801-016-5229-9

139. Deep A, Tiwari U, Kumar P, Mishra V, Jain SC, Singh N, et al. Immobilization of enzyme on long period grating fibers for sensitive glucose detection. Biosens Bioelectron [Internet]. 2012;33(1):190–5. Available from: http://dx.doi.org/10.1016/j.bios.2011.12.051

140. Marques L, Hernandez FU, James SW, Morgan SP, Clark M, Tatam RP, et al. Highly sensitive optical fibre long period grating biosensor anchored with silica core gold shell nanoparticles. Biosens Bioelectron [Internet]. 2016;75:222–31. Available from: http://dx.doi.org/10.1016/j.bios.2015.08.046

141. Chiavaioli F, Biswas P, Trono C, Jana S, Bandyopadhyay S, Basumallick N, et al. Sol-Gel-Based Titania-Silica Thin Film Overlay for Long Period Fiber Grating-Based Biosensors. Anal Chem. 2015;87(24):12024–31.

142. Chiavaioli F, Trono C, Giannetti A, Brenci M, Baldini F. Characterisation of a label-free biosensor based on long period grating. J Biophotonics. 2012;7(5):312–22.

143. Chiavaioli F, Biswas P, Trono C, Bandyopadhyay S, Giannetti A, Tombelli S, et al. Towards sensitive label-free immunosensing by means of turn-around point long period fiber gratings. Biosens Bioelectron [Internet]. 2014;60:305–10. Available from: http://dx.doi.org/10.1016/j.bios.2014.04.042

144. Pilla P, Sandomenico A, Malachovská V, Borriello A, Giordano M, Cutolo A, et al. A protein-based biointerfacing route toward label-free immunoassays with long period gratings in transition mode. Biosens Bioelectron [Internet]. 2012;31(1):486–91. Available from: http://dx.doi.org/10.1016/j.bios.2011.11.022

145. Partridge M, Wong R, James SW, Davis F, Higson SPJ, Tatam RP. Long period grating based toluene sensor for use with water contamination. Sensors Actuators, B Chem [Internet]. 2014;203:621–5. Available from: http://dx.doi.org/10.1016/j.snb.2014.06.121

146. Yang J, Zhou L, Huang J, Tao C, Li X, Chen W. Sensitivity enhancing of transition mode long-period fiber grating as methane sensor using high refractive index polycarbonate/cryptophane A overlay deposition. Sensors Actuators, B Chem [Internet]. 2015;207(Part A):477–80. Available from: http://dx.doi.org/10.1016/j.snb.2014.10.013

147. Korposh S, Selyanchyn R, James S, Tatam R, Lee SW. Identification and quality assessment of beverages using a long period grating fibre-optic sensor modified with a mesoporous thin film. Sens Bio-Sensing Res [Internet]. 2014;1:26–33. Available from: http://dx.doi.org/10.1016/j.sbsr.2014.06.001

148. Yang J, Tao C, Li X, Zhu G, Chen W. Long-period fiber grating sensor with a styrene-acrylonitrile nano-film incorporating cryptophane A for methane detection. Opt Express. 2011;19(15):14696.

149. Konstantaki M, Klini A, Anglos D, Pissadakis S. An ethanol vapor detection probe based on a ZnO nanorod coated optical fiber long period grating. Opt Express. 2012;20(8):8472.

150. Korposh S, Wang T, James S, Tatam R, Lee S-W. Pronounced aromatic carboxylic acid detection using a layer-by-layer mesoporous coating on optical fibre long period grating. Sensors Actuators B Chem [Internet]. 2012 Oct [cited 2016 May 21];173:300–9. Available from: http://www.sciencedirect.com/science/article/pii/S0925400512006740

151. Furukawa H, Cordova KE, O'Keeffe M, Yaghi OM. The chemistry and applications of metal-organic frameworks. Science [Internet]. 2013;341(6149):1230444. Available from: http://www.sciencemag.org/content/341/6149/1230444.full

152. Farha OK, Eryazici I, Jeong NC, Hauser BG, Wilmer CE, Sarjeant AA, et al. Metal-organic framework materials with ultrahigh surface areas: Is the sky the limit? J Am Chem Soc. 2012;134(36):15016–21.

153. Kreno LE, Leong K, Farha OK, Allendorf M, Duyne RP Van, Hupp JT. Metal À Organic Framework Materials as Chemical Sensors. Chem Rev. 2012;112:1105–25.

154. Betard A and, Fischer RA. Metal À Organic Framework Thin Films : From Fundamentals to. 2012;1055–83.

155. Mueller U, Schubert M, Teich F, Puetter H, Schierle-Arndt K, Pastré J. Metal–organic frameworks—prospective industrial applications. J Mater Chem [Internet]. 2006;16(7):626–36. Available from: http://pubs.rsc.org/en/content/articlehtml/2006/jm/b511962f

156. Suh MP, Park HJ, Prasad TK, Lim D. Hydrogen Storage in Metal À Organic Frameworks. 2012;782–835.

157. Li J-R, Kuppler RJ, Zhou H-C. Selective gas adsorption and separation in metal-organic frameworks. Chem Soc Rev [Internet]. 2009 May [cited 2016 May 26];38(5):1477–504. Available from: http://www.scopus.com/inward/record.url?eid=2-s2.0-65349158272&partnerID=tZOtx3y1

158. Li J, Sculley J, Zhou H. Metal À Organic Frameworks for Separations. 2012;869–932.

159. Yoon M, Srirambalaji R, Kim K. Homochiral metal-organic frameworks for asymmetric heterogeneous catalysis. Chem Rev. 2012;112(2):1196–231.

160. Greeves N. No Title. chemtube3D.com.

161. Cohen SM. Postsynthetic methods for the functionalization of metal-organic frameworks. Chem Rev. 2012;112(2):970–1000.

162. Lei J, Qian R, Ling P, Cui L, Ju H. Design and sensing applications of metal-organic framework composites. TrAC - Trends Anal Chem [Internet]. 2014;58:71–8. Available from: http://dx.doi.org/10.1016/j.trac.2014.02.012

163. Doherty CM, Buso D, Hill AJ, Furukawa S, Kitagawa S, Falcaro P. Using functional nano- and microparticles for the preparation of metal-organic framework composites with novel properties. Acc Chem Res. 2014;47(2):396–405.

164. Kneipp K, Wang Y, Kneipp H, Perelman LT, Itzkan I, Dasari RR, et al. Single molecule detection using surface-enhanced Raman scattering (SERS). Phys Rev Lett. 1997;78(9):1667–1670.

165. Nikoobakht B, El-Sayed MA. Surface-Enhanced Raman Scattering Studies on Aggregated Gold Nanorods †. J Phys Chem A [Internet]. 2003 May [cited 2016 May 11];107(18):3372–8. Available from: http://www.scopus.com/inward/record.url?eid=2-s2.0-0037657957&partnerID=tZOtx3y1

166. Sugikawa K, Furukawa Y, Sada K. SERS-active metal-organic frameworks embedding gold nanorods. Chem Mater. 2011;23(13):3132–4.

167. Bux H, Liang F, Li Y, Cravillon J, Wiebcke M. Zeolitic Imidazolate Framework Molecular Sieving Membrane Titania Support. J Am Chem Soc. 2009;131:16000–1.

168. Eddaoudi M, Kim J, Rosi N, Vodak D, Wachter J, O'Keeffe M, et al. Systematic design of pore size and functionality in isoreticular MOFs and their application in methane storage. Science [Internet]. 2002 Jan 18 [cited 2016 Mar 23];295(5554):469–72. Available from: http://www.scopus.com/inward/record.url?eid=2-s2.0-0037127013&partnerID=tZOtx3y1

169. Chui SSY, Lo SMF, Charmant JPH, Orpen a G, Williams ID. A Chemically Functionalizable Nanoporous Material [Cu_3(TMA)_2(H_2O)_3]_n. Science (80-) [Internet]. 1999;283(February):1148–50. Available from: http://www.jstor.org/stable/2896750

170. Liu B, Fischer RA. Liquid-phase epitaxy of metal organic framework thin films. Sci China Chem. 2011;54(12):1851–66.

171. Liu J, Redel E, Walheim S, Wang Z, Oberst V, Liu J, et al. Monolithic High Performance Surface Anchored Metal−Organic Framework Bragg Reflector for Optical Sensing. Chem Mater [Internet]. 2015 Mar 24 [cited 2016 Apr 25];27(6):1991–6. Available from: http://www.scopus.com/inward/record.url?eid=2-s2.0-84925727378&partnerID=tZOtx3y1

172. Wannapaiboon S, Tu M, Sumida K, Khaletskaya K, Furukawa S, Kitagawa S, et al. Hierarchical structuring of metal–organic framework thin-films on quartz crystal microbalance (QCM) substrates for selective adsorption applications. J Mater Chem A [Internet]. 2015 [cited 2016 May 26];3(46):23385–94. Available from: http://www.scopus.com/inward/record.url?eid=2-s2.0-84947776922&partnerID=tZOtx3y1

173. Makiura R, Motoyama S, Umemura Y, Yamanaka H, Sakata O, Kitagawa H. Surface nano-architecture of a metal-organic framework. Nat Mater [Internet]. 2010;9(7):565–71. Available from: http://www.ncbi.nlm.nih.gov/pubmed/20512155

174. So MC, Jin S, Son H, Wiederrecht GP, Farha OK, Hupp JT. Layer-by-Layer Fabrication of Oriented Porous Thin Films Based on Porphyrin-Containing Metal − Organic Frameworks. 2013;(L):1–4.

175. Shekhah O, Fu L, Sougrat R, Belmabkhout Y, Cairns AJ, Giannelis EP, et al. Successful implementation of the stepwise layer-by-layer growth of MOF thin films on confined surfaces: mesoporous silica foam as a first case study. Chem Commun. 2012;48(93):11434.

176. Nijem N, F??rsich K, Kelly ST, Swain C, Leone SR, Gilles MK. HKUST-1 thin film layer-by-layer liquid phase epitaxial growth: film properties and stability dependence on layer number. Cryst Growth Des. 2015;15(6):2948–57.

177. Shekhah O, Wang H, Zacher D, Fischer RA, Wöll C. Growth mechanism of metal-organic frameworks: Insights into the nucleation by employing a step-by-step route. 2009 Jun 22;48(27):5038–41.

178. Huang A, Bux H, Steinbach F, Caro J. Molecular-sieve membrane with hydrogen permselectivity: ZIF-22 in LTA topology prepared with 3-aminopropyltriethoxysilane as covalent linker. Angew Chemie - Int Ed. 2010;49(29):4958–61.

179. McCarthy MC, Varela-Guerrero V, Barnett G V., Jeong HK. Synthesis of zeolitic imidazolate framework films and membranes with controlled microstructures. Langmuir. 2010;26(18):14636–41.

180. Xu G, Yao J, Wang K, He L, Webley PA, Chen C sheng, et al. Preparation of ZIF-8 membranes supported on ceramic hollow fibers from a concentrated synthesis gel. J Memb Sci. 2011;385–386(1):187–93.

181. Guo H, Zhu G, Hewitt IJ, Qiu S. Twin copper source" growth of metal-organic framework membrane: Cu3(BTC)2 with high permeability and selectivity for recycling H2. J Am Chem Soc. 2009;131(5):1646–7.

182. Huang A, Liang F, Steinbach F, Caro J. Preparation and separation properties of LTA membranes by using 3-aminopropyltriethoxysilane as covalent linker. J Memb Sci. 2010;350(1–2):5–9.

183. Shekhah O, Wang H, Kowarik S, Schreiber F, Paulus M, Tolan M, et al. Step-by-step route for the synthesis of metal-organic frameworks. J Am Chem Soc. 2007;129(49):15118–9.

184. Hermes S, Schröder F, Chelmowski R, Wöll C, Fischer RA. Selective nucleation and growth of metal-organic open framework thin films on patterned COOH/CF3-terminated self-assembled monolayers on Au(111). J Am Chem Soc. 2005;127(40):13744–5.

185. Biemmi E, Scherb C, Bein T. Oriented growth of the metal organic framework Cu(3)(BTC)(2)(H(2)O)(3).xH(2)O tunable with functionalized self-assembled monolayers. J Am Chem Soc. 2007;129(26):8054–5.

186. Lew CM, Cai R, Yan Y. Zeolite thin films: From computer chips to space stations. Acc Chem Res. 2010;43(2):210–9.

187. Guerrero VV, Yoo Y, McCarthy MC, Jeong H-K. HKUST-1 membranes on porous supports using secondary growth. J Mater Chem. 2010;20:3938.

188. Zou X, Zhu G, Zhang F, Guo M, Qiu S. Facile fabrication of metal–organic framework films promoted by colloidal seeds on various substrates. CrystEngComm [Internet]. 2010;12(2):352. Available from: http://xlink.rsc.org/?DOI=b912470e

189. Li Y-S, Bux H, Feldhoff A, Li G-L, Yang W-S, Caro J. Controllable synthesis of metal-organic frameworks: From MOF nanorods to oriented MOF membranes. Adv Mater [Internet]. 2010 Aug 10 [cited 2016 May 26];22(30):3322–6. Available from: http://www.scopus.com/inward/record.url?eid=2-s2.0-77955391856&partnerID=tZOtx3y1

190. Yoo Y, Lai Z, Jeong HK. Fabrication of MOF-5 membranes using microwave-induced rapid seeding and solvothermal secondary growth. Microporous Mesoporous Mater [Internet]. 2009;123(1–3):100–6. Available from: http://dx.doi.org/10.1016/j.micromeso.2009.03.036

191. Yusenko K, Meilikhov M, Zacher D, Wieland F, Sternemann C, Stammer X, et al. Step-by-step growth of highly oriented and continuous seeding layers of [Cu2(ndc)2(dabco)] on bare oxide and nitride substrates. CrystEngComm. 2010;12:2086.

192. Ameloot R, Stappers L, Fransaer J, Alaerts L, Sels BF, De Vos DE. Patterned Growth of Metal-Organic Framework Coatings by Electrochemical Synthesis. Chem Mater [Internet]. 2009 Jul 14 [cited 2016 May 26];21(13):2580–2. Available from: http://www.scopus.com/inward/record.url?eid=2-s2.0-67650670715&partnerID=tZOtx3y1

193. Cui Y, Yue Y, Qian G, Chen B. Luminescent functional metal-organic frameworks. Chem Rev. 2012;112(2):1126–62.

194. Guo H, Zhu Y, Qiu S, Lercher JA, Zhang H. Coordination modulation induced synthesis of nanoscale Eu(1-x)Tb(x)-metal-organic frameworks for luminescent thin films. Adv Mater [Internet]. 2010 Oct 1 [cited 2016 May 26];22(37):4190–2. Available from: http://www.scopus.com/inward/record.url?eid=2-s2.0-77957583791&partnerID=tZOtx3y1

195. Kumar P, Deep A, Kim K-H. Metal organic frameworks for sensing applications. TrAC Trends Anal Chem [Internet]. 2015;73:39–53. Available from: http://www.sciencedirect.com/science/article/pii/S0165993615001090

196. Hu Z, Deibert BJ, Li J. Luminescent metal-organic frameworks for chemical sensing and explosive detection. Chem Soc Rev [Internet]. 2014;43(16):5815–40. Available from: http://www.ncbi.nlm.nih.gov/pubmed/24577142

197. Ren XY, Lu LH. Luminescent nanoscale metal-organic frameworks for chemical sensing. Chinese Chem Lett [Internet]. 2015;26(12):1439–45. Available from: http://dx.doi.org/10.1016/j.cclet.2015.10.014

198. Cui Y, Chen B, Qian G. Lanthanide metal-organic frameworks for luminescent sensing and light-emitting applications. Coord Chem Rev [Internet]. 2014 Aug [cited 2016 May 26];273–274:76–86. Available from: http://www.scopus.com/inward/record.url?eid=2-s2.0-84901601295&partnerID=tZOtx3y1

199. Park KS, Ni Z, Côté AP, Choi JY, Huang R, Uribe-Romo FJ, et al. Exceptional chemical and thermal stability of zeolitic imidazolate frameworks. Proc Natl Acad Sci U S A. 2006;103(27):10186–91.

200. Banerjee D, Hu Z, Li J. Luminescent metal-organic frameworks as explosive sensors. Dalton Trans [Internet]. 2014 Jul 28 [cited 2016 May 26];43(28):10668–85. Available from: http://www.scopus.com/inward/record.url?eid=2-s2.0-84903445963&partnerID=tZOtx3y1

201. Liu L, Hao J, Shi Y, Qiu J, Hao C. Roles of hydrogen bonds and π–π stacking in the optical detection of nitro-explosives with a luminescent metal–organic framework as the sensor. RSC Adv [Internet]. 2015 [cited 2016 May 26];5(4):3045–53. Available from: http://www.scopus.com/inward/record.url?eid=2-s2.0-84962464662&partnerID=tZOtx3y1

202. Qu X-L, Gui D, Zheng X-L, Li R, Han H-L, Li X, et al. A Cd(<scp>ii</scp>)-based metal–organic framework as a luminance sensor to nitrobenzene and Tb(<scp>iii</scp>) ion. Dalt Trans [Internet]. 2016;6983–9. Available from: http://xlink.rsc.org/?DOI=C6DT00162A

203. Liu W, Yin X-B. Metal organic frameworks for electrochemical applications. TrAC Trends Anal Chem [Internet]. 2015;5(11):9269. Available from: http://dx.doi.org/10.1016/j.trac.2015.07.011%5Cnhttp://linkinghub.elsevier.com/retrieve/pii/S0165993615002617

204. Morozan A, Jaouen F. Metal organic frameworks for electrochemical applications. Energy Environ Sci [Internet]. 2012 [cited 2016 Apr 19];5(11):9269. Available from: http://www.scopus.com/inward/record.url?eid=2-s2.0-84867633411&partnerID=tZOtx3y1

205. Ma W, Jiang Q, Yu P, Yang L, Mao L. Zeolitic imidazolate framework-based electrochemical biosensor for in vivo electrochemical measurements. Anal Chem. 2013;85(15):7550–7.

206. Ferreira GNM, da-Silva A-C, Tomé B. Acoustic wave biosensors: physical models and biological applications of quartz crystal microbalance. Trends Biotechnol. 2009;27(12):689–97.

207. Nazari MA, Orouzandeh MOALIF, Ivarathne CHMD, Idiroglou FOS, Artinez MARUM, Onstas KRK, et al. UiO-66 MOF end-face-coated optical fiber in aqueous contaminant detection. 2016;41(8):1696–9.

208. Hinterholzinger FM, Ranft A, Feckl JM, Ruhle B, Bein T, Lotsch B V. One-dimensional metal-organic framework photonic crystals used as platforms for vapor sorption. J Mater Chem. 2012;22(20):10356–62.

209. Khalil MMH, Shahat A, Radwan A, El-Shahat MF. Colorimetric determination of Cu(II) ions in biological samples using metal-organic framework as scaffold. Sensors Actuators B Chem [Internet]. 2016;233:272–80. Available from: http://linkinghub.elsevier.com/retrieve/pii/S0925400516305615

210. Chong X, Kim KJ, Ohodnicki PR, Li E, Chang CH, Wang AX. Ultrashort Near-Infrared Fiber-Optic Sensors for Carbon Dioxide Detection. IEEE Sens J. 2015;15(9):5327–32.

211. Chong X, Kim KJ, Li E, Zhang Y, Ohodnicki PR, Chang CH, et al. Near-infrared absorption gas sensing with metal-organic framework on optical fibers. Sensors Actuators, B Chem [Internet]. 2016;232:43–51. Available from: http://dx.doi.org/10.1016/j.snb.2016.03.135

212. Pentyala V, Davydovskaya P, Ade M, Pohle R, Urban G. Carbon dioxide gas detection by open metal site metal organic frameworks and surface functionalized metal organic frameworks. Sensors Actuators, B Chem [Internet]. 2016;225:363–8. Available from: http://dx.doi.org/10.1016/j.snb.2015.11.071

213. Pentyala V, Davydovskaya P, Ade M, Pohle R, Urban G. Metal-organic frameworks for alcohol gas sensor. Sensors Actuators, B Chem [Internet]. 2016;222:904–9. Available from: http://dx.doi.org/10.1016/j.snb.2015.09.014

214. Kreno LE, Hupp JT, Van Duyne RP. Metal-organic framework thin film for enhanced localized surface Plasmon resonance gas sensing. Anal Chem. 2010;82(19):8042–6.

215. Ye CC, James SW, Tatam RP. Simultaneous temperature and bend sensing with long-period fiber gratings. Opt Lett [Internet]. 2000;25(14):1007–9. Available from: http://www.ncbi.nlm.nih.gov/pubmed/18064255

216. Partirdge MC. Errant Science [Internet]. Openly peak detecting. 2013 [cited 2017 Jan 9]. Available from: http://errantscience.com/blog/2013/01/23/openly-peak-detecting/

217. Correia R, Blackman OR, Hernandez FU, Korposh S, Morgan SP, Hayes-Gill BR, et al. Highly sensitive contact pressure measurements using FBG patch in endotracheal tube cuff. In: Proceedings of SPIE - The International Society for Optical Engineering. 2016.

218. Hernandez FU, Correia R, Korposh S, Morgan SP, Hayes-Gill BR, James SW, et al. Measurements of endotracheal tube cuff contact pressure using fibre Bragg gratings. In: Proceedings of SPIE - The International Society for Optical Engineering. 2015.

219. Demessence A, Boissière C, Grosso D, Horcajada P, Serre C, Férey G, et al. Adsorption properties in high optical quality nanoZIF-8 thin films with tunable thickness. J Mater Chem. 2010;20(36):7676.

220. Korposh S, James SW, Lee S-W, Topliss S, Cheung SC, Batty WJ, et al. Fiber optic long period grating sensors with a nanoassembled mesoporous film of SiO2 nanoparticles. Opt Express. 2010;18(12):13227–38.

221. Cookney J, Ogieglo W, Hrabanek P, Vankelecom I, Fila V, Benes NE. Dynamic response of ultrathin highly dense ZIF-8 nanofilms. Chem Commun [Internet]. 2014;50(79):11698–700. Available from: http://www.ncbi.nlm.nih.gov/pubmed/25142780

222. Ishaq IM, Quintela A, James SW, Ashwell GJ, Lopez-Higuera JM, Tatam RP. Modification of the refractive index response of long period gratings using thin film overlays. Sensors Actuators, B Chem. 2005;107(2):738–41.

223. Silberberg M. Chemistry, The Molecular Nature of Matter and Change. 4th ed. New York: McGraw-Hill; 2006.

224. Domènech-Gil G, Samà J, Pellegrino P, Barth S, Gràcia I, Cané C, et al. Gas nanosensors based on individual indium oxide nanostructures. Procedia Eng [Internet]. 2015;120:795–8. Available from: http://dx.doi.org/10.1016/j.snb.2016.07.084

225. Health and Safety Executive. EH4O / 2005 Workplace exposure limits EH4O / 2005 Workplace exposure limits. Eh40/2005. 2011;(March 2013):1–74.

226. Kao KW, Hsu MC, Chang YH, Gwo S, Andrew Yeh J. A Sub-ppm acetone gas sensor for diabetes detection using 10 nm thick ultrathin InN FETs. Sensors (Switzerland). 2012;12(6):7157–68.

227. Deng C, Zhang J, Yu X, Zhang W, Zhang X. Determination of acetone in human breath by gas chromatography-mass spectrometry and solid-phase microextraction with on-fiber derivatization. J Chromatogr B Anal Technol Biomed Life Sci. 2004;810(2):269–75.

228. Anderson JC. Measuring breath acetone for monitoring fat loss: Review. Obesity. 2015;23(12):2327–34.

229. Gutierrez-Sevillano, Juan Jose Vicent-Luna JM, Dubbeldam D, Calero S. Molecular mechanisms for adsorption in Cu-BTC metal organic framework. J Phys Chem C. 2013;117(21):11357–66.

230. Shah MN, Gonzalez M a, McCarthy MC, Jeong H-K. An unconventional rapid synthesis of high performance metal-organic framework membranes. Langmuir [Internet]. 2013;29(25):7896–902. Available from: http://www.ncbi.nlm.nih.gov/pubmed/23721152

231. Ramalho O, Wyart G, Mandin C, Blondeau P, Cabanes PA, Leclerc N, et al. Association of carbon dioxide with indoor air pollutants and exceedance of health guideline values. Build Environ. 2015;93(P1):115–24.

232. Smolander M, Hurme E, Ahvenainen R. Leak indicators for modified-atmosphere packages. Trends Food Sci Technol. 1997;8(4):101–6.

233. Hassan AK, Nabok A V, Ray AK, Lucke A, Smith K, Stirling CJM, et al. Thin films of calix-4-resorcinarene deposited by spin coating and Langmuir–Blodgett techniques: determination of film parameters by surface plasmon resonance. Mat Sci Engr. 1999;8–9:251–5.

234. Murphy RP, James SW, Tatam RP. Multiplexing of fiber-optic long-period grating-based interferometric sensors. J Light Technol. 2007;25(3):825–9.

235. Health and Safety Executive. Workplace health, safety and welfare. 2013;19. Available from: http://www.dontbreakbritain.org/uploaded/documents/Workplace (Health, Safety and Welfare) Regulations1992 (Approved Code of Practice)11-4892.pdf